UNIVERSITY
of
GLASGOW

Investigation of Orthogonal Blade-Vortex Interaction using a Particle Image Velocimetry Technique

Juliana Marie Early BEng

Dissertation submitted to the University of Glasgow
for the Degree of Doctor of Philosophy

Department of Aerospace Engineering, March 2006

The work contained within this thesis was carried out under a grant from the United States Army Research, Development and Standardization Group – United Kingdom, grant number N62558-02-M-6011.

Abstract

The complex flowfield which is associated with a rotor wake gives rise to the multitude of aerodynamic interactions that may occur during rotorcraft operation. These interactions may give rise to undesirable noise and lead to unacceptable performance degradation, and as such the investigation of the fundamental mechanics of such interactions has grown in importance in the past few years. One such interaction, that which occurs between the tail rotor and the trailing tip vortices shed from the main rotor assembly, is the focus of the current investigation. As the purpose of the tail rotor is to provide a balance for the torque of the main rotor, these types of interaction will adversely impact on the overall rotorcraft performance.

The basis of the present thesis has been an experimental investigation of the orthogonal BVI, in which the axis of the interacting vortex (in the plane of the vortex core axial flow) is nominally orthogonal to the interacting blade chordline, representing the tail rotor interaction. The tests have been conducted using a specifically designed facility at the University of Glasgow, with the flow interrogated using a Particle Image Velocimetry (PIV) technique. The PIV method allows global flowfield information to be obtained pertaining to the nature of the interaction. The methodology was benchmarked against synthetic flowfields, and with the accuracy of the flowfield measurements improved dramatically with the implementation of the Forward/Reverse Tile Test (FRTT), which improved the accuracy in the flowfields to 3% in two-dimensional interrogation, and 5% in three-dimensional.

The interrogation of the flowfield around a representative tail rotor blade demonstrated that the characteristics imparted vortex due to the BVI event could be attributed to the manner in which the axial flow component of the vortex was affected by the interaction. The results for the isolated flow conditions agreed well

with those from previous measurements of the vortical structure, and the post-interaction structure clearly indicated distinct differences determined by the direction of the axial flow relative to the blade chordline. Initial testing indicated that the thickness ratio had a marked effect on the progression of the OBVI, and for a suitably high thickness ratio, there was little evidence to suggest that the vortex core axial flow is 'cut' by the interacting body in the manner observed for the lower thickness ratios. For lower thickness ratios, as the vortex core is blocked by the interacting blade surface, the retardation of the axial component on the blade lower surface leads to a rapid redistribution of the fluid into the surrounding flow, and the corresponding enlargement and distortion to the vortex tangential velocity components promoted by the radial outflow. On the upper blade side, regions of negative axial flow velocity indicate the presence of some fluid passing down through the core towards the surface of the blade, which are accompanied by a split divergence pattern around the vortex core. The effects immediately behind the trailing edge continue to be of interest due to the manner in which the vortex might be regenerated after the interaction and before any subsequent interactions with following blades. A relative lack of distortion within the out-of-plane component indicates that a rapid regeneration of the axial flow component may occur once the vortex has passed over the trailing edge.

The use of passive control techniques in reduction of the effects associated with the orthogonal BVI have also been addressed, considering the effect of a counter-rotating vortex pair on the progression of the interaction. Although the inclusion of a notch in the leading edge and outboard sweep on the rotor blade producing the representative trailing tip vortex did produce a well defined inboard vortex structure, there is evidence to suggest that this structure is ingested into the outboard tip vortex, as there is no significant modification to the progression of the OBVI.

Acknowledgements

Firstly, I would like to thank my supervisor, Dr. Richard Green, for all of his help, support and encouragement throughout. To follow that, I would also like to thank Dr. Douglas Thomson, for being the voice of reason at every stage, and Professor Frank Coton for all his help and time.

To everyone in the workshop – Tony Smedley, Davy Perrins, Neil Owen, Jimmy Carr, John Kitching, Cammie Millar and Aaron Fraser, who put up with a lot.

I also owe many thanks to the following people: Dave Lawrie, Calum Watterson, Naomi Crawford, Simon Hall, Mark Price, Ricky Curran, Professor Raghunathan, Sylvie Castagne, Karen Agnew and probably a dozen more people that I can't think of at the moment, who all had their own way of giving me advice.

I would especially like to thank my mum and dad, who have been there for me and given me all the support I could ever ask for and more throughout my entire time in Glasgow.

The work contained within this thesis was carried out under a grant from the United States Army Research, Development and Standardization Group – United Kingdom, grant number N62558-02-M-6011.

Contents

List of Figures

Nomenclature

General Symbol	Definition	Units
c	Blade Chord	m
C_T	Rotor Thrust Coefficient	--
D	Displacement	m
d_n	Cylinder n diameter	m
d_p	Particle Diameter	m
dx_1, dy_1	Particle Location Image 1	m
dx_2, dy_2	Particle Location Image 2	m
h	Helicity Density	--
I	Blade Impact Parameter	--
l	length	m
M_{TP}	Mach Tip Number	--
r	Radial Distance from Core Centre	m
T	Blade Thickness	m
t'	Time at t_1	s
t''	Time at t_2	s
Δt	Change in Time	s
u,v,w	Local Flow Velocity components	ms^{-1}
$U\infty$	Freestream Velocity	ms^{-1}
U_f	Fluid Velocity	ms^{-1}
U_p	Particle Velocity	ms^{-1}
ω_z	z component of vorticity	--
x,y,z	Co-ordinates within wind tunnel working section	m
x_1, y_1, z_1	Co-ordinates in Image 1	m
x_2, y_2, z_2	Co-ordinates in Image 2	m
x_p, y_p, z_p	Co-ordinates of Particle	m
V	Relative Velocity	ms^{-1}
V_x	Axial Velocity of the Vortex Core	ms^{-1}
V_z	Normal Velocity of the Vortex Core	ms^{-1}

Greek Symbol	Definition	Units
α_1, α_2	Viewing Angle in x-z plane	deg
α_{tpp}	Rotor Tip Path Plane Angle	deg
β_1, β_2	Viewing Angle in y-z plane	deg
ε	Error Measurement	--

$\mu(rotor)$	Rotor Advance Ratio	--
μ	Dynamic Viscosity	$kgm^{-1}s^{-1}$
ρ_p	Particle Density	kgm^{-3}
σ	Vortex Core Diameter	m
ω	Rotor Rotational Speed	$degs^{-1}$
Δ	Divergence	--
Γ	Circulation	--
Ω	Angular Velocity	$degs^{-1}$

Abbreviations

Symbol	Definition
BVI	Blade Vortex Interaction
CCD	Charge Coupled Device
dB	Decibel
DPIV	Digital Particle Image Velocimetry
FFT	Fast Fourier Transform
FRTT	Forward and Reverse Tile Test
HHC	Higher Harmonic Control
HSI	High Speed Impulsive
HWA	Hot Wire Anemometry
IA	Interactional Aerodynamics
IBC	Individual Blade Control
LBC	Local Blade Control
LDV	Laser Doppler Velocimetry
LIF	Laser Induced Fluorescence
NACA	National Advisory Committee for Aeronautics
OBVI	Orthogonal Blade-Vortex Interaction
PBVI	Parallel Blade-Vortex Interaction
SNR	Signal to Noise Ratio
2D2C PIV	Two Dimensional, Two Component PIV
2D3C PIV	Two Dimensional, Three Component PIV

Chapter 1 : Introduction

This thesis is intended to extend the current knowledge base in the field of helicopter interactional aerodynamics, deepening the understanding of the mechanisms behind the orthogonal blade-vortex interaction. The specific issue of the deformation of the vortex as the interaction progresses is addressed, considering the effect not only to the vortex core, but also to the local surrounding flow field. This particular issue forms part of the larger problem of helicopter interactional aerodynamics, and the problem is considered in light of the current understanding of many of the related interactions which occur in rotorcraft operation.

1.1 Helicopter Interactional Aerodynamics

The helicopter rotor wake is one of the most complicated flows existing in the field of aerodynamics. The three dimensional structure of the wake is often irregular, making the study of its features extremely challenging. Unlike the wake of a fixed wing aircraft, the wake of the helicopter rotor has a tendency to remain close to the rotor, resulting in the observed complicated, induced flowfield (Leishman, 1998), which in forward flight involves three-dimensional, unsteady, transonic, viscous aerodynamic phenomena (Johnson, 1986). In order to be able to study the interactions which are undergone by this wake structure, it is first important to understand the origins of the major components of the rotorcraft wake, and the features which are associated with them.

The trailing tip vortices shed from the rotor blades contribute to (and dominate) the formation of the wake, the trajectories of which trace out closely epicycloidal (helical) paths (Leishman, 2000) [Figure 1-1]. These vortices are formed as a direct consequence of the differential pressure field which exists across the rotor plane of a lifting helicopter blade, produced to support its own weight as well as providing the necessary thrust for

the forward movement (Surendiah, 1996). A shear layer is trailed behind the blade, formed by the merging of the boundary layer on both the upper and lower surfaces of the blade, contained both negative and positive vorticity (often referred to as the vortex sheet). The strength of this sheet is related to the circulation over the blade, and rapidly produces two distinct vortices, which occur at the tip and hub of the rotor blade [Figure 1-2]. The diffuse inboard vortex sheet at the rotor blade hub is often dissipated by its own viscosity much more quickly than the substantially stronger outboard sheet which is formed at the rotor blade tip. It is this stronger outboard sheet which leads to the formation of the tip vortex structure [Figure 1-3].

It should be noted, however, that in the case of multi-bladed helicopter configurations, the weaker inboard vortices may combine to form a single vortex which is significantly stronger than the corresponding tip vortex, but this tends to be carried down and aft, and hence away from the operating region of the rotor blades.

The tip vortex structures tend to have high circulation values and swirl velocities, and relatively small viscous cores due to the large pressure differences which tend to exist at rotor blade tips (Leishman, 2000) [Figure 1-4]. A strong axial velocity also exists in the core region (Kim & Komerath, 1995), which is directed wake-like towards the blade of origin [Figure 1-5]. The axial flow velocity has been measured to be roughly of the same order of magnitude as the inflow velocity into the rotor plane.

The structure of the trailing tip vortices may be easily divided into four distinct flow regions, as described by Tung et al. (1983):

(1) The viscous core, the innermost region which is dominated by viscous diffusion.

(2) The turbulent mixing region, which is dominated by turbulent diffusion (in this region, the tangential velocity attains its maximum at the point of the maximum velocity radius).

(3) The transition region, where the turbulent region makes the transition to the outer inviscid region.

(4) The irrotational region, where the measured circulation is constant.

Further study of the tip vortex formation (Leishman, 1996) indicated that it attained its maximum strength downstream within a 90° rotation of the rotor, with the average circulation slowly decreasing from this point onwards. The size of this tip vortex (defined by the radial location where swirl velocity in the vortex core is a maximum) is directly related to the blade thickness, typically measuring 10-15% of the blade chord (Chigier & Corsiglia, 1971). The peak tangential velocity was measured to be approximately $^1/_3$ of the rotor tip speed.

The vortex wake structure may take on a variety of forms, which are dependent upon the flight regime the helicopter is operating under. During the forward flight regime, the wake is skewed backwards by the oncoming flow and there is 'an increased mutual proximity of the portions of the vortex filaments' (Leishman, 1998). This results in stronger vortex-vortex interactions occurring, which in turn induce complications in the trajectory of the wake. As the forward flight speed increases, the wake may be observed to roll up to form two merging vortex bundles, which may be likened to the vortices which are generated from the tips of low aspect ratio wing sections (Leishman, 1998).

In recent times, there has been a significant emphasis placed on the requirement to produce cheaper rotorcraft with higher performance ratings, consequently leading to higher rotor tip speeds, and the rotor disk plane to be moved closer to the airframe (Conlisk, 2001). These significantly higher rotor speeds will generally result in higher disk loadings, which have a direct impact on the energy levels within the rotor wake. These increased energy levels will therefore affect the nature of the interactions which this wake will partake in (Sheridan & Smith, 1980).

Due to the persistence of these structures, a single trailing tip vortex is capable of partaking in a multitude of distinct interactions. These may occur many times, with one

or multiple airframe structures, or with other trailing tip vortex structures which exist in the wake [Figure 1-6]. Within the variety of interactions which may occur (Sheridan & Smith, 1980), the two most important are the main-rotor/tail-rotor interactions, the subject of the current study, and the wake-fuselage interactions (Conlisk, 2001).

Trailing vortex interactions form only a small part of a very large area of unsteady fluid dynamic problems, known under the broad heading of body-turbulence interactions. The turbulence field in question can take many forms, ranging from fully three-dimensional, uncorrelated turbulence (Wilder & Telionis, 1998), right through to the highly coherent vortex structures which are the subject of the current study. This field includes all incidences of vortices impacting onto bodies, which include cylinders, aerofoils, fins and protrusions. These interactions in turn give rise to the associated unsteady loadings, sound generation and vibration, as well as promoting variations in the local heat transfer coefficients at the interacting surfaces.

1.2 The Blade-Vortex Interaction

The Blade-Vortex Interaction (better known as the BVI) is one of a multitude of aerodynamic interactions which may occur between rotorcraft trailing tip vortices and the surrounding structures (both solid and fluid) within the sphere of operation. As the environmental issues which surround rotorcraft operation continue to be revised, rotorcraft manufacturers find themselves caught in ever changing design trade-offs, balancing the requirements for performance and cost efficiency demanded by the customer, with the fulfilment of the strict government imposed noise regulations. These regulations have almost elevated the importance of noise attenuation to equal that of performance, safety and reliability. As one of the major noise sources within rotorcraft operation is directly related to helicopter interactional aerodynamics (or IA, as it is known (Sheridan & Smith, 1980)), study of interactions, such as the BVI, have become increasingly important [Figure 1-7].

Helicopter aerodynamic noise may be categorized as being the result of one of five distinct aerodynamic events. The most intense of these, the High Speed Impulsive (HSI) noise (Lowson, 1992, Yu, 2000), occurs as a consequence of the compressible flow field due to the high tip Mach number on the rotor advancing side. Above a certain Mach number, the noise pulse may be observed to change suddenly, as the local shockwaves are no longer contained in the near field and propagate to the acoustic far field. The Mach number at which this occurs is referred to as the delocalization Mach (Yu, 2000). Although this is the most intense source, it tends to only be of note in the far field, as it propagates directly forward in the rotor plane [Figure 1-8], often leaving the pilot unaware of its presence (Yu, 2000). Blade tip shape and tip velocity have been identified as the most important consideration in the alleviation of HSI, and many concepts such as tapering, lowering of tip speeds, blade sweep and thin blades have been employed in order to control the compressibility effects which lead to its production (Yu, 2000). Although this is one of the major noise sources, it should be noted that HSI noise is more of a concern for older helicopters.

Rotational noise is a result of the force which is exerted on the air by the blades passing through, such as when the rotor blades are generating lift. The steady and varying loads which exist on the rotor blades as they rotate about the azimuth results in the production of a low frequency noise. The loading noise is due to the harmonic blade airloads, which dominate the rotational noise at low rotor blade tip Mach numbers. Since low frequencies propagate well in air, rotational noise can make rotorcraft detectable from long distances. It can also be a source of airframe vibration (as with most noise sources), and has been linked to acoustically induced structural fatigue.

The third noise source is a result of the blade passage through the air, producing a disturbance as a result of the displacement of the air. This is often referred to as the thickness noise, as it is dependent upon the thickness of the rotor blade. These disturbances are generally seen to propagate in the plane of the rotor. This is classified under the same broad heading of noise sources as the blade-vortex interaction (see below), known as periodic noise (Santa Maria, 1999).

'Broadband' noise (also known as non-deterministic loading noise), is produced through a multitude of physical mechanisms (Brentner & Farassat, 1994), all of which lead to the production of unsteady pressure fluctuations on the surface of the rotor blades (examples of such being turbulence within an attached/separated boundary layer, laminar vortex shedding or trailing edge noise). This type of noise is also one of the most difficult to predict using the current acoustic modelling techniques, and is hence the least understood.

The final aerodynamic phenomenon occurs at lower operating speeds, the Blade-Vortex Interaction (BVI), and has been found to be the most intense noise source within this flight regime, the maximum intensity occurring during vertical descent and landing. BVI is a direct result of the trailing tip vortex system which is produced by the rotor blades (as described in Section 1.1) colliding with a following rotor blade, either existing within the main rotor assembly, or further downstream within the tail rotor assembly.

The presence of three idealized configurations of interaction between a rotor blade and an approaching tip vortex are generally accepted (Conlisk, 2001) – the parallel and perpendicular interactions, and the direct collision in which the core of the vortex is locally destroyed (otherwise known as the 'normal' or 'orthogonal' interaction) [Figures 1-9, 1-10]. These result in the impulsive pressure fluctuations across the interacting blades, hence leading to the production of a distinctive noise signature – the low/mid frequency ('slapping') noise generated within the main rotor, and the 'bubbling' noise which is associated with the conventional tail rotor [Figure 1-11] (although it should be noted that this noise is more akin to a 'whine' in helicopters which have been fitted with a Fenestron).

The dominant interaction within the main rotor assembly is that of the parallel interaction, occurring when a trailing tip vortex from a blade within the main rotor assembly interacts with a succeeding blade (also within the main rotor). Due to the nature of this interaction, the vortex core and the interacting blade axes are parallel. As the interaction progresses, the core is 'cut' in the plane of its vortex core axial flow axis,

leading to the generation of low/mid frequency noise. There has been a considerable level of previous work conducted on the parallel BVI, both computationally and experimentally, focusing on two main aspects of the interaction, the effect of the interaction on the aerofoil, and the effect on the structure of the interacting vortex itself. The majority of studies have focused solely on the effect on the interacting aerofoil, but a limited number of studies do exist which have considered solely the deformation of the vortex core structure during the course of the interaction (Gursul & Rockwell, 1990).

Initial analytical studies by Howe (1976) generated a framework by which the sound produced by the parallel BVI could be assessed. Widnall & Wolfe (1980) progressed to the examination of the effect of the distance of the incident vortex from the interacting blade, showing that if an incident vortex were to pass sufficiently near to the blade (at an offset distance of c/2), then the vortex velocity distribution could be seen to have a considerable effect on the lift distribution and the transient acoustic signal.

The initial stages of the vortex deformation were first modelled for the interaction with a wedge, considering both direct and indirect collisions (Ziada & Rockwell, 1982, Tucker & Conlisk, 1992). The magnitude of the unsteady pressure reached a maximum at the tip of the wedge, and decreased rapidly with time over the surface (Kaykayoglu & Rockwell, 1985). The results of these studies led to the assumption that for an interacting vortex of sufficiently large strength and size compared to the local radius of curvature, that a leading edge tip vortex would be generated, which has since been demonstrated in several studies (Lee & Bershader, 1994).

Pressure measurements of the parallel BVI (Caradonna et al., 1981) identified a convective disturbance in the aerofoil pressure history which could be attributed to the passage of the interacting vortex over the surface of the blade. Subsequent investigations of the pressure time history associated with this interaction (Horner et al., 1992, Masson et al., 1998) indicated that it was dominated by the build up of the leading edge suction peak, which began to form as the vortex approached the leading edge, and its subsequent collapse as the interactional process progressed, which agreed well with the earlier

studies of the interaction with a wedge. This was accompanied by a build up and collapse of both the integrated pressure and normal force coefficients. A notable difference was also observed in the convection rate of the two halves of the split core over the surface of the blade, with the 'half' passing over the aerofoil upper surface moving considerably faster than the equivalent section of the 'cut' vortex core on the lower surface.

Calculations of the lift fluctuation accompanying the interaction (Poling et al., 1987) indicated that this fluctuation occurred with a period much smaller than the time required for the vortex to traverse from the leading to the trailing edge of the interacting blade. Further numerical studies using a discrete vortex method (Qian & Vezza, 1999) also predicted that for the strong vortex interactions occurring within the parallel BVI, a vortex induced local flow separation would occur, which had previously been missed in many studies. This agreed with the experimental visualizations performed by Ham (1974), who also observed a local separation, which occurred in the region of the most intense vortex induced loading.

Two main features dominate the progression of the parallel BVI (Yu, 2000): the unsteady pressure fluctuations, concentrated mainly at the leading edge of the interacting blade, and are responsible for the noise generation, and the strong radiated directivity pattern, which is predominantly forward and down (at approximately 30/40 degrees in the plane of the rotor), which tends to make the pilot aware of the noise, unlike with HSI noise. Suggestions have been put forward that connect this directionality to the advance ratio, and that careful selection of advance ratio may be used to control it (Yu, 2000). The pressure fluctuations across the blade surface also lead to an impulsive loading, contributing to control degradation, increased pilot workload and a corresponding instrument wear. The complexity of this interaction process has, however, made any advancements in the understanding, and eventual control, of the phenomenon slow, as the inherent complexity of the interaction is so tightly bound to the flight regime that the rotorcraft is operating under. Small changes in the flight condition (i.e. the rate of descent) have been observed to give rise to major changes in the radiated noise field

(Lowson, 1992), which in turn relates to a modification in the interaction process which is undergone between the wake and the rotor.

The streamwise interaction of a vortex with a blade (also known as the perpendicular BVI) gives rise to a series of physical features, described by Bodstein et al. (1996). Unlike the parallel BVI, this interaction is centred on only a fraction of the blade span. The trajectory of the interacting vortex is displaced in the spanwise direction, and a local separation zone is generated on the surface of the blade. Vortex breakdown is observed to begin near the maximum thickness of the blade for cases of indirect collision, or just upstream of the stagnation point for direct collisions. Studies by Philippe & Armand (1978) indicated that this interaction could lead to an increase in drag of up to 40%, while only resulting in a slight decrease in lift.

The interaction which occurs within the tail rotor assembly, in its limiting configuration, is best known as the orthogonal, or normal, interaction, and is discussed in detail in Section 1.3.

The noise production associated with these interactions has been proposed to be governed by four non-dimensional helicopter variables; the hover tip Mach number, M_{TP}, the rotor thrust coefficient, C_T, the rotor advance ratio, μ(rotor), and the rotor tip-path plane angle, α_{tpp} (Schmitz et.al., 2000), and four parameters which are specific to the interaction itself; the incoming vortex strength, Γ, the lift produced by the blade, L, the length over which the interaction occurs (which can generally be given by the interacting blade chord, c, and the miss distance of the interaction (Hardin & Lamkin, 1986). Optimisation of the rotor configuration in order to modify some, or all, of these parameters has been the main focus of most of the investigations into the control of the blade-vortex interaction phenomena.

It is also of importance to note that although emphasis is placed on the occurrences of BVI within rotorcraft operation, it may also be observed in cases of chopping of a pump intake vortex by turbine blades, the impact of ship or torpedo hull vortices on the propeller blades (Gossler & Marshall, 2001), or the ingestion of ambient turbulence into

aircraft fans, in all cases leading to an undesirable performance degradation. The widespread occurrence of this interaction serves to highlight the importance of a full investigation of the phenomenon and the effects of the interaction on performance, as noise generation and performance capabilities are of considerable significance in both civil and military operation.

1.3 Characteristics of Tail Rotor Interactions

Despite the significant contribution of the tail rotor aerodynamic interactions to rotorcraft performance, research has focused primarily on numerical and experimental simulation of the parallel and perpendicular BVI. The orthogonal BVI (OBVI) has remained relatively unexplored, even though it has long been identified as an area of specific interest for helicopter interactional aerodynamics (Sheridan & Smith, 1980). The tail rotor itself performs three significant functions (Leishman, 2000): provision of rotor torque reaction to the fuselage, heading selection while in hover, and sideslip angle selection while in flight. It is often incorrectly thought to perform as a propeller or as a small main rotor. Instead, the tail rotor provides thrust with air entering from all directions, and it is not trimmed for wind or flight velocities with cyclic pitch, as with the main rotor. It operates in extremely adverse aerodynamic and dynamic conditions, and it is required to produce both positive and negative thrust (Lynn et al., 1970). The flowfield which surrounds the rotor is strongly influenced by the operating regime of the aircraft. The aerodynamic interactions which result in unsteady blade loading and associated noise generation are dependent upon the main rotor downwash, and therefore factors such as ground effects may exert an influence. Control degradation may be attributed to the tail rotor operating in the vortex ring state, the influence of the main rotor wake on the tail rotor, and fuselage weathercock instability in rearward flight, and this is discussed in detail in the work of Prouty (1986) and Srinivas et al. (1993). Coton et al. (2004) presented a concise history of the work within the field of tail rotor interactional aerodynamics, concluding that unlike many fluid dynamic phenomena, there had been relatively little work done in this area, and that in order to accommodate future accurate prediction of tail rotor acoustics, the modelling of the interactional aerodynamics will have to be refined.

The influence of the main rotor wake on the tail rotor may be characterized by simplifying the problem to a single vortex / single tail rotor blade interaction, known as the 'orthogonal interaction', because in its limiting configuration the axis of the vortex is perpendicular to the chord of the interacting tail rotor blade. Whereas the parallel and perpendicular interactions do not necessarily result in a direct collision with the interacting rotor blade, and examples exist where the vortex will pass over the surface of the blade while still exerting an influence, the orthogonal BVI involves an unavoidable collision, which results in the rapid distortion of the vortex core (Rockwell, 1998). Understanding of this interaction is important for tail rotor sizing, and in the design process for the empennage configuration. The progression of this interaction is determined by a combination of the Blade Impact Parameter ($2\pi\sigma U/\Gamma$), the ratio of the freestream velocity to the maximum swirl velocity, and the thickness parameter (T/σ), the normalized blade thickness, identified by Krishnamoorthy & Marshall, 1998. These parameters give rise to the three distinct regimes of the OBVI, which are directly influenced by these parameters.

For a sufficiently low impact parameter, the boundary layer on the interacting body surface may be observed to separate prior to the impact of the vortex core (Krishnamoorthy & Marshall, 1998). This is often known as the 'wrapping' or 'strong' vortex regime, where boundary layer fluid shed from the body wraps around the interacting vortex, and hence dominates the process. These secondary vortices occur in a series of loops which are found to originate from different locations along the blade span, and move radially closer to the interacting vortex as they wrap around it. This leads to both deformation of the original vortex core, as well as ejection of vorticity, eventually leading to the outer layers of the core being stripped away, leaving a surround of secondary vorticity.

For large thickness ratios, where the body size is much larger than the vortex core diameter (Krishnamoorthy & Marshall, 1998), the core can be observed to bend in both

the chordwise and spanwise directions as it approaches the interacting body. After considerable bending occurs, the boundary layer of the interacting body will separate in the form of a sheet of vorticity, which will then wrap around the approaching vortex, quickly disrupting it and leading to the formation of an upwardly propagating vortex breakdown event.

For those cases in which the impact parameter is found to be high, the nature of the vortex response to the interaction process is governed by the thickness parameter (Krishnamoorthy & Marshall, 1998). In the case of the interaction with a thin blade (small thickness parameter), the vortex will not deform significantly, and the boundary layer of the interacting body does not separate prior to the impingement of the vortex core onto the surface of the blade. As the vortex passes onto the surface of the blade, viscous diffusion will lead to the vortex lines within the interacting vortex to attach to those within the blade boundary layer, the point at which the vortex core is described as having been 'cut' by the blade. It is this final regime that is most likely to be encountered within the BVI under study.

Once the vortex has passed over the leading edge of the interacting blade, the axial flow within the vortex core will be 'blocked' by the blade surface, the presence of the axial flow resulting in an asymmetry between the upper and lower sides of the interacting blade (Liu & Marshall, 2004). On the lower blade surface, the vortex core axial flow is directed towards the interacting body surface, and this 'blocking' results in a redistribution of the vorticity within the core radially outwards (Lee et al., 1998), and a corresponding core enlargement (Cary, 1987, Johnston & Sullivan, 1992). This enlargement of the core has been likened to the propagation of a vortex 'shock' (Krishnamoorthy & Marshall, 1998) through the fluid structure away from the surface of the blade, which leads to the observed 'bulging' of the vortex core close to the surface of the blade. On the opposing blade surface, where the vortex core axial flow is directed away from the surface of the rotor blade, the core is observed to 'thin' (Johnston & Sullivan, 1992), an effect of the gradual discontinuity through the core, referred to as the

vortex 'expansion' wave. It has also been observed that the decrease in core radius on the upper blade surface results in an increase in the axial flow component, and an increase in the swirl velocity at the periphery of the vortex core (Lui & Marshall, 2004). The increase in swirl velocity subsequently leads to a separation of the boundary layer and ejection of fluid from the interacting surface boundary layer, just upstream of the vortex core. Marshall and Liu (2004) also noted that in the interaction of a columnar vortex with axial flow with a blade in a situation where thickness parameter is low, the blocking of the core axial flow occurred quickly enough to ensure that there was no apparent separation of leading edge boundary layer fluid observed.

The use of the terms 'shock' and 'expansion' were used in the work of Marshall & Krishnamoorthy (1994) due to the observed similarity between the equations governing the axial motion in the vortex core to those of one-dimensional compressible gas dynamics, in which the gas density is replaced by the vortex core area.

Vortex cutting is also accompanied by entrainment of boundary layer fluid both upstream and downstream within the vortex core, and by the accompanying formation of upstream and downstream propagating vorticity waves (Krishnamoorthy & Marshall, 1998).

In a similar process to that observed during the parallel BVI, as the trailing vortex impacts onto the surface of the interacting blade, a suction peak (Doolan et al., 2000) is formed at the leading edge on the upper blade surface (where the axial flow component is directed away from the surface of the blade). This is accompanied by the formation of a corresponding pressure pulse on the lower surface, due to the asymmetry introduced by the axial flow component [Figure 1-12, 1-13] (Liu & Marshall, 2004). As the vortex convects over the chord of the blade, a suction ridge is maintained over the upper surface of the blade, while on the lower surface, a weak pressure ridge is visible up to approximately the quarter chord position. After this point, it appears to convert to a weak suction ridge over the remainder of the chord. A large normal force is observed when the blade first severs the interacting vortex core at the leading edge, which quickly diminishes with increasing distance over the chord of the blade. As the vortex passes

onto the leading edge of the blade, it experiences a large nose-up pitching moment, which rapidly becomes negative as it passes over the quarter chord before returning to its pre-interaction value as the vortex passes over the trailing edge. The maximum lift coefficient associated with the orthogonal blade-vortex interaction has been identified as being attributable to a function of the vortex impact velocity, axial velocity, core radius and density (Liu & Marshall, 2004), as modelling of the behaviour of the interaction indicated that there was an approximately linear relationship between the blade-vortex impact velocity and the core axial velocity

As the trailing vortices tend to be extremely persistent in nature, a single vortex may be observed to interact several times before it will fully dissipate. For this reason, it is necessary to consider the manner in which the pre-cut vortex behaves. Tests conducted examining the pressure history of an interaction pre-cut vortex with a blade in an orthogonal manner (Doolan et al., 2000) showed that the interaction proceeded in a very similar manner to the 'clean' interaction case, with the only noticeable difference being in the greatly reduced magnitude observed in the pressure time histories of the interaction. This would be indicative of a possible re-establishment of the vortex core axial and tangential components occurring post-interaction [Figure 1-14, 1-15].

The interaction of a trailing tip vortex with a stationary blade in the orthogonal sense has been modelled and investigated by a series of researchers, but there is little experimental modelling of the interaction of the vortex with a moving rotor. Coton et al. (2004) conducted a series of tests to record the pressure variation over the tail rotor during the interaction. The results of this study were in good agreement with the previous modelling of the interaction (Doolan et al, 2000, Wang et al., 2004) , indicating the increased regions of pressure and suction on the opposing blade surfaces on the initial impact of the trailing tip vortex, which quickly diminished as the vortex passed over the blade surface.

Although the majority of experimentation in this area has been confined to wind tunnel and computer simulation, a limited amount of in-flight experimental data are available for comparison. Acoustic in-flight experimentation, carried out with an instrumented Lynx

helicopter (Leverton et al., 1977), mounted microphones externally in order to record the noise patterns in set flight regimes. This provided evidence that the 'burble' noise could indeed be attributed to the intersection of the tail rotor with the tip vortices shed from the main rotor assembly. It also went on to verify that the reversal of the tail rotor could significantly reduce the effect of the tail rotor passing noise in the far field, while effectively eliminating the 'burble' noise. It predicted that this could lead to a reduction in the noise detectibility range of the helicopter by up to a half. Further test results were obtained through the instrumentation of one of the tail rotor blades of a Lynx AH Mk5 (Ellin, 1994), in which a series of pressure sensors were mounted on the blade to record data during controlled flight regimes. By conducting tests in this manner, information about the dominant effects in the tail rotor disk for a variety of different flight regimes were acquired, both of these test schedules providing invaluable data for validation of the experimental and computational modelling.

1.4 Control of Rotorcraft Trailing Tip Vortices

There are many different techniques which may be applied within rotorcraft operation which are designed to either modify the trailing tip vortex structure, and hence control the subsequent interactions, or to modify the operating regime of the rotor blades themselves in order to introduce a 'miss' distance and therefore avoid the interaction altogether (McAlister et al., 2001). Such devices range from simple, passive control techniques (such as the injection of air into the tip (Coton et al., 2001), the use of spoilers or stub-wings (Yu et al., 1997), or the alteration of the blade planform (Chen et al., 2001)), through to complicated active control techniques (such as higher harmonic control (HHC) (Van der Wall, 2000), individual blade control (IBC) (Yu, 2000), and local blade control (LBC) (Yu, 2000)).

One such control technique which is of current interest is the modification of blade tip sections in order to produce a 'system' of vortices, rather than the single trailing tip vortex as produced from a rectangular blade planform. Such systems may be produced in

a variety of different configurations, such as the co-rotating vortex pair produced by the proposed Vane tip (Brocklehurst & Pike, 1993, Tyler & Vincent, 1996), or the successful British Experimental Rotor Programme (BERP) tip [Figure 1-16], developed through a collaborative project between Westland Helicopters and the Royal Aircraft Establishment (1976-1986). At medium to high incidence, this tip produces two counter-rotating vortices, appearing to lead to a reduction in BVI noise generation, proposed to be a result of the alteration of the tip vortex structure benefiting the interaction (Lowson, 1992, Perry et al., 1998, Yeager et al., 1997).

A study of the parallel twin BVI event examined the nature of the aerodynamic loading on the interacting blade due to the passage of a counter-rotating vortex system. As the interaction progressed, it was observed that the vortices drifted further apart [Figures 1-17, 1-18]. This was considered to be an effect of the rotational component induced by the rotor, as the vortex separation remained constant in studies where the rotational component was removed (Masson et al., 1998). The interaction of the twin vortex system also gave rise to smaller normal force and quarter-chord pitching moment coefficients than were observed for comparable interactions with a single vortex structure.

However, the manner in which these control techniques affect the progression of the associated aerodynamic interactions has not been fully examined, although their performance benefits have been well-documented. Further investigation of the effects of the modification of the blade tip section on such interactions would aid understanding of how these modifications benefit the overall rotorcraft, and assist decisions made on the continuation of research in the many diverse fields.

1.5 Objectives of the Present Study

The nature of the Orthogonal Blade-Vortex Interaction has led to a significant number of studies, many of which have been referenced within this introduction, but there is still a large gap in the knowledge base surrounding the nature of these interactions. As noted

by the work of Sheridan and Smith (1980), the tail rotor interaction is one which is of particular interest in the field of interactional aerodynamics, but remains relatively unexplored compared to the parallel and oblique interactions. As the requirements for design and performance continue to evolve in response to increased customer demands, the need to understand the mechanics behind these interactional processes has become elevated. The work contained within this thesis addresses this issue, and the following chapters will document a fundamental study of the deformation of a trailing tip vortex and the surrounding fluid undergoing a representative orthogonal blade-vortex interaction.

The preliminary studies of the orthogonal BVI performed by Copland (1997), Doolan et al. (2000a) and Green et al. (2000) indicated that there were several unique features associated with the interaction, which still remain unknown. As the vortex core passes onto the blocking surface, the axial flow is subjected to a compression on one side of the blade, with previous visualisation revealing the radial outflow from the vortex core. This is also apparent in the large expansion of the core close to the surface. What remains less understood is the progression of the vortex core across the surface where the axial flow is directed away from the interacting surface. The pressure measurements of the interaction revealed a suction ridge across the surface as the vortex core passes over. These negative pressure readings, although of nowhere near the same magnitude as the peak pressure readings accompanying the lower surface interaction, indicates two potential features of this flow: that the fluid is drawing away from the surface in order to re-establish the disturbed axial flow (negative peak), and that the interaction on this side of the blade has a less significant effect on the surrounding flow than the corresponding lower surface interaction (magnitude of the signal).

This interaction has far reaching effects within a variety of different flows, and its effects are not localised to the tail rotor interaction which is the subject of the current study. Its potential occurrence in nearly every instance of turbulent fluid ingestion highlights the significance of being able to understand the mechanisms behind the interaction entirely

so that potential methods of alleviation the effects of this interaction may be investigated with a greater degree of confidence.

The subsequent behaviour of the interaction is dictated by the manner in which the trailing tip vortex is first 'cut'. As described above, this initial impact is dictated by two parameters – the thickness parameter, and the impact parameter (Krishnamoorthy & Marshall, 1998). This therefore allows two different sorts of modification to be made in order to affect the progression of the interaction – either by increasing the thickness parameter through increasing the interacting blade thickness, or decreasing the impact parameter through modification of the rotor blade producing the wake system.

The first of these parameters, the thickness parameter, is probably unlikely to be of interest within the sphere of tail rotor aerodynamics, as the use of thicker blades would impact negatively on the overall design, but it should be considered that an orthogonal interaction with a high thickness parameter is still likely to occur within the general subject of helicopter interactional aerodynamics, with trailing tip vortices potentially interacting with the surrounding airframe. It remains, however, of interest to the study of the orthogonal blade-vortex interaction how the thickness of the interacting body can influence the progression of the interaction, and what the potential effects of such modifications to the initial deformation process are likely to have on the overall progression of the interaction.

The second parameter, the impact parameter, although not directly studied, is one of the influencing factors in the many passive control devices which are employed. The majority of these devices work by modifying the maximum swirl velocity in the vortex core, typically by modifying the size of the vortex core, and as such lessening the effects of the interaction. There have been many such attempts, and several have been relatively successful, although the manner in which many of these devices work is still not understood. The BERP tip, presented in section 1.4, is one such successful

implementation of the passive control techniques, but the actual manner in which the vortices produced interact with the blade is still not completely understood, with little known about the manner in which the counter-rotating vortex system progresses with increasing distance from the producing rotor blade.

This work follows on from the work of Copland (1997) and Doolan (2000a). The remainder of the work has been split into three complementary bodies of work – the visualization of the idealized orthogonal blade-vortex interaction, in which the interaction of a single representative vortex with a rectangular blade is studied; the study of the effects of one of the significant interactional parameters, the thickness parameter, and the consequences of the modification of this parameter on the progression of the interaction; and the final section which will consider some of the techniques which have been introduced to attempt to alleviate some of the undesirable outputs of such interactions, focussing on the introduction of passive control through blade tip modification. Each of these pieces of work are significant to the complete understanding of the interactional process, and complement the current state of knowledge surrounding this phenomenon.

The global visualisation of the interaction using a particle image velocimetry technique serves to extend the available mathematical modelling (Lee et al., 1998), pressure history (Doolan et al., 2000) and LIF data (Krishnamoorthy & Marshall, 1998), providing a wholefield view of the progression of the interaction, focussing not only on the deformation undergone by the interacting vortex, but also the effects of the deforming vortex core on the surrounding flowfield. The work of Liu and Marshall (2004) indicated that the focus of the rotorcraft aerodynamics community was possibly incorrectly concentrated on the accurate prediction of circulation of rotor wake vortices, and should be more correctly focussed on the accurate prediction of vortex core radius and the axial flow component, as these were of much greater significance to the understanding of this interaction. Coton et al. (2004) echoed the call for further research of this fluid phenomenon, highlighting the benefits of acquiring data for the precise modelling of the tail rotor interactions which will further advance the acoustic prediction methodologies.

This dissertation is focussed on redressing this balance, and providing a detailed data set, quantifying the nature of the interacting vortex core.

The main body of the dissertation is divided into 6 chapters, which are headed by this introduction.

In Chapter 2, the experimental simulation of the orthogonal blade-vortex interaction is introduced. As well as describing the experimental arrangement which is employed, the methodology behind the Particle Image Velocimetry technique used to visualise the interaction will also be discussed.

In Chapter 3, the results of a study of the interaction of a single trailing tip vortex with a stationary rectangular blade in the orthogonal sense are presented, tracking the flow from the initial vortex severing through to the final passage into the blade trailing edge region.

Chapter 4 will extend the work in order to introduce a study of the modification of the blade tip structure, and the effect that this has on the interaction of the trailing vortex system with a representative tail rotor blade.

In Chapter 5, a detailed discussion of the results presented in Chapters 3 and 4 will be provided, highlighting the salient features noted in the examination of the results, and presenting a comparative study of the effects of the interaction of the trailing tip vortex generated by the two different blade tip sections (rectangular and variable).

In Chapter 6, the conclusions of all the work in Chapters 3-5 are provided, and a series of recommendations for future work made.

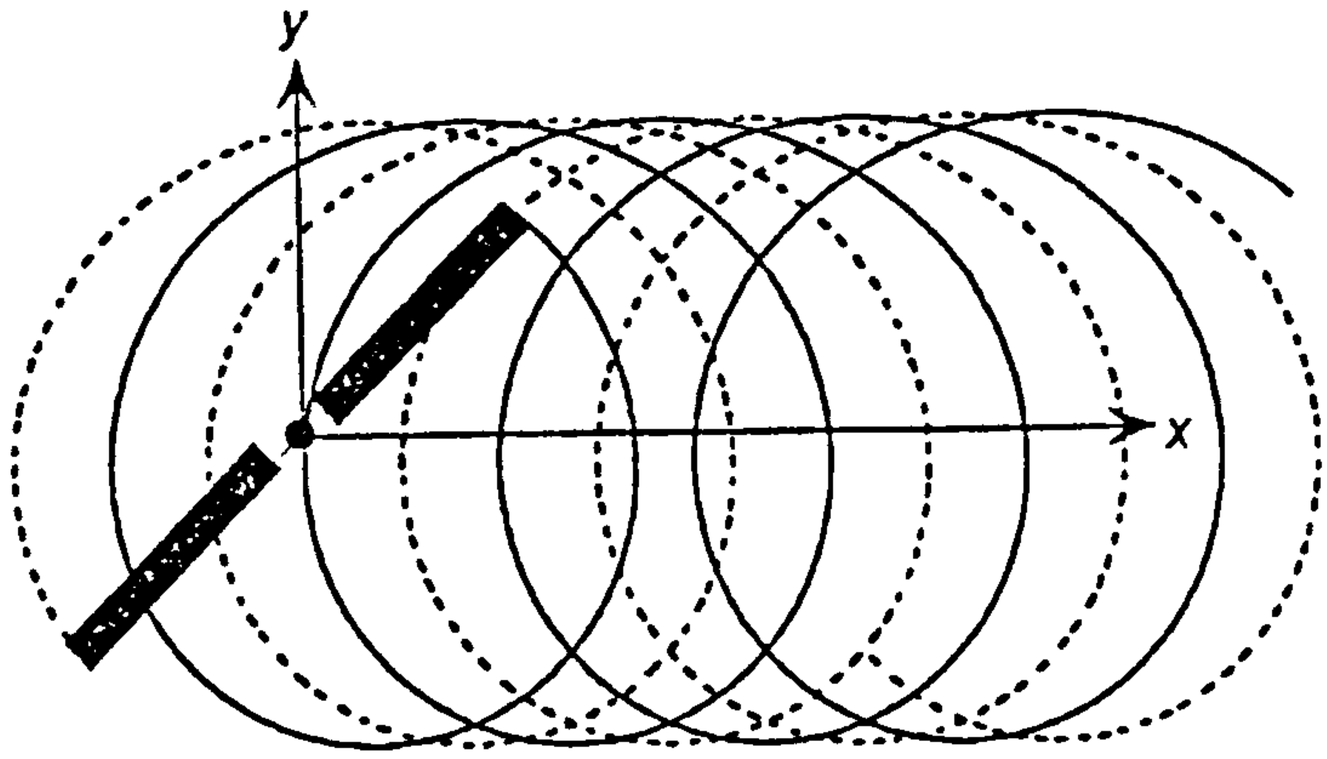

Figure 1-1 Plan view of the helical tip vortex trajectories from a twin-bladed rotor in forward flight. With increasing forward flight speed, the wake becomes progressively more skewed (Leishman, 2000)

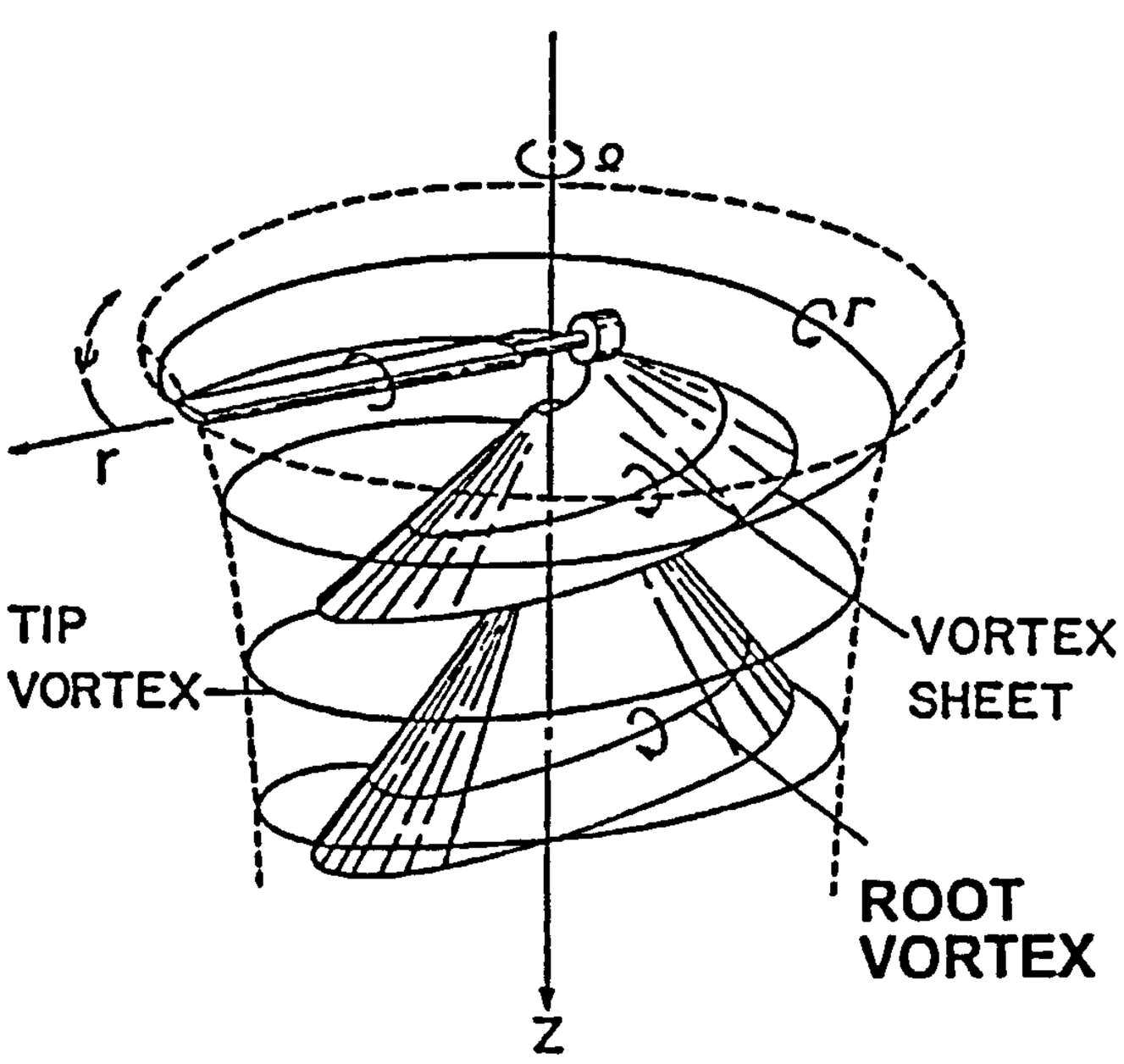

Figure 1-2 Sketch of helicopter rotor wake from a single-bladed rotor indicating relative positions of the wake tip and root vortices (Gray, 1992)

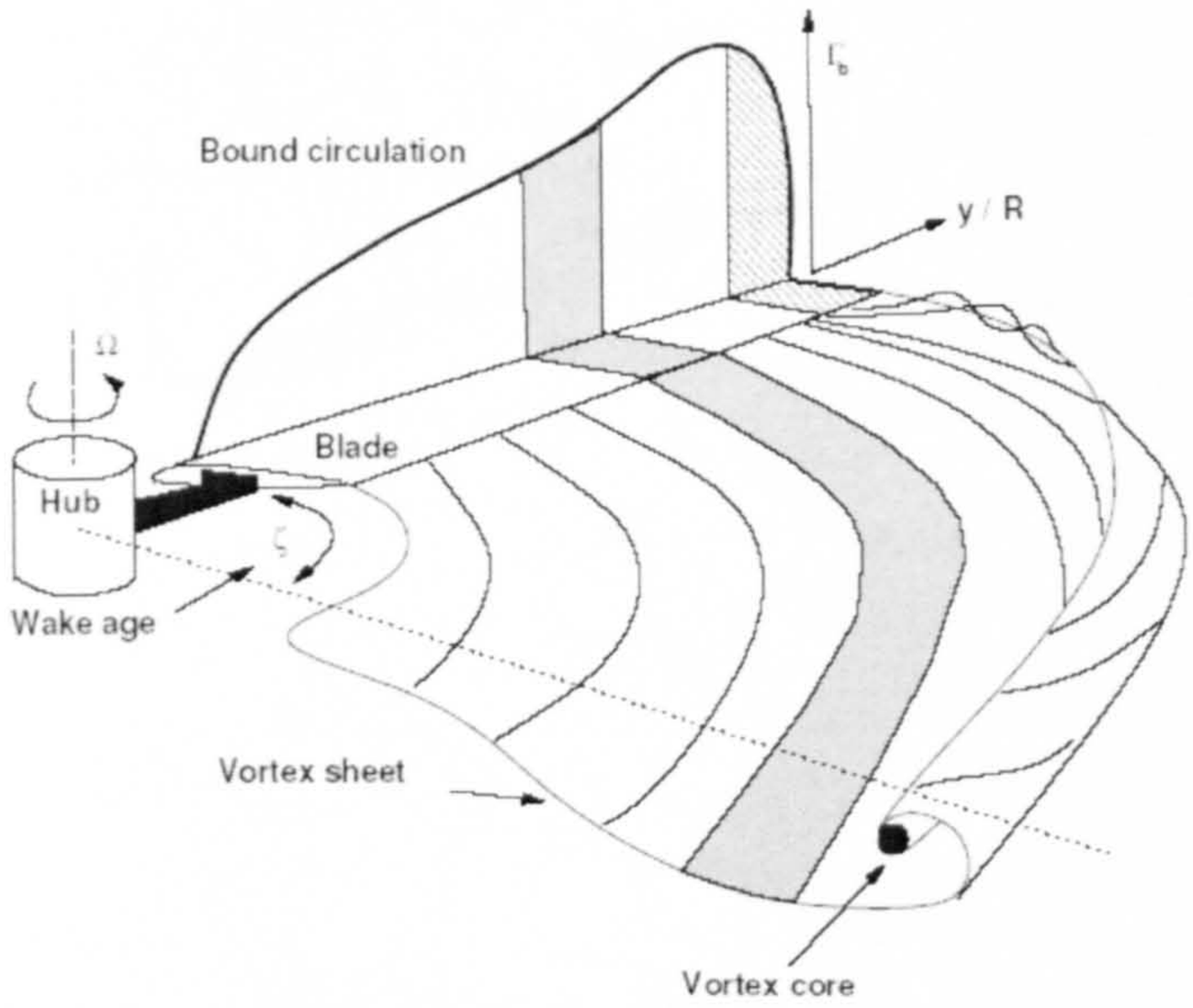

Figure 1-3 Schematic showing bound circulation and the corresponding trailing wake on a rotor blade (Martin & Leishman, 2002)

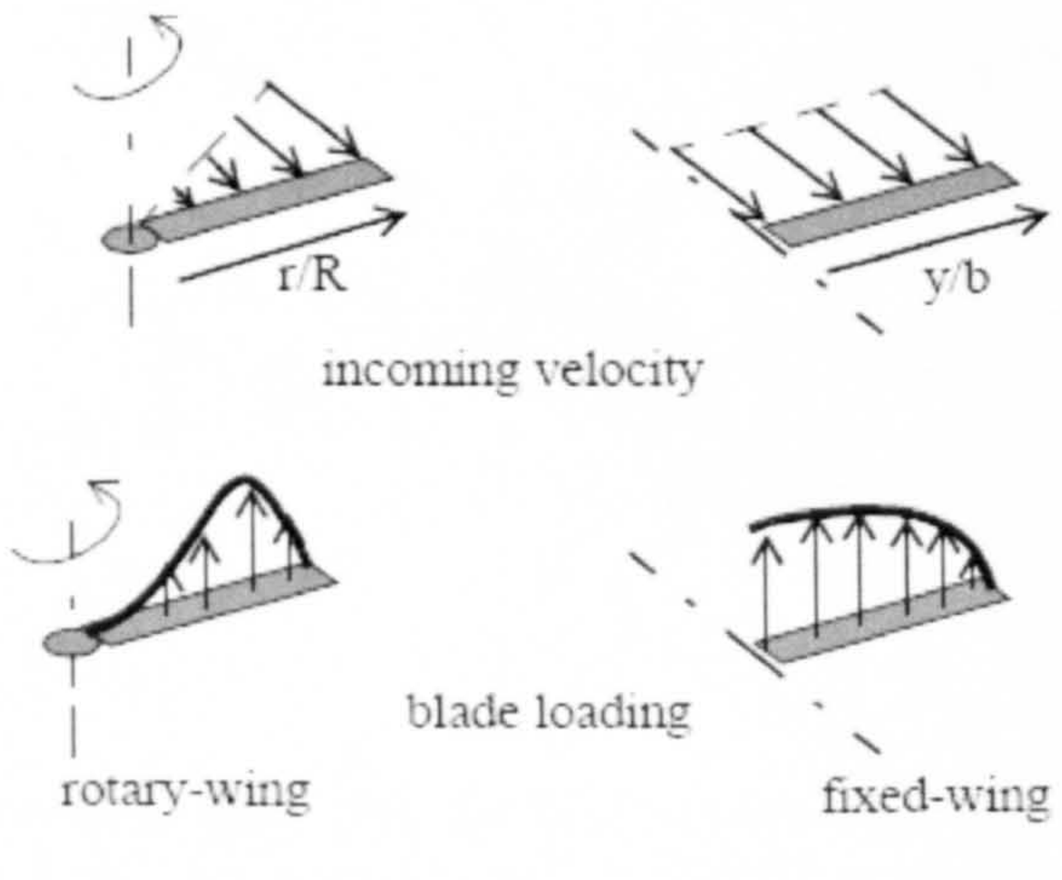

Figure 1-4 Spanwise Loading Distribution in a Fixed Wing Compared to a Rotary Wing (Mahalingham, 2000)

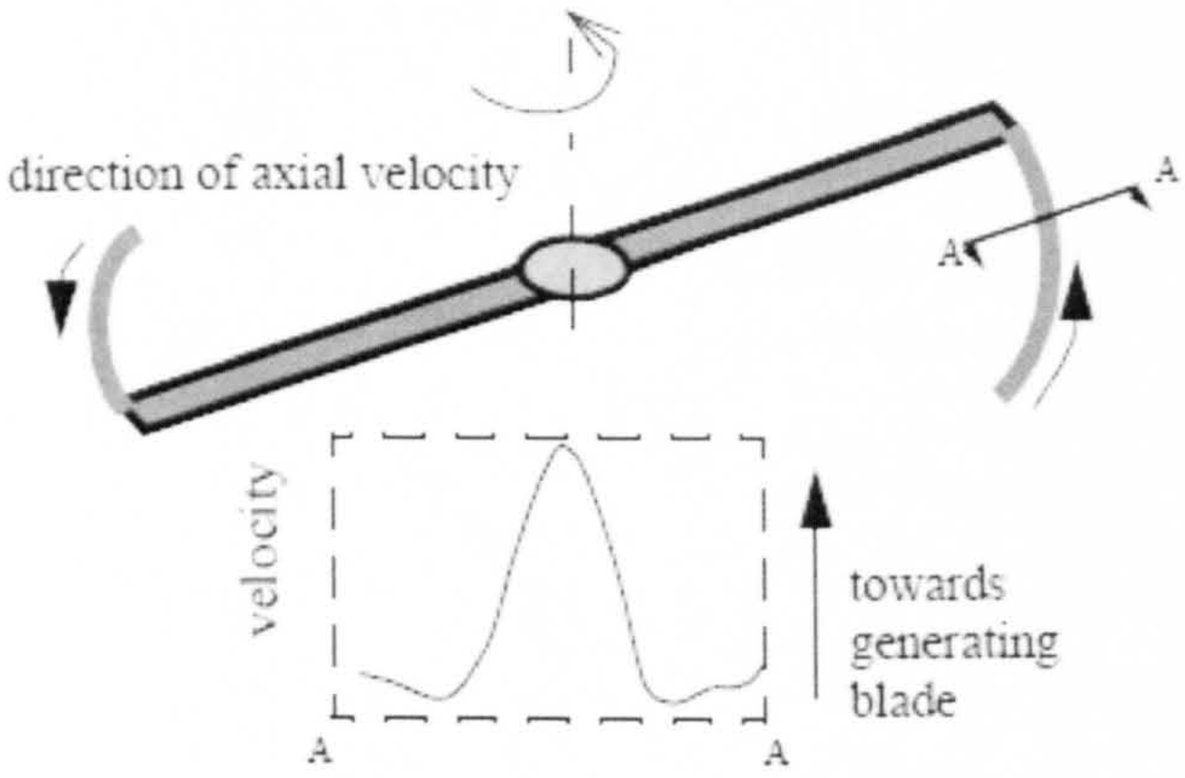

Figure 1-5 Core axial flow in a rotary wing tip-vortex (Mahalingam, 2000)

Figure 1-6 Schematic indicating the flow structure and some of the relevant aerodynamic phenomena associated with rotorcraft operation in forward flight (Leishman, 2000)

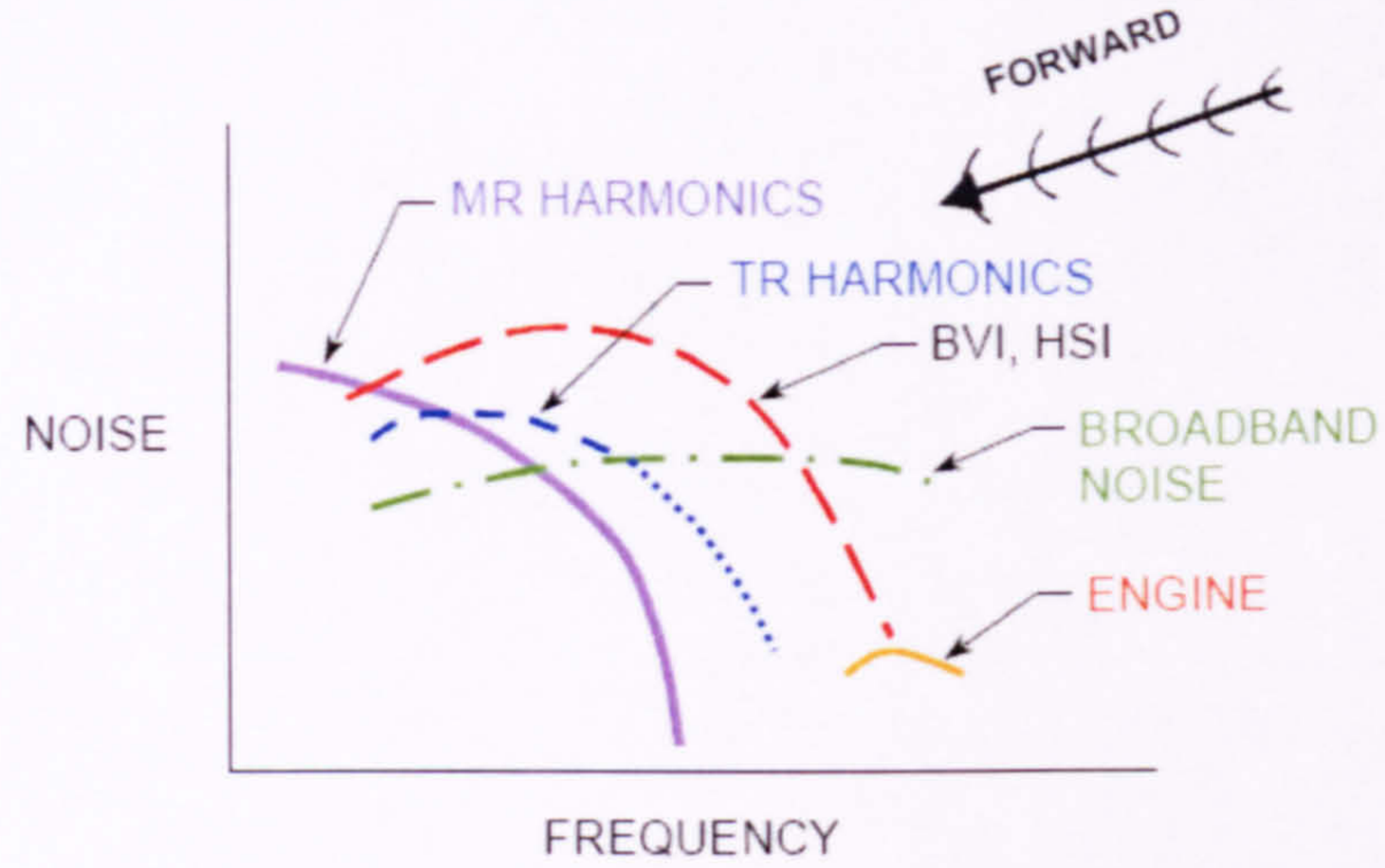

Figure 1-7 Helicopter Noise Sources (Edwards & Cox, 2002)

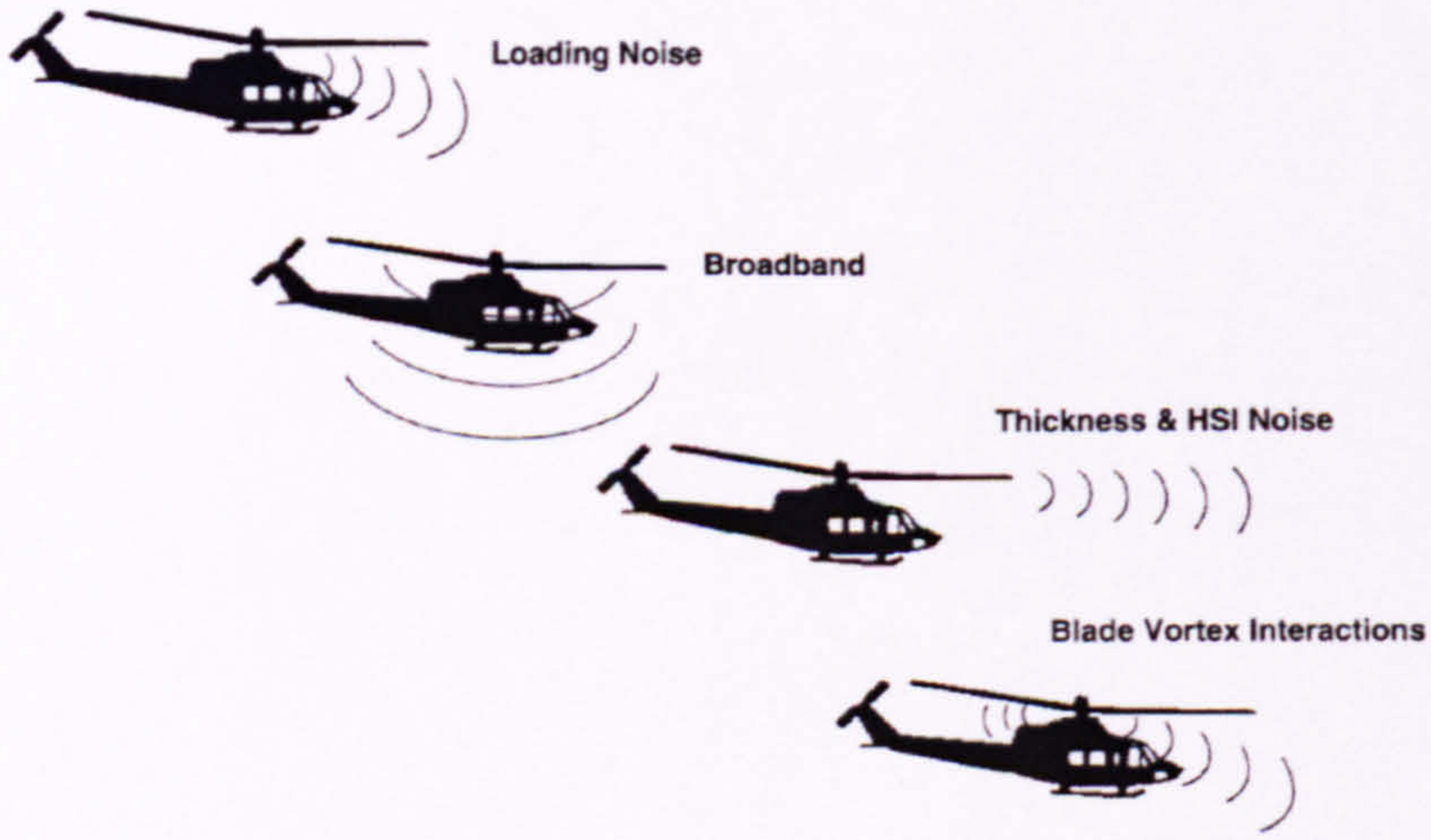

Figure 1-8 Noise Directivity Patterns associated with helicopter operation (Edwards & Cox, 2002)

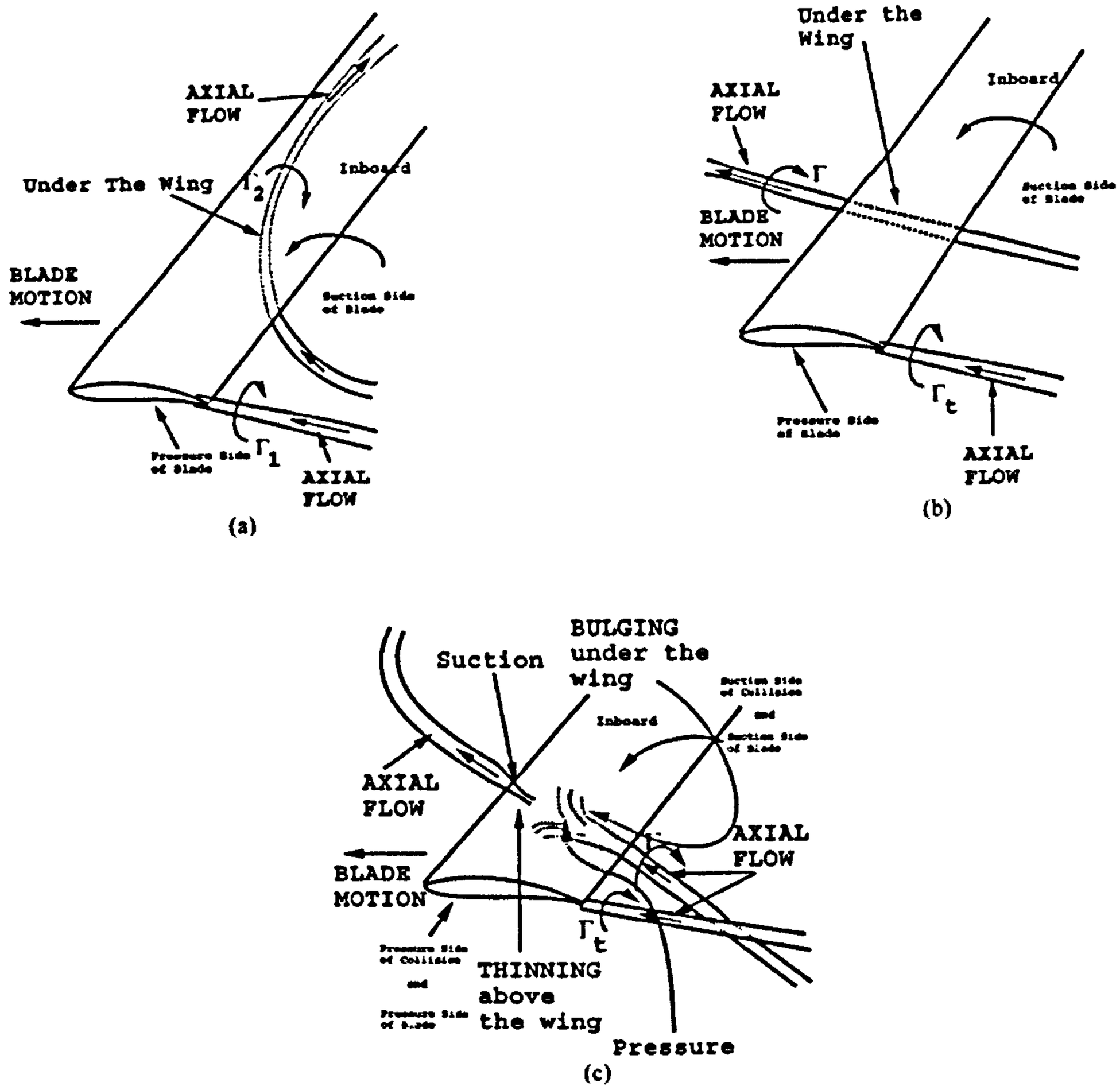

Figure 1-9 Sketch of the most common BVI events: (a) almost parallel interactions; (b) almost perpendicular interactions; and (c) oblique collision. (Conlisk, 2001)

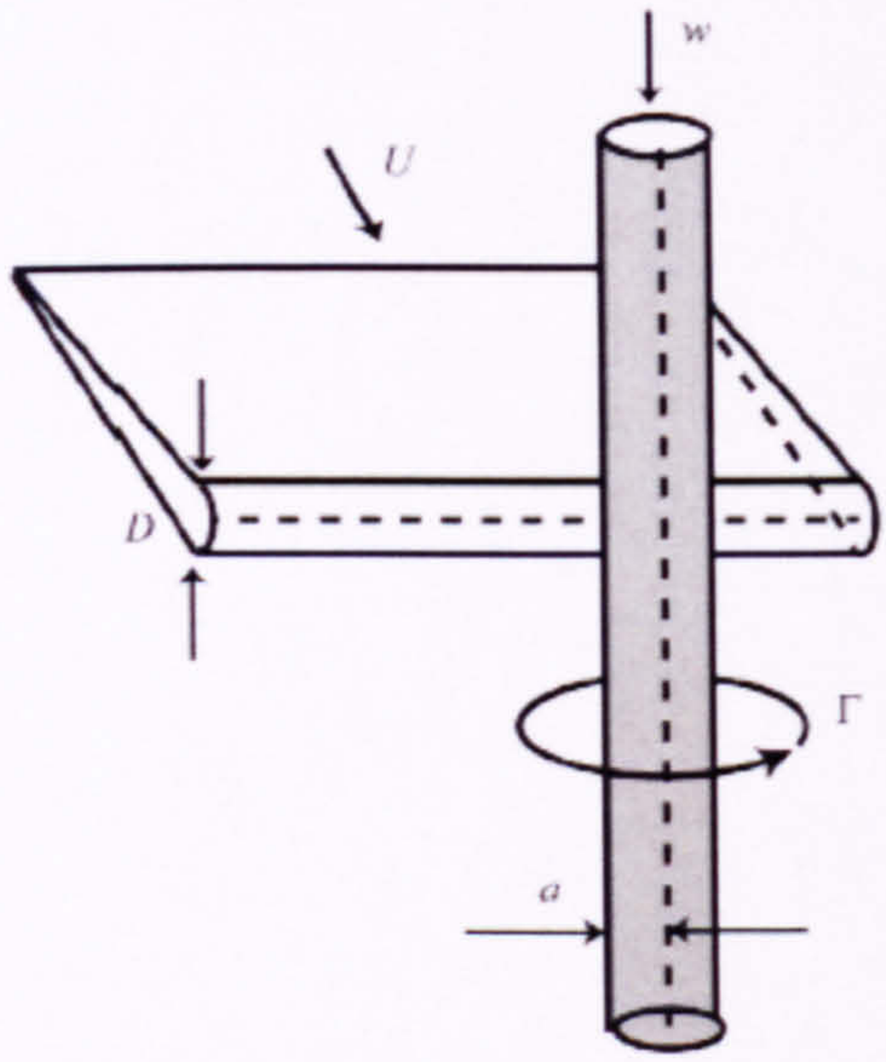

Figure 1-10 Schematic of a blade passing orthogonally into a columnar vortex (Coton et al., 2004)

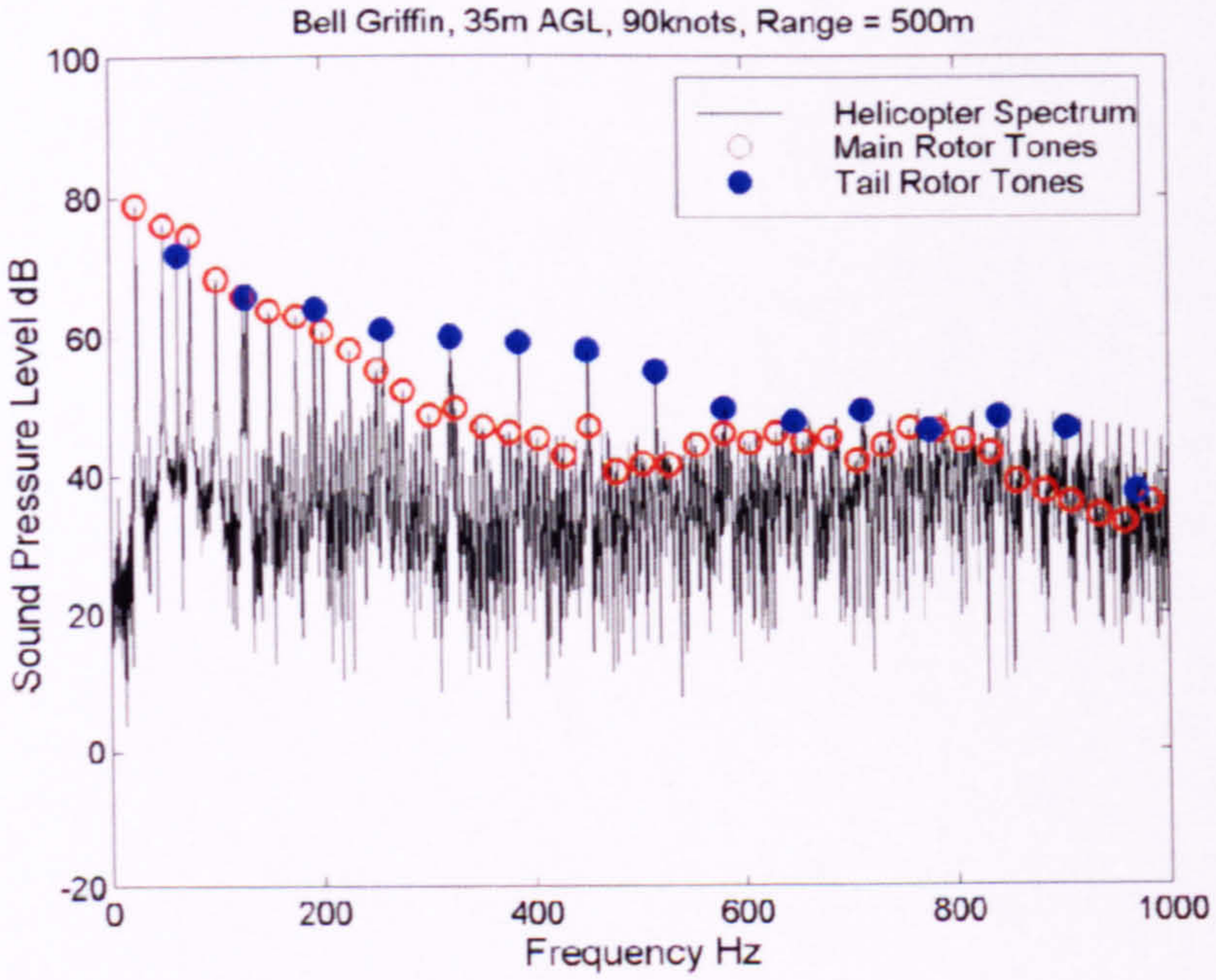

Figure 1-11 Typical noise spectrum from a helicopter in forward flight highlighting both the main and tail rotor tones (Martin et al, 1989).

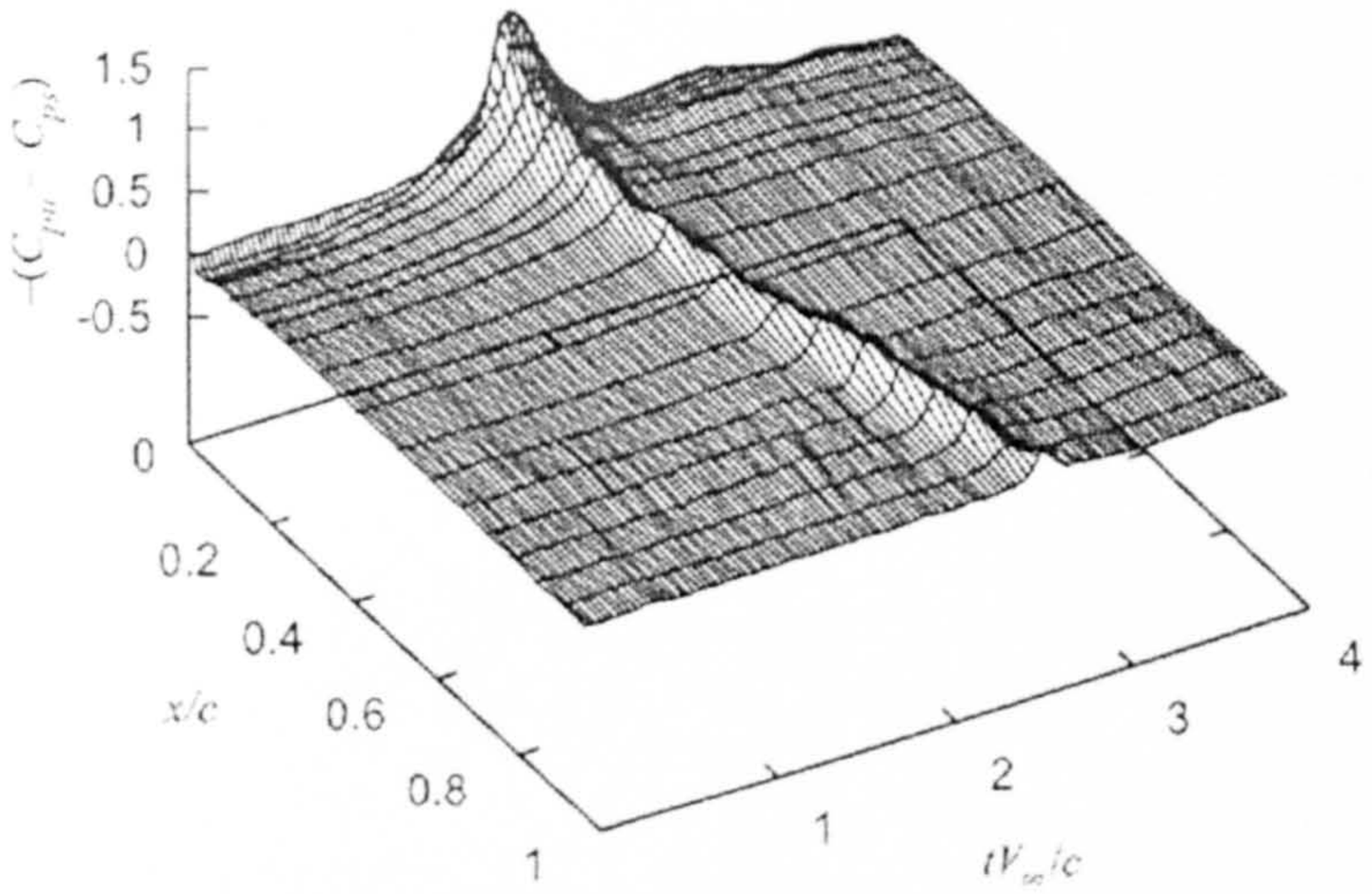

Figure 1-12 Unsteady upper surface pressures during a clean orthogonal interaction (Coton et al., 2004)

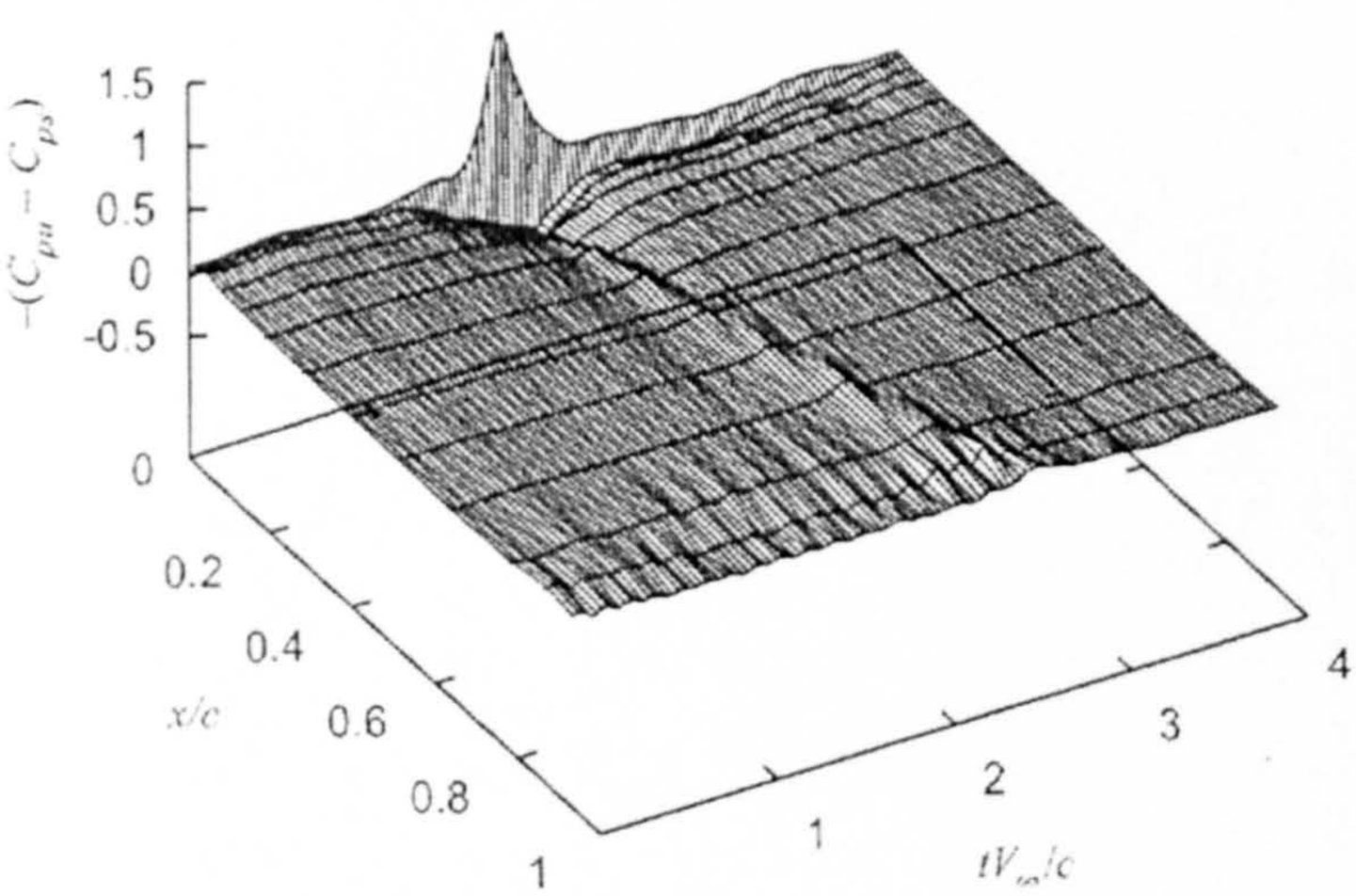

Figure 1-13 Unsteady lower surface pressures during a clean orthogonal interaction (Coton et al., 2004)

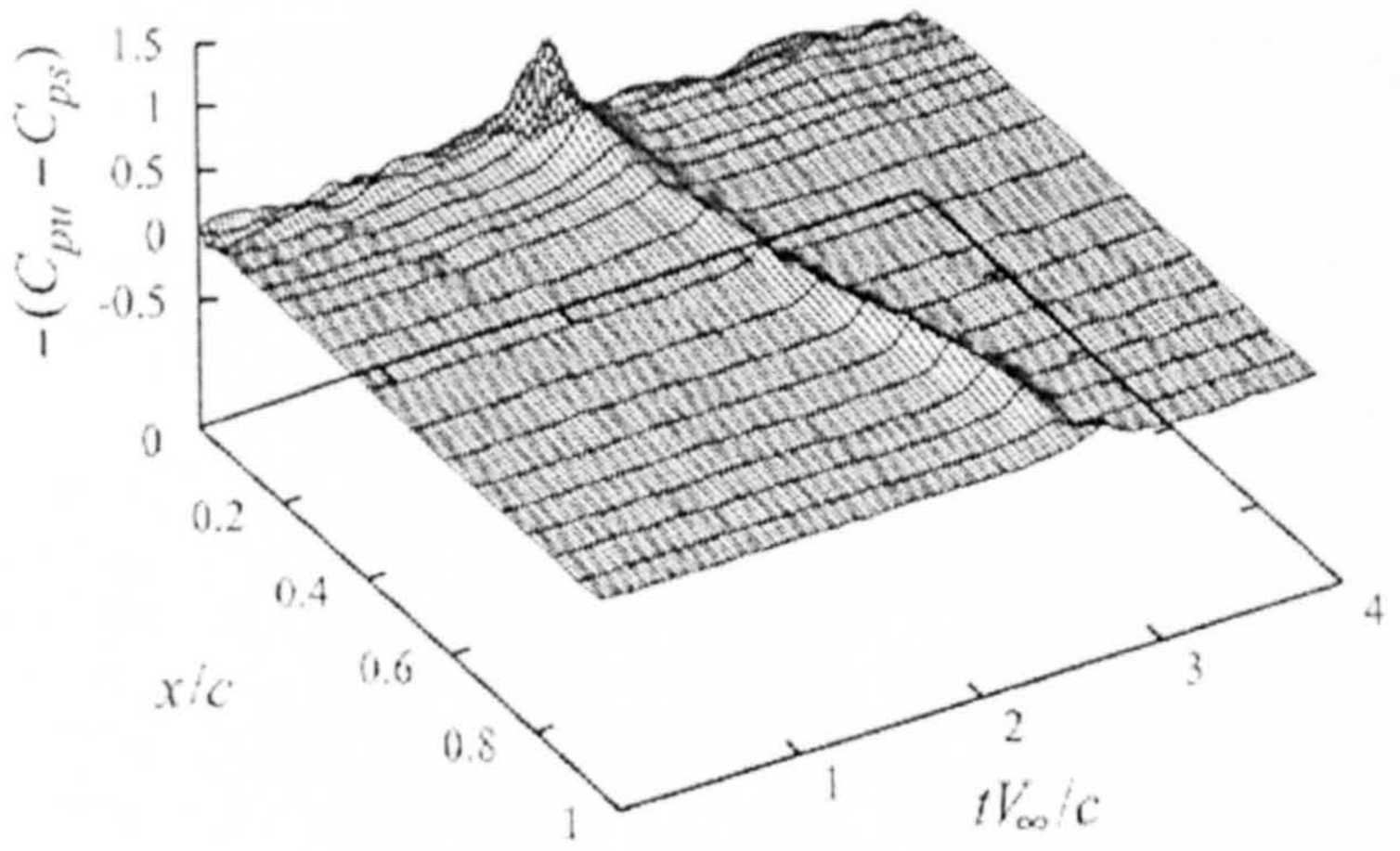

Figure 1-14 Unsteady upper surface pressures during a secondary orthogonal interaction (Doolan et al., 2001)

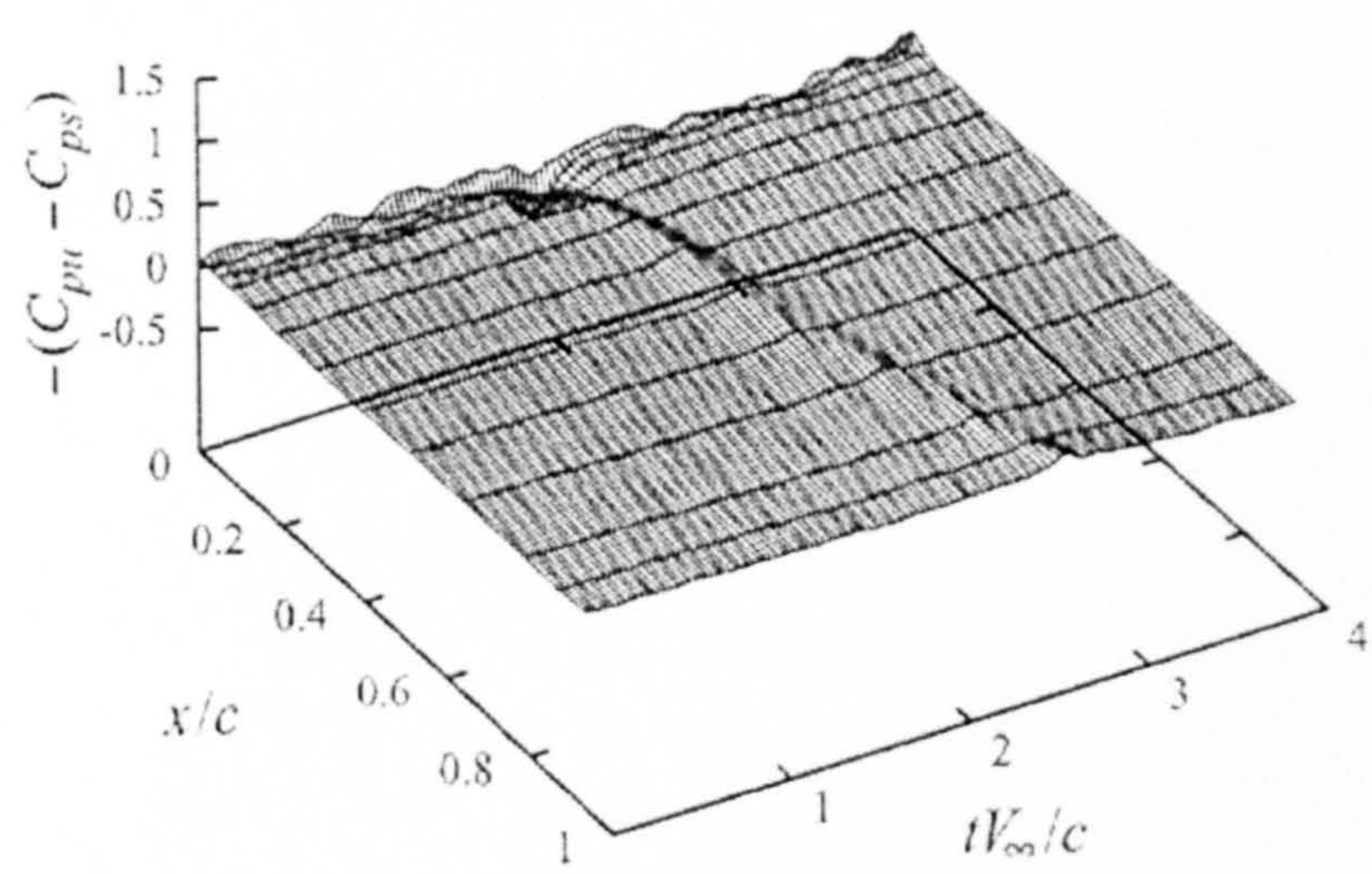

Figure 1-15 Unsteady lower surface pressures during a secondary orthogonal interaction (Doolan et al., 2001)

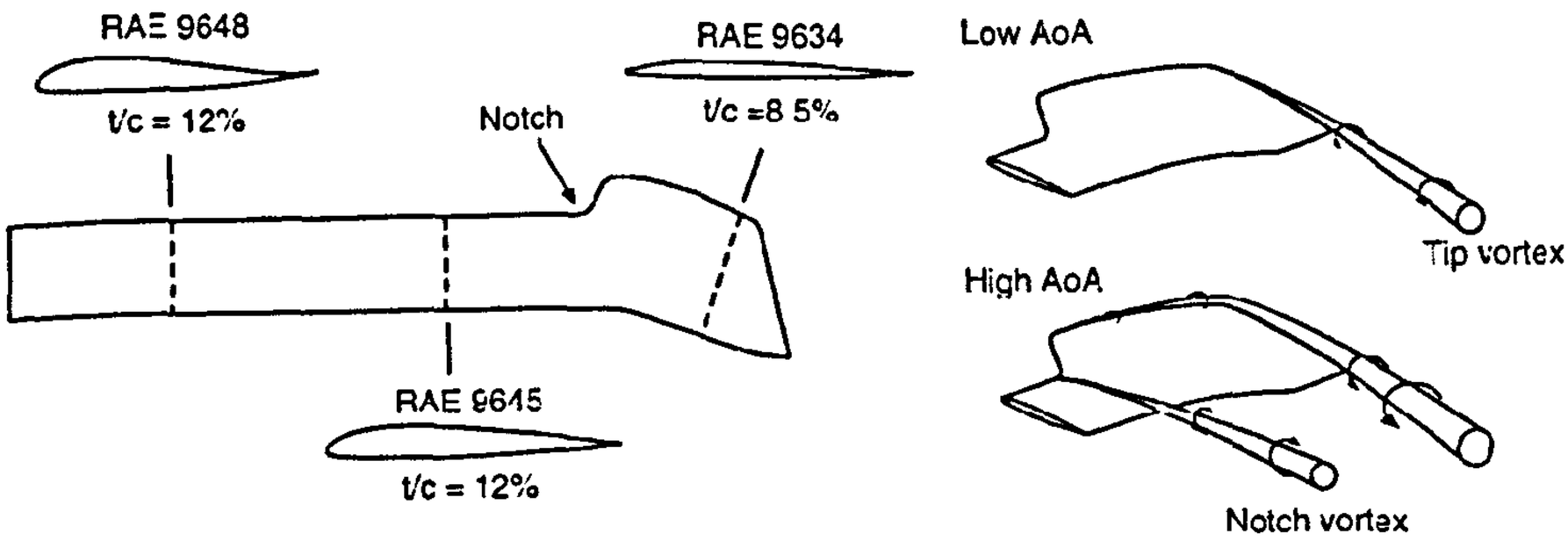

Figure 1-16 Distribution of the aerofoil sections on the BERP tip, and the generation of the vortex structures for low and high angles of attack (Yu, 2000)

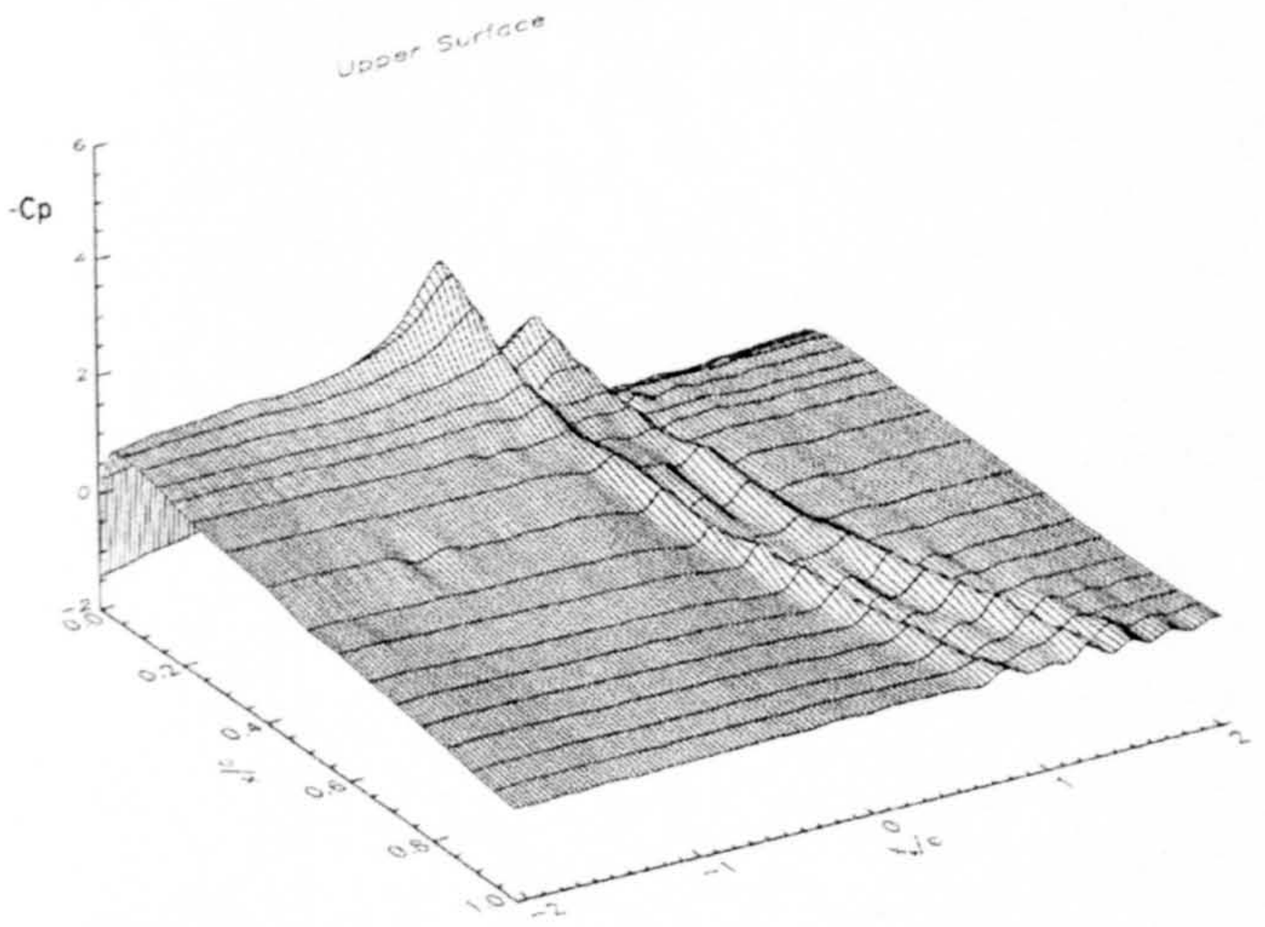

a) Cycle 1 of 16

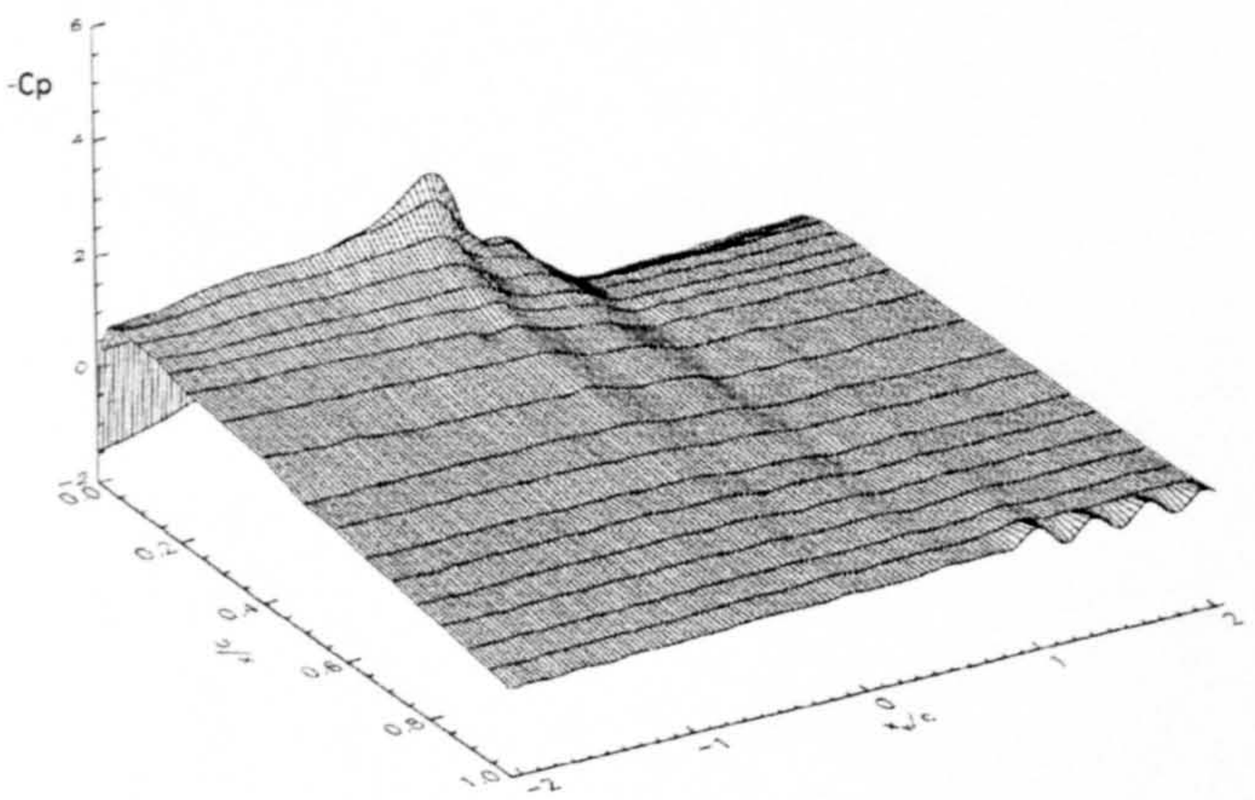

b) Cycle 10 of 16

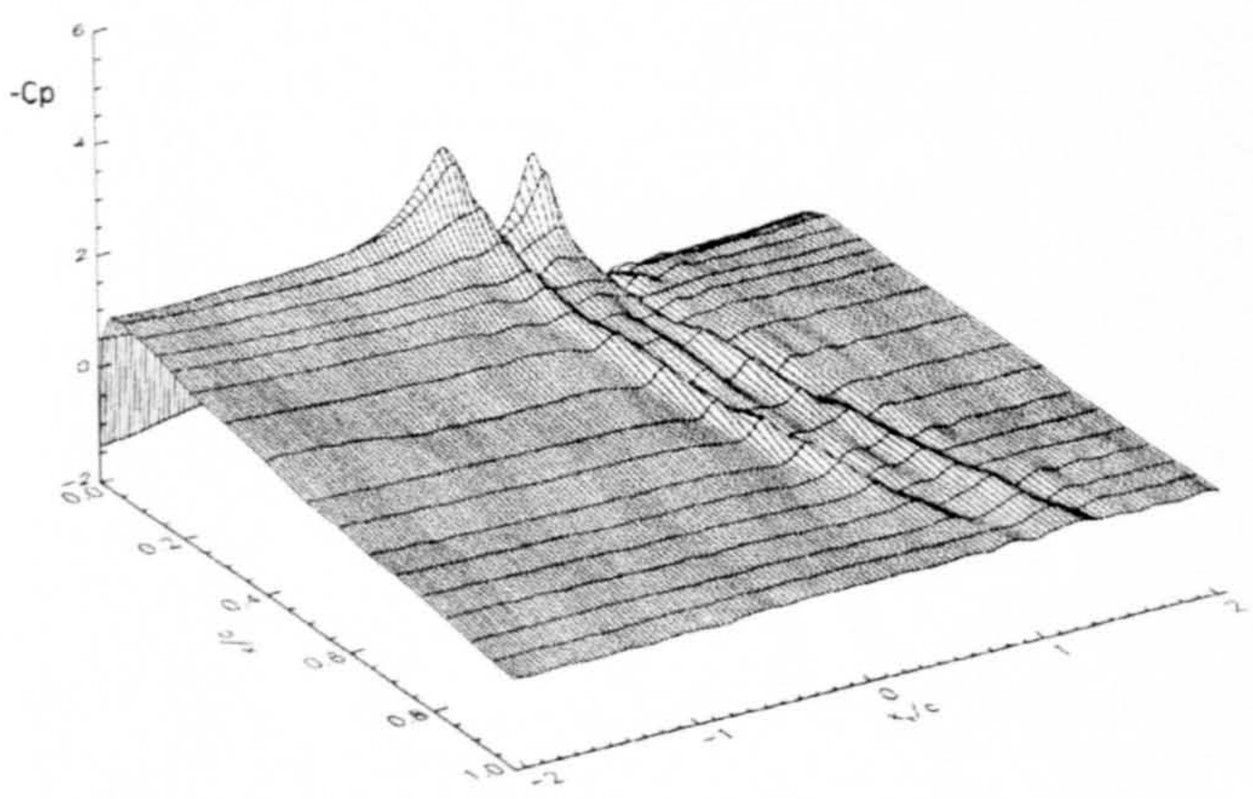

c) Cycle 13 of 16

Figure 1-17 Upper surface pressure variation for a parallel interaction with a twin vortex system (Coton et al., 2005)

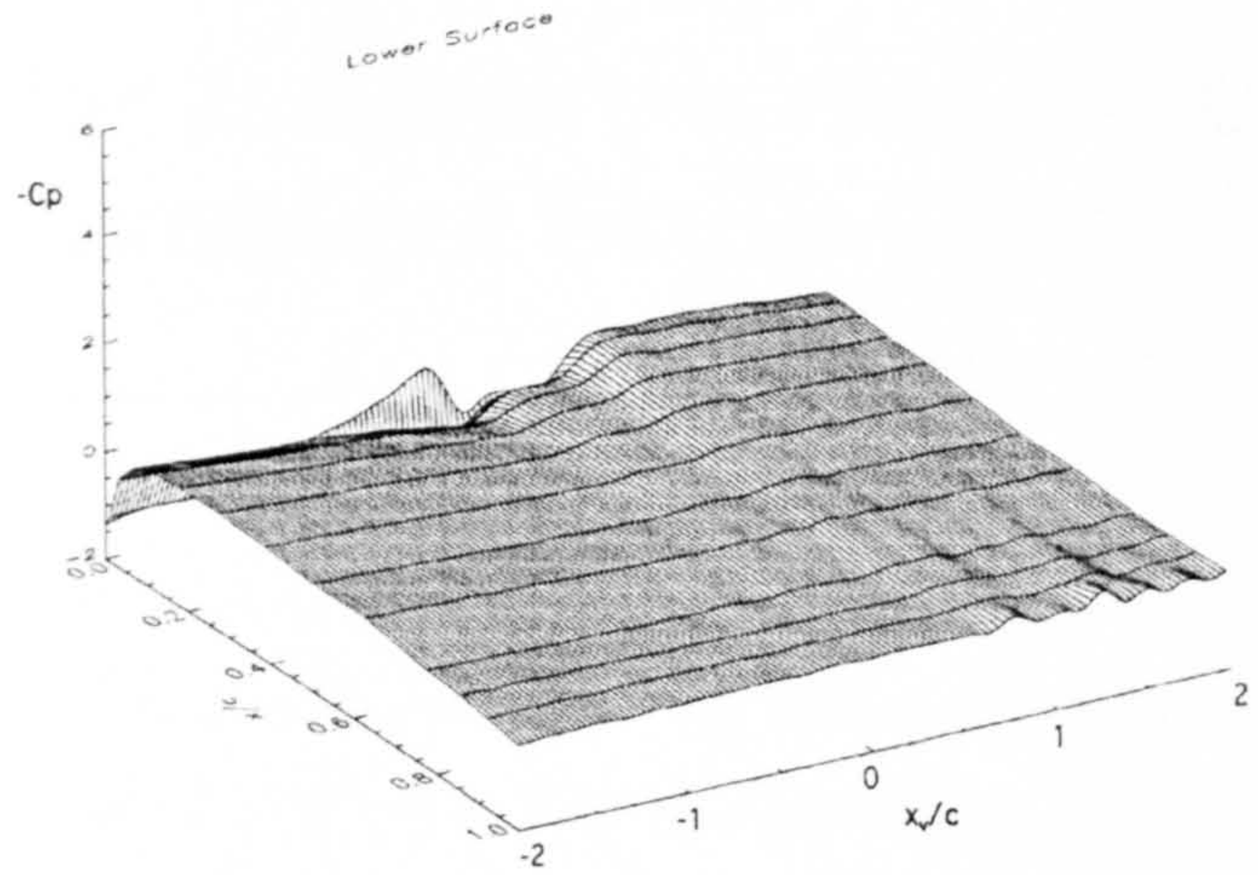

a) Cycle 1 of 16

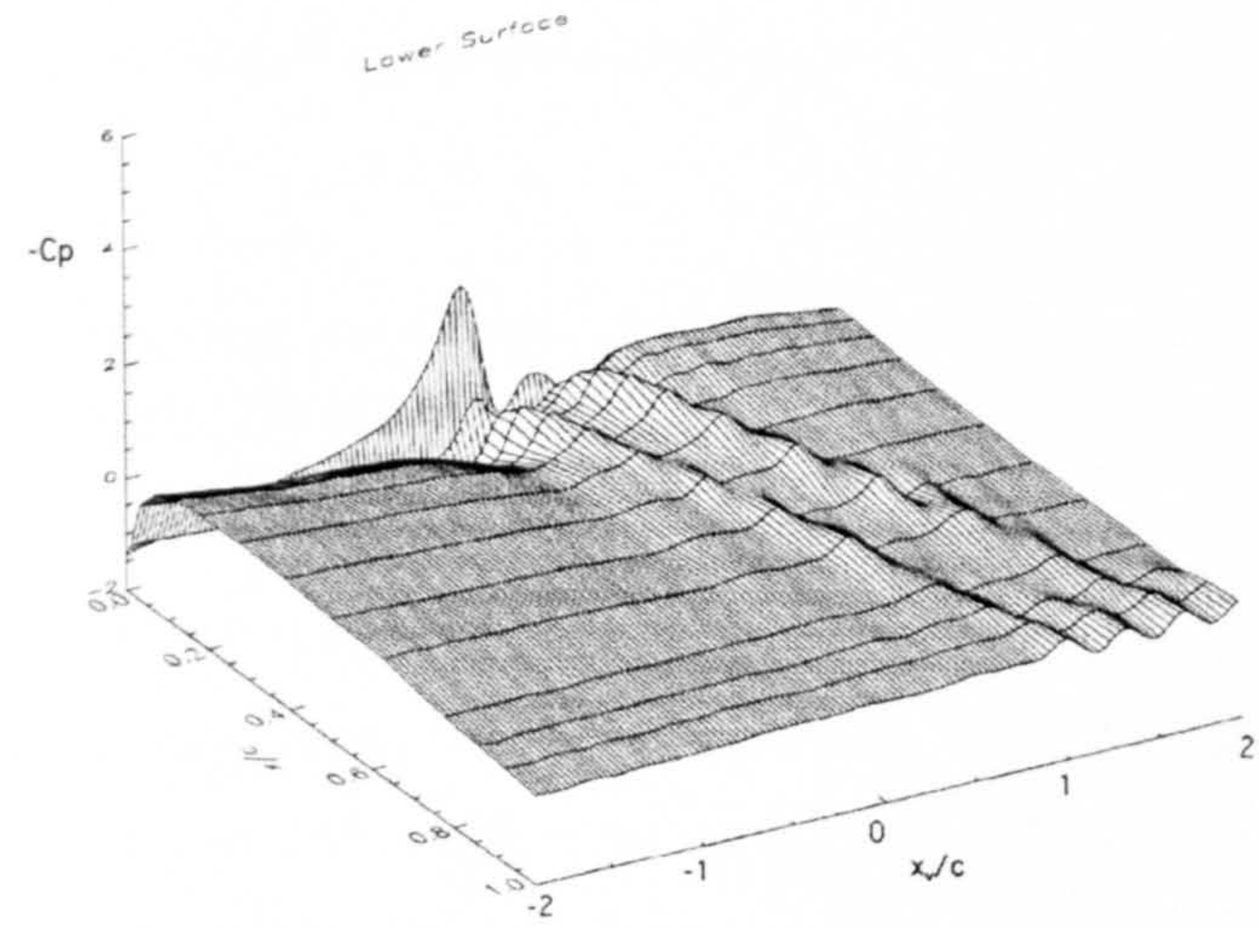

b) Cycle 10 of 16

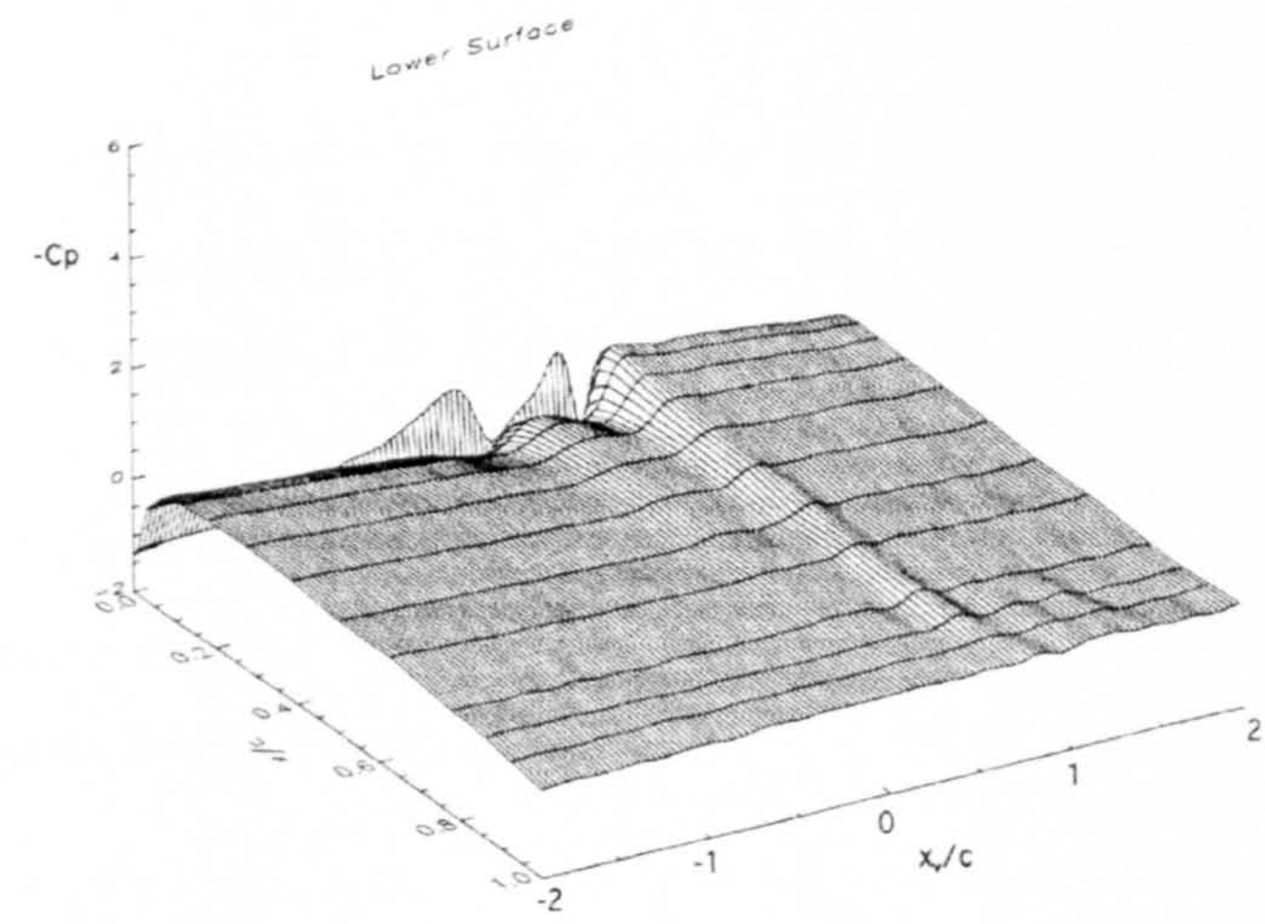

c) Cycle 13 of 16

Figure 1-18 Lower surface pressure variation for a parallel interaction with a twin-vortex system (Coton et al., 2005)

Chapter 2: Experimental Simulation of the Orthogonal Blade-Vortex Interaction

The simulation of the orthogonal blade-vortex interaction has been performed using an established experimental methodology, previously documented by Doolan et al., 2000a, and Copland, 1997. The following description will provide an outline of the experimental arrangement employed, as well as highlighting any modifications introduced throughout the testing programme.

2.1 Experimental Modelling of a Single Vortex Interaction with a Stationary, Rectangular Blade

For the purpose of simulating a trailing tip vortex similar in structure to that produced by a helicopter main rotor assembly in the forward flight regime, a specifically designed vortex generator (Copland, 1997) was constructed in order to produce the representative trailing tip vortex structure.

Numerical simulation of the rotor wake produced by the vortex generator was conducted by Copland (1997), demonstrating that the wake geometry is primarily determined by three physical parameters:

1 Wind tunnel velocity, U

2 Blade rotational speed, ω

3 Positioning of the hub axi

The relative magnitudes of the tunnel velocity and the rotor rotational speed will determine the extent to which the wake is skewed, while the hub positioning relative to the test aerofoil will determine the curvature and elongation of the rotor wake.

It is important that the rotor blade of the vortex generator is positioned close to the working section in order to minimize the effects of vortex dissipation, while ensuring the generation of a well structured vortex with a high local convective velocity.

The physical parameters for the experimental setup were determined as a result of this study. These are given as:

1. The rotating shaft location would need to be approximately 3.2m downstream from the settling chamber
2. The rotational speed has a maximum of 600rpm (10Hz)
3. The pitch profile
4. The rotor blade length of 0.75m

Geometric sizing of the rotor was accomplished through a mixture of physical (ease of installation, construction) and aerodynamic considerations (NACA 0015 profile, chord-length 0.1m and aspect ratio of 6.6 based on the final length of the rotating blade (omitting clearance for hub). The final dimensioning gave a blade of tip radius 0.75m from the hub centre, 0.66m total blade length (Copland, 1997)). The adopted blade configuration is a rigid blade with no flap or lag hinges so as to increase confidence in the vertical location of the produced trailing tip vortex.

The incorporated pitch mechanism is loosely based upon that which is found in a helicopter. The pitch arm component is split into two elements, comprising of a horizontal pitch arm, and vertical pitch link, connected by a small needle bearing and clevis. This construction enables the pitch link to remain vertical throughout a complete 360° rotation (this allowed the size of the static cam on which the pitch

link rests to be reduced). The radial movement of the roller attached to the pitch link is also constrained through an arm which is attached to the lower rotating shaft. With the pitch and constraining arms horizontal, the blade is held at an incidence of 10 degrees.

The pitch profile of the cam which the roller rests on is divided into four 90 degree phases. The pitch profile for the vortex generation is split into four 90° phases: within the first phase, the blade is at zero degrees incidence, with the blade pointing into the settling chamber of the wind tunnel, and the roller is at its lowest position. During the second phase, the blade is pitched up to ten degrees as the pitch and constraining arms return to horizontal, and it is held at a constant of ten degrees through the third phase. During the final phase, the blade is pitched back down to zero degrees. Throughout the final phase, a spring housed internally within the hub ensured that that roller remained in contact with the hub.

The periodic vortex produced convects into the wind tunnel working section, with previous modelling of this interaction providing information on the vortex trajectory (Copland, 1997). In accordance with the conclusions of the numerical simulation, the wind tunnel is operated at $20ms^{-1}$ with the vortex generator revolving at 500rpm. This gives an interacting blade Reynolds number of $2x10^5$ for a blade chord of 0.1524m.

The vortex generator is equipped with an optical sensor on the rotating shaft which not only allows rotational speed measurement for control, but also provided the necessary trigger impulse for use with the PIV data acquisition software.

Hot wire anemometry (HWA) studies, performed by Doolan et al.(1999), revealed that the convecting vortex had a nominal diameter of 0.015m, and a vortex strength of approximately $0.6m^2s^{-1}$ (this agrees well with the previous predictions of (Chigier & Corsiglia, 1971, which considered the velocity profile of a vortex produced by a fixed wing). Since the blade impact parameter for this interaction is high and the

thickness ratio is sufficiently small, it may be assumed that the vortex will be 'cut' by the interacting blade, rather than be subjected to the influence of the blade boundary layer wrapping around the vortex core structure (as documented by Krishnamoorthy & Marshall, 1994).

In order to simplify the model of the interactional process, a stationary, uninstrumented, symmetrical blade (NACA 0015, c=0.1524m) was placed in the working section of the 1.15m x 0.8m closed return, low speed wind tunnel at the University of Glasgow. The blade is located at an offset of 0.225m from the wind tunnel centreline and 12-13 chordlengths downstream of the vortex generator (in accordance with the modelling requirements identified by Copland, 1997). This offset from the wind tunnel centre line ensures that the approach angle of the interacting vortex is 90°, while protecting the vortex from being obscured by any wake that may be produced from the shaft of the vortex generator [Figure 2-1, 2-2].

The curvature of the interacting blade makes it impossible to closely align the illuminating lightsheet to the surface of the blade. In order to examine the vortex near to the interacting surface, the blade was replaced with a sheet of glass (300mm long in order that a suitably thick boundary layer has developed across the plate), fixed in place of the interacting blade. The lightsheet was then aligned at a distance of 2mm from the interacting surface in order to interrogate the flow. In this instance, either side of the interacting surface was interrogated singly.

The examination of the effects of the thickness parameter (previously defined as T/σ by Krishnamoorthy and Marshall, 1998) required modification of the thickness of the interacting body relative to the approaching trailing tip vortex. In order to accomplish this, the same experimental arrangement as above was employed, but the blade section was replaced with a series of circular cylinders ($\frac{d_1}{\sigma} = 2$, $\frac{d_2}{\sigma} = 3.5$, $\frac{d_3}{\sigma} = 5$) in order to attain the required variations in the thickness parameter.

2.2 Experimental Modelling of a Twin Vortex Interaction with a Stationary, Rectangular Blade

For the simulation of the interaction of a twin vortex system with a stationary blade, a rotor blade was specifically designed with a modified blade tip section to produce a system of two counter-rotating vortices (similar to that which would be produced by the BERP rotor tip (Perry et al., 1998)). The blade had a constant NACA 0015 section from the root to 85% span, at which point the chord of the blade was varied to produce the 'paddle' tip (Yeager et al., 1997), with a notch on the leading edge to produce the inboard trailing tip vortex. Across the tip, a constant symmetrical NACA 0015 profile was maintained, with ¼ chord position of each successive section offset to produce the blade tip sweep [Figure 2-3].

Initial experimental analysis of the vortex system produced by the blade section was conducted in order to assess the effectiveness of the modified blade tip section with the blade oriented to a series of fixed angles (-5° to 15°) in order to interrogate the flow in the trailing edge region (wind tunnel velocity $5ms^{-1}$).

In order to incorporate the 'flapping' effect, the blade was then mounted on a ball screw assembly about the ¼ chord position in order oscillate and pitch the blade about ten degrees incidence with defined frequency (1hz) and amplitude (0.05m). Again, the wind tunnel working velocity was set to $5ms^{-1}$ (corresponding to the previous work of Ramaprian & Zheng, 1998), and the trailing edge region again interrogated.

In order to provide a comparative base, the examination of the flowfield behind a stationary and oscillatory rectangular blade for the same flow conditions as outlined above was also conducted.

Finally, the modified blade replaced the rectangular blade section on the vortex generator (as described above in Section 2.1), and the interaction of the twin vortex

system with a stationary blade (NACA 0015, c=0.1524m) interrogated through the use of the PIV technique (described in Section 2.3). The pitch cycle, revolution rate and tunnel speed were matched to those of the single vortex interaction case (rotor revolution speed of 500rpm and a wind tunnel running at 20 m/s).

2.3 Visualisation and Quantification of the Orthogonal Blade-Vortex Interaction

The traditional method for studying the helicopter rotor wake has been through the use of flow visualization techniques. These have included the use of balsa dust, smoke, cavitation, natural condensation, hydrogen or helium bubbles, schlieren, shadowography and interferrometry (Leishman, 1998). These techniques have been used in the study of multiple phenomena associated with helicopter operation, such as vortex formation, shock and acoustic waves, aerodynamic interactions, multi-rotor flows, and the wake roll-up in forward flight. All of these methodologies, although successful, have still not provided the detailed, quantitative data of the flowfield aerodynamics which are required in order to fully understand the mechanics associated with this interaction.

The Particle Image Velocimetry technique provides an effective method by which the interaction may both be visualized, and the flowfield interrogated. The techniques used are described in the following section.

The Particle Image Velocimetry technique (better known as PIV) is a non-intrusive optical measuring technique, which provides instantaneous global velocity information about a flowfield. In contrast to the more traditional single point measurement techniques (such as HWA and LDV), the PIV technique facilitates acquiring the necessary quantitative data alongside visualization of the spatial structure of the velocity field (Willert, 1997).

The methodology behind the PIV technique is based upon the inferrance of the fluid velocity properties from the motion of artificially introduced tracer particles (Westerweel, 1997). If it were to be assumed that these tracer particles were ideal, then:

1. They would exactly follow the fluid motion
2. They would not alter the flow or the associated fluid properties
3. They would not interact with one another

The velocity measurements that are obtained are, therefore, not true fluid velocity measurements, but an indirect measurement through the displacement of the tracer particles, D, within a finite time frame, Δt (where $\Delta t = t'' - t'$).

Therefore,

$$D(X;t',t'') = \int_{t'}^{t''} v[X(t),t]dt$$

[Equation 1]

where v[X(t)] is the velocity of the tracer particles within the flow.

If the ideal conditions were to be true, then v[X(t)] would be equal to the local fluid velocity u[X,t]. Within most experimental simulations, v[X,t] will only provide an approximation of the fluid velocity [Figure 2-4], as it is (almost) impossible to find tracer particles which will exactly follow the flowfield under investigation.

Another consideration when calculating the local fluid velocity in this manner is that the displacement which is being calculated, D(X; t′,t′′), will only provide the average velocity over a time Δt. Therefore, it is not possible for D to provide an

exact representation, but only an approximation with an associated finite error, ε, where:

$$\|D - u \cdot \Delta t\| \leq \varepsilon$$

[Equation 2]

This error ε is often negligible, as a result of the spatial and temporal scale of the flow being large with respect to the spatial resolution and exposure time delay of the images, and the dynamics of the tracer particles which are being imaged.

Flow information can be only be obtained from locations were tracer particles are present, and since these are randomly distributed throughout the flow, the displacement of individual tracer particles constitutes a random sampling of the displacement field, with different samples often providing different displacement fields D (dependency on seeding densities, etc). From Westerweel (1997), the implication is that the displacement field should be sampled at a density which matches the smallest length scale of the spatial variation in D. Since the displacement field may be regarded as a low-pass filtered representation of u, with a cut-off filter which is equal to ||D||, the displacement field should be sampled with an average distance which is smaller than the particle displacement (Westerweel, 1997). Therefore if a measurement in which the average distance between distinct particles is large, then D cannot resolve the full displacement field. However, in conditions where the seeding densities are high, it is not possible to identify matching particle pairs unambiguously. It is therefore convenient to refer to the tracer particles in terms of a tracer particle pattern, with the tracer particles constituting a random pattern associated with the fluid.

In order to ascertain whether a particle will closely follow the flow, the equation for unsteady motion of a suspended spherical particle (Basset, 1888) may be used. It relates the instantaneous relative velocity V between the particle and fluid, to the instantaneous velocities U_p and U_f, where $V = U_p - U_f$.

$$\frac{\pi d_p^3}{6}\rho_p\frac{dU_p}{dt} = 3\pi\mu d_p V + \frac{\pi d_p^3}{6}\rho_f\frac{dU_f}{dt} \quad \frac{1}{2}\frac{\pi d_p^3}{6}\rho_f\frac{dV}{dt} \quad \frac{3}{2}d_p^2(\pi\mu\rho_f)^{\frac{1}{2}}\int\frac{dV}{d\xi}\frac{d\xi}{(t \quad \zeta)^{1/2}}$$

[Equation 3]

Melling (1997) describes the implementation of this relation. The first two terms account for the acceleration force and the viscous resistance force which is described by Stokes' Law. As the acceleration of the fluid leads to a pressure gradient in the vicinity of the particle, an additional force is accounted for in the third term. The fourth term describes the resistance of an inviscid fluid to the acceleration of the suspended sphere, which is given by potential flow theory. The combination of the first, third and fourth terms provides a description of the acceleration force which is acting on the sphere, whose mass is increased by a 'virtual' mass equivalent to half of the fluid mass displaced by the sphere. The final term in the expression is the Basset history integral, which defines the resistance caused by the unsteadiness of the flowfield.

Stokes' drag law is considered to apply when the particle Reynolds number is smaller than one, and provides a conservative estimate of the tracking abilities of an artificially introduced particle.

Although this description of particle motion is sufficient for most flows which may come under investigation, there are some cases in which body forces are present which will induce additional effects. In swirling flows (such as the vortical flow which is under examination in the current study), the centrifugal force will accelerate the particles out of the vortex core and into the surrounding flowfield (Leishman, 1996). This is further complicated by the difficulties which may be encountered introducing particles into the core in the first place (as described by Durst, 1981).

Lecuona et al. (2002) considered the trajectories of seeding particles introduced into vortex-induced flows for situations where the particles could be described as 'heavy' (i.e. the particle density is substantially greater than the fluid density). When considering spherical particles in the range of 1-2μm, with an associated seeding density ratio of fluid to particle of 10^{-3} (which would be a typical ratio for the seeding of air with oil droplets), the analysis of the trajectories indicated that the error in the ability of the particles to trace the flow was extremely small for the azimuthal component (the effect of gravity in the order 10^{-5} and the analysis error of 10^{-4}). However for the radial component, there is a more notable effect, which leads to the ejection of the particles out of the vortex core. The time for the particles considered in this study to be ejected from the core and into the surrounding flow was only 0.3 seconds: this could be increased through substantially reducing the size of the particles, but this could lead to other undesirable effects (i.e. difficulty in recording due to the poor light scattering abilities of smaller tracer particles).

These findings were in agreement with the study conducted by Leishman (1996) on the modelling of the seeding particle dynamics in tip vortex flows, considering the typical parameters for the UH-60 Blackhawk rotor, through the solution of the differential equations of motion of a seed particle in two dimensional cylindrical flow, given by:

$$\frac{dV_{rp}}{dt} = \frac{V_{\vartheta p}^2}{r} + \frac{1}{\tau_v}(V_r - V_{rp}) \qquad \text{and} \qquad \frac{dV_{\vartheta p}}{dt} = -\frac{2V_{\vartheta p}V_{rp}}{r} + \frac{1}{\tau_v}(V_\vartheta - V_{\vartheta p})$$

[Equation 4] *[Equation 5]*

(assuming Stokes drag law and spherical particles, with a given swirl and radial velocity). It should be noted that these equations are coupled by the Coriolis term (Leishman, 1996).

Again, the particles inside the vortex core quickly spiral outwards from the vortex core, leading to the creation of a void, with particles which are further away from the vortex core following a more circular path. The radial velocity errors were again found to be much larger than the equivalent swirl errors, with these errors dominating up to a distance of two core radii from the vortex axis, with a peak distribution in particles observed well outside the viscous core. Again, the size of the particles had a significant influence, with the smaller particles being subject to a much smaller error ratio (<1μm) than larger particles under the same flow conditions.

The accuracy with which the particles trace the fluid flow is only one of the considerations in seeding selection. As most object planes are viewed at 90°, the light scattering abilities of the seeding particles when illuminated with a monochromatic light source must also be considered, as the choice of the optimal diameter of particles is a compromise between adequate tracer response of the particles in the fluid, and a high signal-to-noise ratio (SNR), which requires large particles. In recent times, MIE theory has been extended in order to include Gaussian illuminating beams, which allows the evolution of the profile of a particle image on a recording medium to be tracked as a function of the particle radius.

The illumination for the PIV system which has been utilized within this study is provided by two Spectra Physics GCR-13-10 frequency-doubled, double-pulsed Nd:YAG lasers, which run at a nominal repetition rate of 10Hz, with a pulse duration of 8ns. The beams produced are passed into the wind tunnel working section through the use of an arrangement of mirrors, a beam-shaping telescope and a cylindrical lens arrangement, which produce a lightsheet in the vertical plane. This is then passed into the working section from above to illuminate the region of interest in the flow [Figure 2-5]. The lightsheet produced is approximately 1mm in thickness within the interrogation region, but this may be adjusted through the telescopic lens arrangement.

Seeding is provided by a Taylor Scientific smoke generator, which introduces Shell Ondina E.L. 'oil mist' into the flow, each particle having a nominal diameter of 2μm. The image capture system consists of two eight bit Kodak Megaplus ES 1.0 digital cameras, each of 1k x 1k resolution, operating in triggered double-exposure mode and two National Instruments PCI 1424 digital frame grabbers. The synchronization of the cameras, frame grabbers and laser synchronization system are programmed and controlled through LabVIEW® on a PC.

2.3.1. 2D2C Particle Image Velocimetry Technique

The 2D2C Particle Image Velocimetry (PIV) technique is the base PIV technique, in which a plane in the flow is illuminated and images of the plane taken from an orthogonal direction. This allows the two dimensional vector components to be calculated for a projection of the flow into the illuminated plane.

The analysis of the PIV images and vector validation are carried out simultaneously by a cross-correlation through application of a standard FFT and a window shifting technique. The application of the FFT is generally preferred for evaluation due to the increased processing time over the other correlation techniques, such as via the direct and normalized correlation schemes (the use of the FFT has been shown to reduce analysis time by as much as $1/50^{th}$ - the direct correlation scheme requires $O[M^2N^2]$ calculations to be performed, whereas the discrete Fast Fourier Transform only requires $O[N^2 \log N]$ calculations, bases on the matrix of size (m,n)). The limitations of applying the FFT-based cross correlation are two-fold: (1) unlike the direct cross correlation, the FFT may only be applied to infinite domains, and (2) for computational efficiency, the FFT-CC must be applied to samples which are square and of a size to the power of two (i.e. 4x4, 16x16, 32x32, etc.). The validation method is referred to as the Forward/Reverse Tile Test (FRTT) [Figure 2-6]. This technique involves splitting the image pairs into a series of discrete, equally-sized adjacent tiles (typically 32x32 pixels), and calculation of the mean particle image

displacement for each tile using a standard FFT and sub-pixel accurate detection routine in order to avoid peak-locking effects (within a typical PIV measurement, in order to achieve sub-pixel accuracy, a smooth curve is fitted through data points in the vicinity of the discrete correlation peak, but this method of curve fitting causes a bias towards discrete values of displacement – as discussed in Raffel et al., 1998 – and is referred to as the peak-locking error) . Two new tiles and their associated particle image displacements are then defined from this. From the comparison of the central vector with the two projected vectors, wild vectors may be significantly reduced within the flow field. Previous descriptions (Green et al., 2000) of the implementation of this technique also address the accuracy of the method.

The pixel displacements are then converted into equivalent spatial displacements using a transfer function, which represents a photograph of a calibration grid placed in the working section of the wind tunnel within the illuminated region. The grid is typically a 10cm x10cm regularly spaced array of black dots on a white background, each at 5mm intervals. A local co-ordinate system based on the centroid of each of these dots may then be used to evaluate the local transfer functions. This accounts for stretching and rotation of the image due to the camera lens, which may lead to a distortion in the vector maps. The flow field associated with the orthogonal blade-vortex interaction may be assumed to be a uniform flow of $20ms^{-1} \pm 10ms^{-1}$ due to the passage of the vortex. The accuracy of the system was assessed by recording a uniform flow and comparing the PIV data with velocity data from a pitot-static measurement. From a number of runs in a speed range from $10ms^{-1}$ to $30ms^{-1}$, the worst case error was found to be 3%, and this tended to occur at low seeding density. The application of the previously-mentioned FRTT scheme has been observed to improve vector map accuracy, especially at low seeding densities (Green et al., 2000), which addresses the issues of the difficulty of introducing seeding into swirling flows, as mentioned above [Figure 2-6].

Post processing steps may also be employed in order to further reduce the number of wild vectors appearing in the vector maps. The most common approach taken for this comprises of data validation and interpolation (as described by Noguiera et al, 1997). It should be noted that a high level of such vectors may be found within the vortex core, due to the ejection of the smoke particles by the relatively high rotational velocity gradient which exists within the vortex core.

In order to calculate the vorticity ($\omega = \frac{\partial v}{\partial x} - \frac{\partial u}{\partial y}$) within the core, the vorticity for one tile is calculated by a circulation method. This is then averaged over four adjacent tiles in order to reduce the effect of errors present within the flow. A similar methodology is employed for the calculation of divergence ($\Delta = \frac{\partial u}{\partial x} + \frac{\partial v}{\partial y}$) within the two-dimensional space, but the data are averaged over 9 tiles.

In order to visualize the progression of the orthogonal blade-vortex interaction, the telescopic lens arrangement is used to introduce a lightsheet into the wind tunnel working section from above. This illuminates the required region in the flow, as dictated by the vortex/blade orientations and location.

As the system that is currently in use in the University of Glasgow is comprised of two Kodak Megaplus ES 1.0 and 2 Spectra Physics Nd:YAG lasers, it is possible to set up two independent PIV systems (one camera / one laser) in order to facilitate simultaneous tracking of flow features in separate regions within the flow. This particular feature of the system was exploited in order to examine the interaction on either side of the interacting blade surface simultaneously [Figure 2-7].

Figure 2-7 indicates the relative position of the illuminating lightsheet for each of the configurations examined for the investigation of the single vortex interaction with the stationary, rectangular planform. Figure 2-8 also provides information on

the relative position of the lightsheet for the examination of the twin vortex system. Figure 2-9 shows the actual experimental setup for the interrogation of the upper and lower blade surfaces simultaneously using the twin laser system, with the two laser sheets and their orientation relative to the interacting blade shown.

2.3.2. The 2D3C (Stereoscopic) Particle Image Velocimetry Technique

The use of a two component Particle Image Velocimetry technique is a valuable tool for an initial study of any fluid motion. However, limitations in the use of this technique quickly become apparent in studies where there is an appreciable three dimensionality to the flow under examination, as the 'classical' PIV technique only records the projection of a velocity vector in a two dimensional plane, with information about any out-of-plane components subsequently lost. In the case of flows where this out-of-plane component is significant, such as that of the current study, this may lead to an unrecoverable error in the calculation of the local velocity vector. The requirement for the recovery of all flow information in three dimensions has been highlighted in many areas of research (Willert, 1997), and a variety of techniques have been developed through which this may be accomplished (for example, holographic PIV and dual-plane PIV). The most straight forward to implement is the use of an additional camera viewing from a different perspective. This is commonly referred to as the Stereoscopic Particle Image Velocimetry (2D3C) technique. It should, however, be noted at this point that although the most common SPIV technique requires two cameras, there are methodologies which allow this type of stereo recording to be achieved through the use of a single camera with an arrangement of mirrors placed in front of the lens to produce the two images required for evaluation.

When comparing the three available PIV methodologies for three-dimensional interrogation of a flow field (stereoscopic, holographic and dual plane), the SPIV is

often the easiest to implement, as it essentially uses the same software as the two component system. There are two standard approaches to the stereoscopic particle image velocimetry technique, either the lens translation method, or the angular displacement method with a tilted backplane (the Scheimpflug condition) (Prasad & Jensen, 1995).

The translational methodology uses two cameras whose axes are orientated parallel to one another, and orthogonally to the lightsheet being viewed. Both of these cameras will view a common area encompassing a line of symmetry of the two camera system, but viewing from two off-axis directions. The angular approach also utilizes two cameras, but with the axes rotated so that they intersect at the centre of the region being recorded [Figure 2-10]. Although the displacement methodology is easier to implement, limitations are often found due to the camera lenses being used at limit, and hence leading to degradation in particle image quality. For this reason, it is more common to use the angular displacement methodology, as has been utilized in the current study.

The angular displacement method requires that the object plane is no longer parallel to the lens plane. With this arrangement, it becomes increasingly difficult to obtain particle images that are well focused throughout the image plane due to the perspective effects. To overcome this, the Scheimpflug condition is enforced, in which the object plane, the lens plane and the image plane are co-linear [Figure 2-11].

The Scheimpflug principle (Merklinger, 1996) (named after Theodor Scheimpflug, although it was first proposed by Jules Carpentier) provides a guide for the manner in which a camera lens and/or the backplane should be tilted when focussing upon a plane which is not parallel to the imaging plane. The Scheimpflug condition states that for an object to be correctly focused under these circumstances, the object plane, lens plane and image plane must all meet in a common line. The use of this

condition, however, results in a non-linear magnification across the image plane, which must be accounted for in the calculation of the local velocity vector.

The reconstruction of the velocity field from the two sets of images recorded using this angular displacement technique is accomplished through the application of simple geometric relationships. It is approached through the back projection of the data from the imaging plane to the object plane, which may be accomplished in two ways. The first of these approaches involves the use of a geometric back projection, requiring an extremely accurate setup as it is very sensitive to flaws in the experimental arrangement, such as camera misalignment. The second of these techniques, which is a more flexible approach, is the use of the calibration method, then the use of a generalized function to project the data from the image to the object plane. The projection may then be performed in two ways, either involving the back projection of the image pixel data (known as mapping), or back projection of the displacement vector data, which is known as warping.

In order to compute the three-component displacement vector field, the two component vector field is first computed for each of the camera viewing angles. The third component is then extracted as a result of the combination of the individual two component maps. The back projection connects the image plane with the object plane. The geometric back projection technique is based upon ray tracing, which makes assumptions about the geometry of the optics. An alternative approach is the generalized back projection, which uses a generalized function to connect a point within the image plane to the object plane, and vice versa. Several functions have been suggested in order to accomplish this: second order polynomial (Soloff et al., 1997), second order rational polynomial for a two dimensional calibration (Press et al., 1992), and bicubic splines for a three dimensional calibration scheme (Van Oord, 1997).

For both the warping and mapping algorithms, the two-dimensional vector field is constructed using standard PIV processing methods. In the warping method, the 2D

vector field is obtained first, and each vector is then back projected (warped) from the image to the object plane. In the mapping approach, the images are mapped to the object plane, and the 2D vector field computed for each new image, with the vector scaled to match the dimensions of the object plane.

From this point, there is a standard reconstruction methodology employed in order to recover all three velocity components. The method described is based upon a second order rational polynomial calculation (Willert, 1997).

The following methodology for reconstruction is that which was presented by Willert (1997).

If it is assumed that both the cameras are focussed on a single region, the co-ordinates of the area in the region being interrogated can be described by $L_1(x_1,y_1,z_1)$ and $L_2(x_2,y_2,z_2)$, where 1 and 2 refer to the two different viewing cameras (there is an assumption of a pinhole camera). A point P with the co-ordinates (x_p,y_p,z_p) within the region of interest would be observed to have the displacements (dx_1,dy_1) and (dx_2,dy_2) from the two different viewing angles [Figure 2-12].

The lightsheet may be assumed to be of zero thickness, since the distance from the imaging plane to the object plane will be of several orders of magnitude greater. The angles that are enclosed by the lightsheet normal and the viewing ray are α_1 and α_2 for the separate camera viewing angles within the x-z plane, and similarly β_1 and β_2 within the y-z plane.

These may be reconstructed to give:

$$dx = \frac{dx_2 \tan\alpha_1 - dx_1 \tan\alpha_2}{\tan\alpha_1 - \tan\alpha_2}$$

[Equation 6]

$$dy = \frac{dy_2 \tan\beta_1 - dy_1 \tan\beta_{21}}{\tan\beta_1 - \tan\beta_2}$$

[Equation 7]

$$dz = \frac{dx_2 - dx_1}{\tan\alpha_1 - \tan\alpha_2} = \frac{dy_2 - dy_1}{\tan\beta_1 - \tan\beta_2}$$

[Equation 8]

$$\text{where : } \tan\alpha_1 = \frac{x_p - x_1}{z_p - z_1},\ \tan\alpha_2 = \frac{x_p - x_2}{z_p - z_2},\ \tan\beta_1 = \frac{y_p - y_1}{z_p - z_1} \text{ and}$$

$$\tan\beta_2 = \frac{y_p - y_2}{z_p - z_2}.$$

This is only a general equation for the described arrangement, and given the conditions, it may be necessary to modify it. If the cameras (and hence the imaging planes) are at the same height, β_1 and β_2 will become very small, and as such $\tan\beta_1$ and $\tan\beta_2$ will also become small. This means that only certain forms of these equations may be used to determine the dy and dz components (which are both dependent upon β and $\tan\beta$). There are two equations that may be used to determine the dz component, which makes the problem more straightforward to overcome. The equation governing the dy component may then be modified to give:

$$dy = \frac{dy_1 + dy_2}{2} + \frac{dz}{2}(\tan\beta_2 - \tan\beta_1) = \frac{dy_1 + dy_2}{2} + \frac{dx_2 - dx_1}{2}\left(\frac{\tan\beta_2 - \tan\beta_1}{\tan\alpha_1 - \tan\alpha_2}\right)$$

[Equation 9]

To be able to implement this reconstruction, there are a series of steps that must first be addressed. This displacement data must first be converted from the image plane to the corresponding true displacements within the global coordinate system, which involves the implementation of a calibration technique. A projection between the object plane (X_0, Y_0) and the image plane (X_i, Y_i) may be expressed as:

$$\begin{bmatrix} w_o X_o \\ w_o Y_o \\ w_o \end{bmatrix} = \begin{bmatrix} a_{11} a_{12} a_{13} \\ a_{21} a_{22} a_{23} \\ a_{31} a_{32} a_{33} \end{bmatrix} \begin{bmatrix} w_i X_i \\ w_i Y_i \\ w_i \end{bmatrix}$$

[Equation 10]

where w_0 and w_i are both constants and $a_{33}=1$. This may then be rewritten in standard coordinates to give the non-linear expressions:

$$X_0 = \frac{a_{11} X_i + a_{12} Y_i + a_{13}}{a_{31} X_i + a_{32} Y_i + 1}$$

[Equation 11]

$$Y_0 = \frac{a_{21} X_i + a_{22} Y_i + a_{23}}{a_{31} X_i + a_{32} Y_i + 1}$$

[Equation 12]

If the region that is viewed by both of the camera views is considered, it may be seen that the common area observed is of the form of a rectangle. This projection will map a rectangle onto a general four-sided polygon. Geometric distortions in the image, such as barrelling and pincushioning will be accounted for by extending these expressions to higher orders. The best match for these unknowns are acquired through the use of a method such as the Levenberg-Marquart methodology for non-linear least squares (Press et al., 1992).

The calibration procedure for the stereoscopic arrangement is similar to that which is used for the two component visualisation, using two images of a single target from the two different viewing angles. The coordinates of the markers on the grid are reconstructed, and the Levenberg-Marquart method applied to each of the two sets of image-object pairs to yield the reconstruction coefficients.

In order to visualise the three components of the vortex core during the interaction, the lightsheet (introduced in the same manner as for the 2D2C study) is viewed from the two viewing angles as required for the angular displacement method (as described in the methodology above) [Figure 2-13]. The two Kodak Megaplus ES 1.0 cameras are used in a symmetrical arrangement on one side of the lightsheet, angled to a 15° viewing angle (this viewing angle is limited by the experimental configuration). The cameras / lightsheet combination are then traversed across the surface of the blade in order to fully visualize the complete progression of the interaction. Unlike for the two dimensional arrangement, only a single blade surface is interrogated at a time.

2.3.3 Considerations on the Accuracy of the Particle Image Velocimetry Technique

The Particle Image Velocimetry technique is based upon statistical correlation of sub-regions to determine local flow velocities, and as such is subject to errors arising from the finite tracer particle numbers, volume size and image resolution (Hart, 1998). Bias in the velocity vectors obtained by correlating finite regions can be introduced through a variety of experimental conditions (unmatched particles, particle overlap, image intensity, etc). Correlation errors introduced in this way are most often referred to as outliers - resulting from mismatch in the particle image (in which case a small correlation peak is obtained), and they are (usually) easily identifiable as they tend to be random in both direction and amplitude (the FRTT scheme described above is effective in reducing instances of outliers). Usually these errors are larger than one pixel and are therefore easy to detect. The major factors responsible for outliers are an insufficient number of particles being present in the particle images (Keane & Adrian, 1992), strong velocity gradients and strong three-dimensional flow motions (Hart, 1998) (both of which have an effect on the number of particles entering and exiting the sub-region).

As the number of tracer particles which occur within a sample volume increases, there is a lesser chance of a particle set existing which is of a similar intensity and pattern within a finite space (Hart, 1998). With this in mind, the probability of obtaining the accurate displacement using correlation methods is going to increase with increasing particle density (it has been demonstrated that the number of spurious vectors within correlated sub-regions drops dramatically as the particle density is increased by about ten particle images per region (Keane & Adrian, 1992)) Increasing particle density does have limitations, however, due to finite spatial resolutions and intensities, and a point is reached where the introduction of additional tracer particles will have a negative effect on the correlation. Alternatively, the size of the sample volume could be increased in order to increase the number of tracer particles without increasing seeding density, but this will impact adversely on the resolution.

In addition to excessive velocity gradients and out-of-boundary particle motion, other issues such as non-uniform illumination, particle coalescence, surface reflections and particle image overlap all contribute to sub-pixel bias error (although these effects are usually not as severe (Hart, 1998)).

All the aforementioned factors which cause the DPIV error have one feature in common – they produce noise in particle images (image noise is defined as all contributions other than the particle image itself). The uncertainty in the image noise is defined by the uncertainty in the pixel values. Since particles are described by pixel profiles, the uncertainty in the pixel values results in the uncertainty of the particle locations and hence results in errors of particle displacements. The definition of the correlation function in a discrete domain and the method used to locate the sub-pixel correlation peak can also contribute both to mean-bias errors and to RMS errors.

The particle displacement is usually determined through the cross-correlation of small image masks of singly exposed image pairs. Since the typical correlation can yield thousands of pixel displacements (in the case of a 32x32 tile size interrogation, it would be expected to have 1024 vectors returned), the computational effort associated with calculation is enormous. Considering a square interrogation area of size N, the number of operations performed will be in the order of N^4.

In order to reduce this calculation time, the Fast Fourier Transform is typically used in preference in order to speed up the analysis process, which will reduce the number of operations to the order to $N^2 \ln N$. As mentioned earlier, the adoption of this method does have a number of drawbacks – the FFT is only well defined for infinite domains, the two sub-samples should be square, of equal size and of a size of power 2.

When the difference between the movement of tracer particles in one region of a sample volume versus another is greater than the radius of a single tracer particle, then increasing the sample volume size results in an increase in correlation anomalies without increasing the peak correlation value (Keane and Adrian, 1992). There is, thus, a reduction in the correlated signal-to-noise ratio. This is due to a separation in the correlation peaks of individual particle images that is greater than the width of the correlation of a single particle image against itself. Increasing the sample volume exacerbates the problem as the relative separation in individual particle correlations from one region to another due to gradients in the flow increases as well. It, however, does reduce correlation anomalies associated with particles entering and exiting the sample volume in the time between exposures. As the sample volume is increased, a smaller fraction of particles enter and exit relative to the total number of particles that remain within the sample volume between exposures. Consequently, there is a reduction in correlation anomalies associated with this phenomenon.

The displacement peak maximum in the digital correlation function can be easily located to a precision of 0.5 pixels. However, there are various methods that can be used to estimate the displacement peak location to a more accurate sub-pixel level (Lourenco and Krothapalli, 1995).

The variation of ε has been confirmed to be directly relate to the particle diameter d_p (Adrian, 1991, Prasad et al., 1992). This measurement error has also been identified as being practically independent of the actual displacement (although this doesn't hold for cases were $|u| < 1/2px$; in this situation, the variation of the measurement error appears to be directly proportional to u). Ignoring errors which are attributable to the uncertainty in Δt (which is a valid assumption for flows less than several hundred metres per second (Westerweel et al, 1997)) [Figure 2-14], the RMS error in the velocity measurement is given by:

$$\sigma_u = \frac{\sigma_{\Delta x}}{\Delta t} = \frac{\sigma_{\Delta x}}{M_o \Delta t} \qquad \textit{[Equation 13]}$$

The precise relationship between the RMS displacement error and the properties of the image is complex, and is dependent upon the method which is used to determine ΔX_p. Adrian (1986) asserted that:

$$\sigma_{\Delta x} = c_\tau d_\tau \qquad \textit{[Equation 14]}$$

where d_τ is the diameter of the recorded image, and c_τ is a constant which depends on the ability of the analysis procedure to determine the displacement between the images. Typically, this constant is 1-10% of the image diameter. The recorded image diameter is given approximately by:

$$d_\tau^2 = d_e^2 + d_r^2 \qquad \textit{[Equation 15]}$$

where d_r represents the resolution of the recording medium, and d_e is the diameter of the optical image prior to being recorded. Assuming diffraction-limited imaging and

a Gaussian intensity distribution of the geometric image of the particle, the diameter of the diffracted image of the particle is:

$$d_e^2 = d_s^2 + M_o^2 d_p^2 \qquad \textit{[Equation 16]}$$

where d_p is the particle diameter and the diffraction-limited spot size is given by:

$$d_s = 2.44(1 + M_o) f^{\#} \lambda \qquad \textit{[Equation 17]}$$

where $f^{\#}$ is the f-number of the lens and λ is the wavelength of the light.

Considering the measurement error introduced by the analysis procedure, the flowfield of a two dimensional planar jet impinging on a wall for known flow conditions is considered [Figure 2-15]. The velocity distribution has been calculated by using the three-dimensional large-eddy-simulation (LES) code (Okamoto et al., 2000), and this forms the target flowfield. Figure 2-16 shows the out-of-plane (z) velocity distribution with the contour map. At the impingement point, there is a large out-of-plane velocity. After the injected jet impinges on the wall, the jet flows along the wall. In the area to be interrogated (indicated by 01), there are relatively low three-dimensional effects exhibited by the flow compared to the region of jet impingement (indicated by region 21 in Figure 2-16). Tables 1 and 2 below give the parameters associated with the pre-generated standard images [Figures 2-17 to 2-24].

Table 1 Parameters of pre-generated standard images

Image	$\bar{v}$	v_x	$\overline{\lvert w \rvert}$	$\lvert w \rvert_x$	N	$\bar{d}$	σ_d
01	7.4	15.0	0.017	0.10	4000	5.0	1.4
02	22.0	45.0	0.060	0.30	4000	5.0	1.4
03	2.4	5.1	0.006	0.03	4000	5.0	1.4
04	7.4	15.0	0.017	0.10	10000	5.0	1.4
05	7.4	15.0	0.017	0.10	4000	5.0	1.4
06	7.4	15.0	0.017	0.10	4000	5.0	0.0
07	7.4	15.0	0.017	0.10	4000	5.0	4.0
08	7.4	15.0	0.017	0.10	4000	5.0	1.4

$\bar{v}$ is the average image velocity (pixels/interval) v_x is the maximum image velocity (pixels/interval)

$\overline{\lvert w \rvert}$ is the average out-of-plane velocity (intervals^{-1}) $\lvert w \rvert_x$ is the maximum out-of-plane velocity (intervals^{-1})

N is the number of particles, d is the average particle diameter (pixels) and σ_d is the standard deviation of d (pixels).

Table 2 Description of Case Numbers

Case No.	*Image Size*	*Area*	*Laser Thickness*	*Interval*	*Average Velocity*	*Particle Displacement*	*Standard Deviation*
01	256x256	10x10	2	0.033	8.9	7.5	3.0
02	256x256	10x10	2	0.01	8.9	7.5	3.0
03	256x256	10x10	2	0.1	8.9	2.5	1.0
04	256x256	10x10	2	0.033	8.9	2.5	1.0
05	256x256	10x10	2	0.033	8.9	22	9.0
06	256x256	10x10	2	0.033	8.9	22	9.0
07	256x256	10x10	2	0.033	8.9	7.5	3.0
08	256x256	10x10	0.2	0.033	8.9	7.5	3.0

By analysing these images using the correlation function to be applied to the BVI analysis, the response to a variety of adverse flow conditions (as detailed above) was

calculated, and the measurement error in the mean flow and standard deviation calculated (Table 3).

Table 3 Benefit of the application of the FRTT scheme to a range of adverse flow conditions. Case (a) is without FRTT applied, case (b) is with FRTT applied

Case No.	$\bar{V}$ *px/interval* *(measured)*	$\bar{V}$ *px/interval* *(actual)*	$\bar{V}$ cms^{-1} *(measured)*	$\bar{V}$ cms^{-1} *(actual)*	σ *(measured)*	σ *(actual)*	max v *px/interval* *(measured)*	%
01a	7.0068	7.5	8.294	8.9	4.29	3.0	14.46	6.80
01b	6.9461	7.5	8.2222	8.9	3.2	3.0	10.67	7.616
02a	2.3817	2.5	9.3035	8.9	1.206	1.0	4.2375	4.53
02b	2.2587	2.5	8.823	8.9	1.2247	1.0	3.6267	0.865
03a	10.475	22.0	4.0918	8.9	6.2875	9.0	17.5919	54.02
03b	20.7932	22.0	8.1223	8.9	14.801	9.0	34.9174	8.738
04a	7.8063	7.5	9.2404	8.9	3.596	3.0	13.4444	3.8247
04b	6.9491	7.5	8.2257	8.9	3.34	3.0	10.4927	7.5764
05a	6.6768	7.5	7.9034	8.9	5.1244	3.0	14.9303	14.9303
0.5b	6.9856	7.5	7.5681	8.9	3.589	3.0	10.236	4.236
06a	6.6294	7.5	8.5648	8.9	3.5438	3.0	12.9461	11.828
06b	6.4109	7.5	7.5887	8.9	3.257	3.0	10.3424	14.7337
07a	7.5824	7.5	8.9754	8.9	5.1421	3.0	15.3964	0.8472
07b	7.2923	7.5	8.632	8.9	3.4374	3.0	12.8756	3.011
08a	7.1690	7.5	8.486	8.9	4.18	3.0	13.8941	4.65
08b	6.6419	7.5	8.4621	8.9	3.3085	3.0	10.3594	4.9202

As would be expected, the FRTT scheme drastically improves the performance of the analysis in some of the extreme cases considered (with specific reference to case 03, in which large particle displacements due to long time delays between frames). The analysis presents a high level of accuracy (better than 1%) for cases where there are small inter-frame displacements (case 02), as would be expected, with the accuracy decreasing to 5% in cases of a significantly large out-of-plane component

being present in the flow (as shown in case 08). Case 03 demonstrates the usefulness of the FRTT scheme in decreasing the errors due to outliers in the instance of a large particle displacement inter-frame, in which the unacceptably high error of 54% is decreased to an 8.7% error in measurement. Given that for the current case under investigation the inter-frame particle displacements are to be small with a significant out-of-plane component, the correlation process is demonstrating an accuracy of better than 5% for extreme cases.

The flow was also interrogated for a uniform flow condition, where both the vertical (v) and out-of-plane (w) component should be measured as zero [Figure 2-25, Figure 2-26]. Measurements taken for this condition over a series of 20 runs, given an inter-pulse separation of 35μs and wind tunnel velocity of $20ms^{-1}$ (as per the experimental conditions for the orthogonal blade-vortex interaction simulation), suggested an accuracy of better than 3% in the in-plane velocity measurement (Table 4). Similar measurements were taken for the freesteam flow using the stereoscopic arrangement outlined in Section 2.3.2. For the same flow conditions (inter-pulse separation of 35μs and wind tunnel velocity of $20ms^{-1}$), the stereoscopic visualization suggested an accuracy of better than 5% for visualization within the three reconstructed components (Table 5).

Table 4 Distribution of Mean in-plane flow velocity for freestream flow condition (Two Dimensional Interrogation)

$\bar{u}$	$\overline{ud}$	$\overline{vd}$	σ_u	σ_{ud}	σ_{vd}
19.4026	19.3023	1.3016	2.0799	2.0585	1.7661

Table 5 Distribution of Mean in-plane flow velocity for freestream flow condition (Three Dimensional Interrogation)

$\bar{u}$	$\overline{ud}$	$\overline{vd}$	$\overline{wd}$	σ_u	σ_{ud}	σ_{vd}	σ_{wd}
20.9540	20.7551	-0.5728	0.0481	3.3645	3.6098	2.5401	0.5001

2.4 Summary

Chapter Two has presented the methodology which has been employed in the examination of the orthogonal blade vortex interaction. The design and development of a facility which could be utilized to simulate the orthogonal blade-vortex interaction was first documented in Copland (1997), and the current study has built on this facility.

In order to further develop the knowledge base in this area (pressure measurements made by Doolan et al., 2000, LIF by Marshall & Krishnamoorthy, 1998), particle image velocimetry (PIV) was utilized to obtain quantitative information about the deformation of the vortex core and the surrounding flow field as the interaction progresses. This chapter has presented the background to this methodology, and described its implementation in view of the requirements for this study.

The 1.15m x 0.8m wind tunnel at the University of Glasgow allows for two types of visualization of the interaction to be performed – a two dimensional study of the projection of the flow into a plane using a single laser/camera arrangement, enabling capture of the flowfield on either side of the interacting blade simultaneously, and the stereoscopic visualization, which will allow resolution of all three components of the interaction within a finite depth of field.

The measurement technique and the image processing methodology have been presented, and validation of the system has indicated that the current experimental

arrangement will yield an accuracy of better than 3% for the in-plane measurements using the two-dimensional, two-component reconstruction, and better than 5% for the stereoscopic reconstruction of components.

Chapter Three will present the results of an examination of the vortex deformation of the interaction of a single vortex produced by a rectangular blade, and the effects on the surrounding flowfield as the interaction progresses. This is then complimented with a study of the flowfield and vortex deformation associated with the interaction of a trailing tip vortex produced by a modified blade section with a stationary rectangular blade, in which a twin vortex system is produced by the representative rotor, outlined in greater detail in Chapter Four.

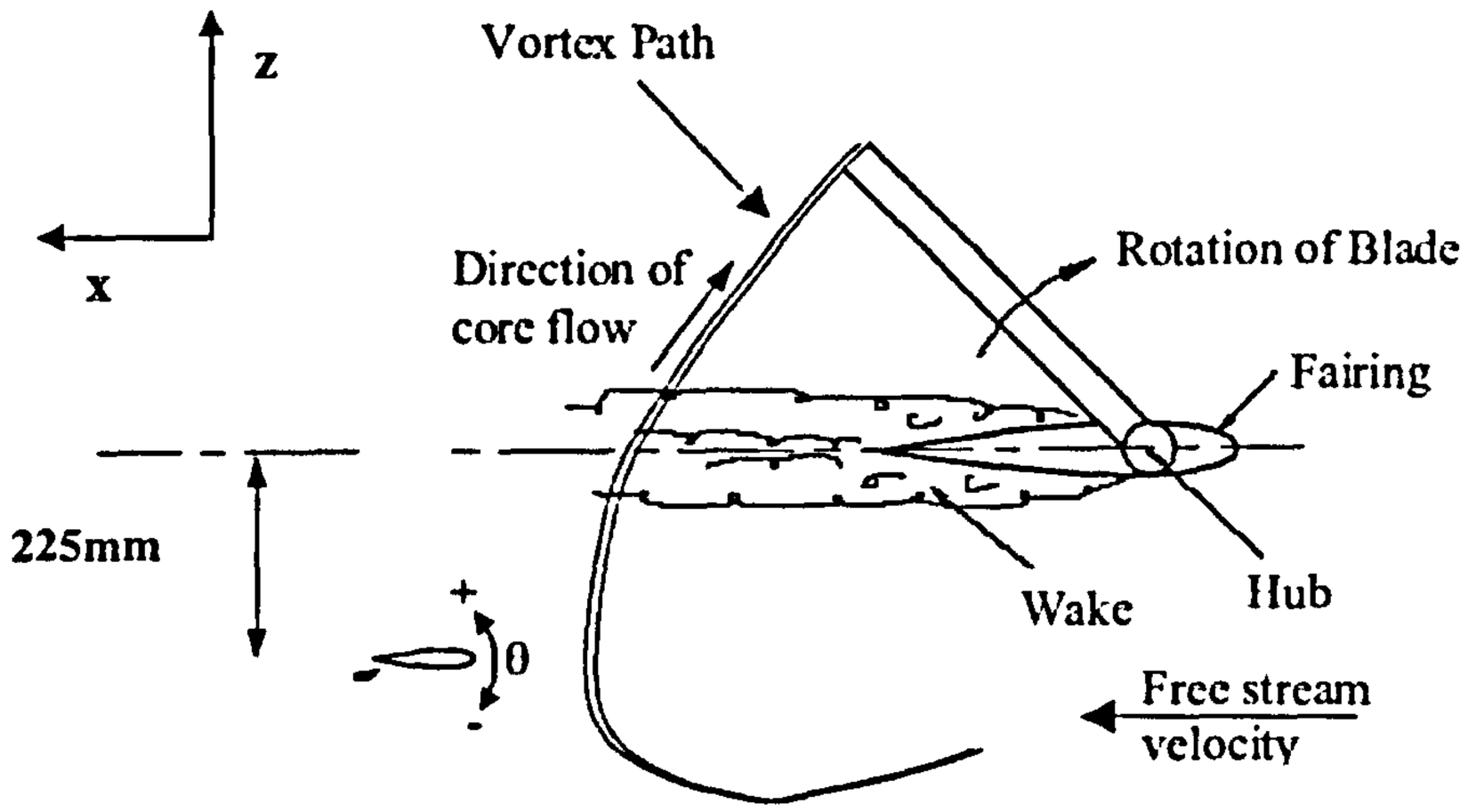

Figure 2-1 Plan View of the Experimental BVI Facility

The experimental setup was pre-determined in work of Copland (1997), which determined the relative position of the interacting tail rotor blade which allowed a representative interaction to occur. The 225mm offset from the wind tunnel centre line is to ensure that the vortex is not obscured by the wake shed from the vortex generator. The y-z axis is indicated

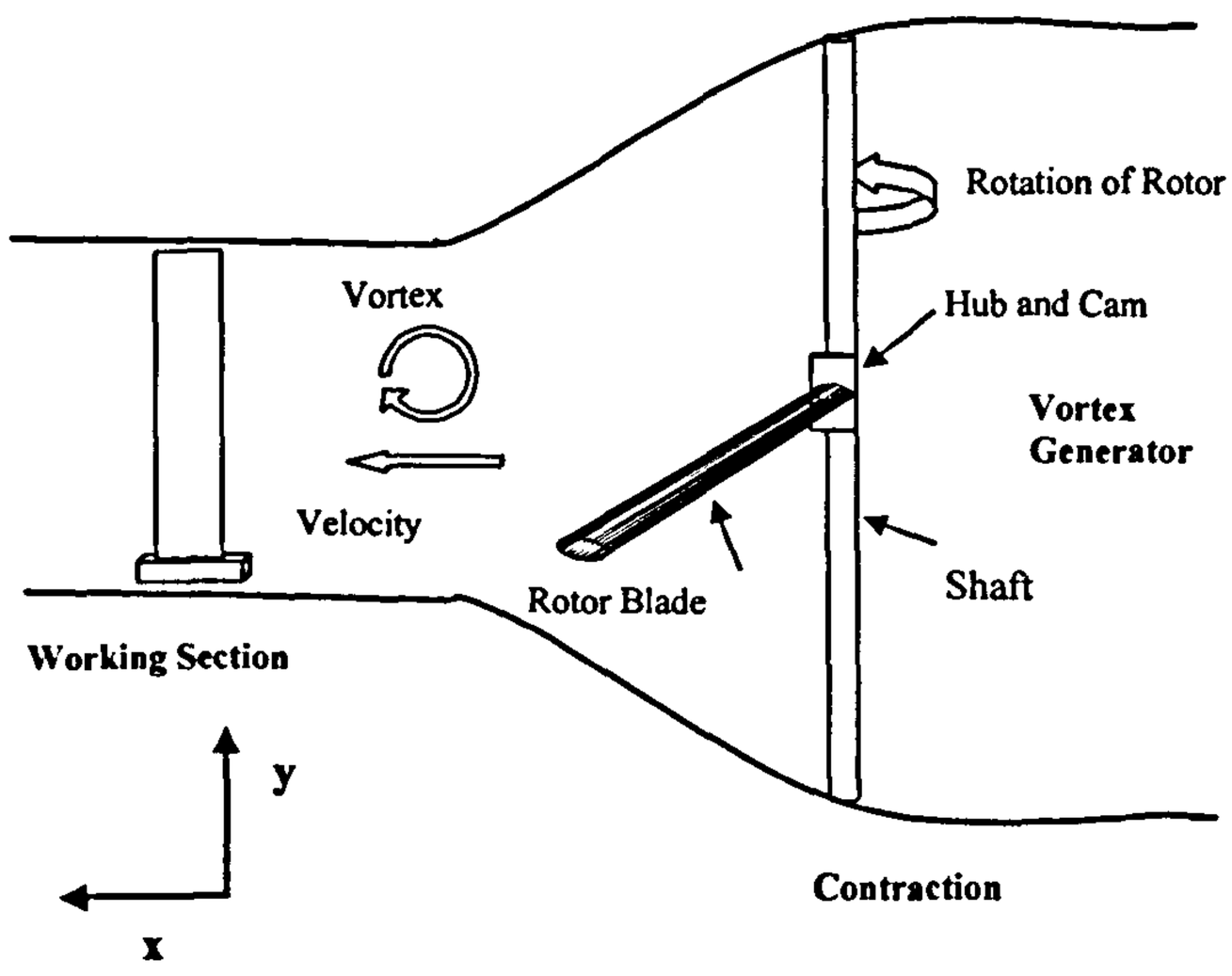

Figure 2-2 The BVI facility in the 1.15m x 0.8m wind tunnel at the University of Glasgow indicating the sense of the x-y axis

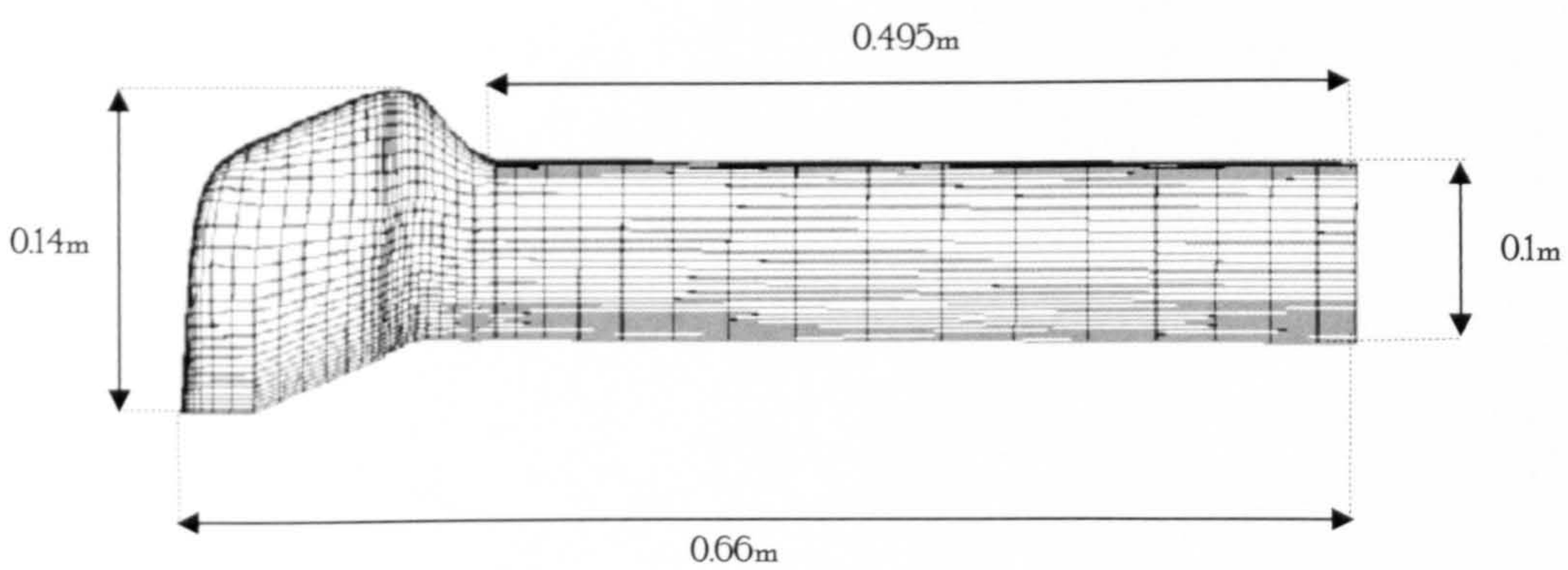

Figure 2-3 Modified Blade Tip Section

The blade section was manufactured in balsa wood, with a strengthing length of aluminium embedded in the leading edge. The basic planform dimensions are similar to those of the BERP tip, incorporating a swept tip and notch to produce the representative counter rotating twin vortices. The maximum sweep is 30^{o}. Similar to the rectangular blade section, the modified rotor blade was pitched about the quarterchord position when attached to the vortex generator.

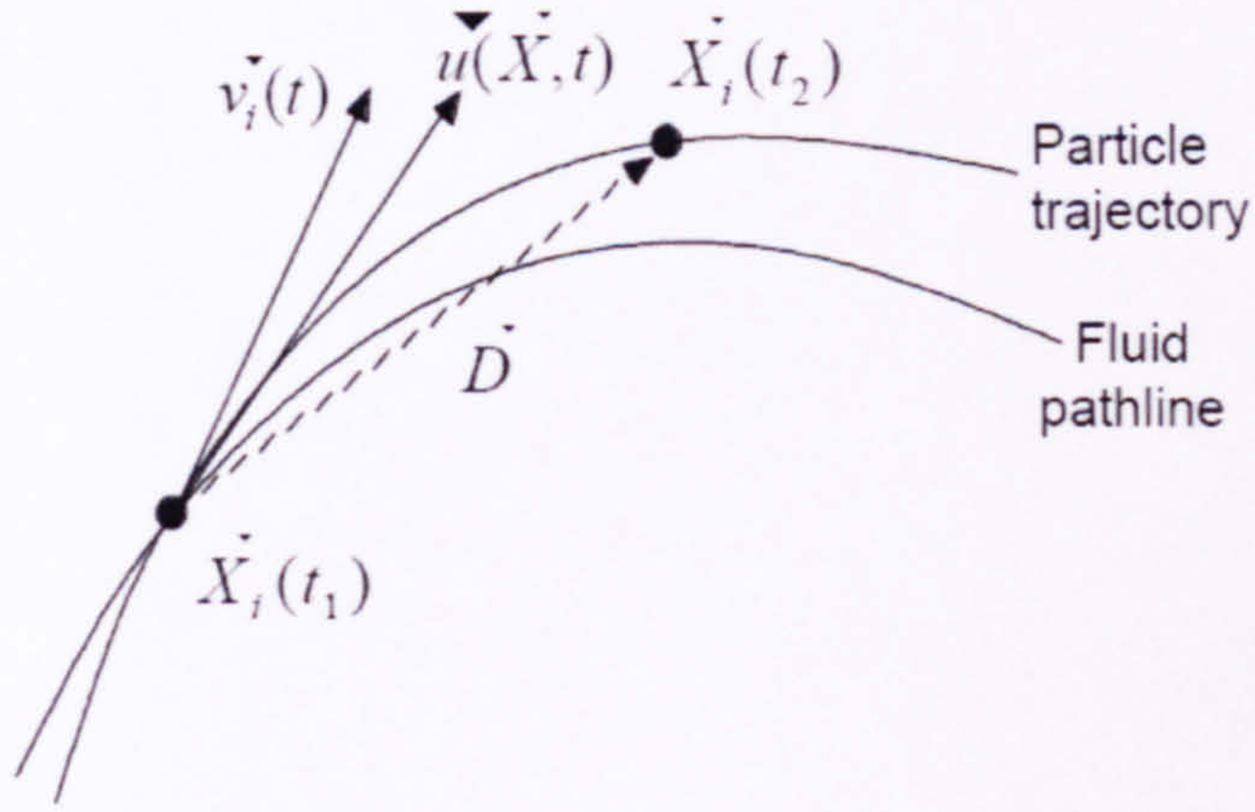

Figure 2-4 Tracer particle trajectory versus fluid trajectory (Westerweel, 1997)

The tracer particles in the flow may be shown to approximately follow the flow that they are seeding. The time lag between the fluid pathline and the particle trajectory may be accounted for by the difference in the fluid and particle densities. The above diagram also explain why the particle image velocimetry technique can only provide an approximation of the path that is followed, the accuracy of which is determined by the laser pulse time delay.

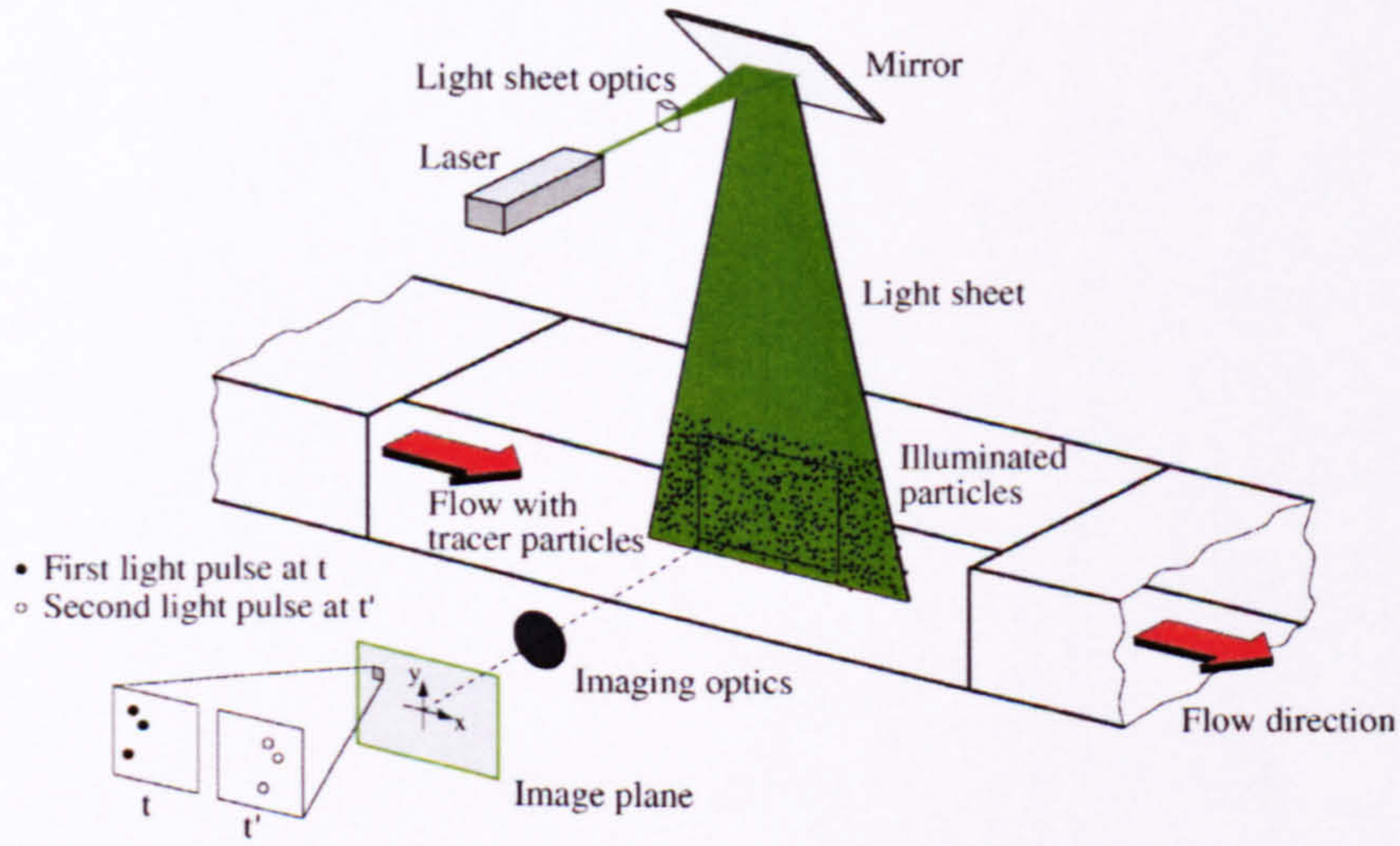

Figure 2-5 Arrangement of particle image velocimetry system for visualization

The simplest arrangement for particle image velocimetry is the 2D2C technique, in which the image plane, imaging lens and object plane are all aligned linearly. For the standard digital PIV, the imaging plane represents the CCD chip.

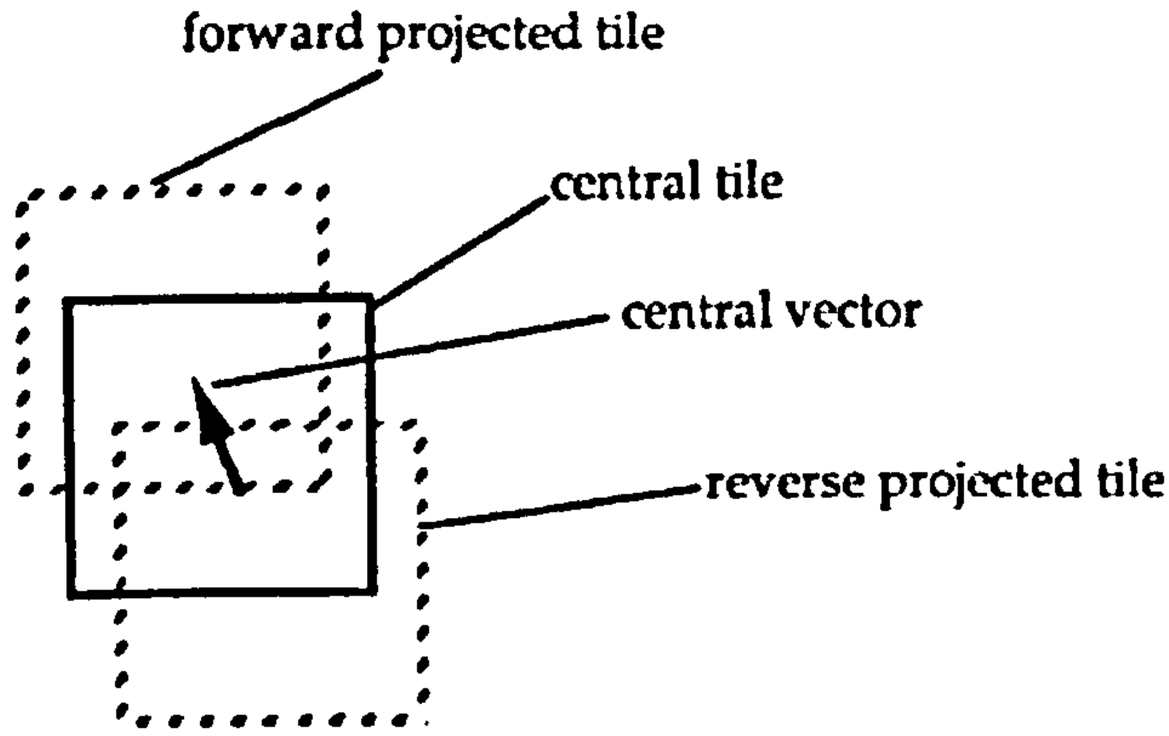

Figure 2-6(a) The shifting notation for the FRTT validation procedure (Green et al., 2000)

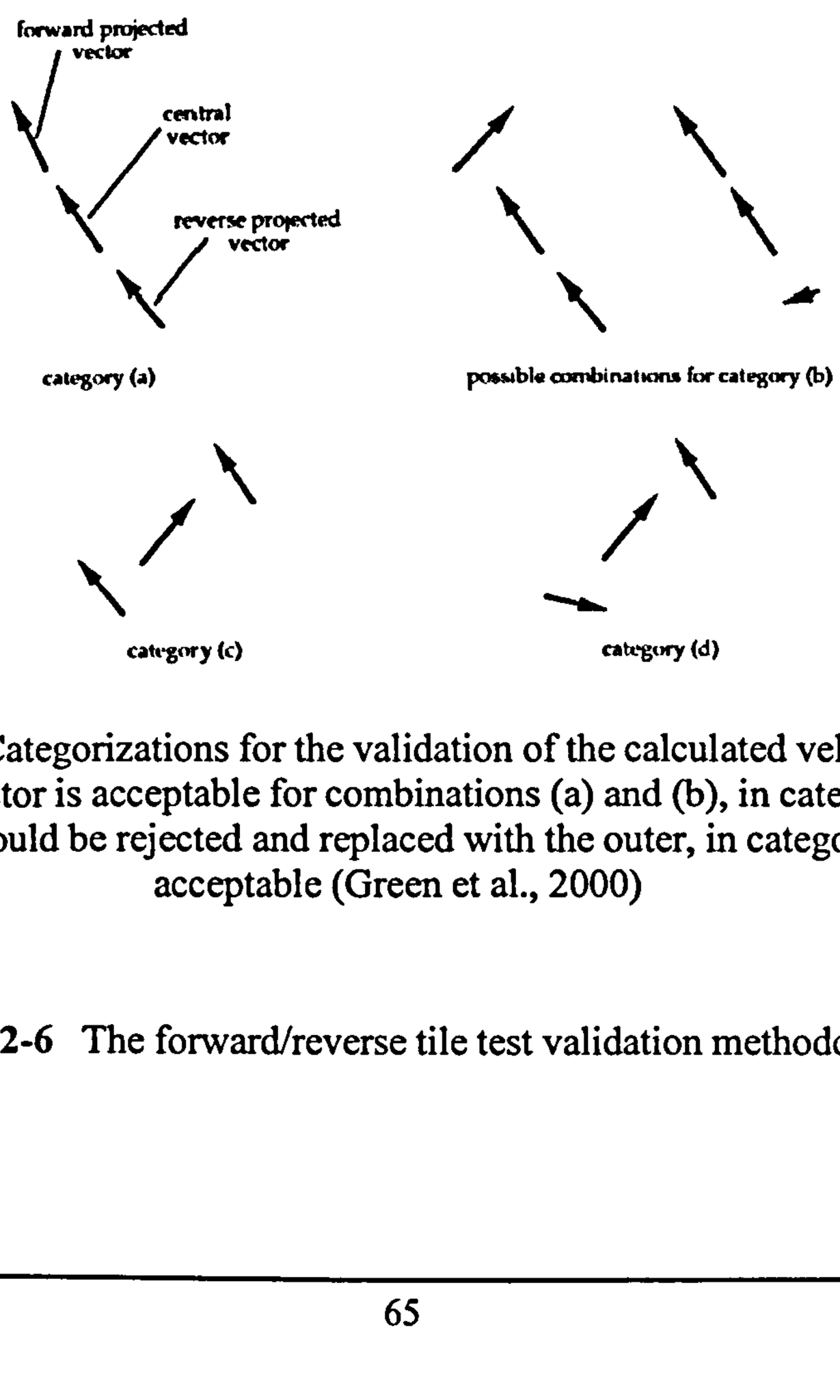

Figure 2-6(b) Categorizations for the validation of the calculated velocity vectors. The central vector is acceptable for combinations (a) and (b), in category (c), the central vector would be rejected and replaced with the outer, in category (d) none is acceptable (Green et al., 2000)

Figure 2-6 The forward/reverse tile test validation methodology

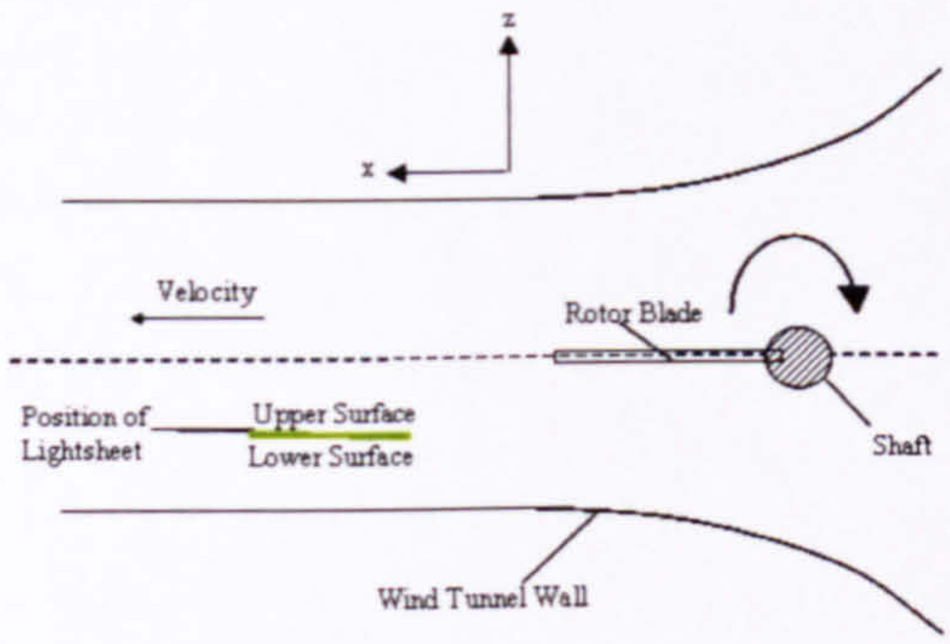

(a) Isolated vortex interrogation case in the x-y plane

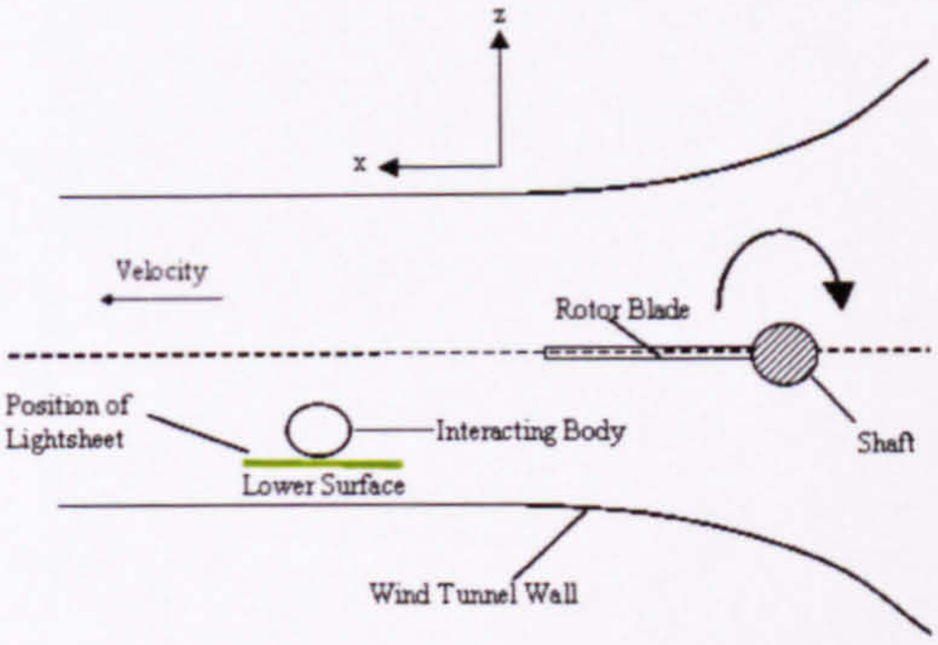

(b) Interrogation of vortex impingement onto circular cylinder in the x-y plane

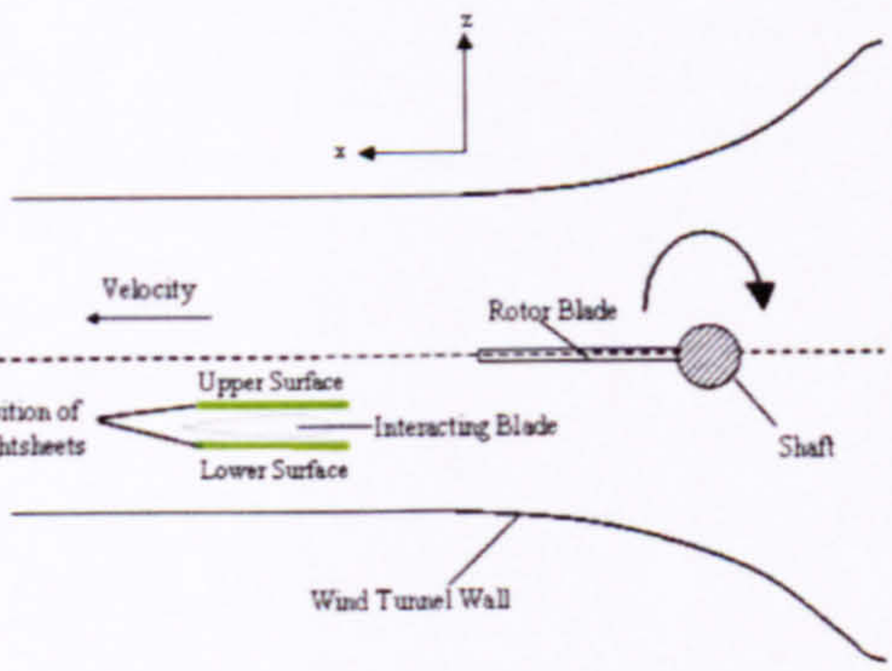

(c) Interrogation of vortex impingent onto representative tail rotor blade in the x-y plane

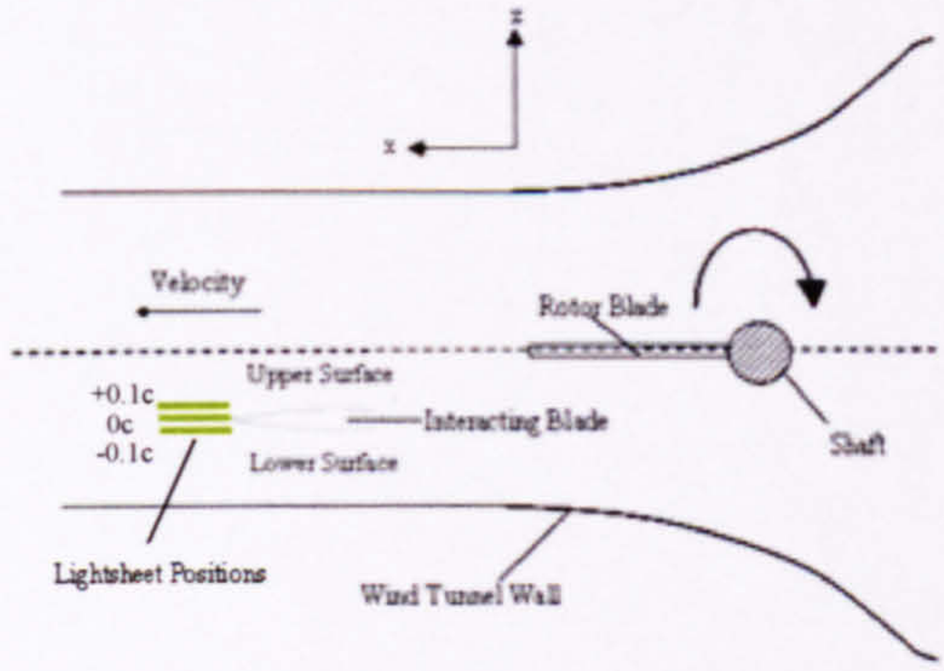

(d) Interrogation of vortex in the x-y plane behind the interacting blade

Figure 2-7 Simple schematic of the relative positions of the lightsheet for the examination of the single vortex interaction with a rectangular blade

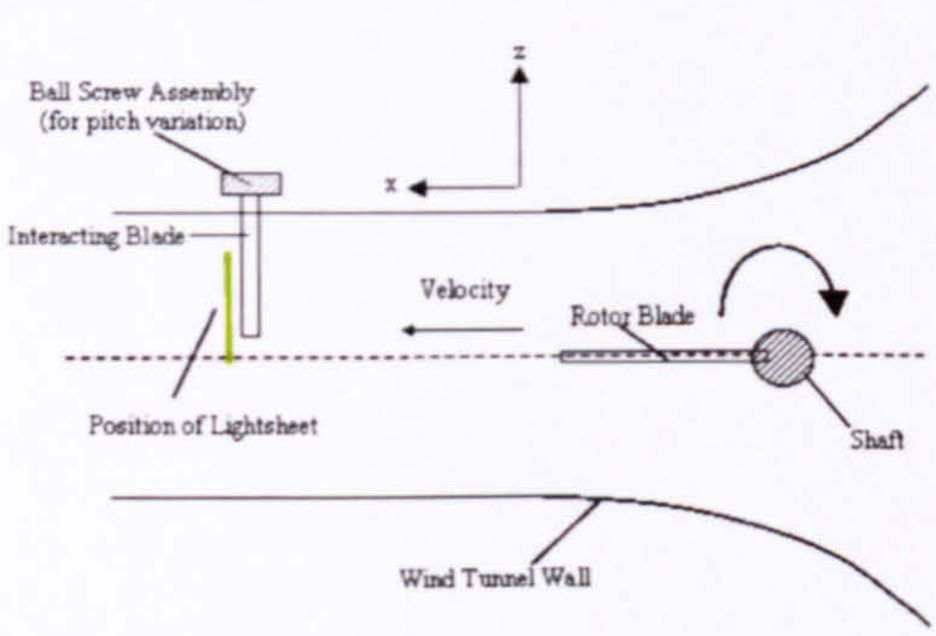

(a) Interrogation of flowfield behind pitching aerofoil in y-z plane

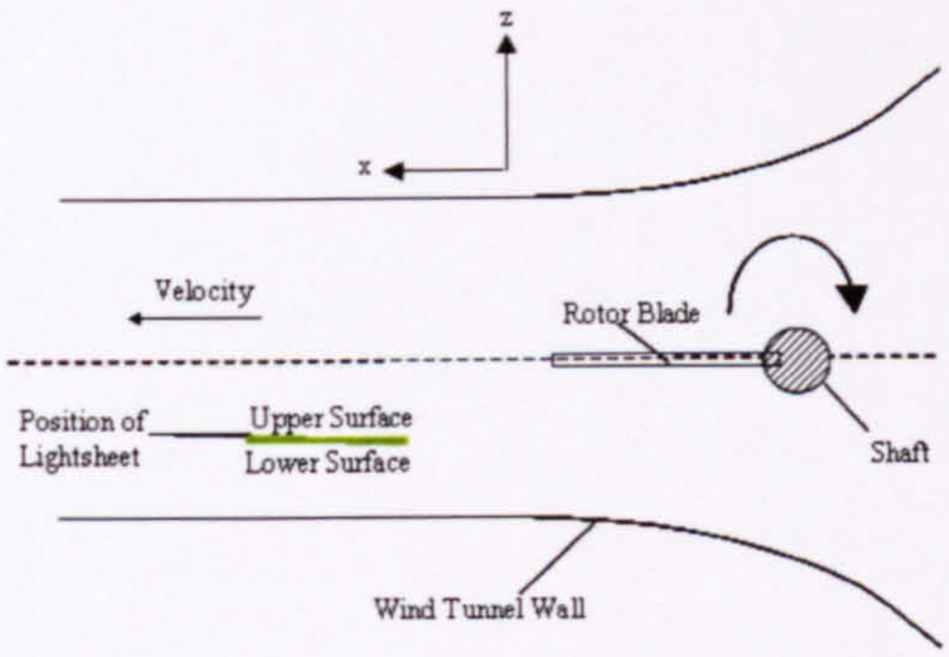

(b) Isolated vortex interrogation case in the x-y plane

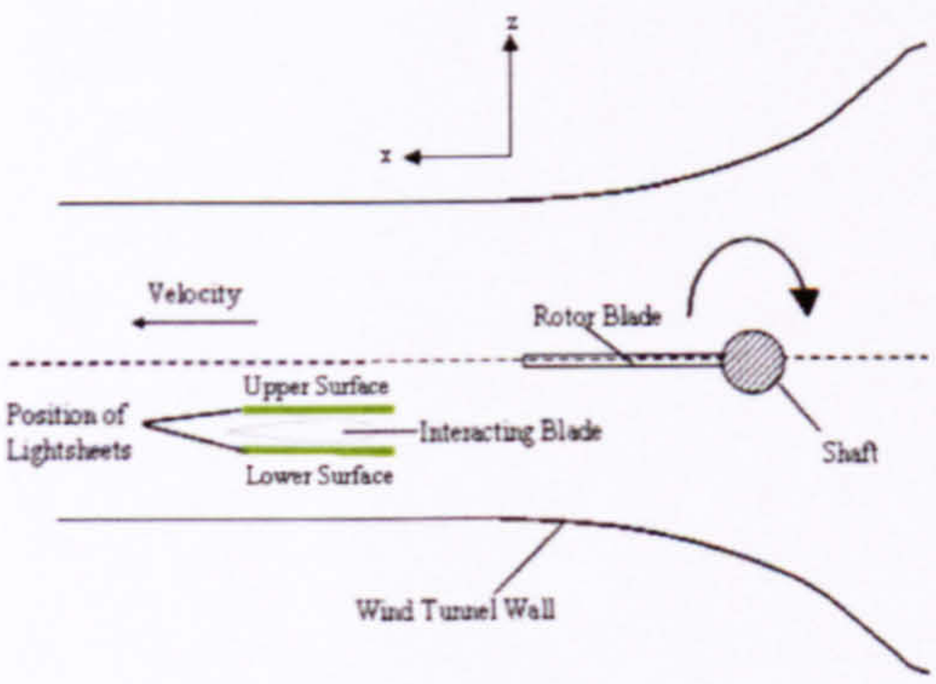

(c) Interrogation of vortex impingent onto representative tail rotor blade in the x-y plane

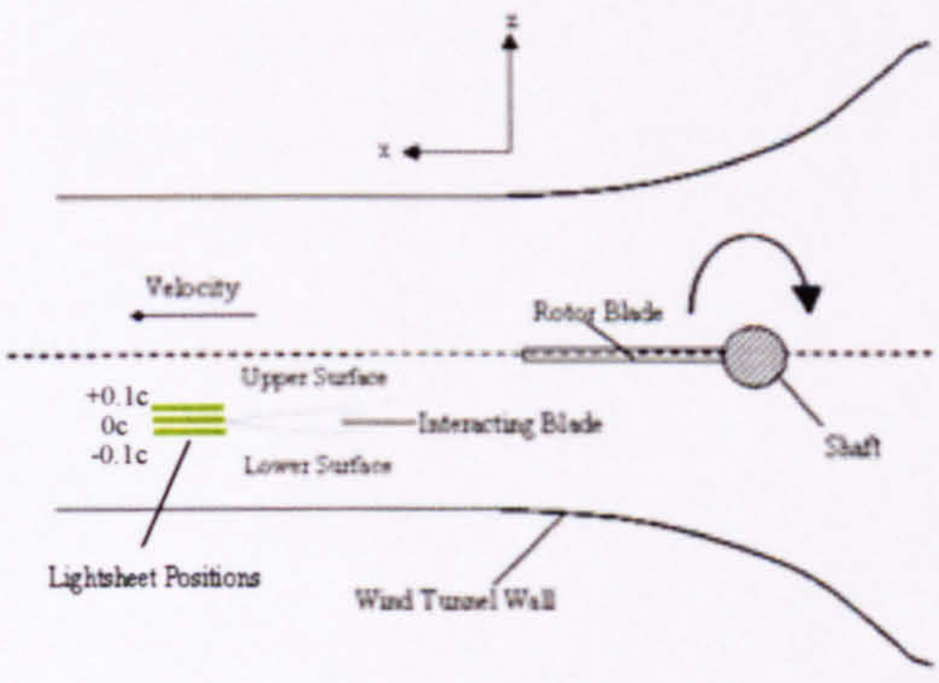

(d) Interrogation of vortex in the x-y plane behind the interacting blade

Figure 2-8 Simple schematic of the relative positions of the lightsheet for the examination of the twin vortex interaction with a rectangular blade

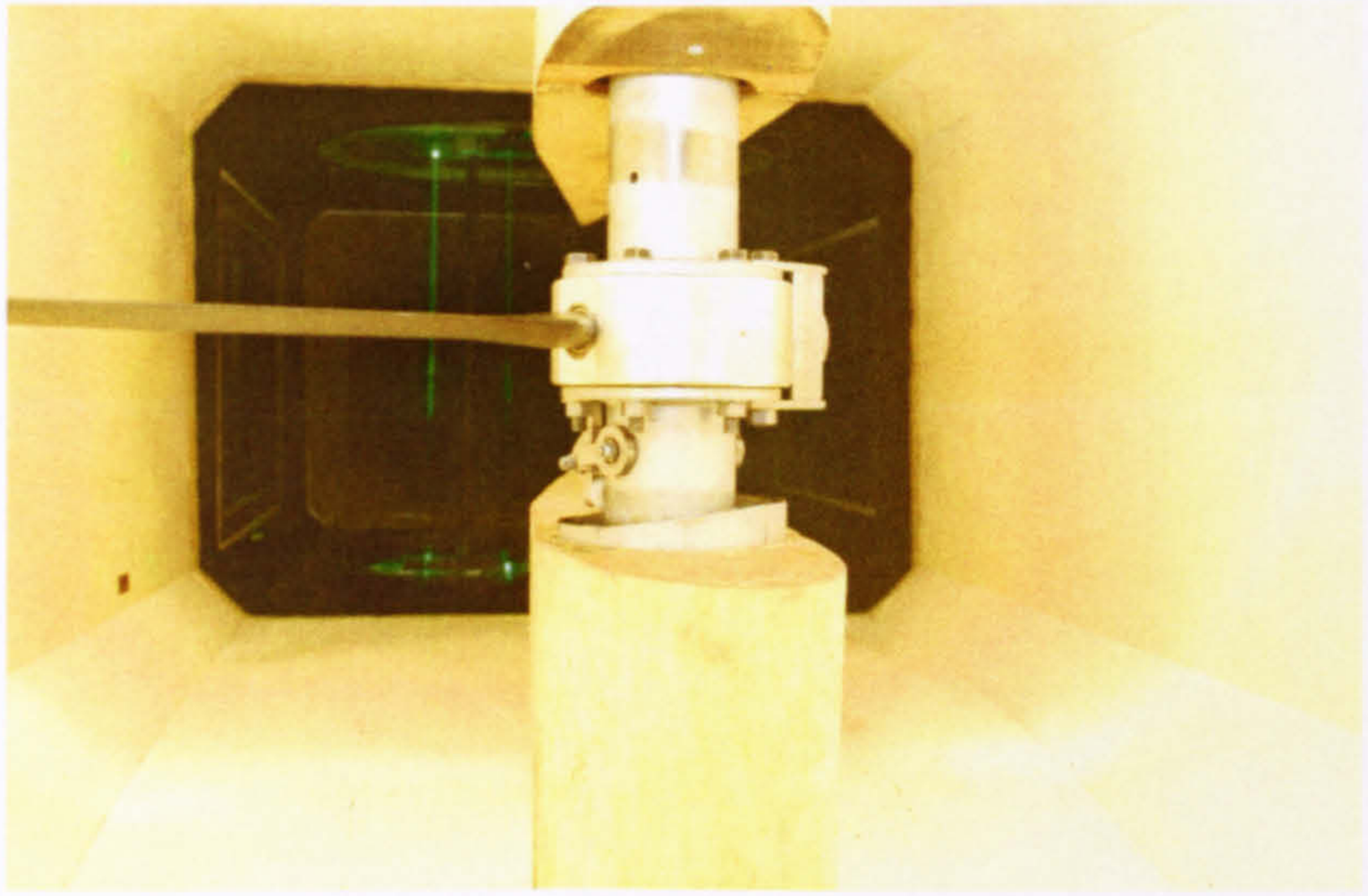

Figure 2-9 The 1.15m x 0.8m facility at the University of Glasgow, with the relative position of the laser sheet shown for lower surface measurements

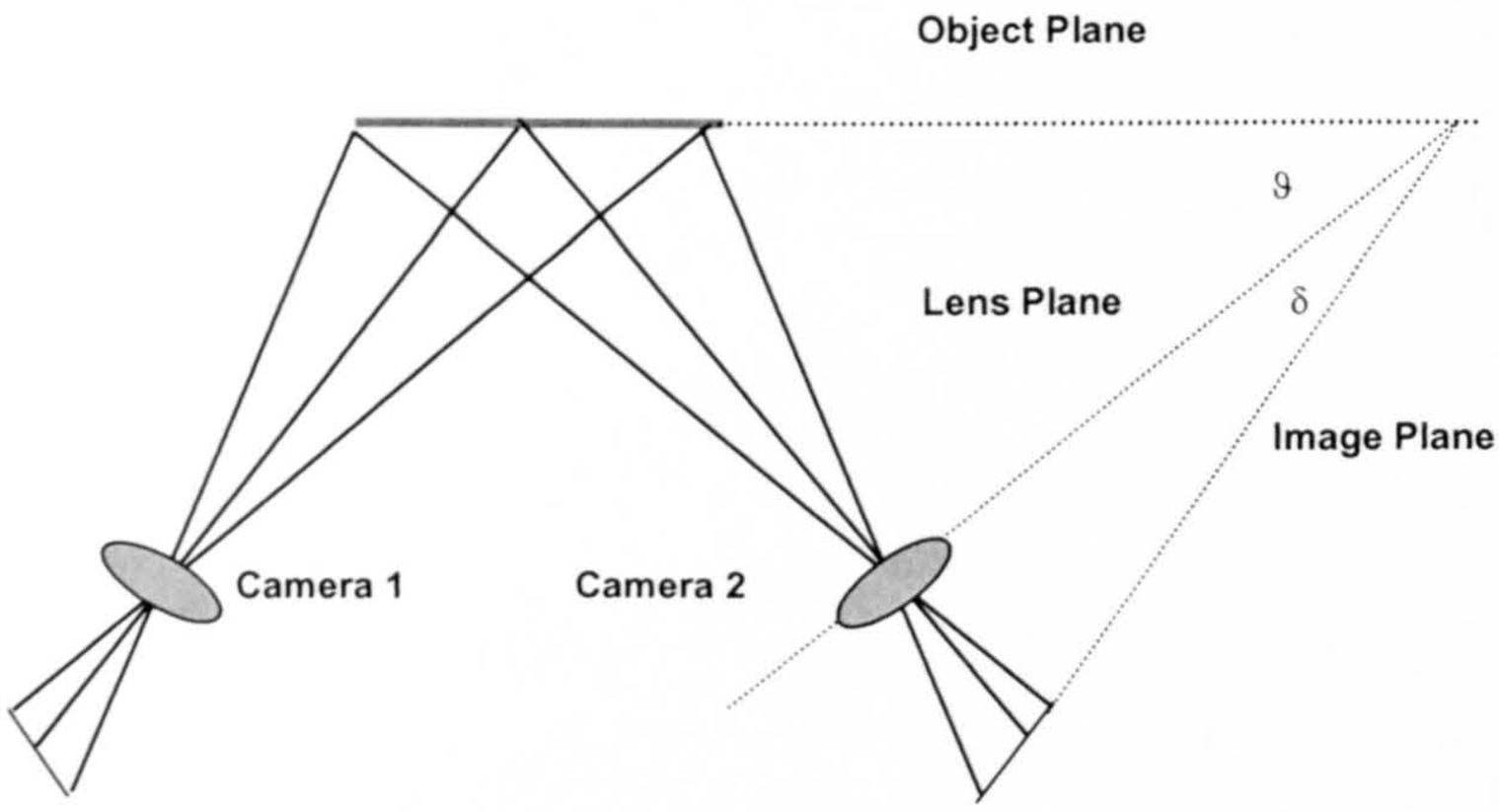

Figure 2-10 Angular stereoscopic particle image velocimetry arrangement introducing the Scheimpflug condition. In order to maximise the viewing area with the stereoscopic technique, the cameras are offset at an angle to one another. As this introduces a focussing problem due to the viewing angle, the backplane is tilted relative to the imaging lens in order to fulfil the Scheimpflug criteria.

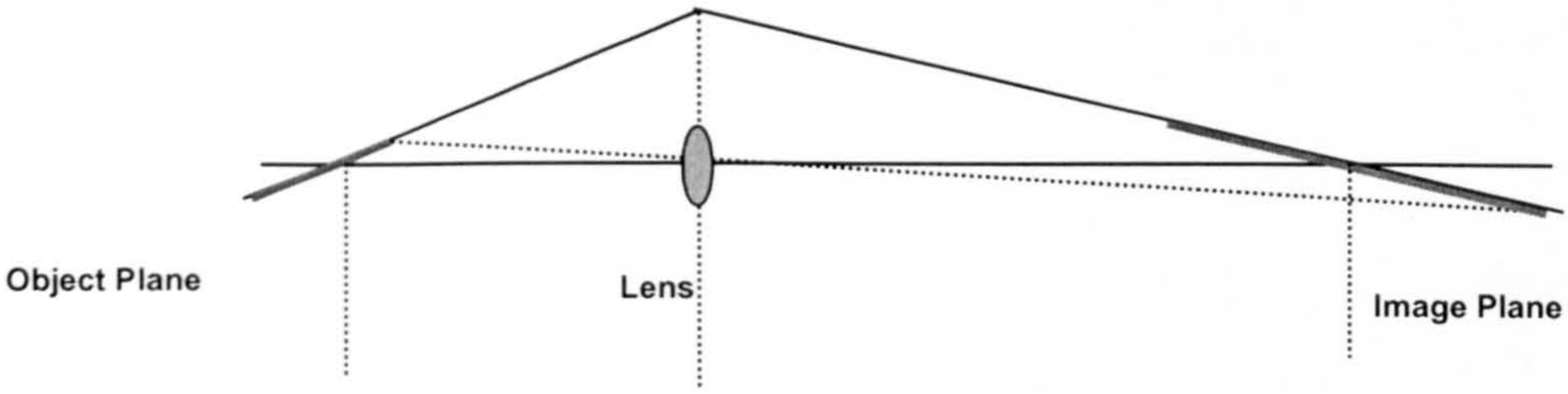

Figure 2-11 Scheimpflug Criteron

Fulfilment of the Scheimpflug criteron requires that the imaging plane is tilted in such a way that a projection of each of the three planes (imaging, lens and object) meet at a common point. By achieving this condition, the focus across the object plane should be achieved.

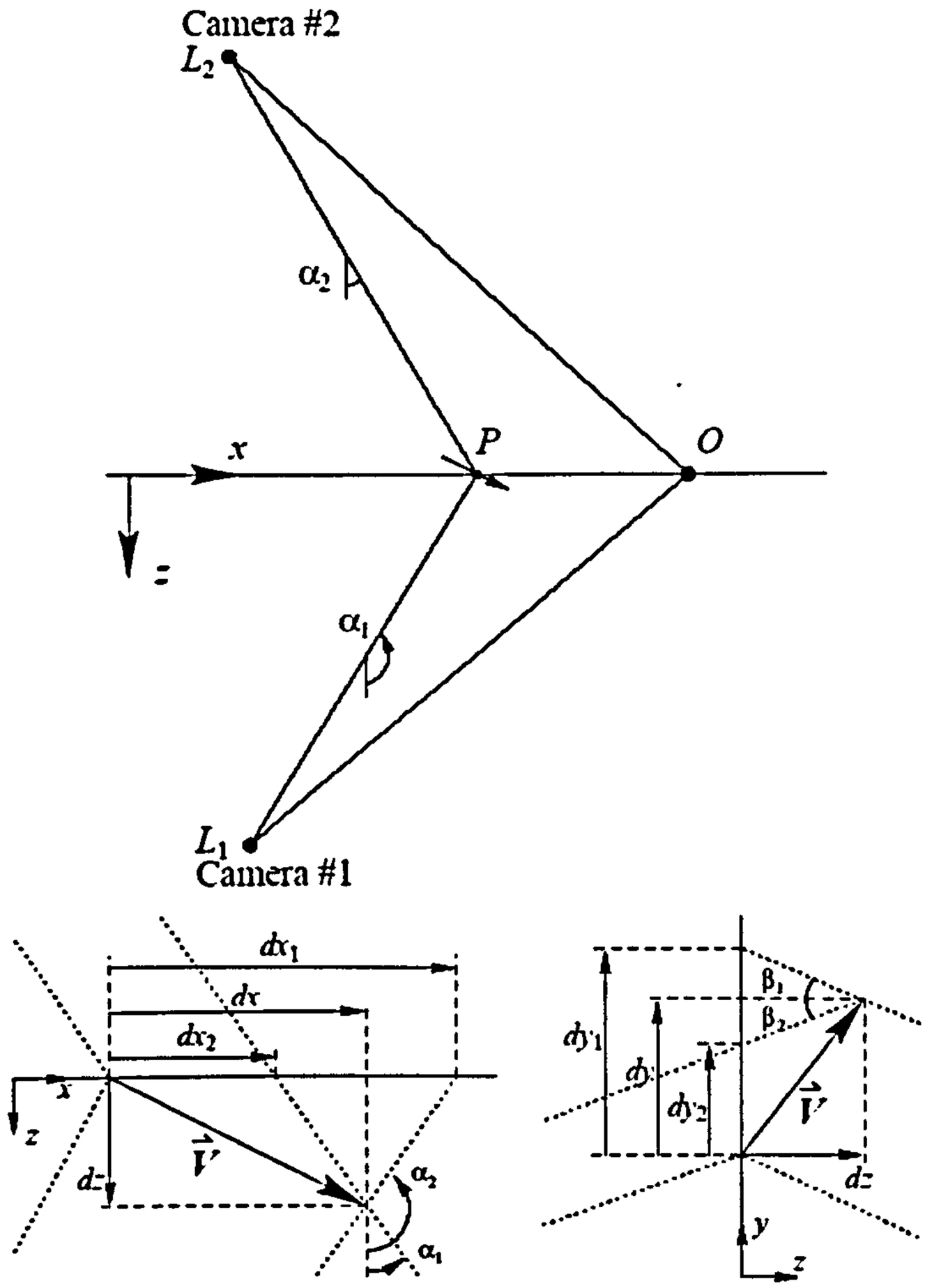

Figure 2-12 Reconstruction Geometry for the Stereoscopic Particle Image Velocimetry (Willert, 1997)

If it is assumed that a point P has the co-ordinates (x_p,y_p,z_p) within the region of interest, it would be observed to have the displacements (dx_1,dy_1) and (dx_2,dy_2) from the two different viewing angles. In order to reconstruct all three components of velocity, it is necessary to consider the measured projections in two planes – the x-z plane and the y-z plane.

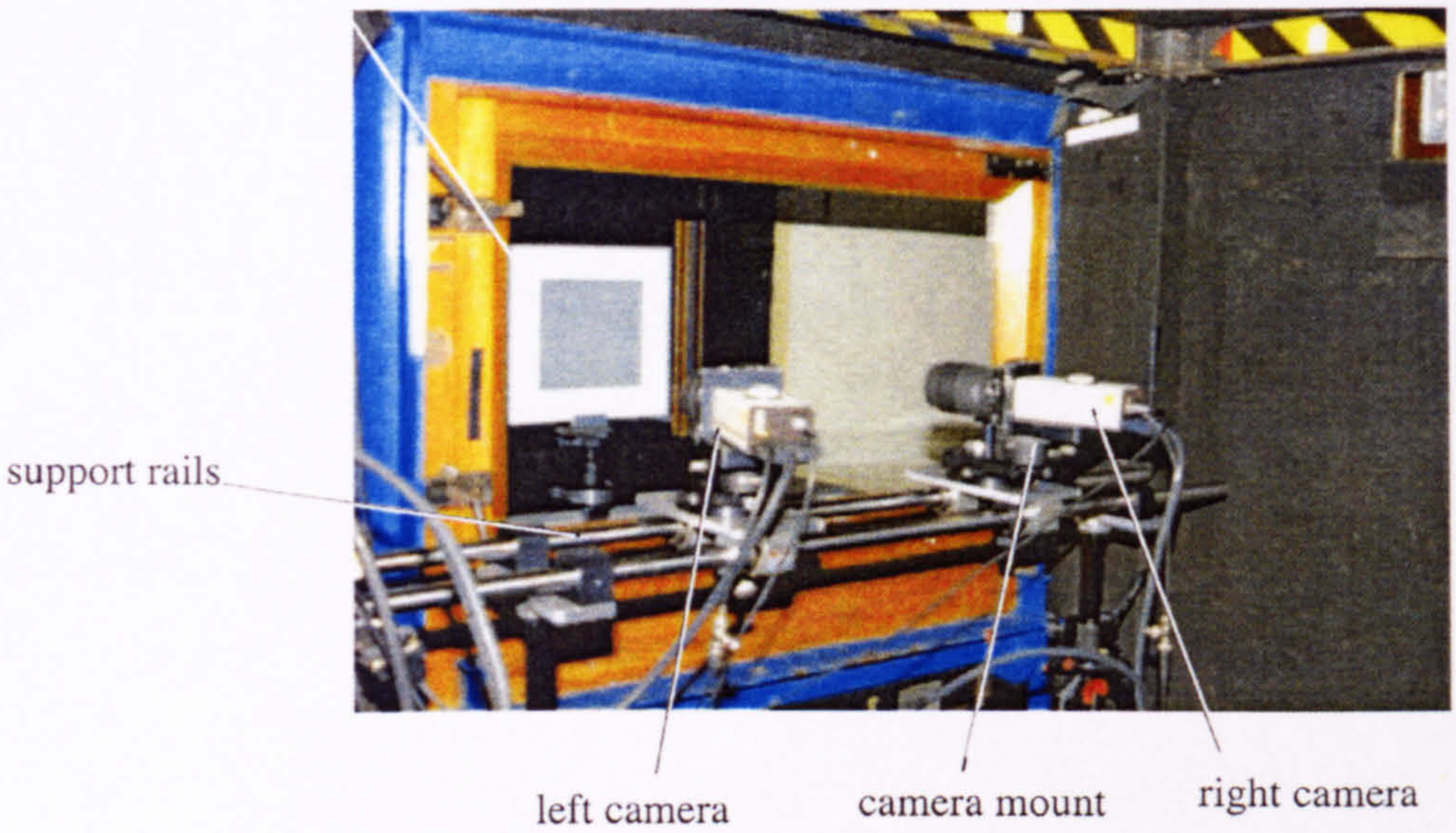

Figure 2-13 Arrangement of cameras for stereoscopic visualization of the Orthogonal BVI at the 1.15m x 0.8m facility at the University of Glasgow

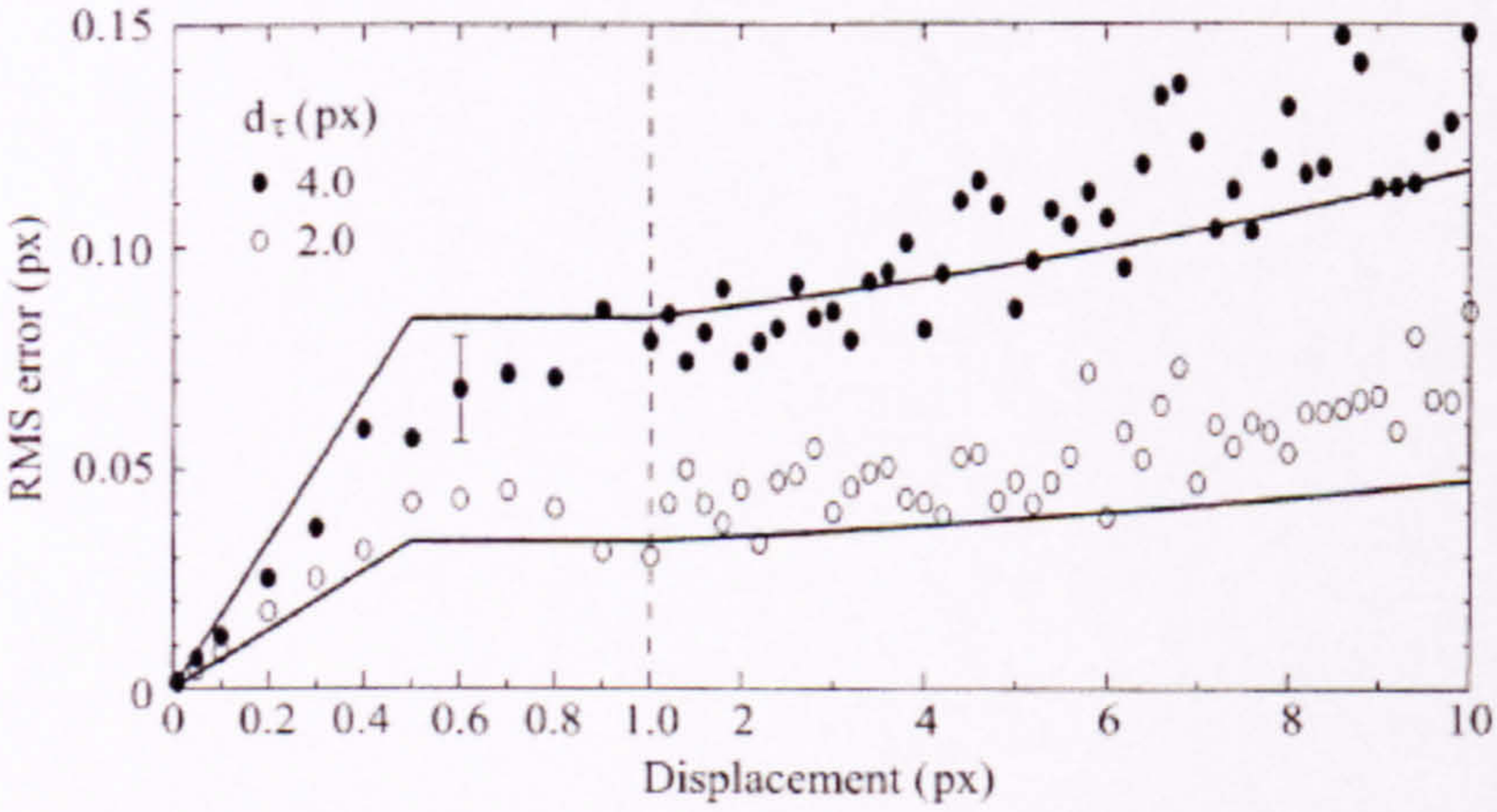

Figure 2-14 RMS estimation error

The RMS estimation error for the displacement as a function of the displacement *u* in pixel units for a 32x32-pixel interrogation region in digital PIV cross-correlation analysis, for particle-images with a diameter of 2 and 4 pixels with an image density of 10, with zero out-of-plane displacement. The solid lines are analytical results (Westerweel 1993); the symbols are obtained from Monte Carlo simulations (the error bar represents the uncertainty of the simulation result) (Westerweel et al., 1997)

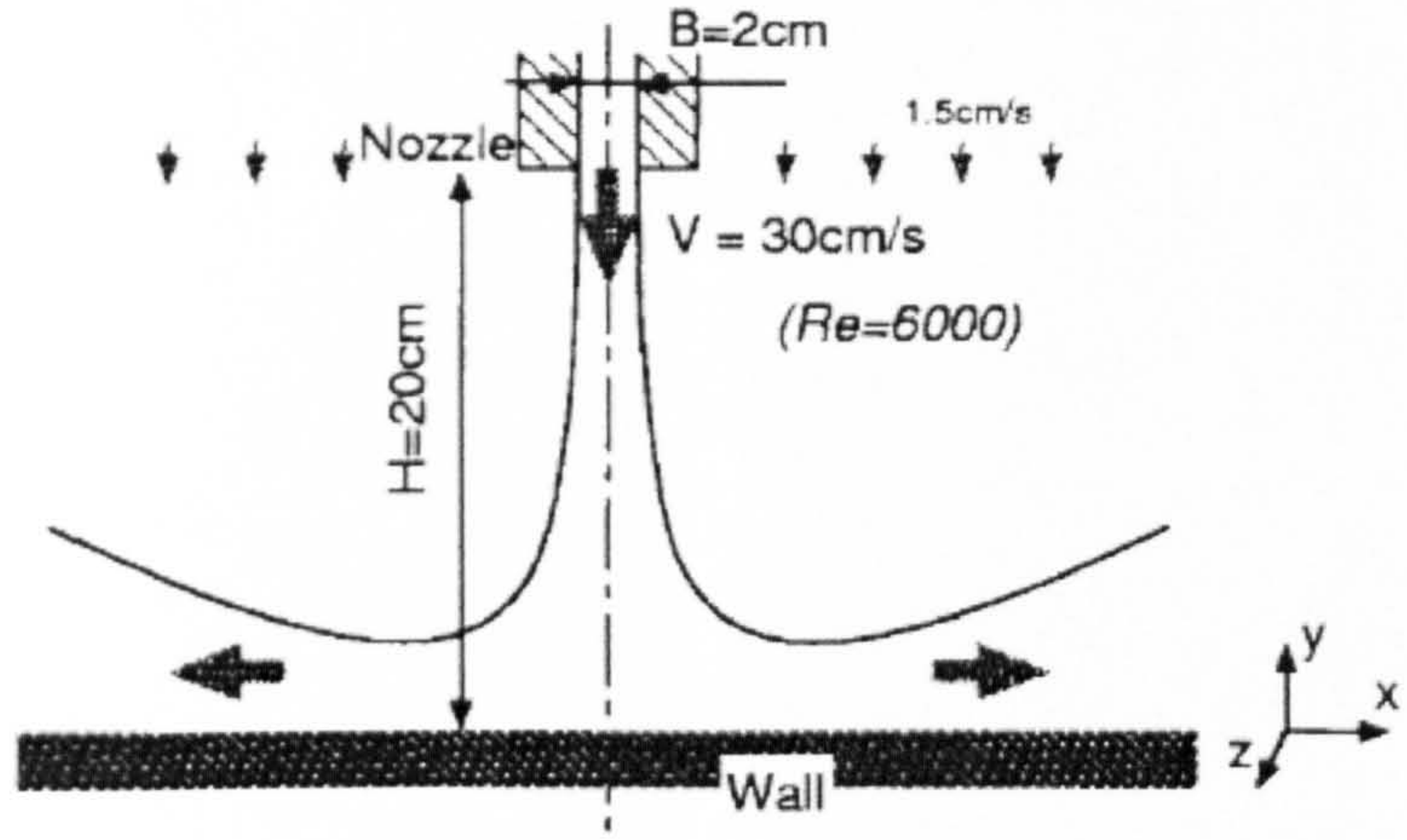

Figure 2-15 A schematic diagram of the target flow field (Okamoto et al., 2000)

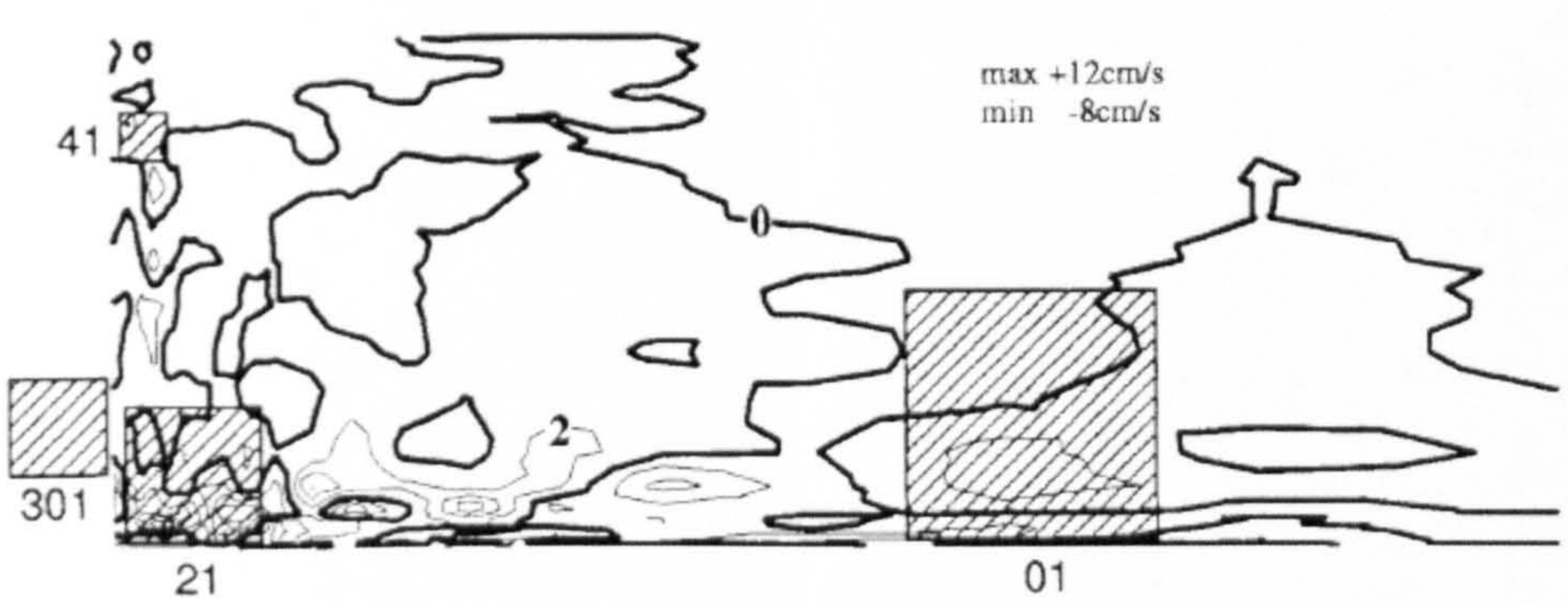

Figure 2-16 The out-of-plane velocity in the target flow field (Okamoto et al., 2000). Region 01 indicates the region interrogated for the eight flow conditions.

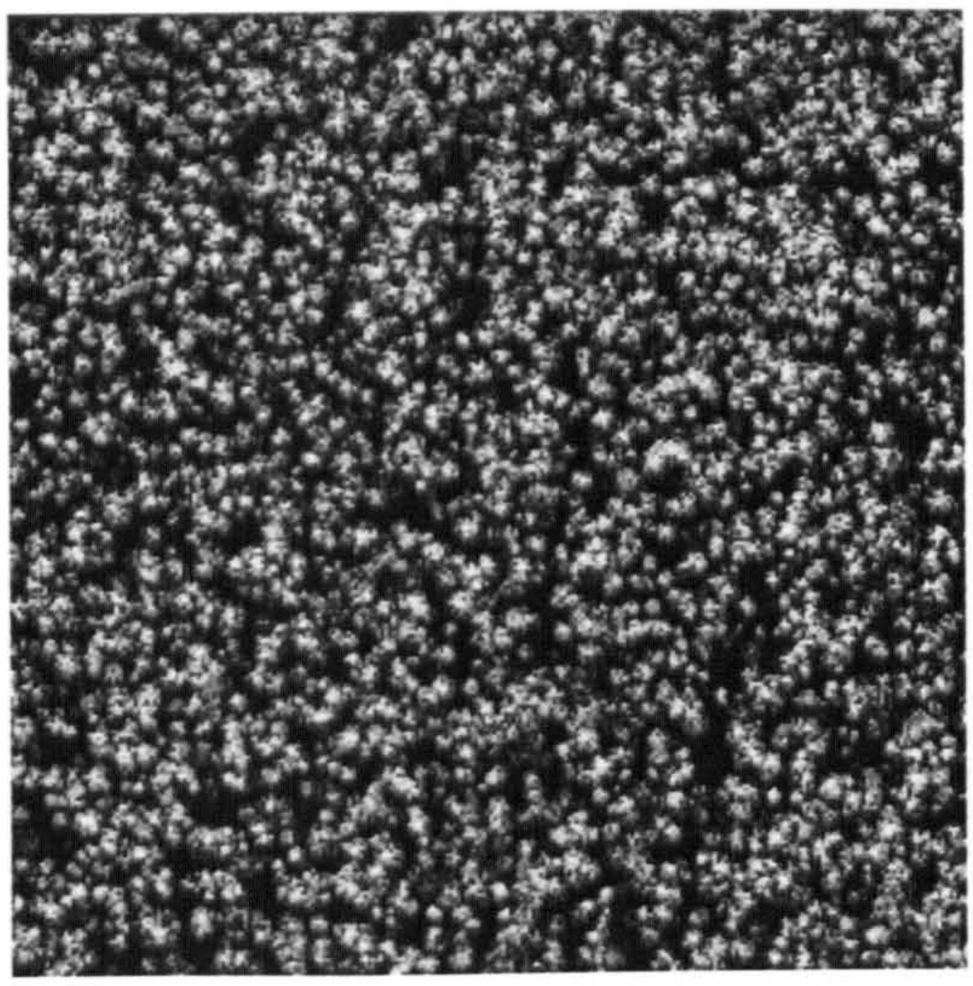

Image 01:1

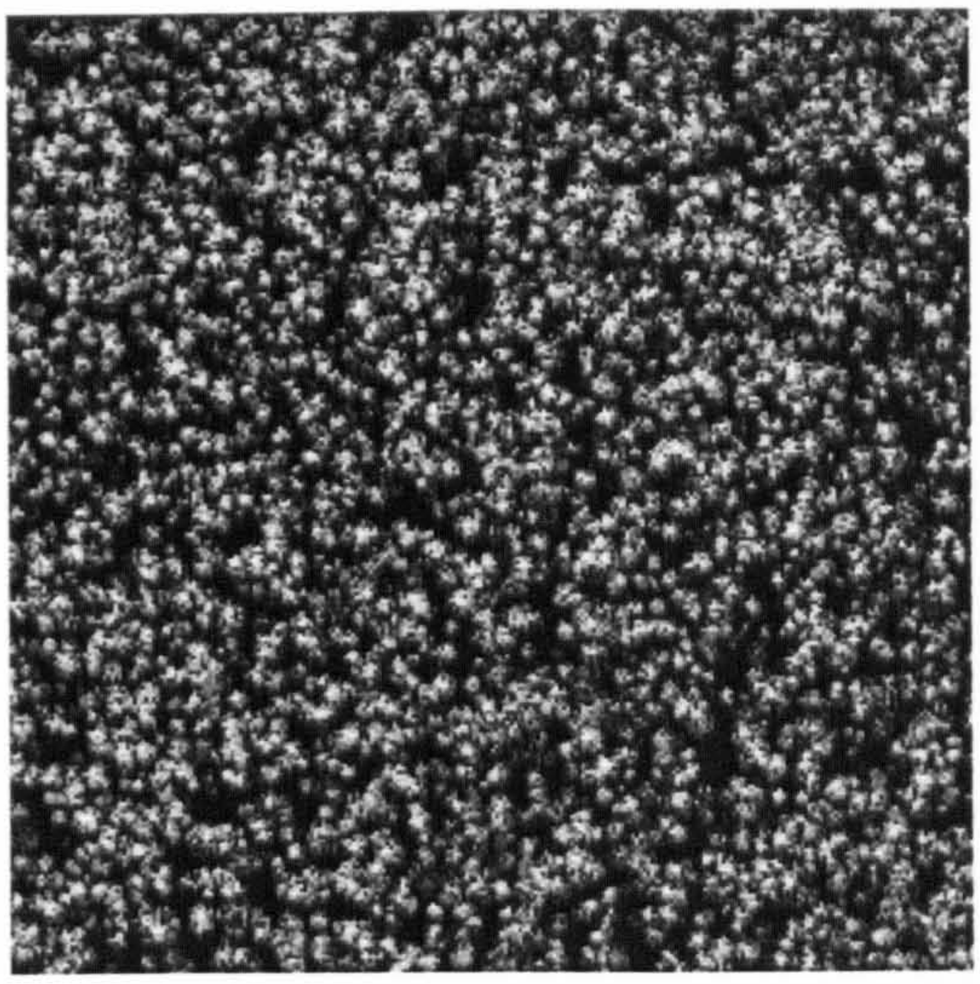

Image 01:2

Figure 2-17 Synthetic Images Case 01: Reference Case

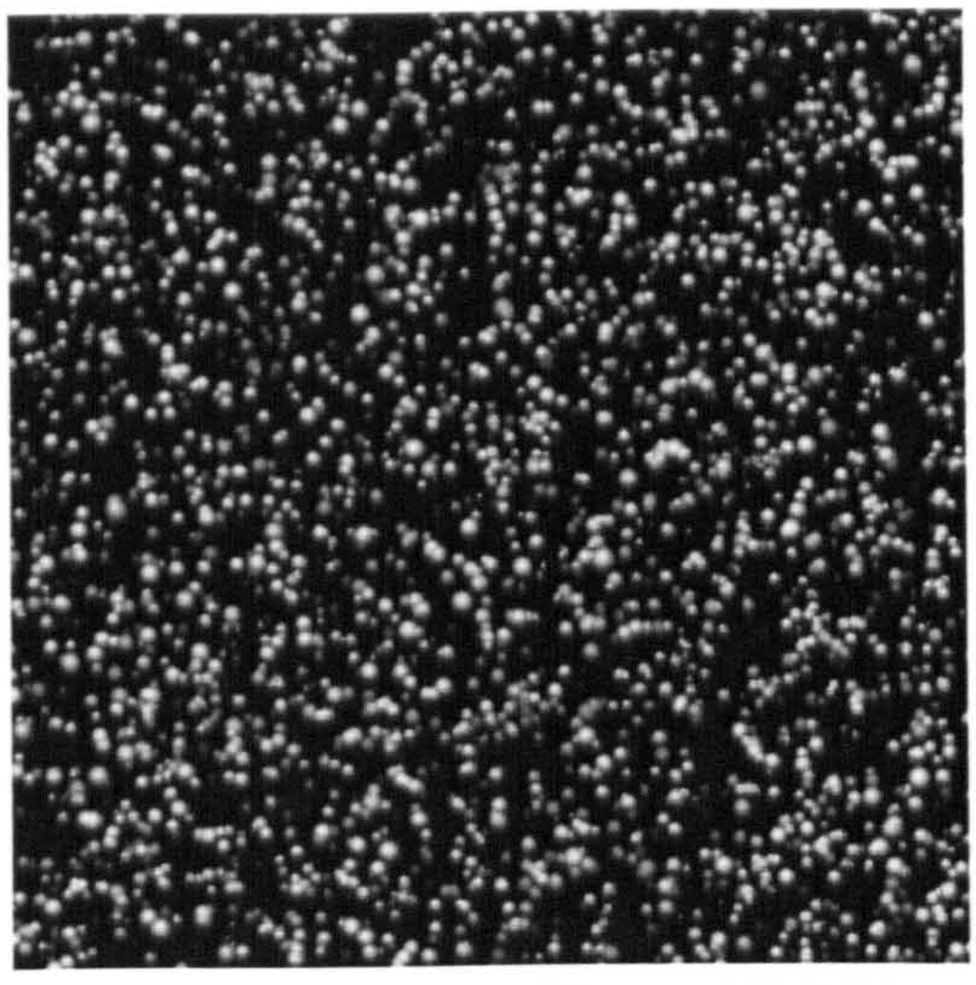

Image 02:1

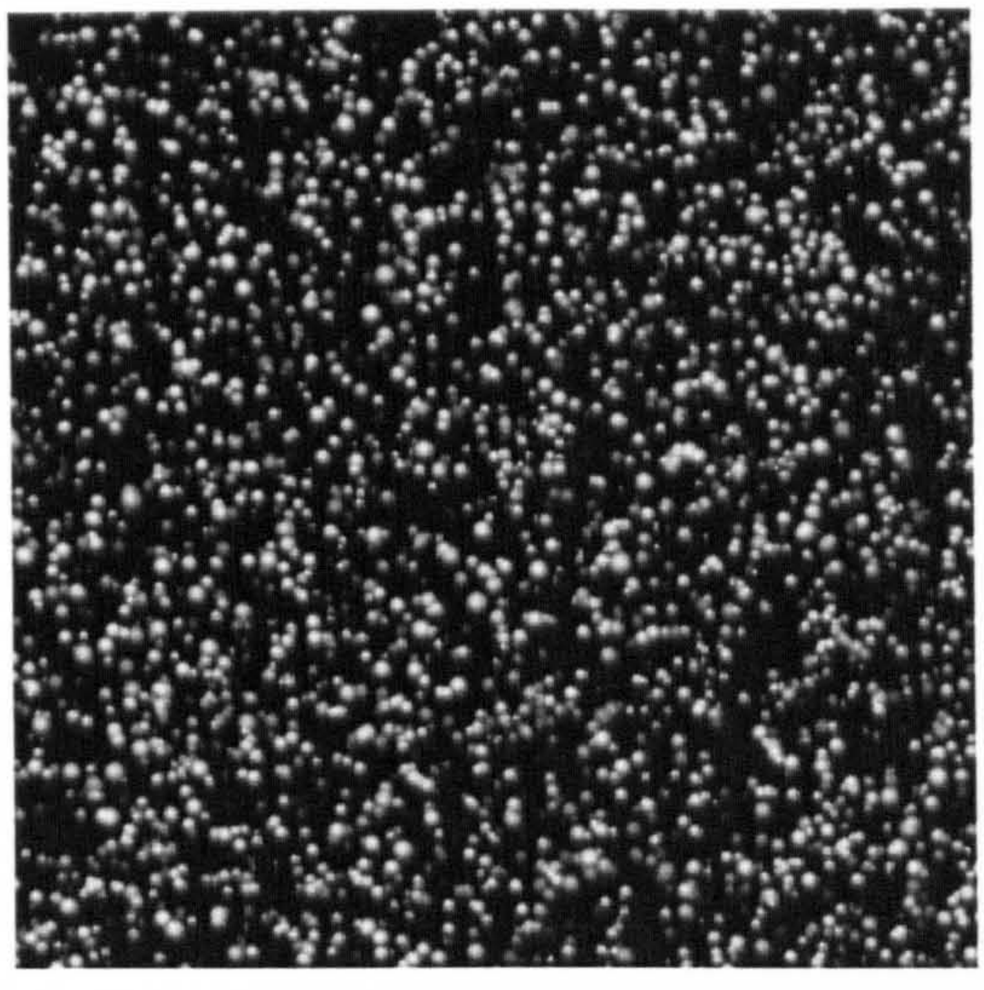

Image 02:2

Figure 2-18 Synthetic Images Case 02 : Small Displacement

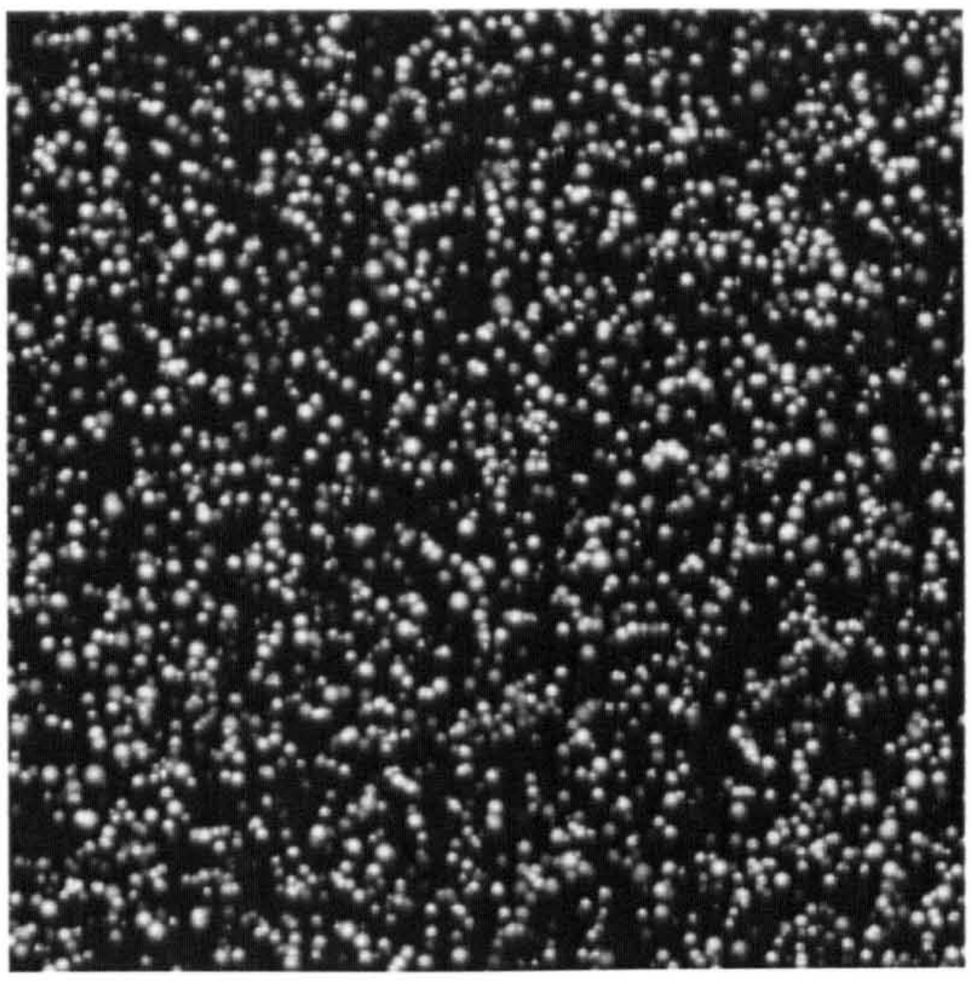

Image 03:1

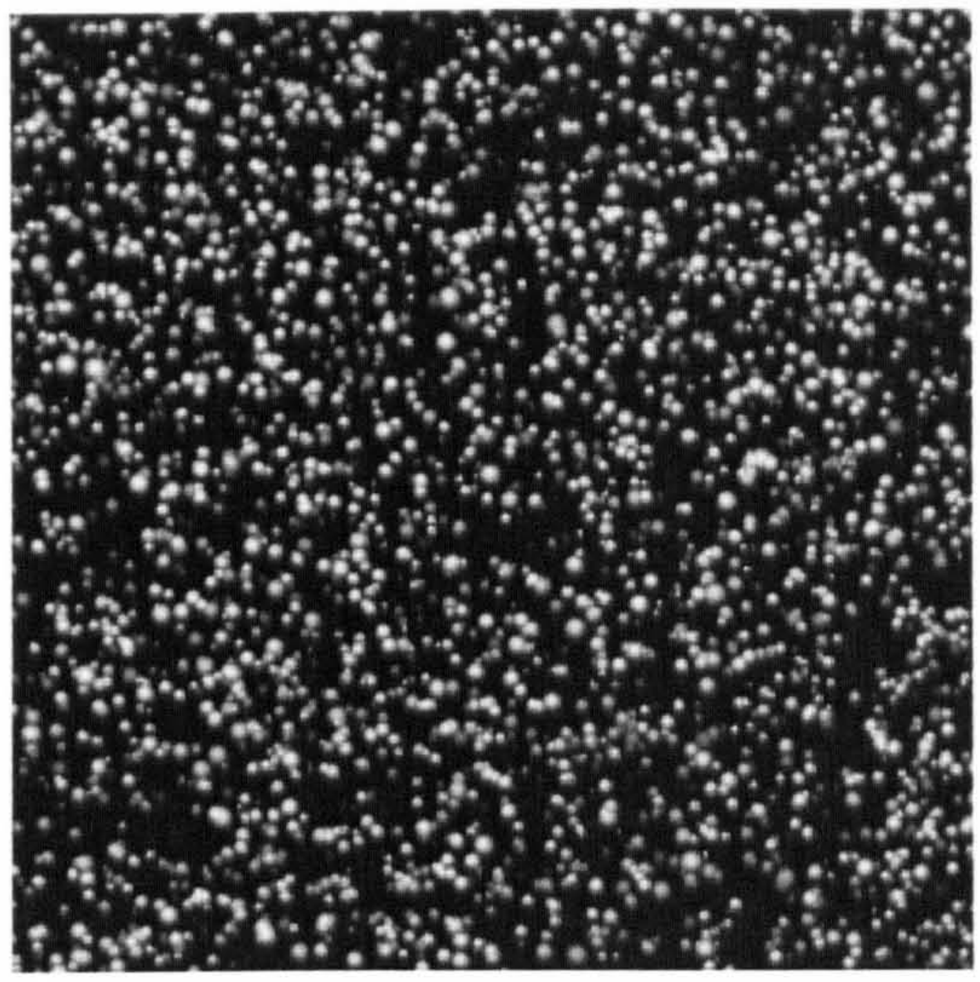

Image 03:2

Figure 2-19 Synthetic Image Case 03: Large Displacement

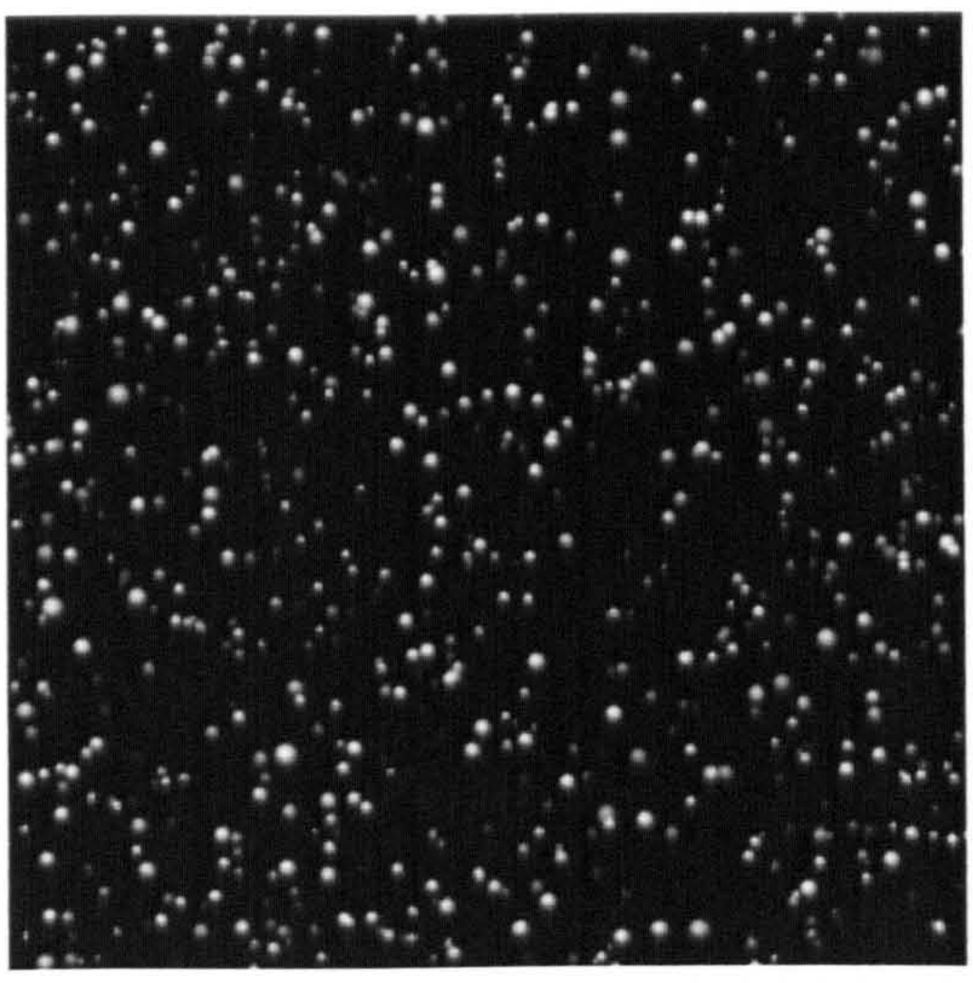

Image 04:1

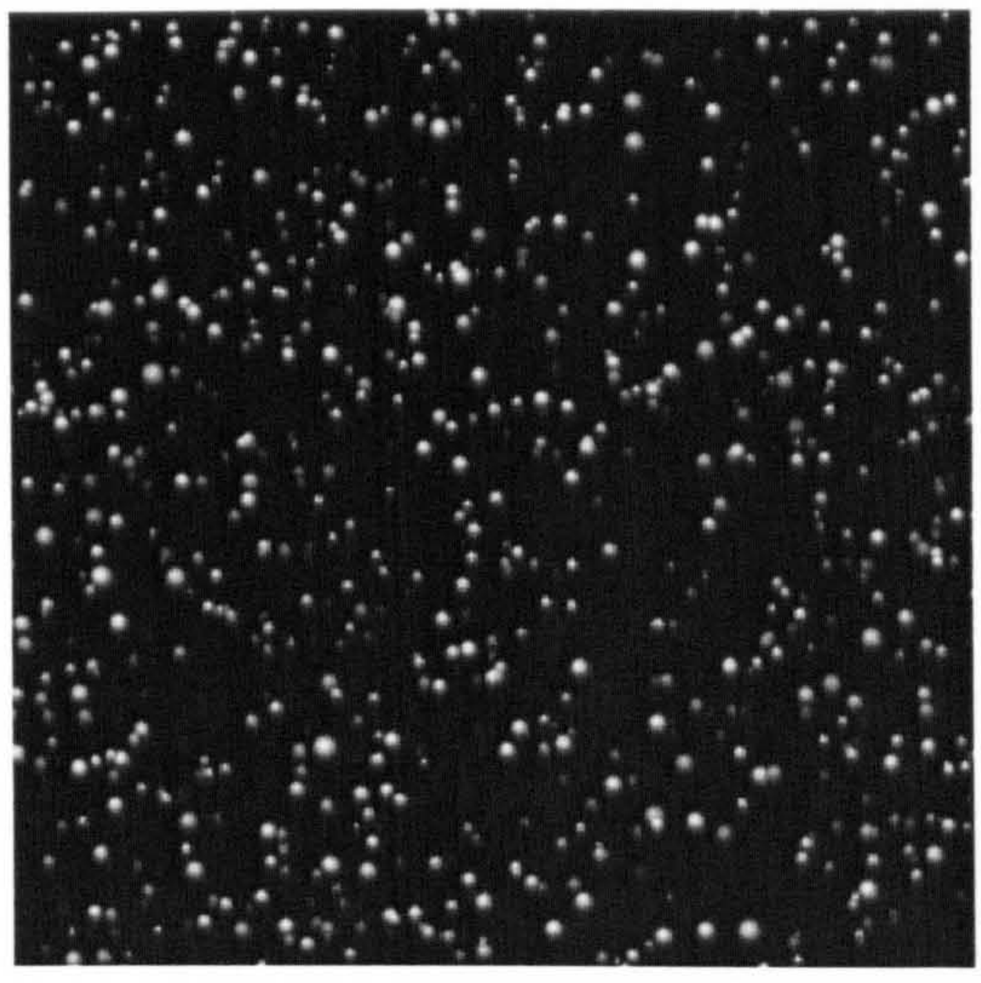

Image 04:2

Figure 2-20 Synthetic Image Case 04: Sparse Particle Distribution

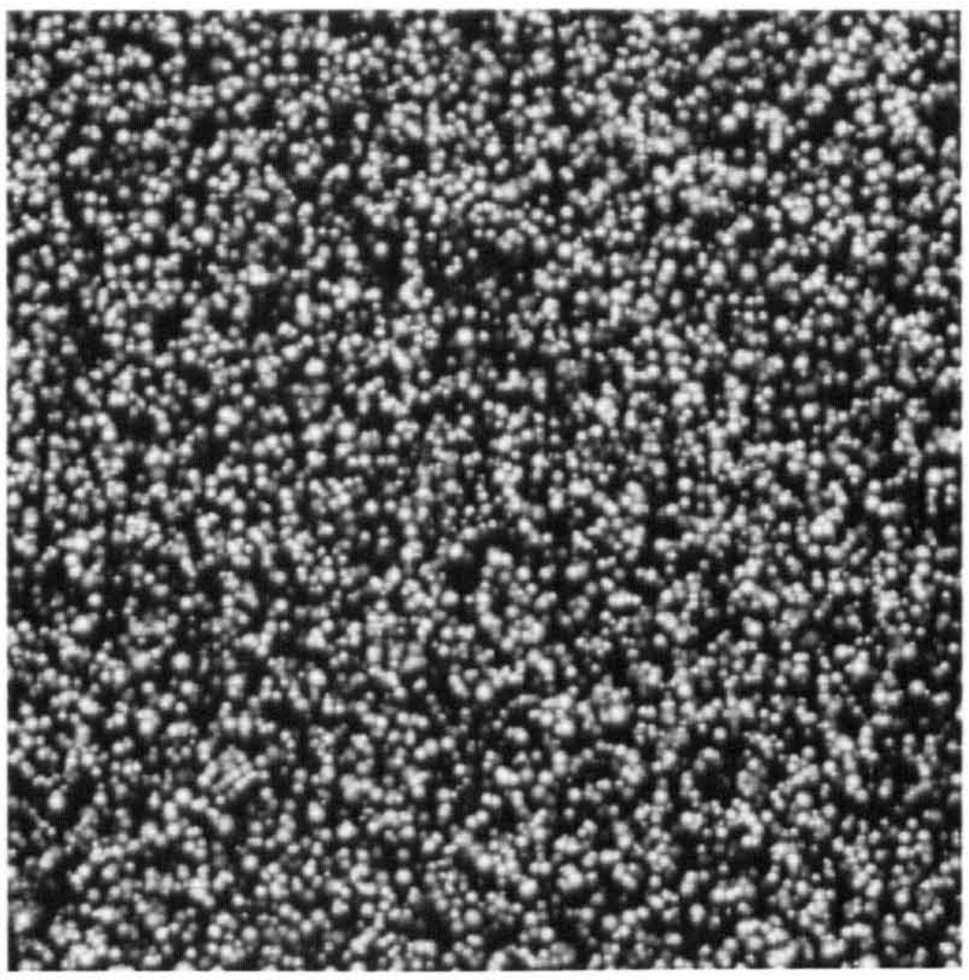

Image 05:1

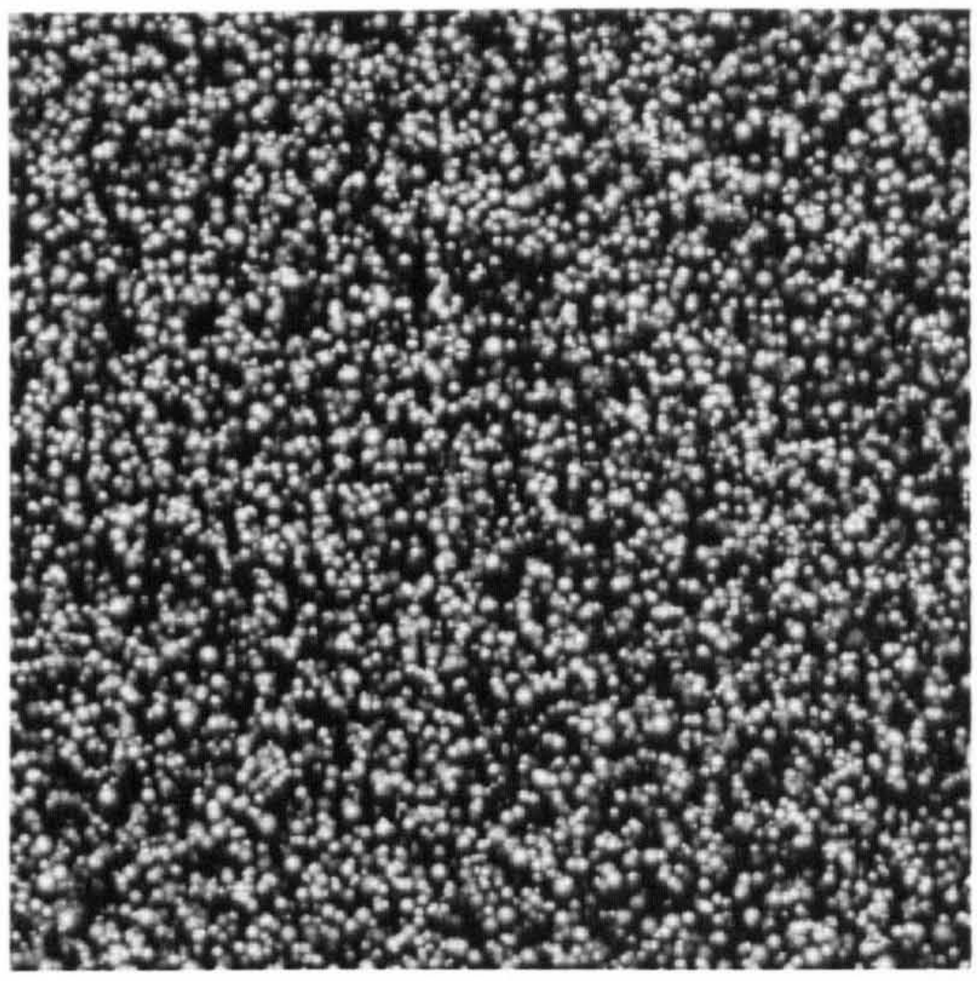

Image 05:2

Figure 2-21 Synthetic Image Case 05: Dense Particle Distribution

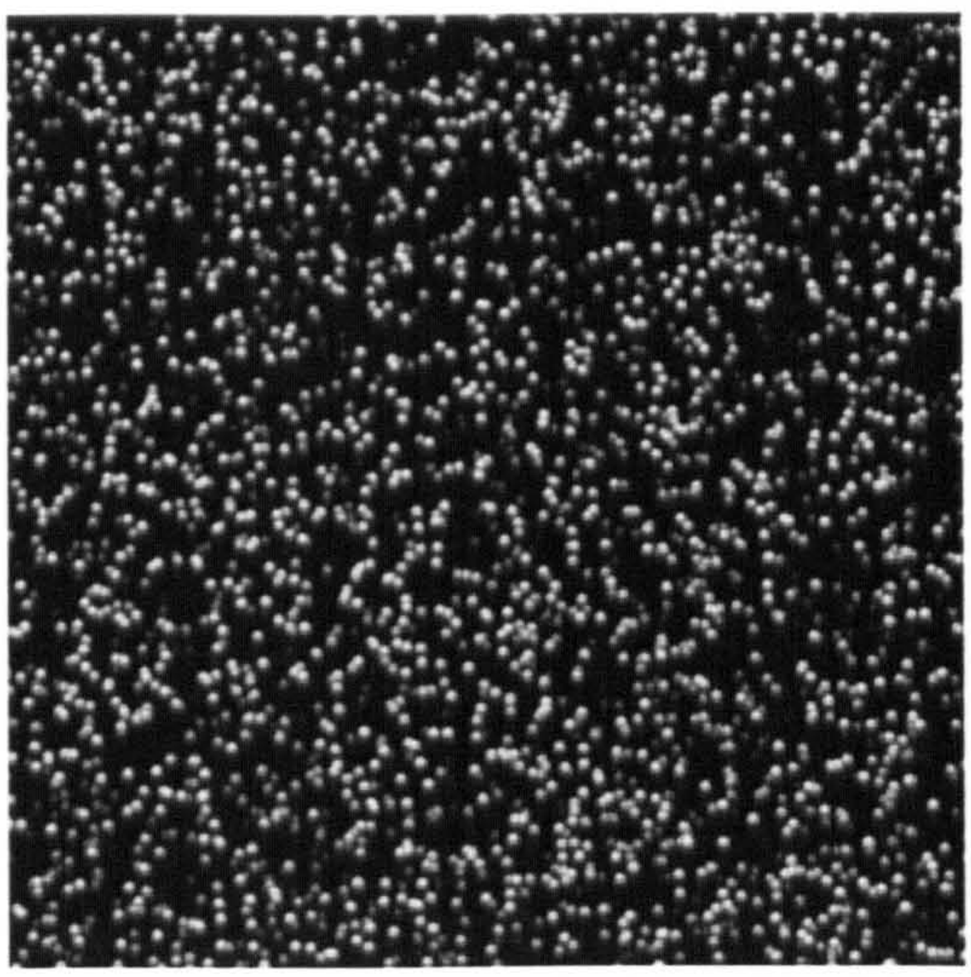

Image 06:1

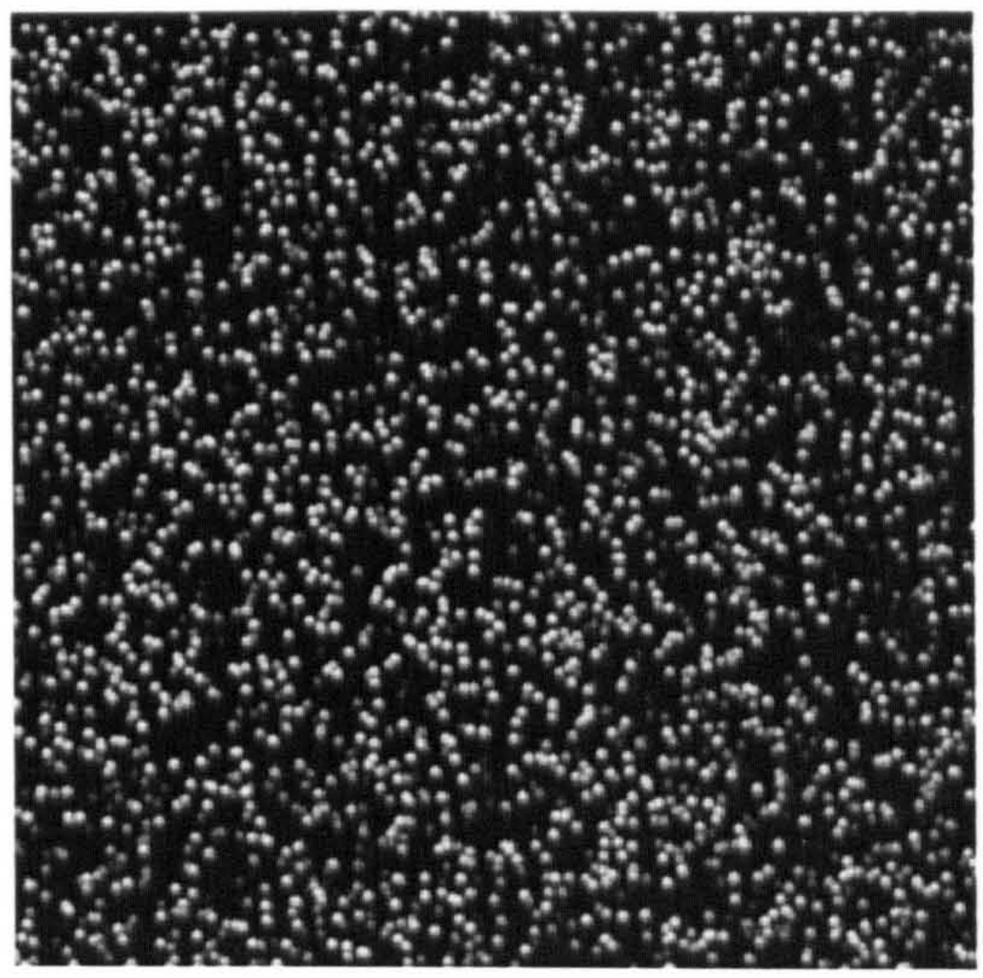

Image 06:2

Figure 2-22 Synthetic Image Case 06: Constant Particle Diameter

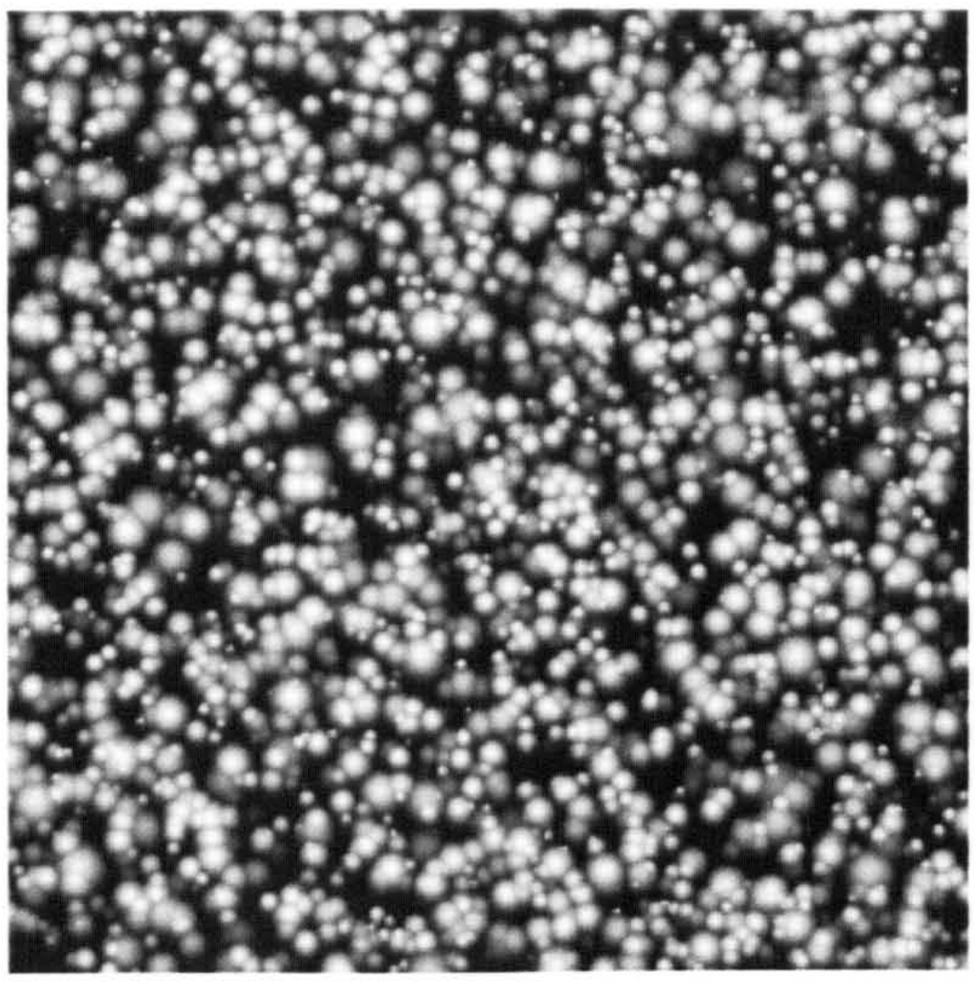

Image 07:1

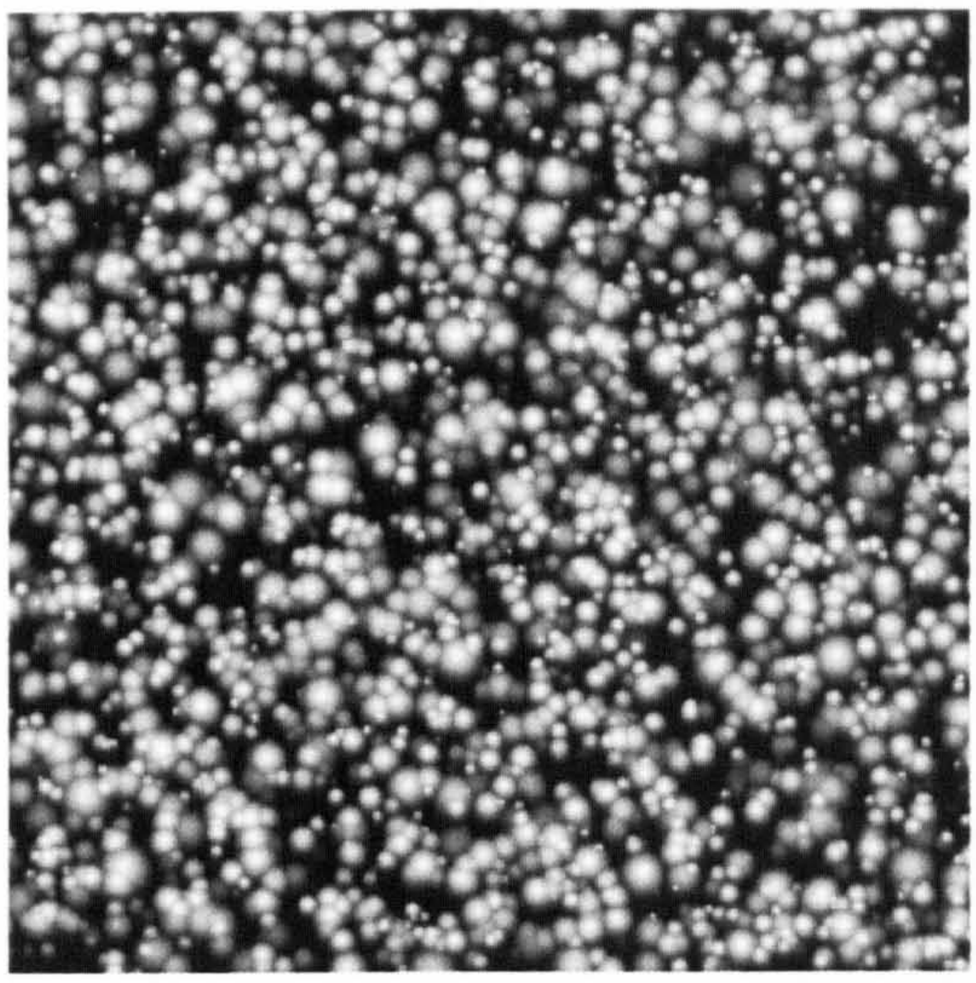

Image 07:2

Figure 2-23 Synthetic Image 07: Large Particle Diameter

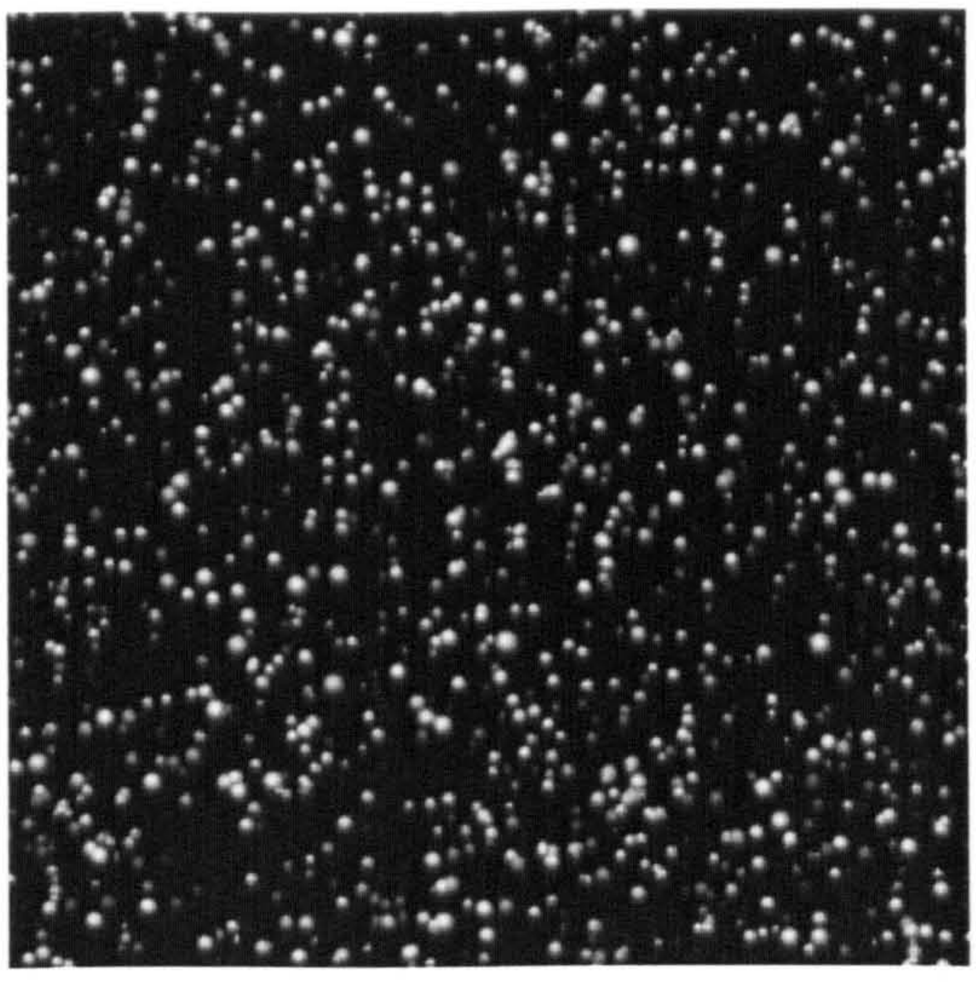

Image 08:1

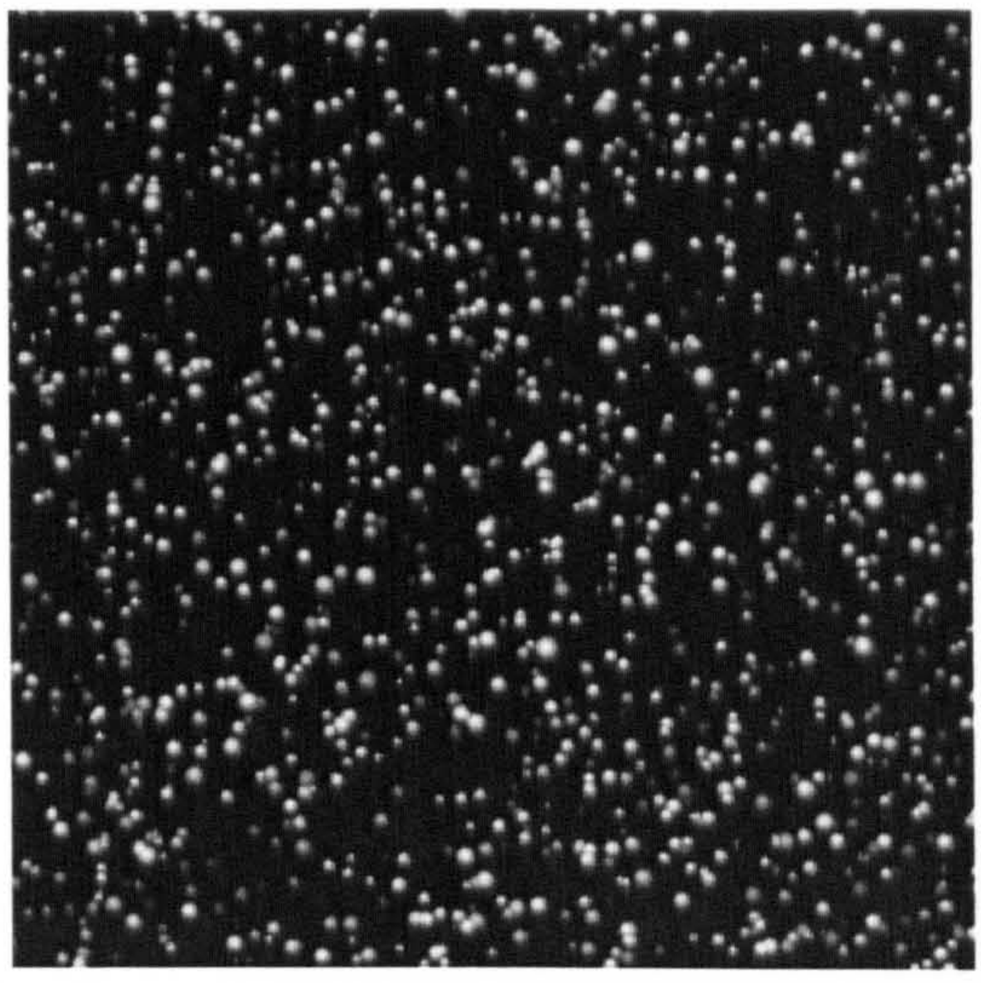

Image 08:2

Figure 2-24 Synthetic Image 08: Large Out-of-Plane Component

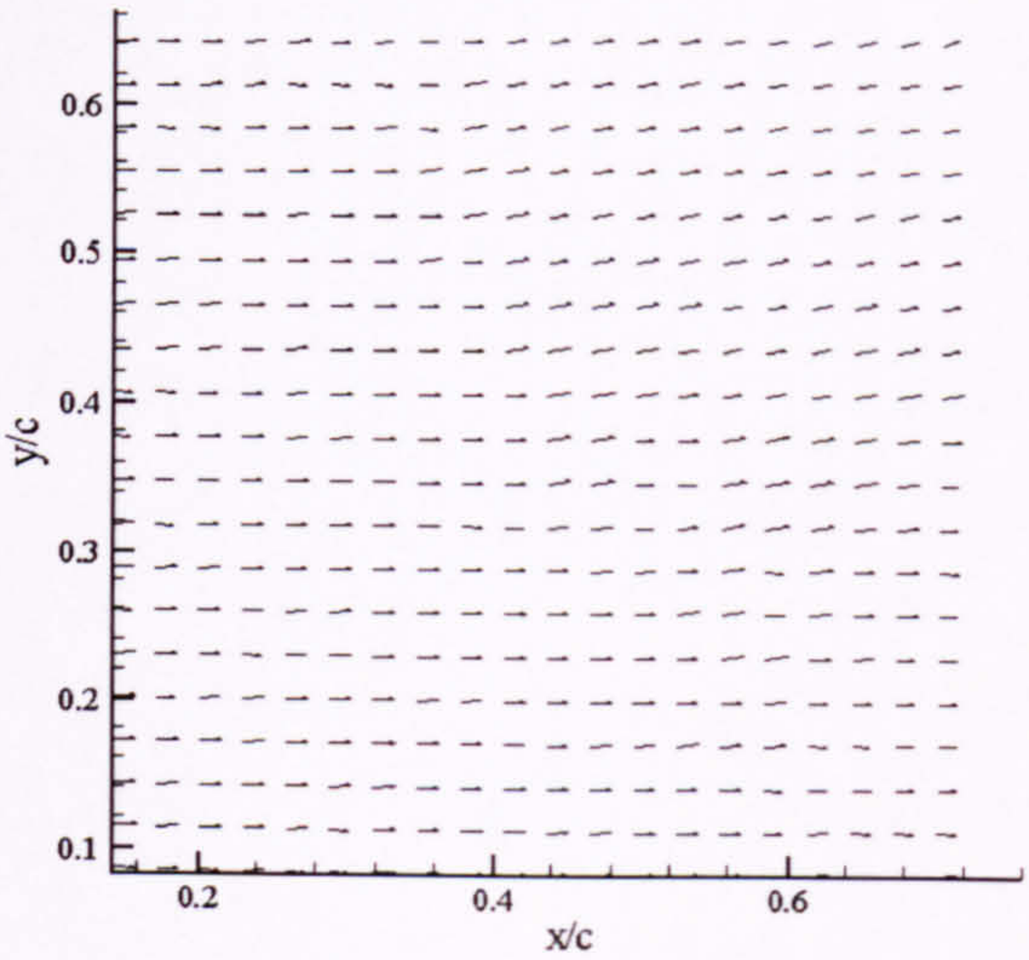

(a) Velocity Vector Plot

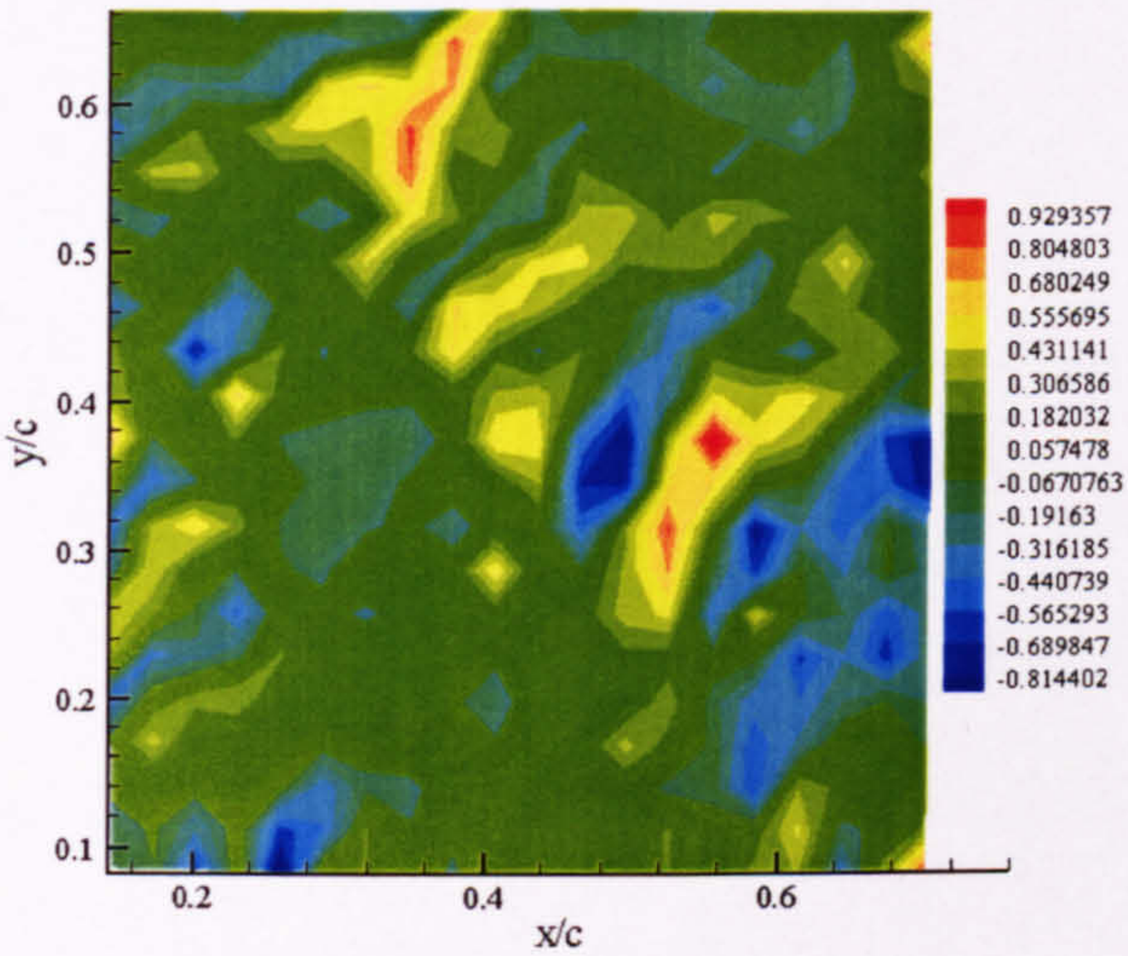

(b) Vorticity Plot

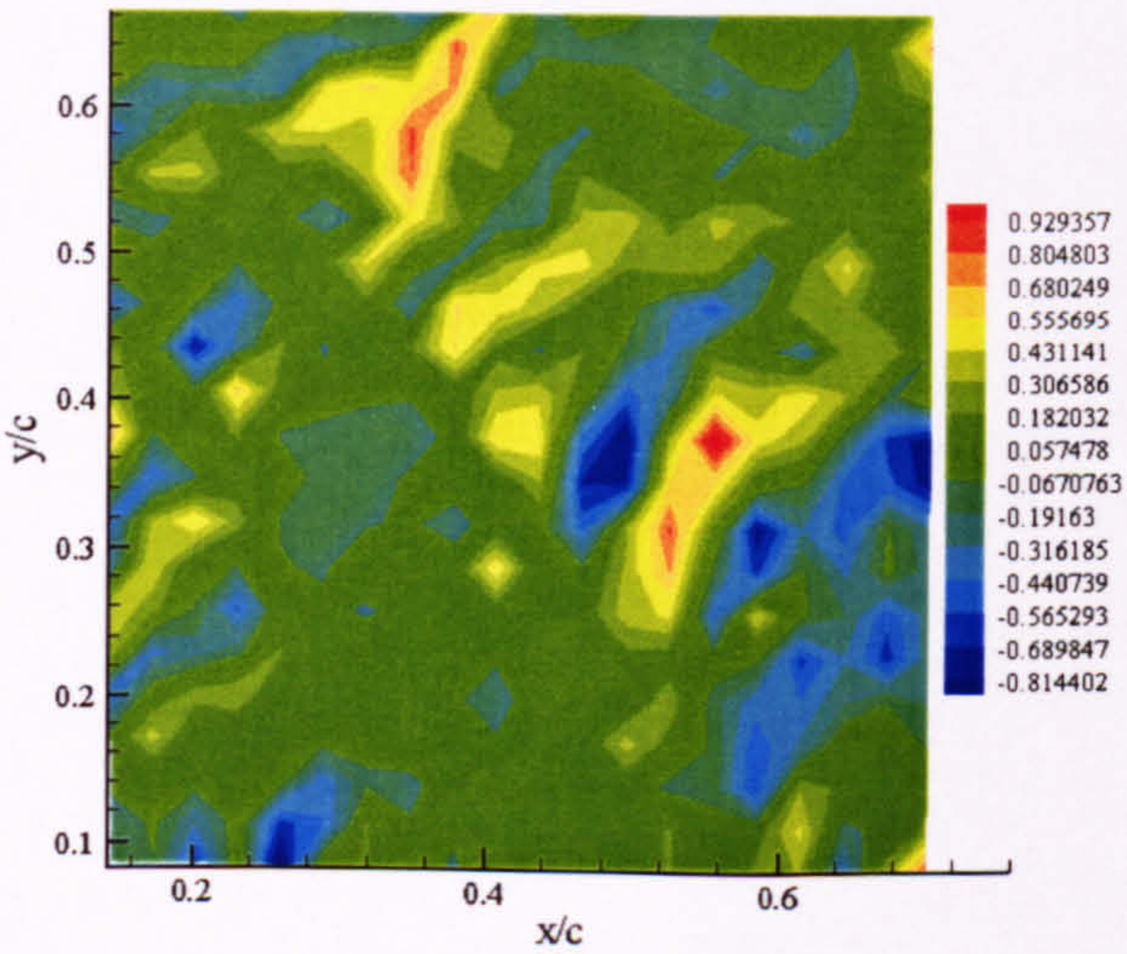

(c) Divergence Plot

Figure 2-25 2D Test Case – Freestream Flow with no *(v,w)* component present in flow.

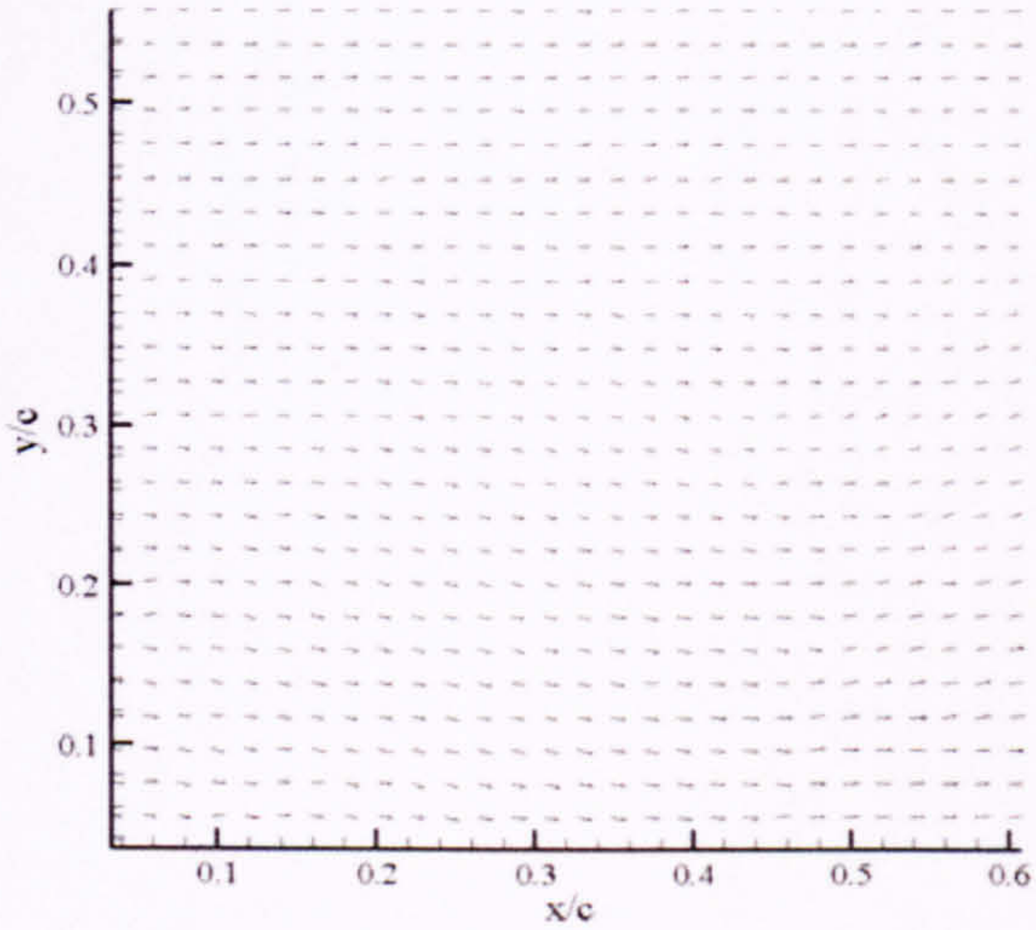

(a) Velocity Vector Plot

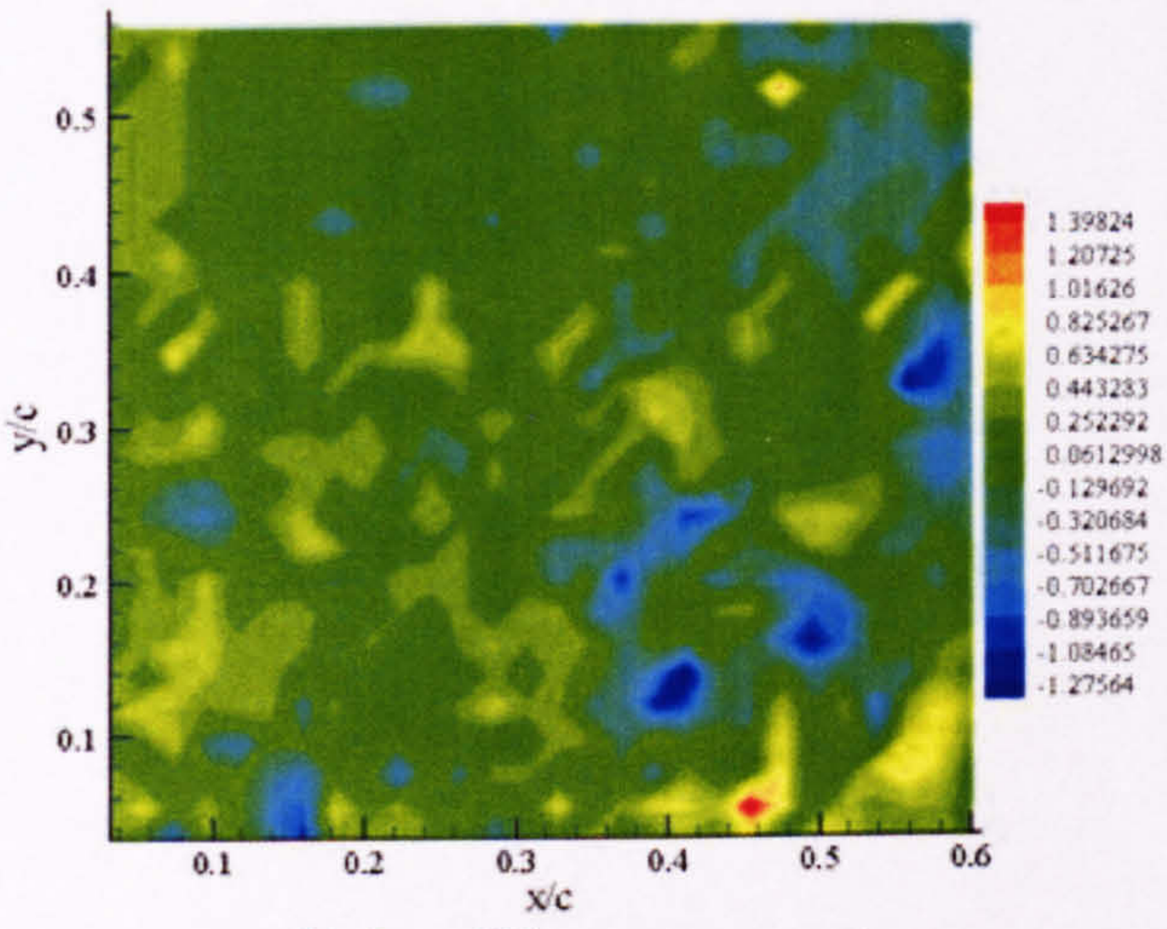

(b) Out of Plane w component

Figure 2-26 3D Test Case –Freestream Flow with no *(v,w)* component present in flow.

Chapter 3:Visualisation of the Interaction of a Single Vortex with a Stationary, Rectangular Blade

A detailed discussion of the aerodynamic characteristics most commonly associated with rotorcraft operation, and more specifically those aerodynamic phenomena which leads to the undesirable loading and acoustic conditions, was presented in Chapter One. This field of helicopter interactional aerodynamics is one that has long been of interest, but the complexity of the unsteady flowfield has made progress slow, as numerical simulations of the flowfield tend to be difficult to perform due to their computationally-intensive nature, and experimental modelling of the interactional behaviour difficult to achieve within controlled conditions. The phenomenon identified as being of particular interest within the community is that of the interaction of the trailing tip vortex structures produced within the main rotor assembly with the surrounding airframe structures (i.e. the fuselage, rotor blades, etc.), as such interactions have long been associated with impulsive airframe loading and as a consequence, the production of a range of low through to high frequency noise signatures.

As momentum has gathered in the investigation of these phenomena, there has still been a relative lack of investigation performed considering the effect of the vortical structures on the empennage, an interaction in which the vortex core is 'cut' perpendicular to its core axial flow, and hence locally destroyed. This particular interaction has long been of interest (Sheridan and Smith, 1980), but due to the complexity of this aerodynamic phenomenon, progress in the understanding of the mechanics of this interaction has been slow.

As the myriad of interactions which are simultaneously occurring within rotorcraft are next to impossible to simulate and isolate within laboratory conditions, Chapter Two presented an experimental arrangement which would enable the interaction of a

representative trailing tip vortex with a stationary rectangular blade to be simulated for interrogation. In order to obtain a global flow field quantification of the mechanics of the interaction, a Particle Image Velocimetry technique was employed.

The following chapter will present the results of the interaction of a single trailing tip vortex produced by a rectangular blade planform. In order to map the entire sequence of the interactional process, the vortical structure was interrogated at a series of locations from the leading edge region through to the trailing edge on either side of the interacting blade section in order to develop a global view of the mechanics of the interaction.

3.1 Structure of the Isolated Vortex Core

The features of the vortex core which may be solely attributed to the interactional process are the main focus of studies of this nature. As such, a thorough understanding of the nature of the vortex prior to undergoing deformation is essential. In order to achieve this, the vortex core is studied in its isolated state (i.e. within the freestream flow with no obstruction present within the wind tunnel working section). This allows any features which have been imparted to the flow as a result of the interaction to be easy to identify through direct comparison.

By removing the interacting blade from the wind tunnel simulation [Figure 2-1, Figure 2-7(a)], and the PIV lightsheet aligned in the position that the blade centreline would have occupied (aligned parallel to the blade chord direction), the isolated vortex core was interrogated in the plane of the vortex core (the x-y plane indicated in Figure 2-2). Vorticity ($\frac{c\omega}{U_\infty}$), divergence ($\frac{c\nabla}{U_\infty}$), and strength ($\frac{\Gamma}{U_\infty c}$) have been non-dimensionalised by the blade chord length (0.1524m) and the freestream velocity ($20ms^{-1}$), x and y locations within the interrogation plane have been non-dimensionalised to the blade chordlength. As there is no reference origin within the isolated state, the origin location is not of consequence for this section.

Measurements of the vortex core in its freestream state reveal a symmetrical structure with no apparent inflow/outflow, as would be anticipated from a fully formed trailing tip vortex.

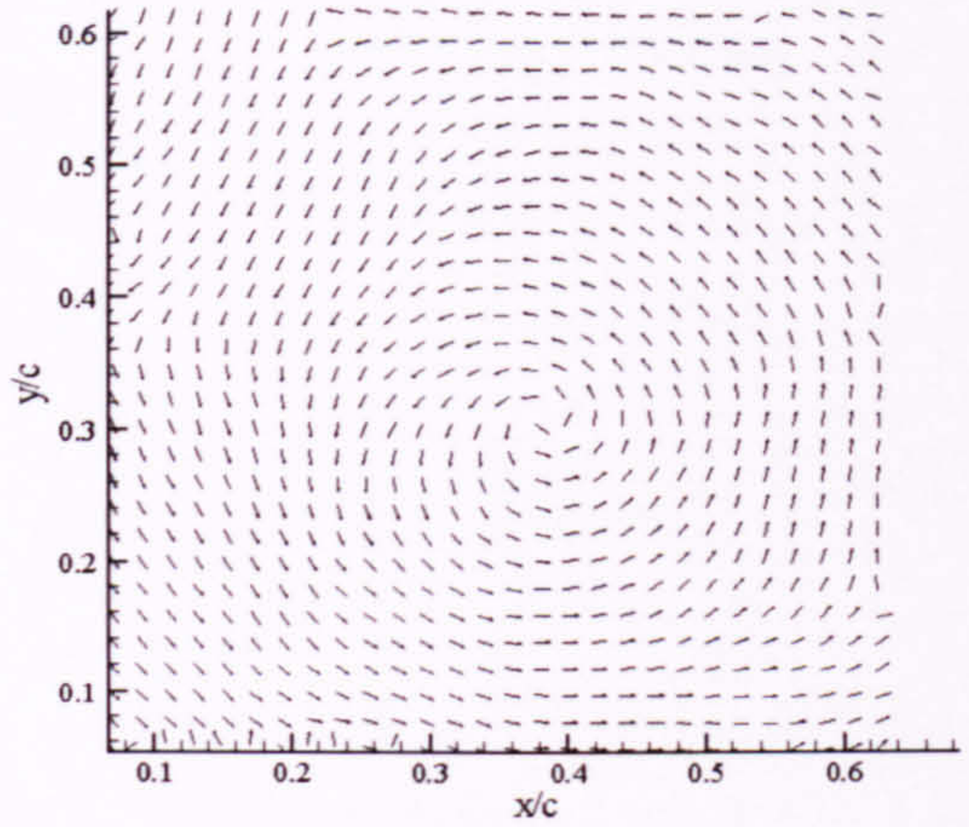

Figure 3-1 The isolated vortex core shows no evidence of radial inflow/outflow as would be expected from a fully developed vortex core. The mean u component has been removed for clarity. Measured peak velocity $0.41U_\infty$.

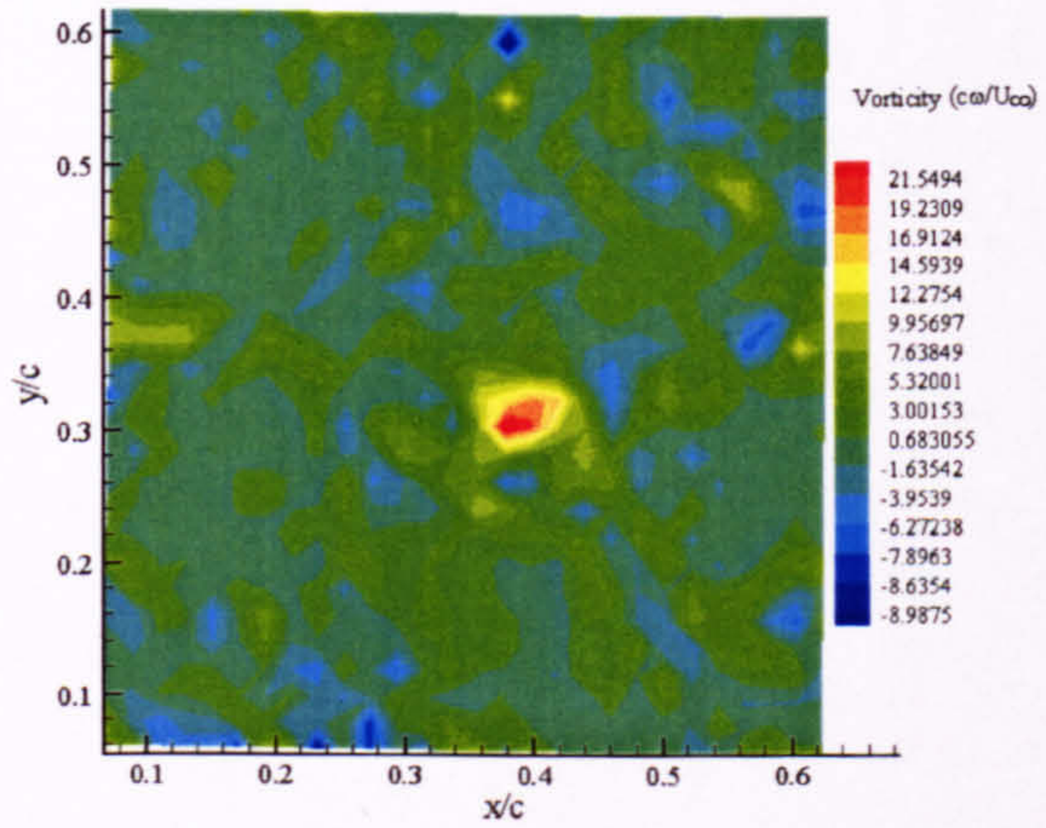

Figure 3-2 The non-dimensional vorticity of the isolated vortex core indicates a peak of $21.5\frac{U_\infty}{c\omega}$, with a clearly defined vortical structure observed.

The core diameter of 0.1c is in agreement with the previous hotwire measurements of Doolan et al. (2000), with a vortex strength of $0.19\frac{U_\infty c}{\Gamma} \pm 0.02$ comparable to previously obtained hotwire data. The measured peak velocity of $0.41U_\infty \pm 0.03$ [Figure 3-1] and

peak vorticity recorded of $21.5\frac{U_\infty}{c\omega} \pm 1.2$ [Figure 3-2] are again in keeping with previous calculations of the modelled trailing tip vortex structure. Figure 3-3 indicates the manner in which the core diameter information is extracted from the PIV data sets.

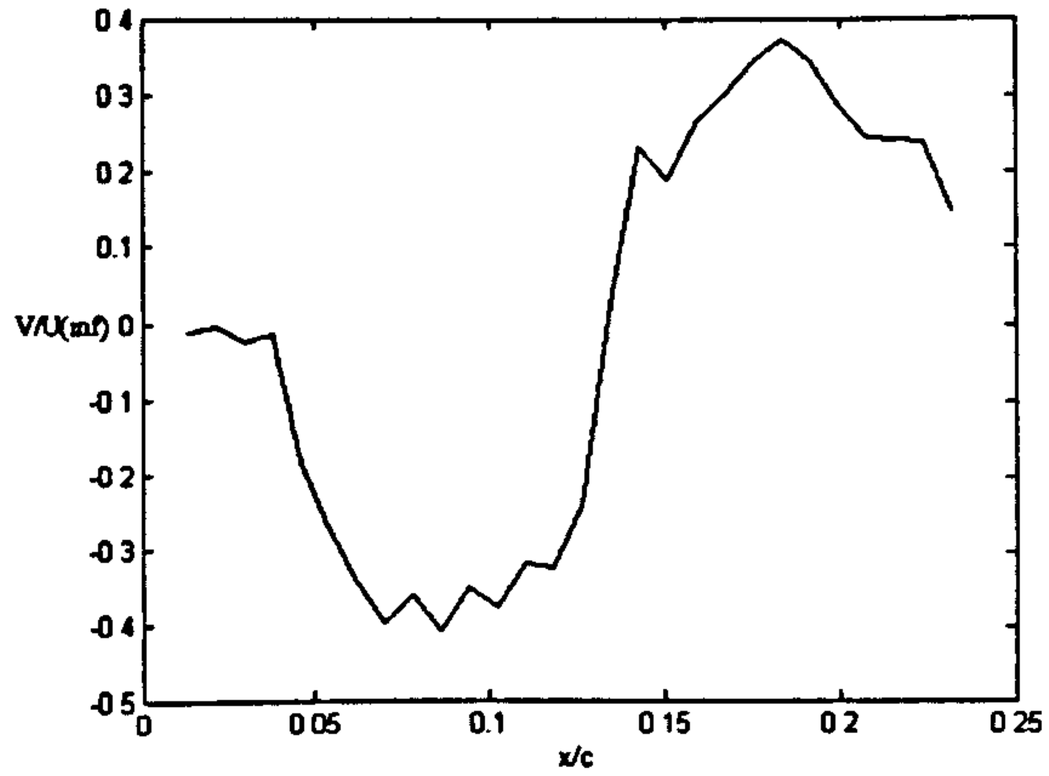

Figure 3-3 The velocity distribution within the flow around the vortex is used to give an estimation from the reconstructed velocity field of the vortex core diameter (as shown above).

Previous work on the dynamics of these interactions has suggested that the progression of the interaction may be attributed to manner in which the axial flow is influenced by the blockage at the blade surface. Figure 3-4 indicates the contours of divergence for the isolated flow field, showing a peak divergence measurement of $4.56\frac{U_\infty}{c\Delta}$ (the divergence field for the isolated vortex was measured as $\pm 4.5\frac{U_\infty}{c\Delta} \pm 0.1$ over 60 records). As the vortex core axial flow should not be subjected to any additional external influences in this state, it would be anticipated that low readings of divergence within the noise threshold would be obtained, as there should not be evidence of mass flow in/out of the vortex core. The stereoscopic view of the isolated vortex core [Figures 3-5] indicates a region of concentrated out-of-plane velocity over the region of the core, indicative of the presence of the axial flow component of the core. The maximum out-of-plane velocity component $0.54U_\infty \pm 0.05$ is similar to that which was recorded by previous hotwire data for the core region.

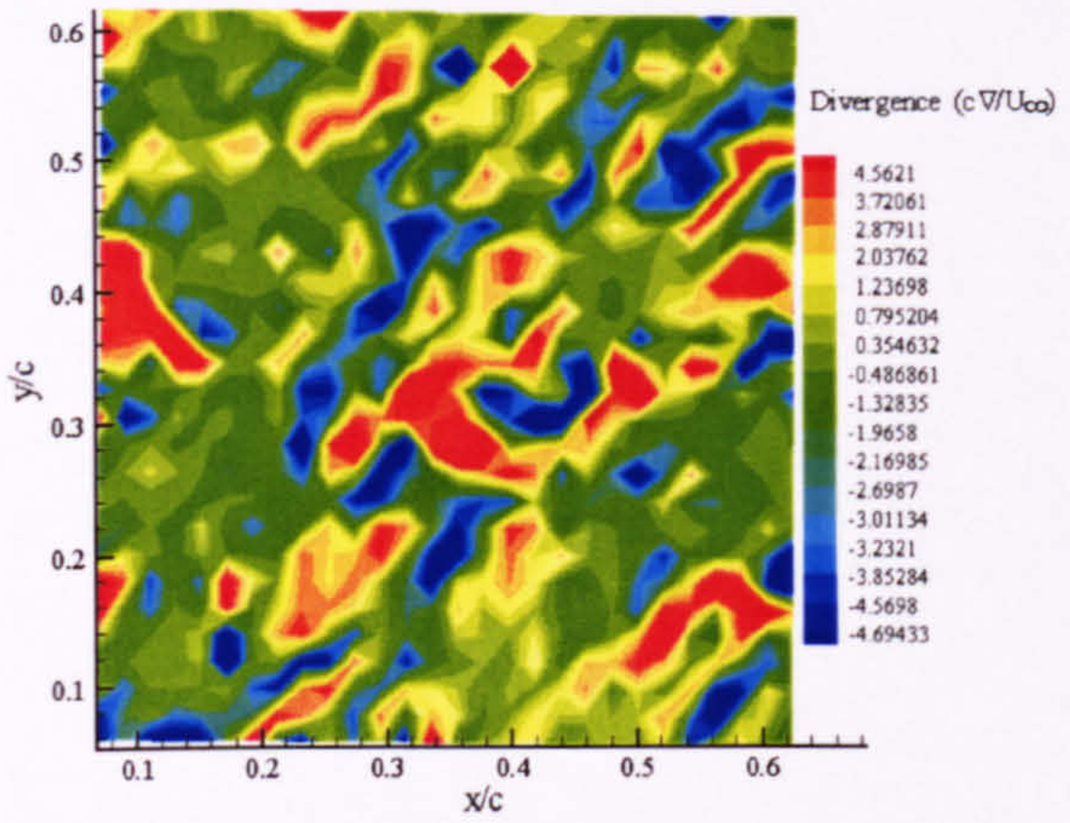

Figure 3-4 The isolated divergence contours indicate that there is no mass inflow/outflow of the vortex core, as would be expected in the undisturbed vortex state. The recorded levels of $\pm 4.5 \frac{U_\infty}{c\Delta}$ are consistent with noise within the flow.

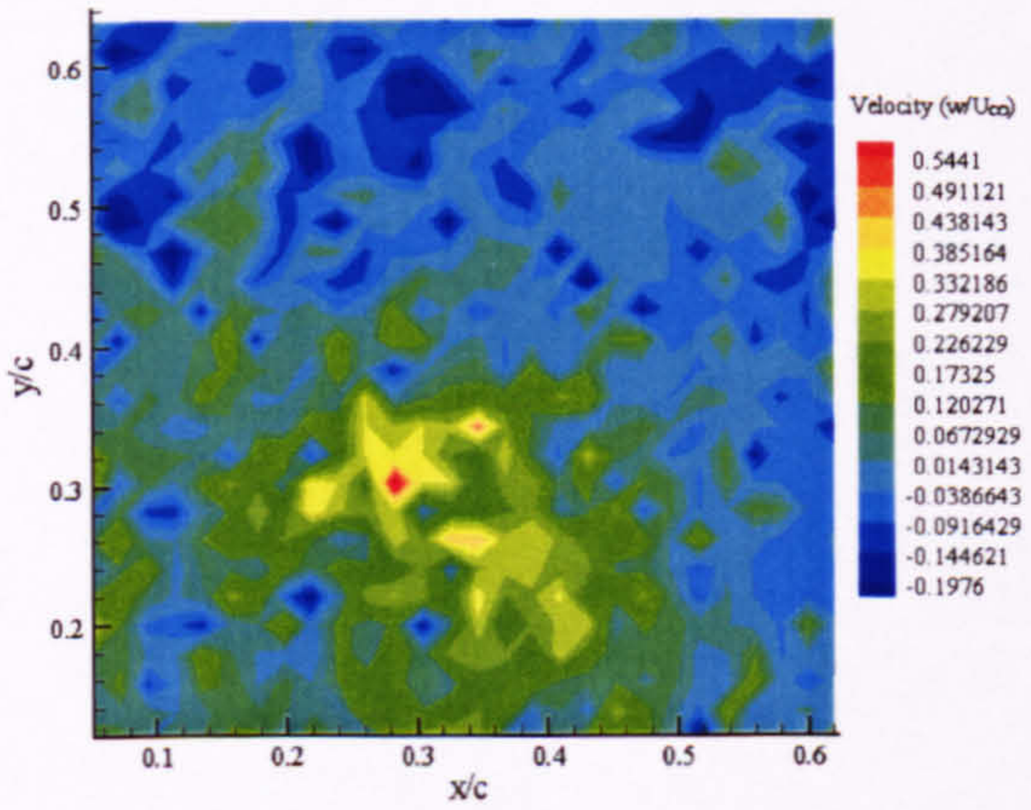

Figure 3-5 Contours of out-of-plane velocity reconstructed from the stereoscopic data. The maximum recorded out of plane velocity is $0.54U_\infty$. The centre of the vortex is located at (0.3, 0.28) as indicated in the 2D projection of the velocity vectors for the out-of-plane reconstruction.

Viewing from a downstream location in the plane of the axial flow component (the y-z plane), Figure 3-6 indicates the presence of a significant z-component within the vortex core. The curvature observed is consistent with the anticipated helical trajectory of the trailing vortex, and the maximum measured axial velocity of $0.6U_\infty \pm 0.08$ is in agreement

with the previous measurements obtained through hotwire anemometry (Doolan et al., 2000).

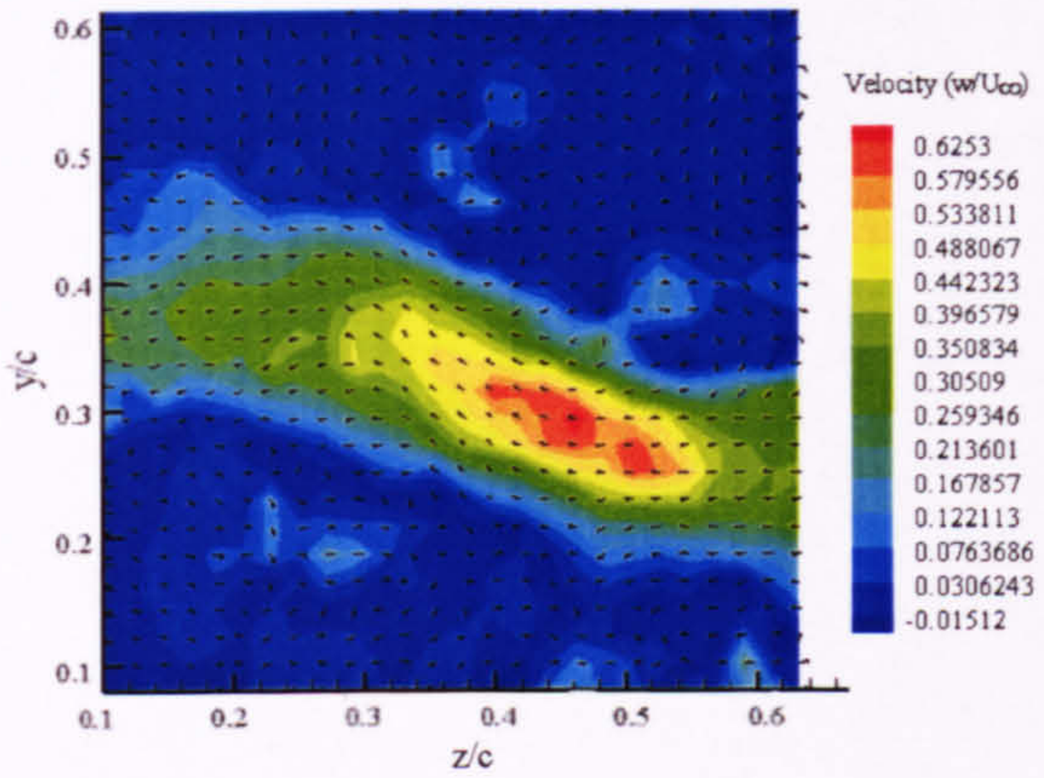

Figure 3-6 Viewing from a downstream location, the vortex axial flow. The max. measured velocity is approximately $0.6*U\infty$ ($\sim 12ms^{-1}$).

3.2 Influence of the Thickness Parameter on the Progression of the Orthogonal BVI

The progression of the vortex-body interaction is influenced by a range of parameters, most notably the Blade Impact Parameter ($\frac{2\pi\sigma U}{\Gamma}$: the ratio of the freestream velocity normal to the body, to the maximum vortex swirl velocity) and the Thickness Ratio ($\frac{T}{\sigma}$: the normalised blade thickness relative to the impinging vortex core diameter), identified by Krishnamoorthy and Marshall (1998). The influence of these two parameters gives rise to three distinct regimes within the BVI, which were previously outlined in Chapter One.

Considering the nature of the two parameters, one is much easier to influence than the other – the modification of the impact parameter is either through the variation of the external flow conditions (i.e. increasing/decreasing U), which will ultimately affect the trajectory of the trailing vortex (which is undesirable for this study), or a modification of

the vortex physical parameters (which will be discussed in greater detail in Chapter Four), whereas the thickness parameter may be easily manipulated through the modification of the interacting blade thickness.

Previous visualisation of the impact of a columnar vortex with a circular cylinder, performed using LIF (Krishnamoorthy & Marshall, 1998) indicated that a substantial change in the interactional process could be observed if the thickness parameter was sufficiently large. By increasing $\frac{T}{\sigma}$ to a sufficiently high level, instead of the vortex being 'cut' at the point of contact, a deformation in both the chordwise and spanwise directions was observed, due to the inviscid interaction with the body. After substantial bending had occurred, the cylinder boundary layer was observed to separate in the form of a vorticity sheet, quickly rolling to form a 'tongue' like structure (which was verified both experimentally and computationally), dominated by a vortex loop which had a vorticity sheet stretched between the legs of the loop. This secondary vorticity then wrapped around the primary vortex core, before gradually being entrained into it.

Gossler and Marshall (2001) identified this secondary vorticity as a product of the proximity of the vortex to the solid body, which leads to the generation of a boundary layer along the body surface. The inviscid bending of the vortex impinging on the body induces an adverse pressure gradient in the axial direction on one side of the body face (Affes et al., 1993), which leads to the eventual ejection of secondary vorticity into the surrounding fluid region. This interaction of the secondary vorticity may give rise to a variety of phenomena, such as the rebound of the vortex from the interacting body surface or the breakdown of the vortex into small scale turbulence.

For a suitably large thickness parameter (>5), the behaviour of the vortex core has been described as either being 'attractive' or 'repulsive' (Marshall & Yalamanchili, 1994). For a low impact parameter, the flow which is induced as a result of the normal flow velocity is weak. This results in the vortex bending mostly in the spanwise direction, leading to a self-inducing velocity of the vortex directed towards the cylinder. This gives the

appearance of the vortex being 'attracted' to the body. For a sufficiently large impact parameter, there is a significant flow induced as a result of the normal freestream velocity, which is large enough to overcome the self-induced velocity of the vortex core. As such, the vortex will bend away from the body (i.e. be 'repulsed'). Any change observed in the vortex core area occurring as a result of the vortex core bending are only noticeable at high impact parameters, and then only after a large amount of stretching had occurred (Marshall & Yalamanchili, 1994).

In order to examine the effect of $\frac{T}{\sigma}$ on the progression of the interaction, the passage of the vortex core over the leading edge of a series of circular cylinders of increasing diameter was examined. Each of these cases gave a discrete thickness parameter (2, 3.5 and 5 respectively) for an impact parameter $\frac{2\pi\sigma_o U_\infty}{\Gamma}$=3.14 and axial flow parameter $\frac{2\pi\sigma_o w_o}{\Gamma}$=1.88 (hence the vortex is described as super-critical (Marshall, 1994)). As the thickness parameter increases, prior studies have shown that this will have a significant effect on the interactional process, with the core disrupted by the boundary layer fluid as it detaches from the surface of the circular cylinder (as observed by Marshall & Yalamanchili, 1994). The work of Marshall and Yalamanchili indicated that, for a thickness parameter of greater than five and a large impact parameter (which is the current case), the interaction of the vortex and the cylinder will be repulsive, i.e. the vortex will bend away from the cylinder surface. In order to visualise the interaction, the laser lightsheet was aligned at 0.0131 z/c (with the z plane indicated in Figure 2-1) from the point of maximum diameter on each of the cylinders in order to prevent the sheet being obstructed by the body, parallel to the centreline of the wind tunnel working section [Figure 2-7(b)] The leading edge of the interacting cylinder is located at 0 x/c for all the cases shown below.

For the case in which $\frac{T}{\sigma_o}$=2, the approaching vortex is similar to that which is observed in the freestream flow.

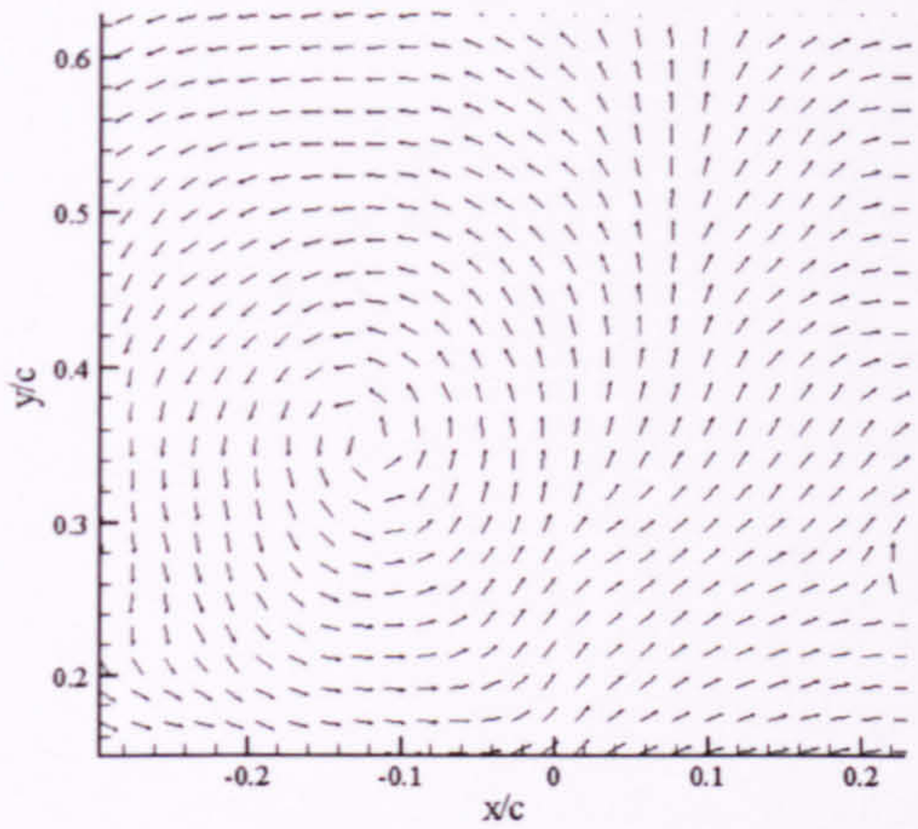

Figure 3-7 The pre-interaction vortex core reveals no significant variation from the isolated core to the radial or tangential components for an interactional thickness ratio of 2 (mean u-component removed for clarity). Lightsheet aligned at 0.013 z/c from the point of maximum thickness on the interacting body. Peak measured velocity of $0.66U_\infty$.

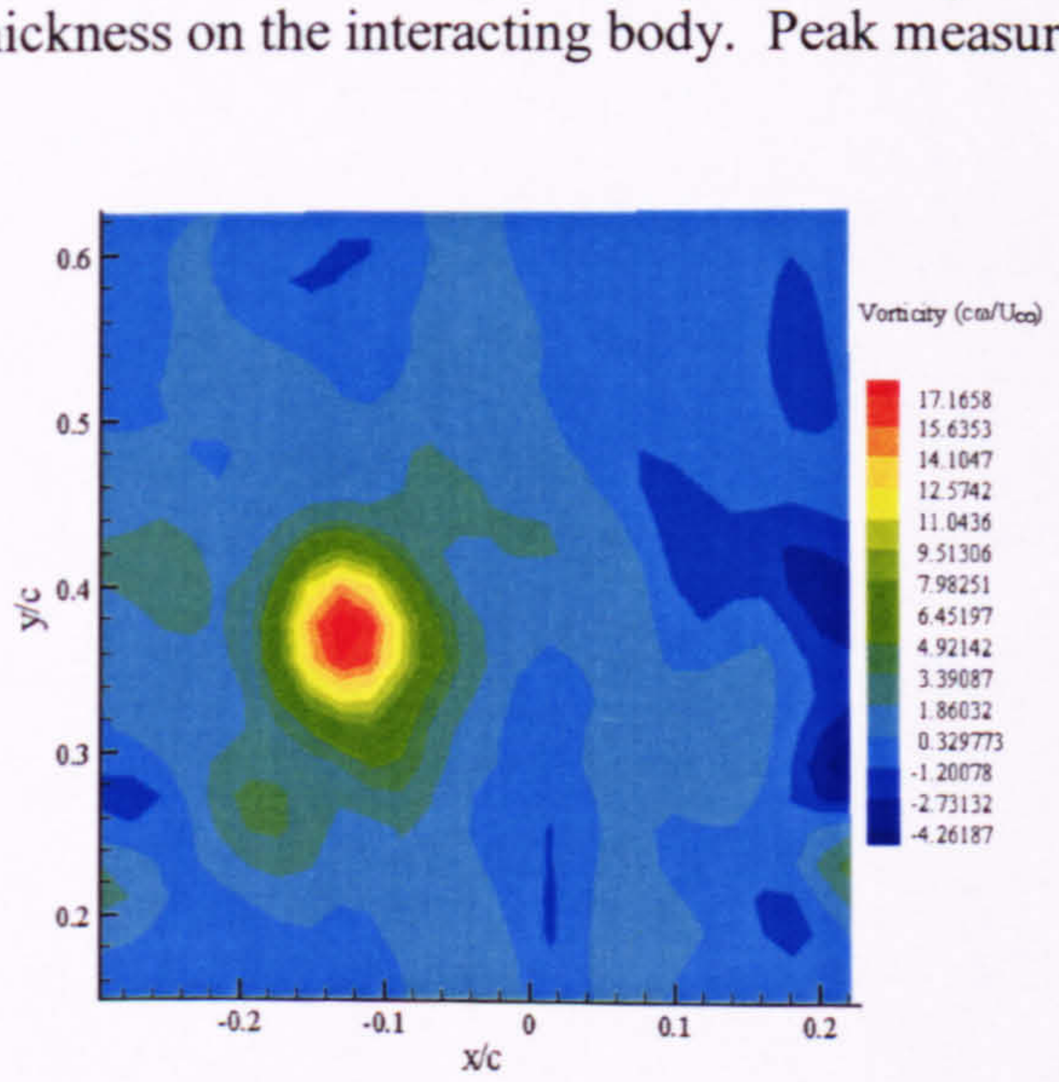

Figure 3-8 The pre-interaction peak non-dimensional vorticity of 17.17$\frac{U_\infty}{c\omega}$ for an interactional thickness ratio of 2 is consistent with the measurements of the isolated vortex core structure. Lightsheet aligned at 0.013 z/c from the point of maximum thickness on the interacting body.

At a distance of just over a core diameter from the interacting surface (Figure 3-7, 3-8), there is no apparent disruption to the structure of the trailing vortex (as would be expected in this case), indicating that there are no downstream effects of the cylinder influencing the vortex prior to the interaction.

As the vortex passes over the leading edge of the cylinder, the interaction progresses in a similar manner to that which is observed for the low thickness parameter studies of Marshall and Krishnamoorthy (1994). The radial re-dispersion of fluid is immediately observed post interaction (Figure 3-9), which is similarly noted in divergence contours, although there is no indication that there are far field effects on the structure of the core due to boundary layer fluid entrainment.

The most notable point is that there is no evidence of a significant change in the vortex core aspect ratio, as would be observed in cases where the vortex has wrapped significantly around the leading edge rather than been completely 'cut' (Figure 3-10). This would lead to the assumption that the vortex has been completely 'cut' at the point of impact onto the cylinder surface, again in agreement with the expectations of a low thickness parameter, high impact parameter interaction of a supercritical vortex structure.

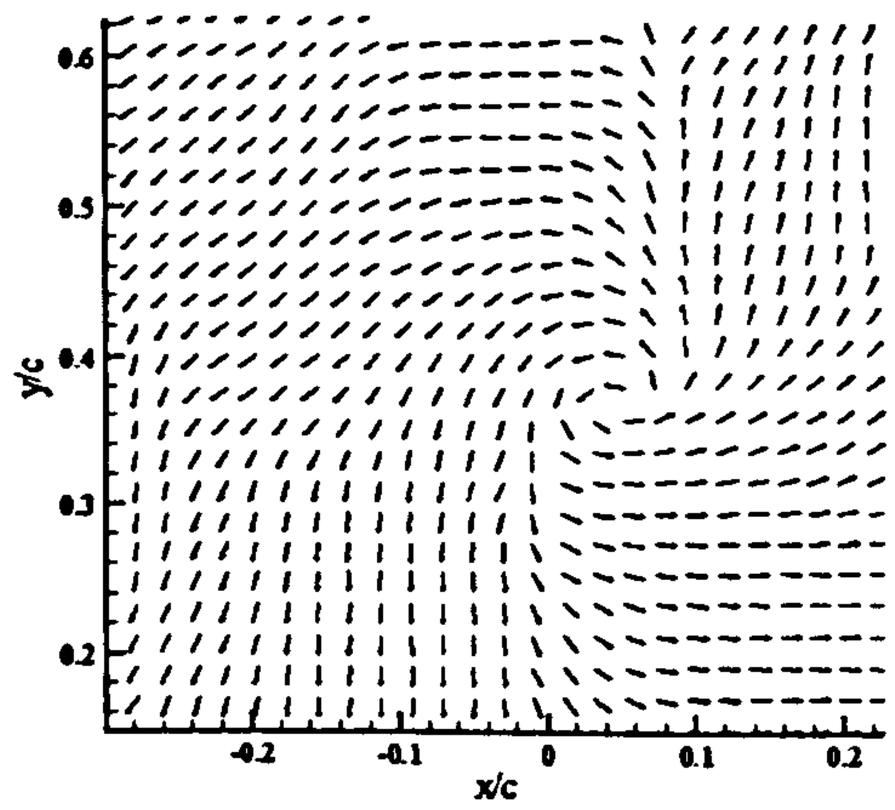

Figure 3-9 The post-interaction vortex core reveals a significant variation to the radial and tangential components for an interactional thickness ratio of 2 (mean u-component removed for clarity). Max. measured velocity $0.65U_\infty$. Lightsheet aligned at 0.013 z/c from the point of maximum thickness on the interacting body.

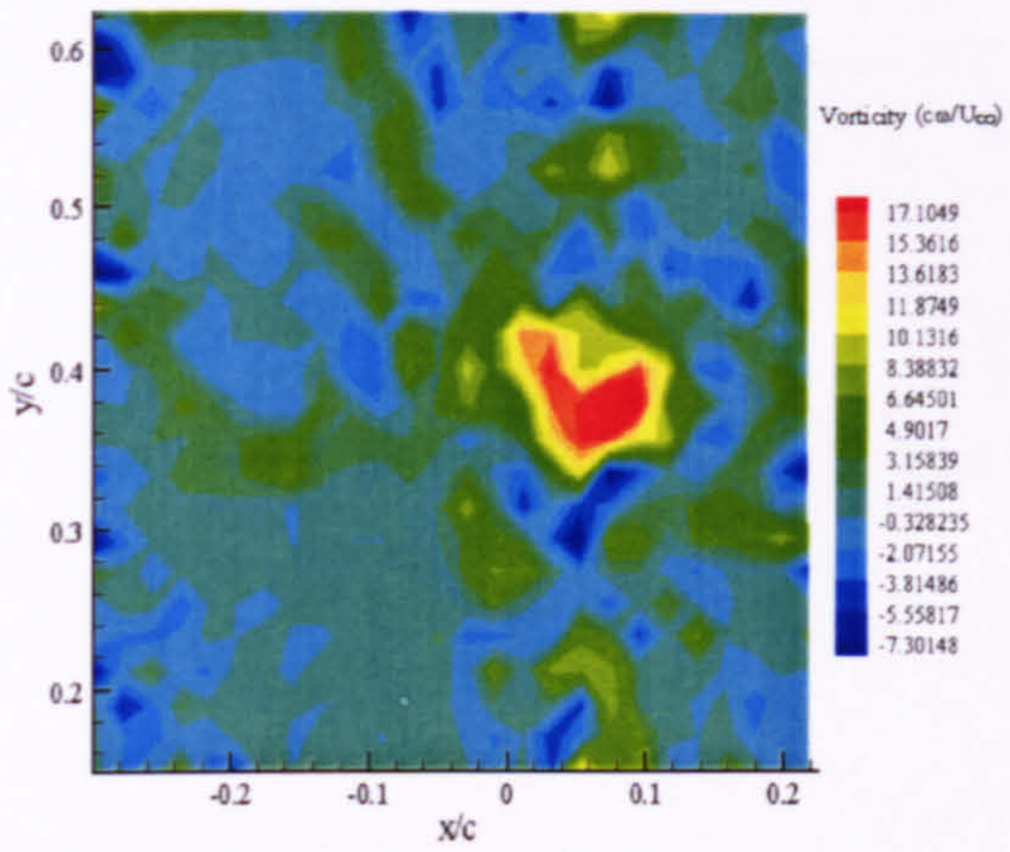

Figure 3-10 The post-interaction peak non-dimensional vorticity of $17.10\frac{U_\infty}{c\omega}$ for an interactional thickness ratio of 2 reveals no significant decrease. This could be attributed to the time period between impact and image capture. Lightsheet aligned at 0.013 z/c from the point of maximum thickness on the interacting body.

By increasing the thickness parameter to 3.5, again there is no deformation apparent within the vortex core, even at less than a core diameter away from the body surface. The obtained vorticity and divergence plots are consistent with the results obtained for the freestream core, again re-emphasising that there are no appreciable downstream effects of the presence of the upstream body on the core structure. Post interaction, there is again a significant radial outflow from the vortex core which is observed in the velocity vector plots, similar in nature to that observed for the lower $\frac{T}{\sigma_o}$. There is no appreciable variation in the peak vorticity levels observed in the vortex core. As the velocity distribution reveals the presence of a significant radial flow, it is possible to assume that the flow is being blocked by the surface, resulting in the observed radial outflow.

A further increase in the thickness parameter to $\frac{T}{\sigma_o}$=5, increases the ratio to the point at which the transition from core severing to core bending was identified to occur**.** Just prior to the impact of the vortex core onto the surface of the interacting cylinder, the core

is again similar to that of the freestream vortex core, with high peak vorticity levels, and no evidence of disturbance to the vortex core axial flow.

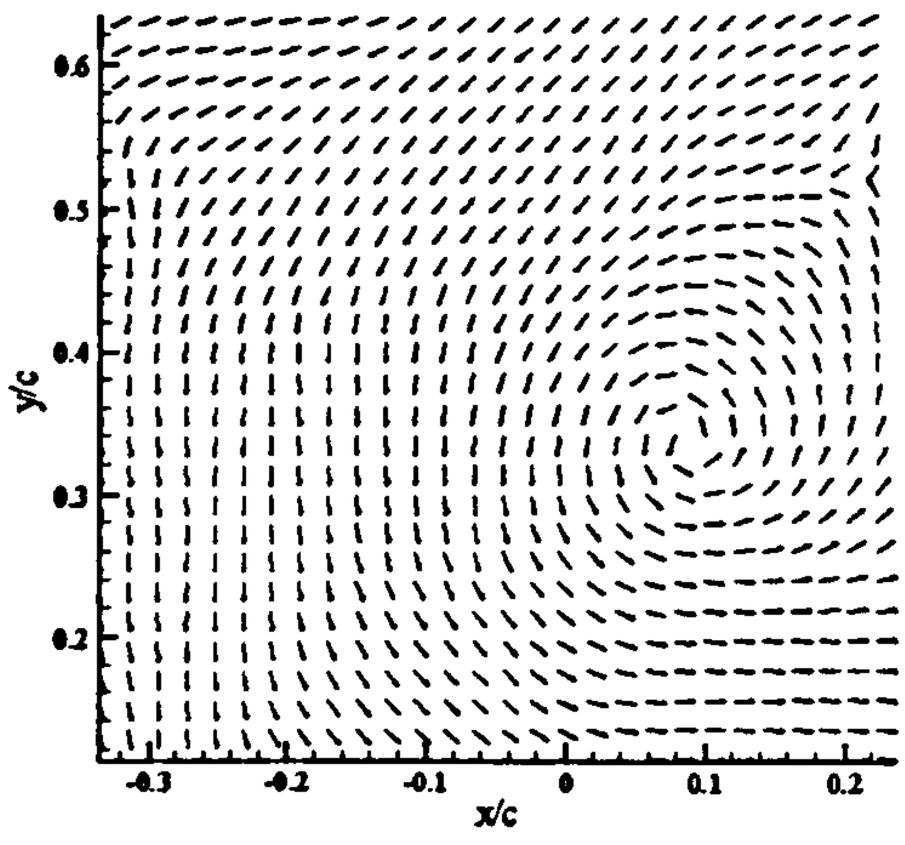

Figure 3-11 The post-interaction vortex core reveals no significant variation from the isolated core to the radial or tangential components for an interactional thickness ratio of 5 (mean u-component removed for clarity). Max. measured velocity $0.47U_\infty$. Lightsheet aligned at 0.013 z/c from the point of maximum thickness on the interacting body.

Of more interest is the nature of the core post-interaction. Within the previously-observed visualisation of the interaction of the trailing vortex with a body, as the vortex has passed onto the surface, the radial re-dispersion of fluid into the surrounding flow has led to a significant alteration in the vortex core structure compared to the isolated vortex core, a result of the impact of the core axial flow onto the surface of the blade. In this case, however, there is no evidence of variation from the isolated core to the post-interaction vortex core (Figure 3-11, 3-12), and no indications of a deceleration of the vortex core axial flow, as would be expected if it had been blocked by a surface.

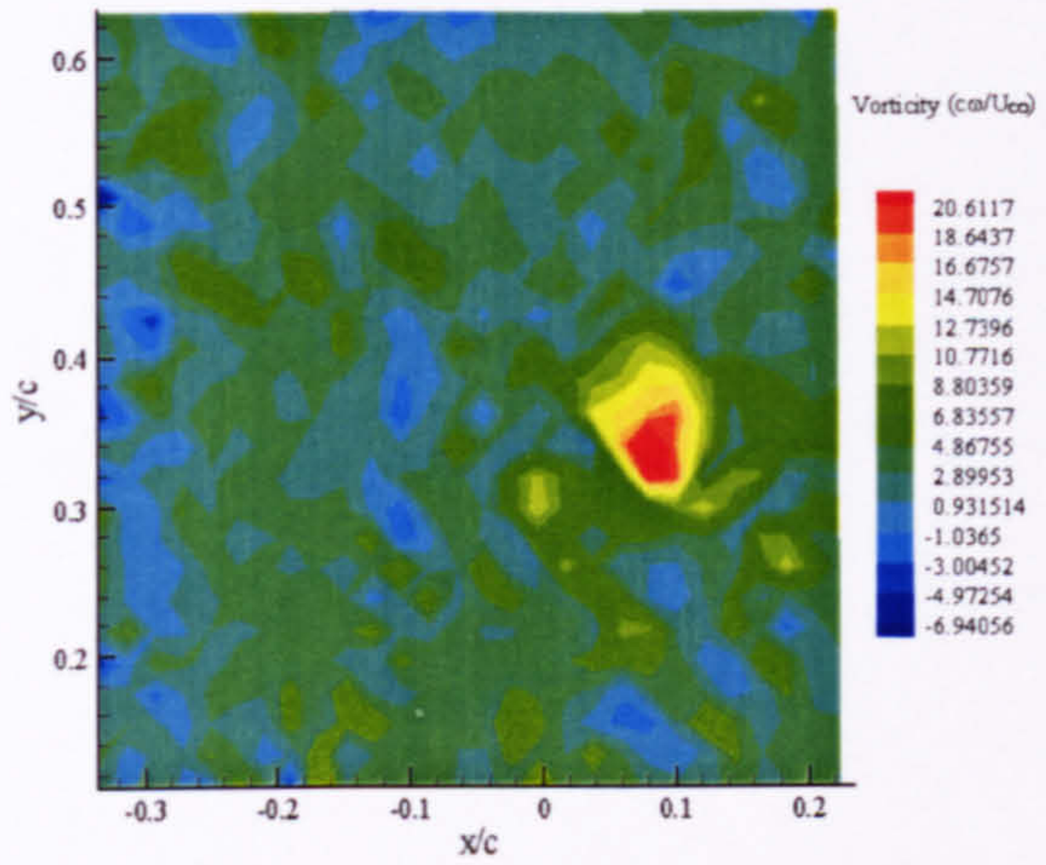

Figure 3-12 The post-interaction peak non-dimensional vorticity of 20.61 $\frac{U_\infty}{c\omega}$ for an interactional thickness ratio of 5 reveals no significant decrease, possibly attributable to the time period between impact and image capture. Lightsheet aligned at 0.01 z/c from the point of maximum thickness on the interacting body.

This is in agreement with the previous measurements of this interaction in all but one respect – there is no observed change to the aspect ratio of the core. This may be attributable to the thickness ratio – it may not be sufficiently high enough to promote a large amount of bending in the core.

3.3 Effect of Vortex Axial Flow 'Blocking' on the Structure of the Tip Vortex

As the vortex collides with the interacting blade, for the given blade impact parameter and the thickness ratio, the vortex is 'cut' by the leading edge of the interacting blade. The two portions of the split vortex then pass over the chord of the blade and into the trailing edge region. On the lower surface side, the axial flow component of the vortex core is directed towards the surface of the blade; on the opposing side (upper surface) the vortex core axial flow is directed away from the surface of the blade and needs to be re-established (this has previously been confirmed through experimental visualization by Krishnamoorthy & Marshall, 1994) [Figure 3-13].

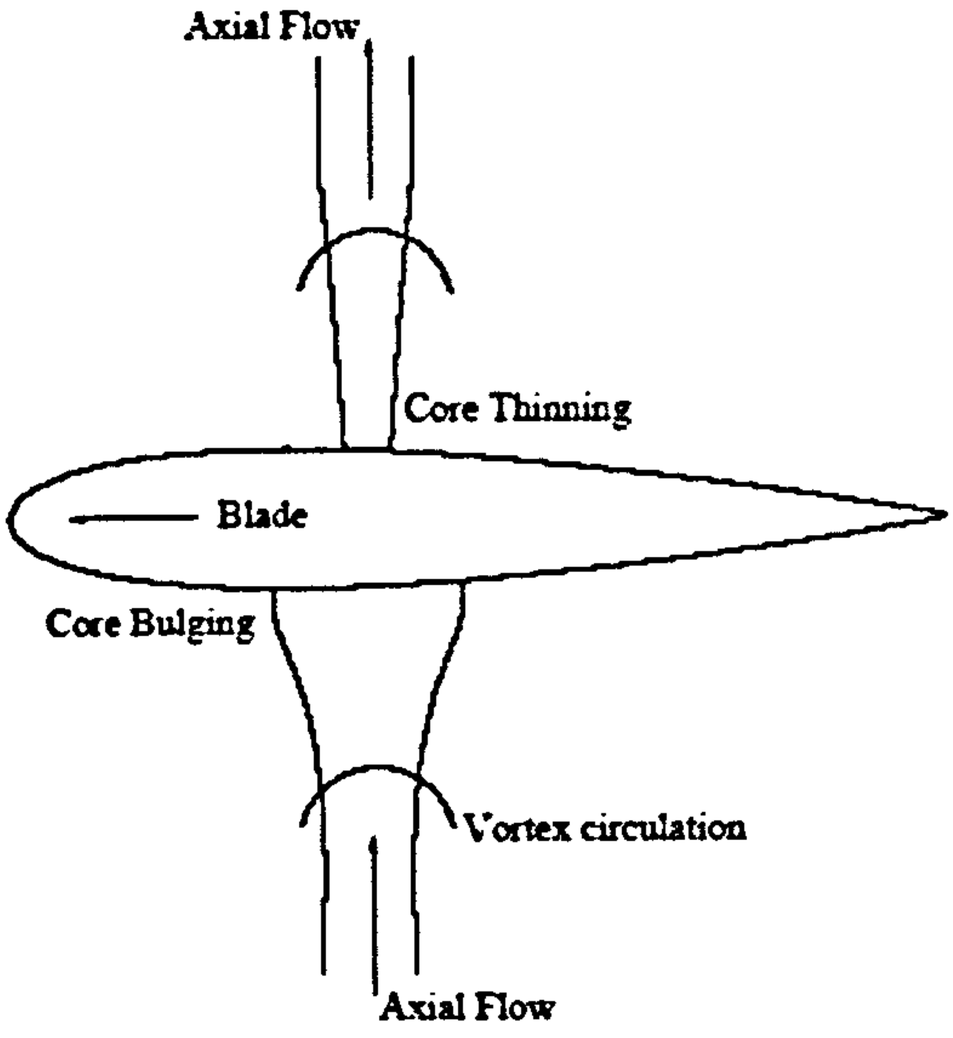

Figure 3-13 Schematic indicating the vortex deformation during the OBVI cutting process

In order to trace the interaction over either side of the blade centre line as the two portions of the core pass over the chord, the two camera/laser systems were set up independently in order to capture images of the two halves of the vortex core simultaneously for the 2D2C PIV study, so as to assess the differences within the vortex core for a single interaction [Figure 2-7(c)]. The lightsheets were directed into the wind tunnel working section parallel to the chord of the interacting blade (in the x-y plane of the working section, as indicated in Figure 2-1), at 15mm from the blade centre line on either side of the blade. At the closest point, the lighsheets were 0.02c (3.5mm) from the surface of the blade. In order to trace the far field effects of the interaction, the lightsheets were then moved away from the surface of the blade in 2mm stages over the mid chord position so as the vortex core could be examined for any change in structure with increasing distance from the blade surface. To compliment this, a 2D3C interrogation of the flow field revealed the features pertaining to the out-of-plane component, the component which has previously been identified as being one of the dominant factors determining the progression of the OBVI. All data are presented in these sections with the blade leading edge as the reference origin.

Finally, in order to assess the effect of the interaction close to the surface of the blade, the representative tail rotor blade was replaced with a sheet of glass, which allowed the laser sheet to be aligned closely with the interacting surface (0.013c) in the x-y plane (refer Figure 2-1), so as to examine the effect of the proximity of the boundary layer on the progression of the interaction.

3.3.1 Structure of the Post-Interaction Vortex Core on the Interacting Blade Lower Surface

As the vortex core passes over the leading edge and onto the surface of the interacting blade, the vortex core axial flow impacts with the surface of the blade. The impingement of the axial flow onto the surface of the blade compresses the out-of-plane component, resulting in a re-distribution of the vorticity radially outwards, which is apparent in the velocity vector plots [Figure 3-14, Figure 3-15] and is also typified by a decrease in the peak vorticity levels and a corresponding increase in the vortex core size [Figure 3-16].

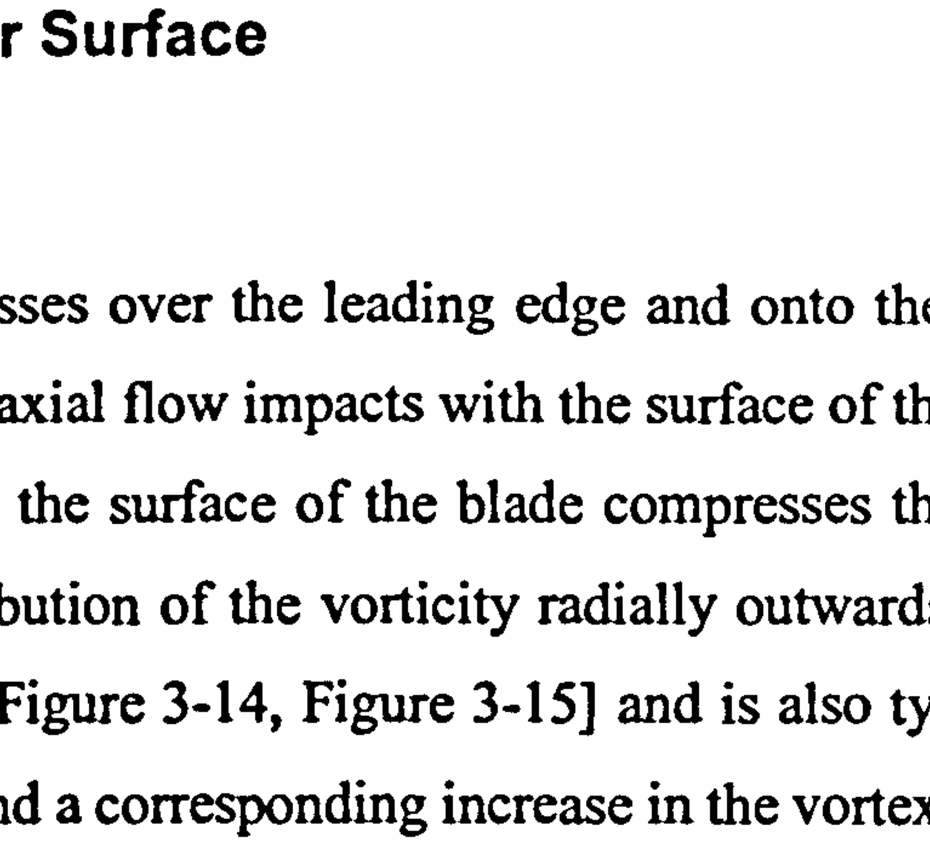

Figure 3-14 The post-interaction vortex core at 0.35 x/c indicates the presence of a significant radial outflow from the core into the surrounding fluid (mean u-component removed for clarity). Measured peak velocity of $0.47U_\infty$. Lightsheet aligned at 0.02 z/c from the blade surface at the quarterchord.

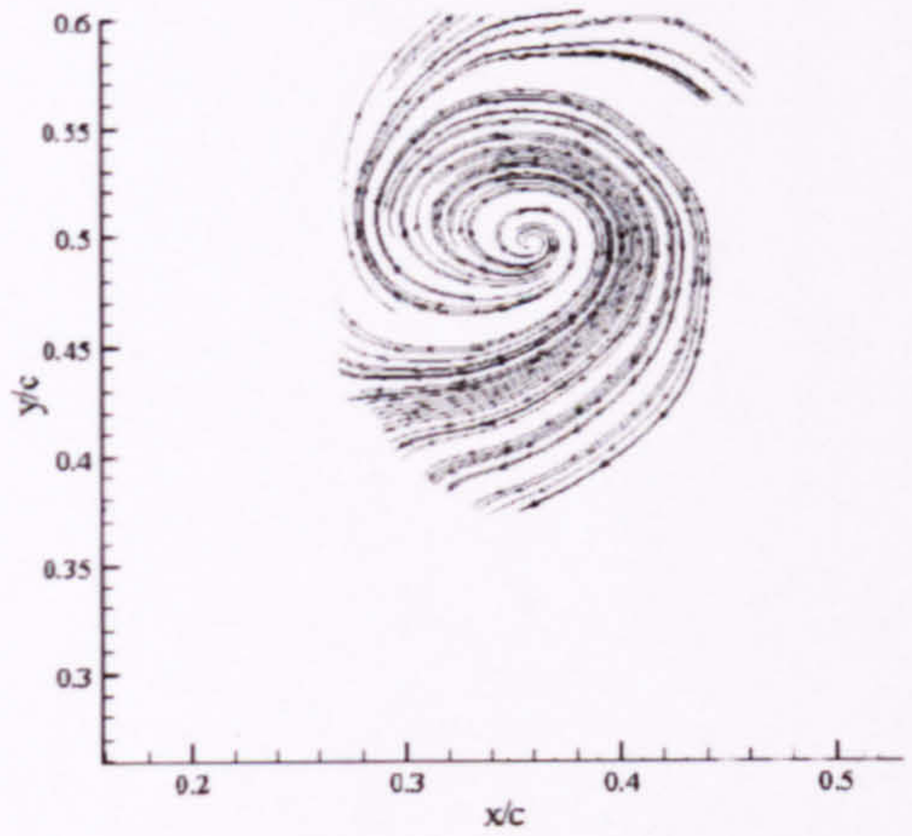

Figure 3-15 The post-interaction vortex core streamlines at 0.35 x/c indicates that a significant radial outflow from the core into the surrounding fluid exists post-interaction. Lightsheet aligned at 0.02 z/c from the blade surface at the quarterchord.

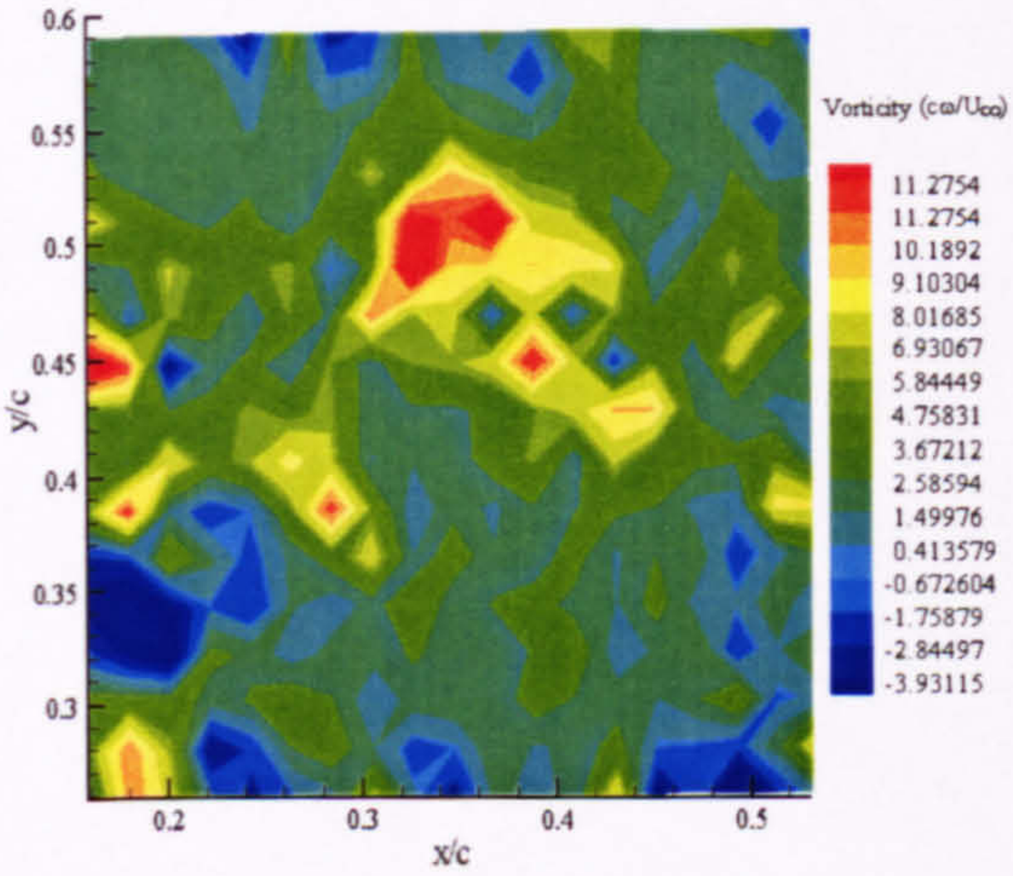

Figure 3-16 The post-interaction peak non-dimensional vorticity at 0.35x/c of 11.27 $\frac{U_\infty}{c\omega}$ reveals a significant decrease, possibly attributable to the redistribution of mass and the core expansion. Lightsheet aligned at 0.02 z/c from the blade surface at the quarterchord.

The divergence patterns indicate that the axial flow appears to decelerate towards the surface of the blade (as would be anticipated, as the vortex core axial flow is blocked by the blade surface), leading to the observed transfer of mass from the core in the radial sense (as also observed by Green et al., 2000), although this is much more clearly demonstrated in the out-of-plane velocity component [Figure 3-17], which indicates a substantial reduction in the peak through-flow velocity.

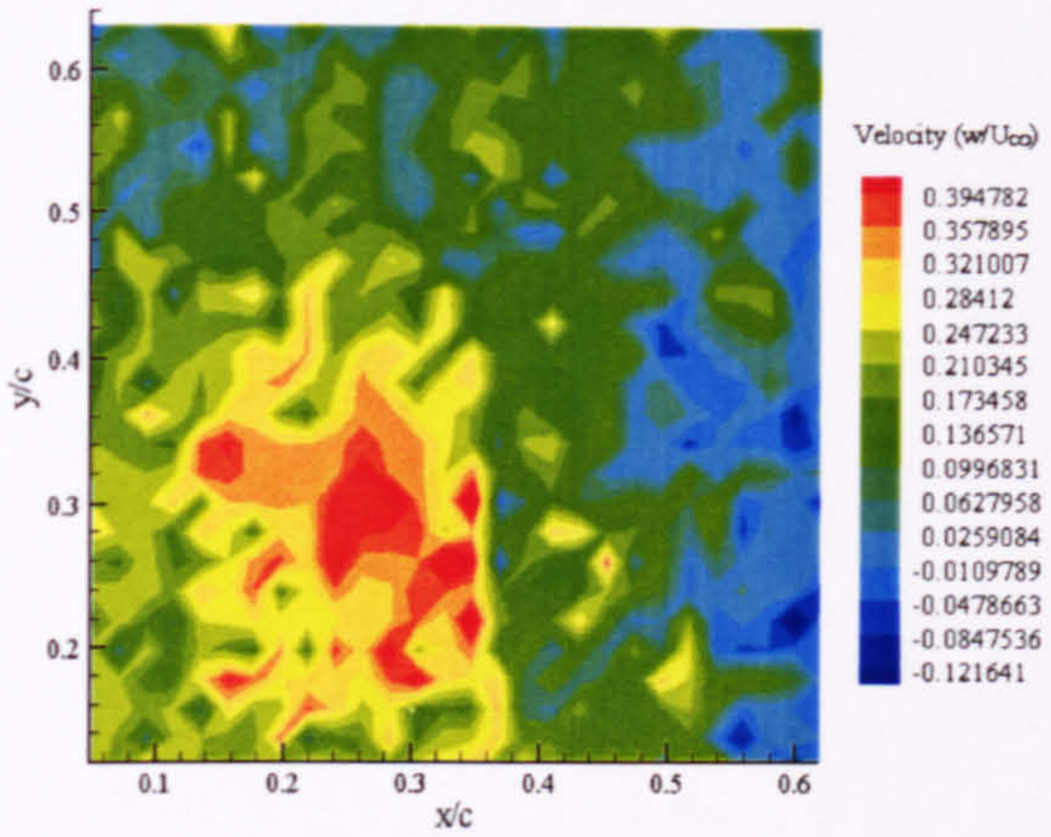

Figure 3-17 Contours of the out-of-plane velocity at 0.3x/c, with a maximum velocity of $0.395U_\infty$ measured. The vortex core centre is located at 0.275, 0.32) as indicated by the projection of the velocity into the x-y plane. Lightsheet aligned at 0.02 z/c from the blade surface at the quarterchord.

As the core passes further across the surface of the interacting blade, the peak vorticity levels are continuing to further decrease as the core size gradually increases under the continuing presence of the significant radial outflow, which again supports the assumption of fluid redistribution in the radial sense from the blocked vortex axial flow into the surrounding flow, while the divergence contours continue to indicate the presence of the axial flow deceleration, which would be expected. This is further supported by the variation in the *dw* component, which clearly shows the radial outflow in the projection of the *u,v* components.

As the lightsheet is moved further from the blade surface, the expansion due to the axial flow blocking is no longer apparent within the vortex core, with the vortex core decreasing from an average diameter of 0.157c ± 0.015 at 0.1c from the blade centre line, to a vortex core diameter of c ± 0.01 at 0.18c from the blade centre line [Figure 3-18, 3-19].

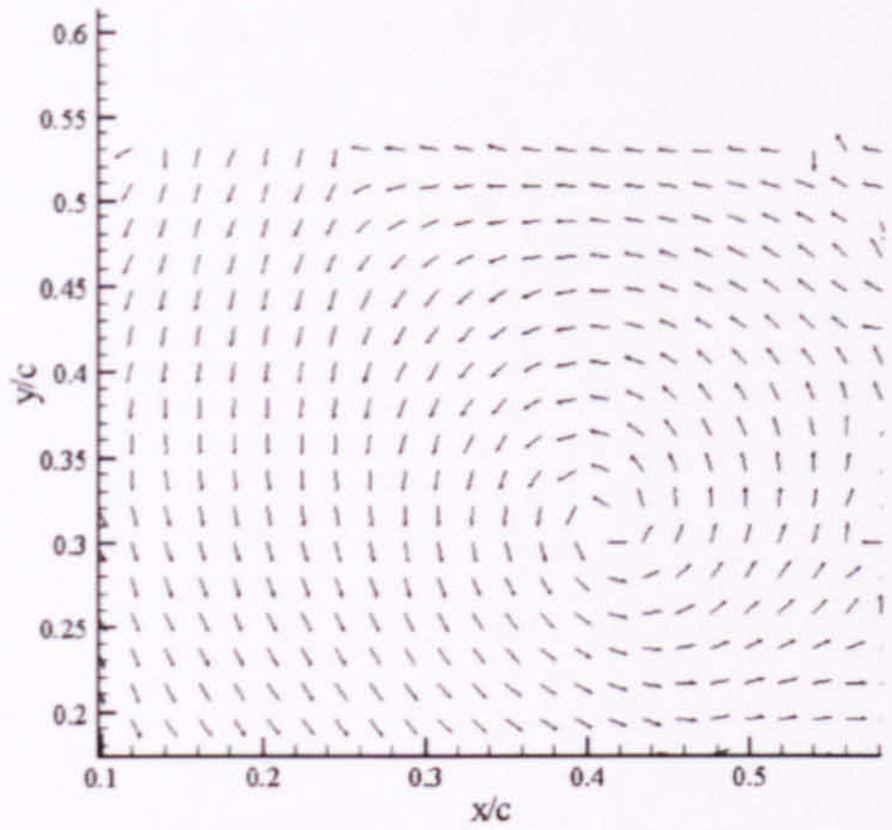

Figure 3-18 The post-interaction vortex core at 0.4x/c at a distance of 0.18c from the interacting surface reveals no significant variation from the isolated vortex appearance (mean u-component removed for clarity). Peak measured velocity peak of $0.43U_{\infty}$. Lightsheet aligned at 0.1 z/c from the blade surface at the quarterchord.

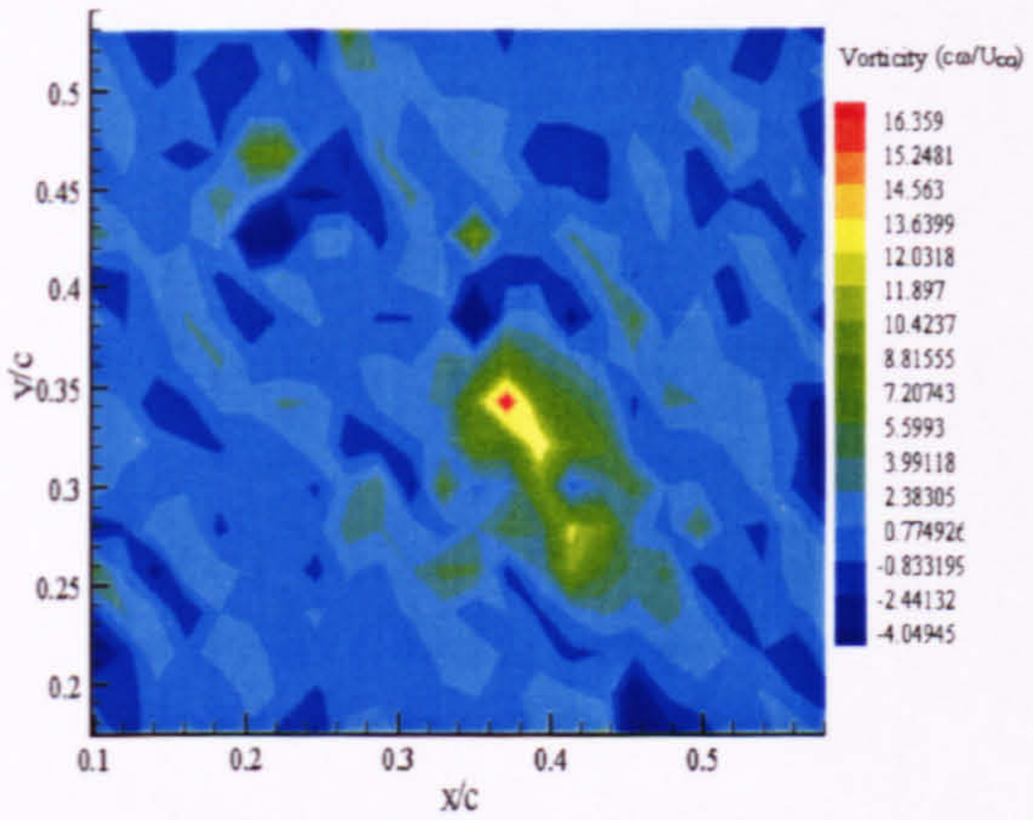

Figure 3-19 The post-interaction peak non-dimensional vorticity of $10.24\frac{U_{\infty}}{c\omega}$ at 0.4x/c at a distance of 0.18c from the interacting surface reveals no significant variation from the freestream flow condition. Lightsheet aligned at 0.1 z/c from the blade surface at the quarterchord.

There is little evidence of the effects of the interaction, specifically the notable radial outflow, which would indicate that the effects of the interaction are highly localised to the surface of the blade, with little communication of the axial flow disruption back up through the core.

As the major interactional features are highly localised to the interacting surface, the features imparted to the vortex core close to the blade surface will determine the nature of reattachment (if any) at the trailing edge of the interacting blade. As the curvature of the blade makes it difficult to align the lightsheet close to the surface, the simulation is performed with a glass plate in place of the interacting blade section. The rounded leading edge glass plate is of sufficient length (2.16c) to allow the development of a suitably thick boundary layer. The lightsheet was then aligned parallel to the surface of the glass, 0.013c from the surface of the glass. The experimental arrangement only allowed for individual measurements to be made of the upper and lower surface, but measurements were made at comparative positions along the surface of the glass plate.

As the vortex passes close to the surface of the blade on the lower surface, the redistribution of the vorticity in the vortex core leads to a significant enlargement of the vortex core. It is no longer as well organized as the study of the interaction with the blade revealed, with the peak vorticity levels significantly reduced [Figure 3-20, 3-21].

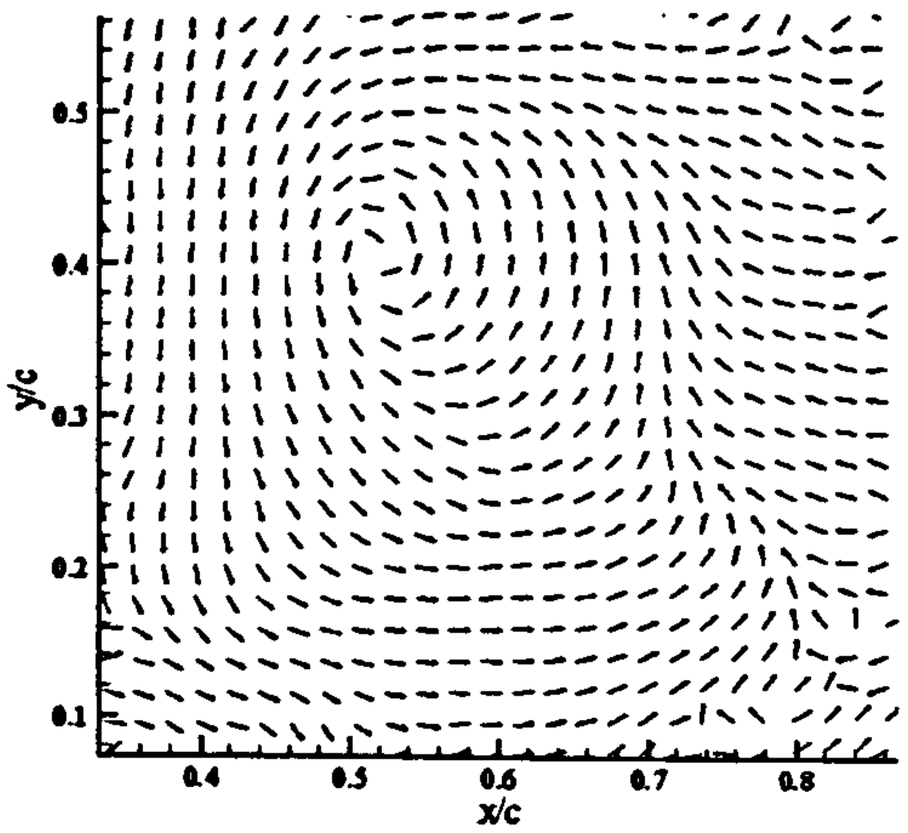

Figure 3-20 The post-interaction vortex core at 0.5x/c at a distance of 0.013 z/c from the interacting surface reveals a significant outflow from the vortex core (mean u-component removed for clarity). Peak velocity of $0.41U_{\infty}$.

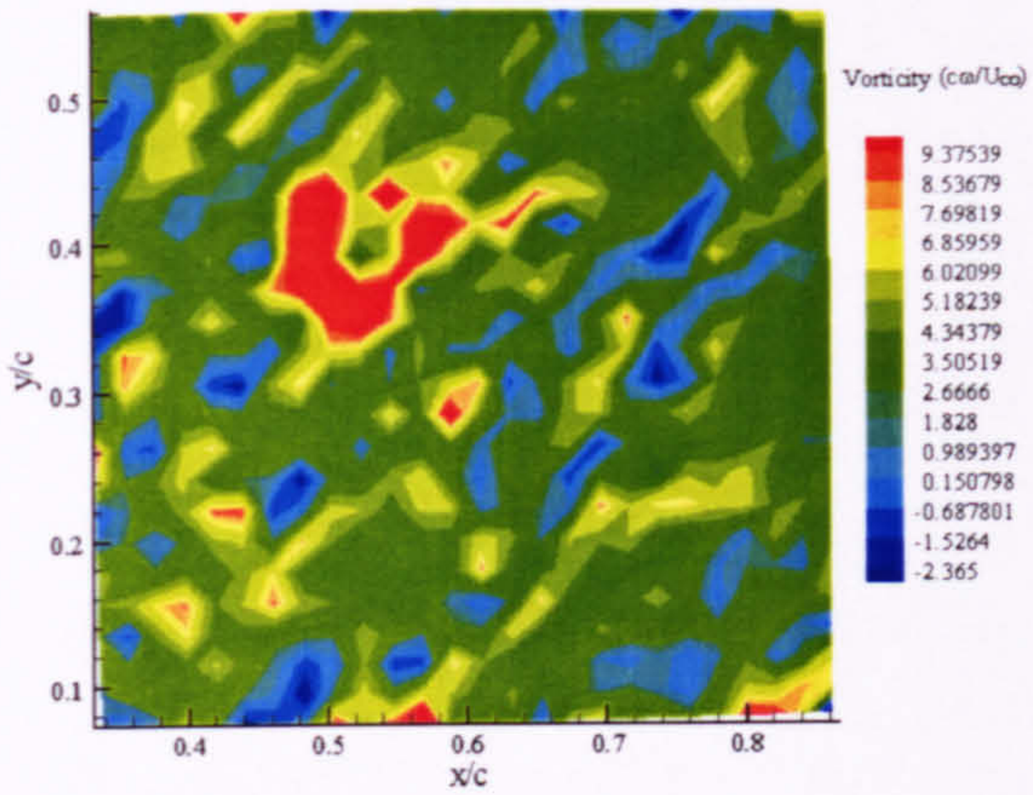

Figure 3-21 The post-interaction peak non-dimensional vorticity of 9.38 $\frac{U_\infty}{c\omega}$ at 0.5x/c at a distance of 0.013 z/c from the interacting surface reveals a substantial reduction in peak vorticity levels.

The divergence patterns close to the boundary layer are not as clear as those obtained further from the surface of the interacting blade, with the divergence level measurements within the limits measured for noise in the flow. As would be expected, the enlargement of the vortex core is still observed, with the core expanding to an average value of 0.16c. The peak vorticity and velocity levels are noticeably lower than the comparative values obtained at 0.1c from the blade centre line, with a substantial decrease in the average circulation, the average circulation value now close to $0.15\frac{U_\infty c}{\Gamma} \pm 0.02$.

As the vortex passes further across the surface, the vortex core continues to undergo a deformation promoted by the redistribution of mass into the surrounding flow, finally reaching a point at which the local axial flow component appears to have been disrupted to the point which it is impossible to distinguish a recognisable vortical structure within the flow.

Previous work (Cohn & Koochesfahani, 1993) on the effects on a vortex which ends in a boundary layer and moves along the boundary has shown rapid entrainment of boundary

layer fluid into the vortex core which promotes a suction velocity within the boundary layer. The obtained PIV data have shown no evidence of this suction velocity within the core, or any movement of fluid away from the interacting surface through the vortex core, as this suction velocity is thought to do, although any such flow would be difficult to isolate in a PIV study.

3.3.2 Structure of the Post-Interaction Vortex Core on the Interacting Blade Upper Surface

The interaction on the upper surface proceeds in a very different manner to the equivalent lower surface interaction due to the nature of the axial flow component. As the vortex passes onto the surface of the blade, the vortex core axial flow is 'cut', but the sense of axial flow is such that it is directed away from the interacting blade surface. The first striking dissimilarity between the upper and lower surface interactions is the lack of the radial outflow from the vortex core, with an apparent reduction in diameter (the core has an average diameter of 0.09c ± 0.003 at 0.1c from the blade centre line) [Figure 3-22, Figure 3-23, Figure 3-24].

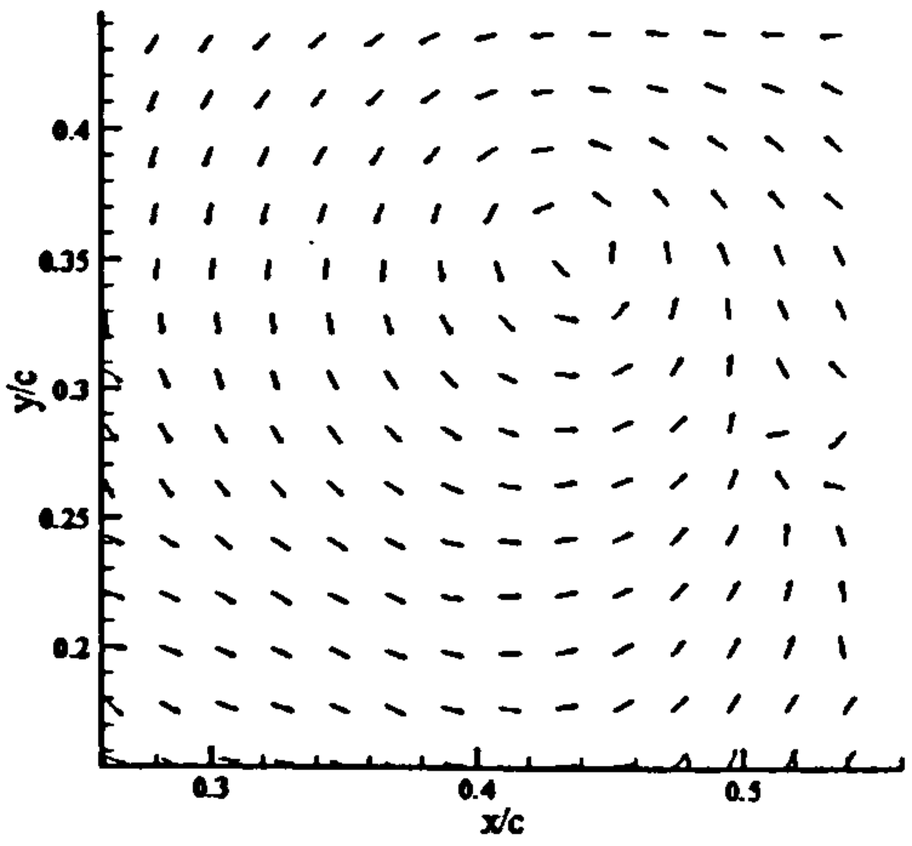

Figure 3-22 The post-interaction vortex core at 0.45 x/c reveals a minor variation from the freestream state in the radial and tangential components in the form of a mild radial inflow (mean u-component removed for clarity). Peak velocity of $0.53U_\infty$. Lightsheet aligned at 0.02 z/c from the blade surface at the quarterchord.

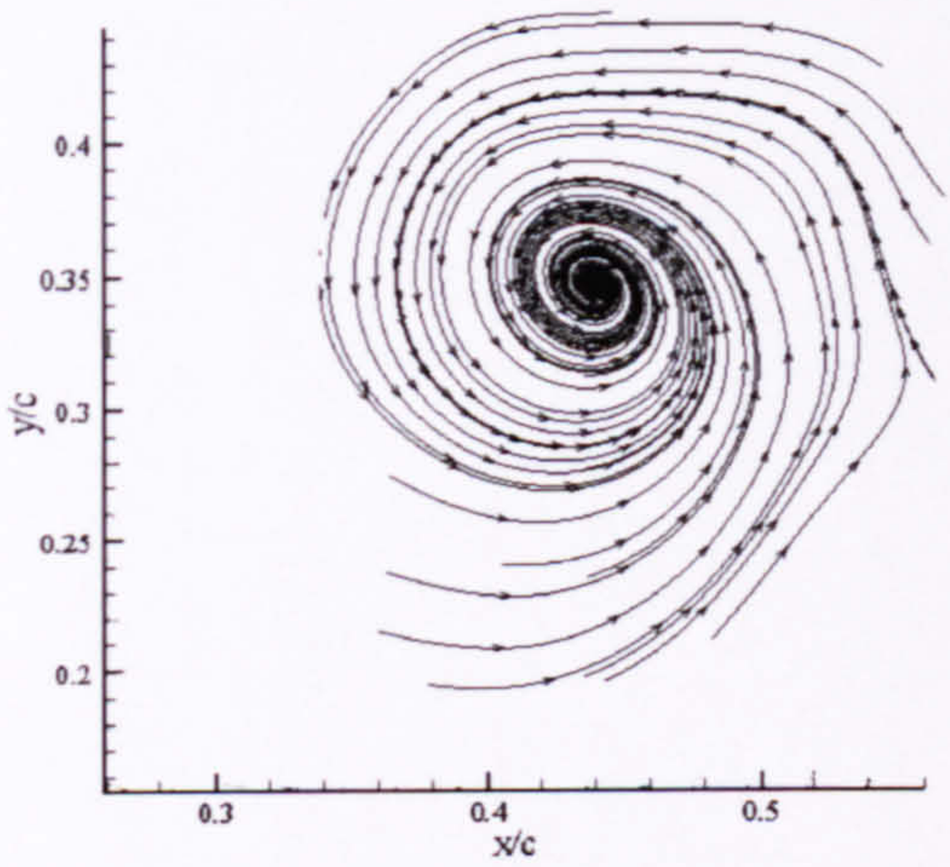

Figure 3-23 The post-interaction vortex core at 0.45 x/c has a mild radial inflow, which is more clearly shown in the streamlines above. Lightsheet aligned at 0.02 z/c from the blade surface at the quarterchord.

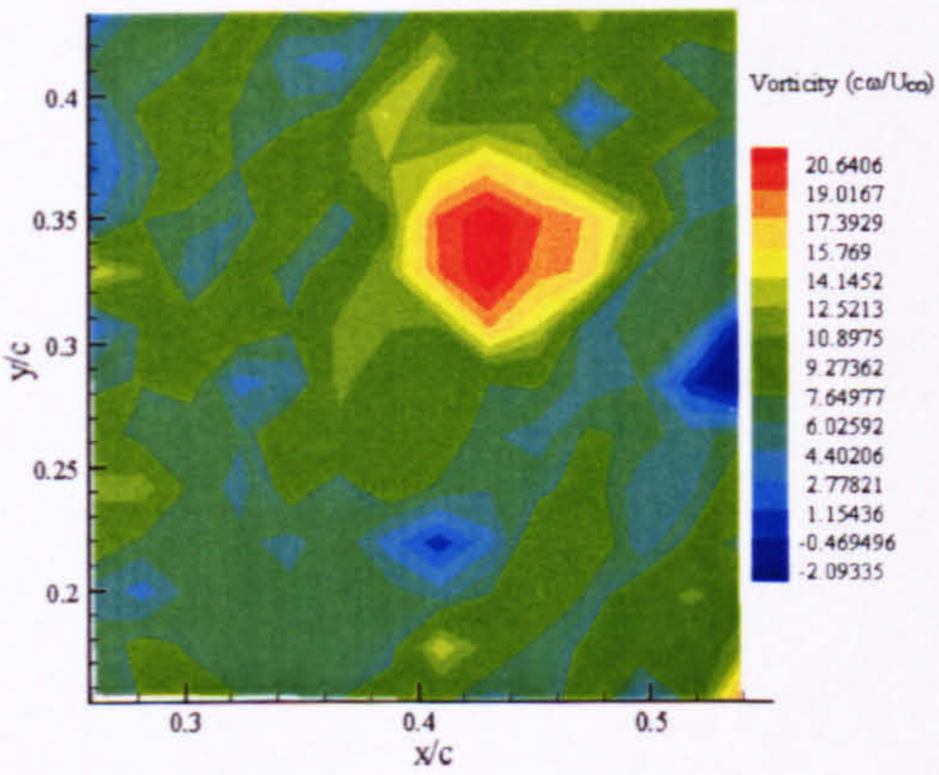

Figure 3-24 The post-interaction peak non-dimensional vorticity at 0.45 x/c of 20.64 $\frac{U_\infty}{c\omega}$ reveals little variation from the freestream flow condition. Lightsheet aligned at 0.02 z/c from the blade surface at the quarterchord.

This reduction in core diameter is accompanied by a radial inflow into the core, a requirement for axial flow re-establishment further from the blade surface. Consideration of the mass flow through the core, however, reveals the most interesting feature associated with this radial inflow; as the vortex core passes over the surface of the blade, there are areas of both positive and negative divergence existing through the core,

indicating the presence of an inflow into the core and a corresponding transfer of mass out of the vortex core into the surrounding flow [Figure 3-25].

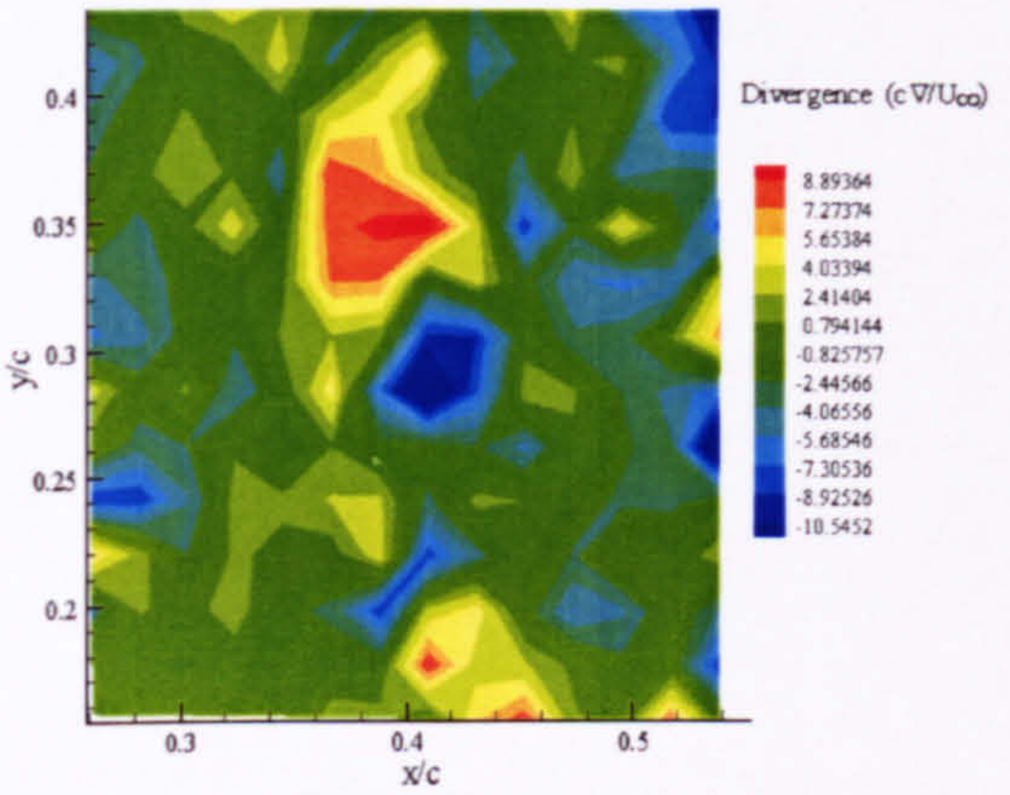

Figure 3-25 The post-interaction peak non-dimensional divergence at 0.45 x/c indicates a variation from the isolated vortex core due to the axial flow acceleration promoted by the blocking of the axial flow with increasing x/c. Lightsheet aligned at 0.02 z/c from the blade surface at the quarterchord.

This is also observed in the *dw* component [Figure 3-26], which clearly indicates the presence of a region of reversed flow over the core. This flow pattern could be as a result of the vortex core re-establishment: as the axial flow is re-established, the vortex core will require to extract mass from the surrounding fluid in order to compensate for the blocking of the core, although this will be discussed in greater detail in Chapter 5.

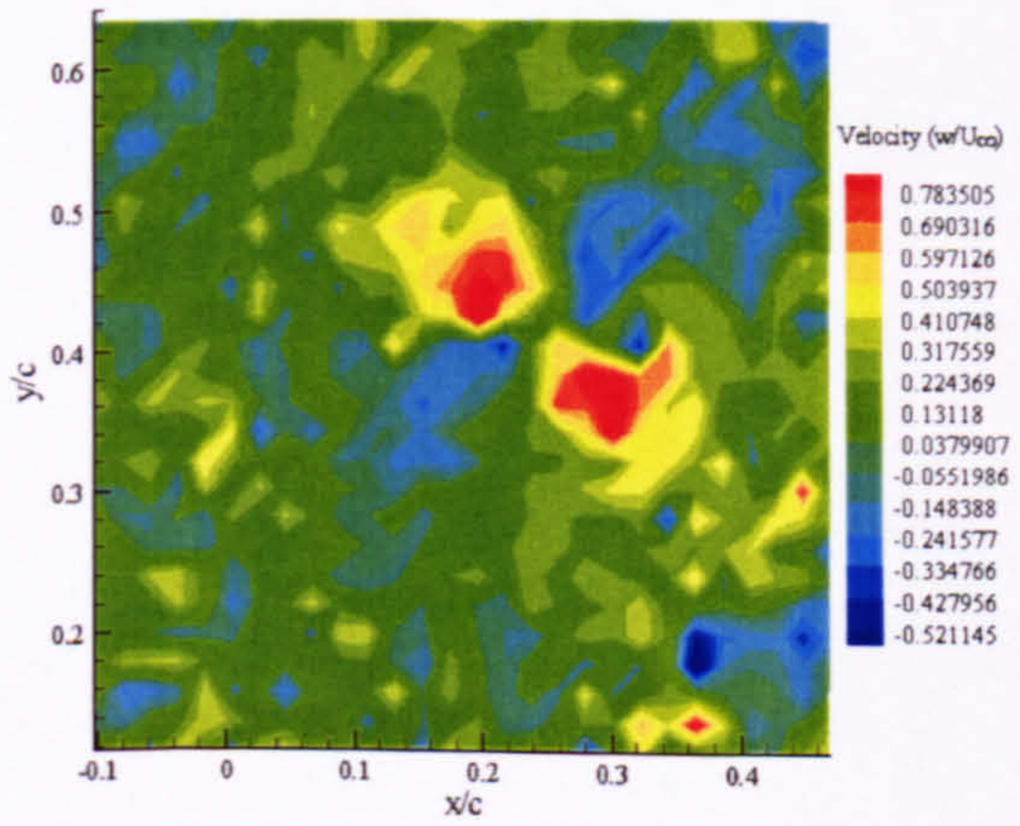

Figure 3-26 The out-of-plane velocity distribution plot for the post-interaction vortex at 0.45x/c indicates a peak velocity of $0.78U_\infty$ within the vortex core. The vortex centre is located at (0.25, 0.42) as indicated by the projection of the velocity in the xy plane. Lightsheet aligned at 0.02 z/c from the blade surface at the quarterchord.

As the core passes further across the interacting blade surface, the increased peak vorticity and radial inflow promoting a reduction in core diameter is still apparent within the velocity and vorticity plots, while the unusual out-of-plane fluid transfer into and out of the vortex core is still visible, indicative of the persistence of features associated with this interactional process.

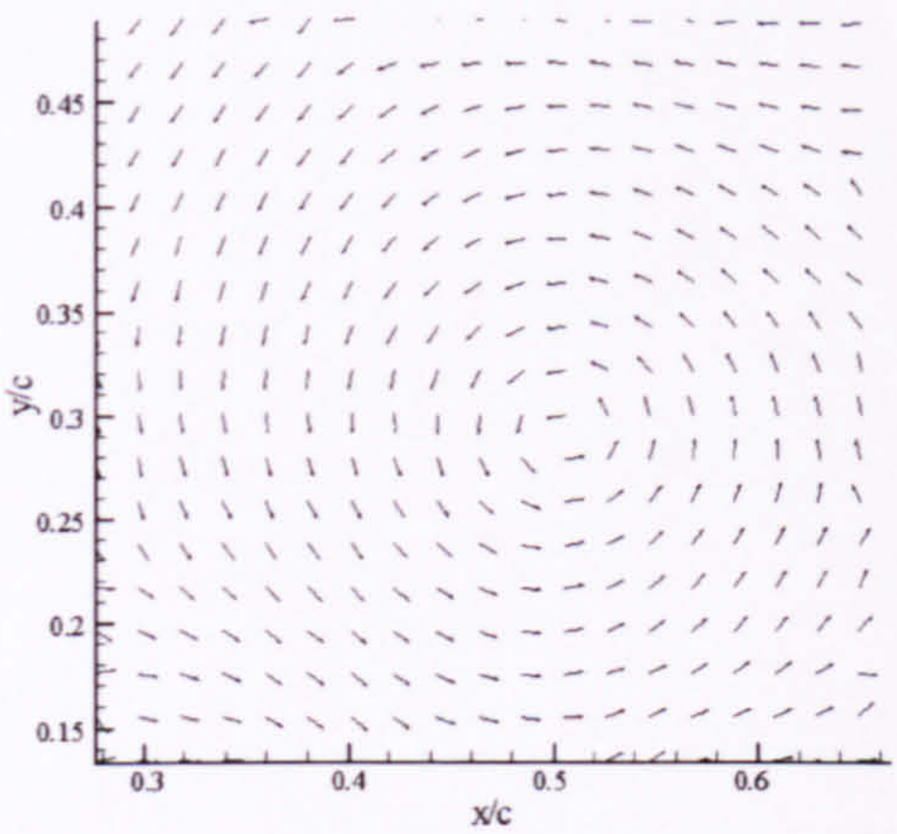

Figure 3-27 The post-interaction vortex core at 0.5x/c at a distance of 0.18c from the interacting surface reveals no significant variation from the isolated state of the radial or tangential components (mean u-component removed for clarity).
Peak velocity of $0.43U_{\infty}$. Lightsheet aligned at 0.1 z/c from the blade surface at the quarterchord.

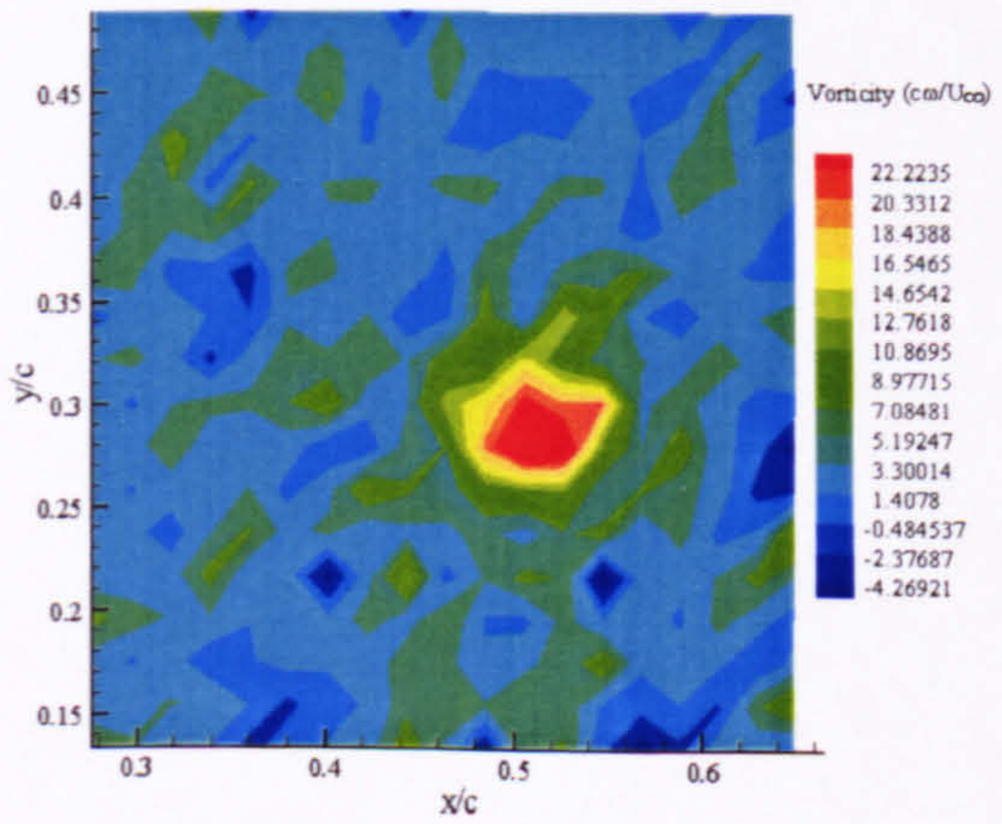

Figure 3-28 The post-interaction peak non-dimensional vorticity of $22.22\frac{U_{\infty}}{c\omega}$ at 0.5 x/c at a distance of 0.18c from the interacting surface reveals no significant variation from the freestream flow condition. Lightsheet aligned at 0.1 z/c from the blade surface at the quarterchord.

Moving further from the surface of the blade, the core has regained its pre-interaction diameter by a distance of 0.12c from the blade centreline, and by 0.2c, there are no observed effects of the interaction present in the core structure [Figure 3-27, 3-28], which supports the supposition that the deformations imparted to the core are highly localised within the structure close to the interacting blade surface, and the transport of these perturbations back through the axial flow is quickly dampened.

Close to the interacting surface (0.013c), there is no observed variation from the isolated vortex state within the vortex core, but the peak vorticity levels are observed to be significantly higher than those of the isolated vortex [Figure 3-29, 3-30].

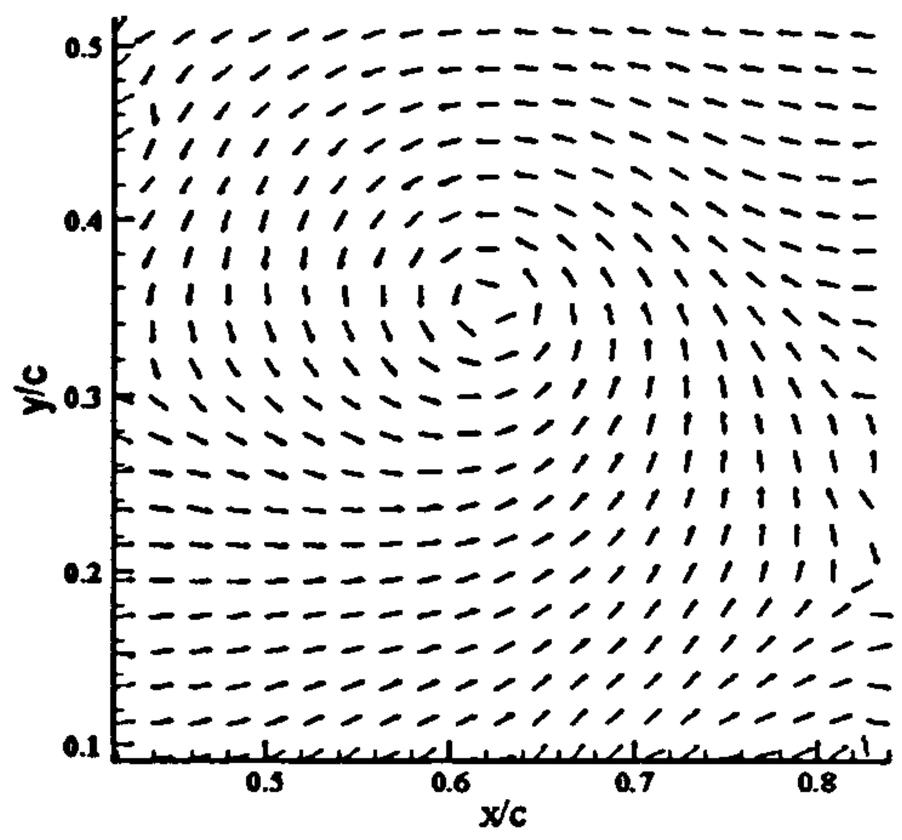

Figure 3-29 The post-interaction vortex core at 0.6x/c at a distance of 0.013 z/c from the interacting surface reveals no significant variation from the isolated vortex state to the radial and tangential components (mean u-component removed for clarity). Peak velocity of $0.5U_{\infty}$.

As the inflow of mass from the surrounding fluid enters the vortex core in order to aid in the re-establishment of the vortex core axial flow, there appears to be a decrease in diameter (as observed before). This reduction in size leads to an increase in the peak vorticity levels. The proximity of the interacting surface at this point appears to have no significant effect. The circulation values within the interacting vortex, however, remain

unaltered unlike the vortex measurements taken for the lower surface, and the maximum velocity associated with the upper surface vortex core remains comparatively high.

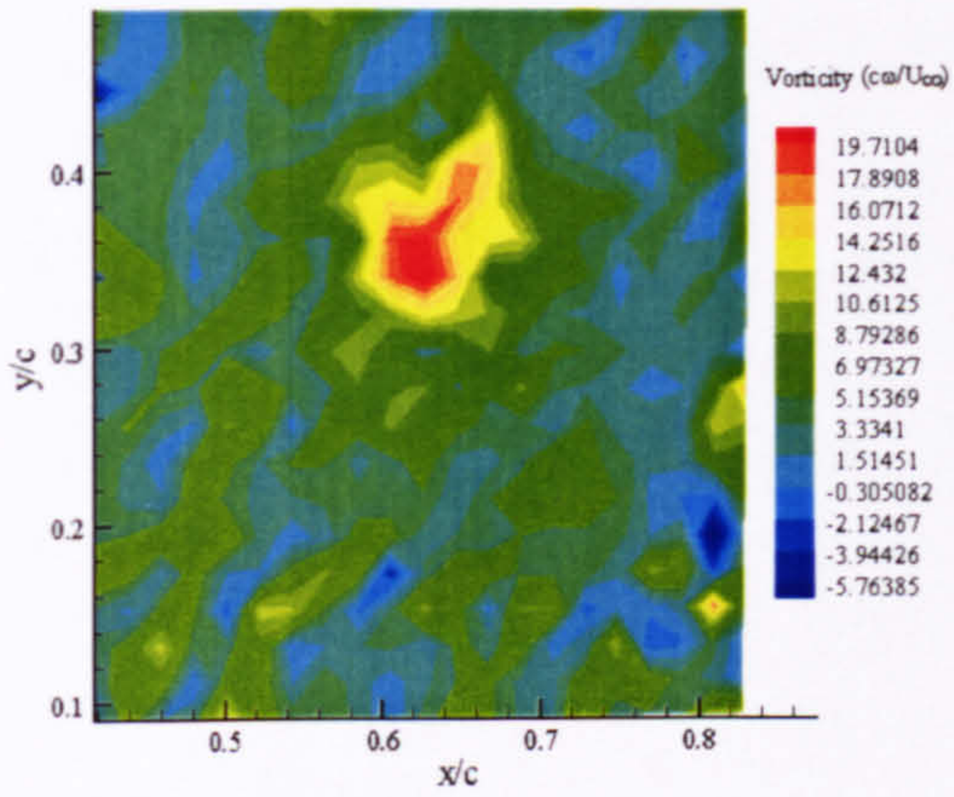

Figure 3-30 The post-interaction peak non-dimensional vorticity of 19.78 $\frac{U_\infty}{c\omega}$ at 0.6x/c at a distance of 0.013 z/c from the interacting surface reveals a substantial reduction in peak vorticity levels.

Again, any entrainment of boundary layer fluid into the vortex core is not apparent within the obtained velocity and vorticity fields. The divergence patterns again indicate the presence of the 'split' in the divergence about the core centre, which could again be attributed to the necessary flow pattern for the re-establishment of the vortex core axial flow close to the surface of the interacting blade. The proximity of the surface appears to have no detrimental effect on the manner in which this process occurs. As the vortex core progresses across the surface, the high vorticity levels are maintained, with the continued presence of a split within the vortex core, indicating that the re-establishment vortex core axial flow is an ongoing process occurring close to the interacting surface.

3.3.3 Structure of the Vortex Core in the Trailing Edge Region of the Interacting Blade

The interacting vortex is extremely persistent in nature, which may lead to the trailing vortex interacting with several rotor blades before fully dissipating. In this situation, it is

necessary to have a clear understanding of the regeneration process, if any, of the interacting vortex, as it will determine the manner in which any subsequent interactions with following blades will occur. As the dynamics of the orthogonal BVI are dominated by the impingement of the vortex core axial flow onto the surface of the interacting blade, the effect on the axial flow and its behaviour in the trailing edge region is of extreme importance as it will dictate the progression of future interactions.

In order to perform image capture of the vortex as it passes into the trailing edge region, a single lightsheet was aligned with the trailing edge, parallel to the chord of the blade. The sheet was then traversed across the working section in order to obtain comparative measurements on the upper (+0.1c) and lower surface (-0.1c) sides. Due to the nature of the measurements obtained, the measurements presented are not those of a single vortex case, but have been taken in equivalent locations downstream of the trailing edge at different times (refer to Figure 2-7(d)).

As the vortex passes over the trailing edge of the interacting blade, the structure of the vortex core directly behind the trailing edge appears to remain coherent in structure, although the peak vorticity levels are substantially reduced compared to the isolated vortex structure [Figure 3-31, 3-32].

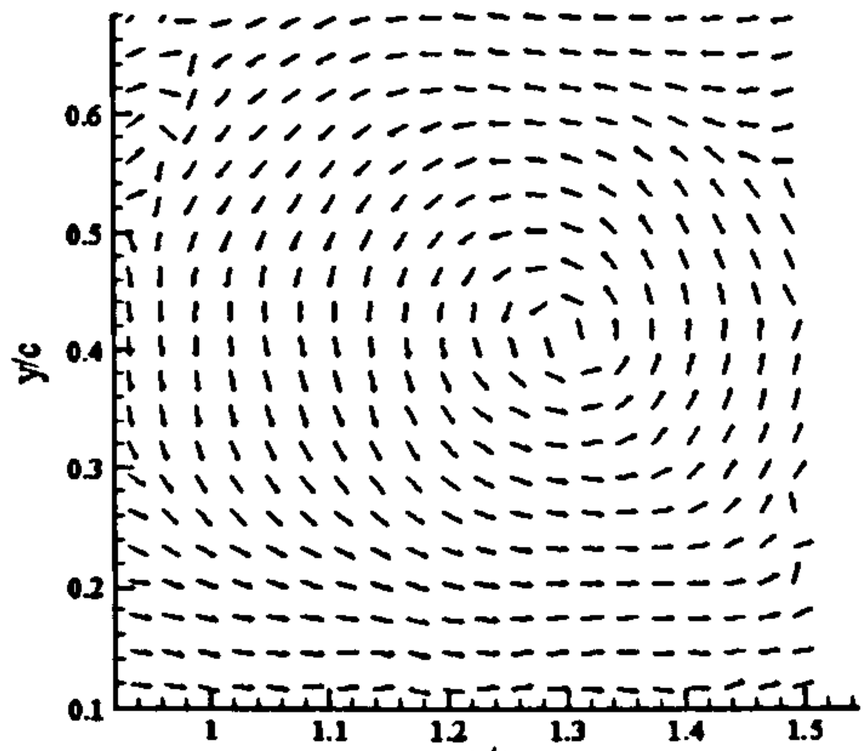

Figure 3-31 The post-interaction vortex core at 1.3x/c at a distance of 0c from the interacting surface in the trailing edge region reveals no significant variation from the isolated state to the radial and tangential components (mean u-component removed for clarity) peak velocity of $0.32U_\infty$. Lightsheet aligned at 0 z/c from the blade surface at the quarterchord.

Measured divergence levels are below the recorded flow noise levels which would indicate that in this region of the flow, there is no variation in the vortex core axial flow velocity, and no mass flow into or out of the vortex core at this point. This is again supported by the three-dimensional reconstruction of the flowfield, which indicates that the out-of-plane velocities through the core at this point are substantially reduced compared to the pre-interaction state [Figure 3-33].

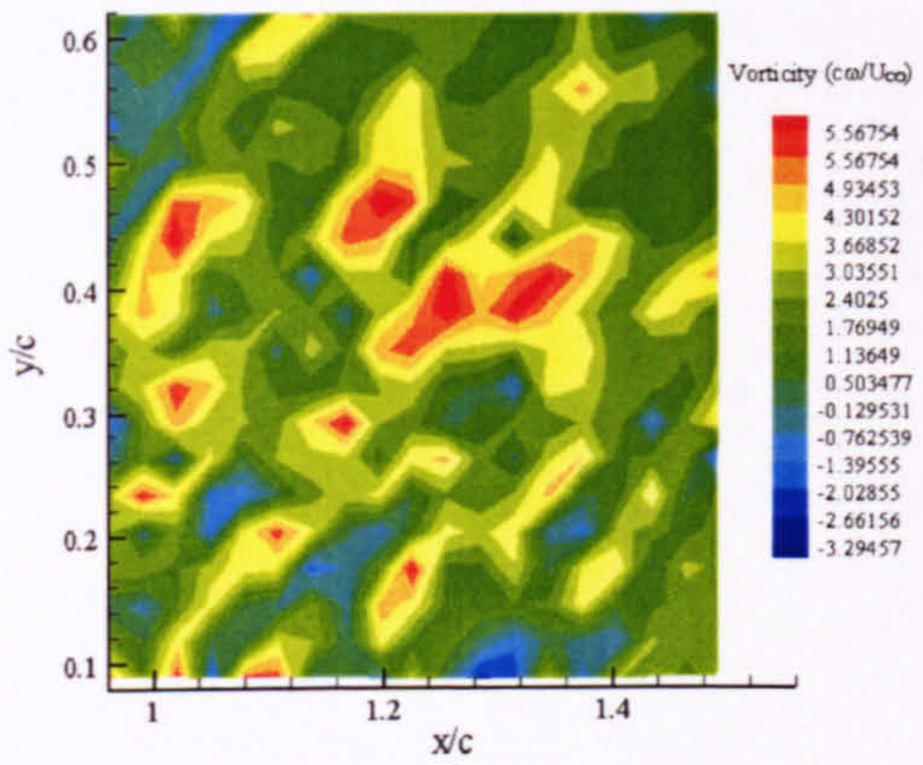

Figure 3-32 The post-interaction peak non-dimensional vorticity of 5.57 $\frac{U_\infty}{c\omega}$ at 1.3x/c at a distance of 0c from the interacting surface in the trailing edge region reveals a substantial reduction in peak vorticity levels. Lightsheet aligned at 0 z/c from the blade surface at the quarterchord.

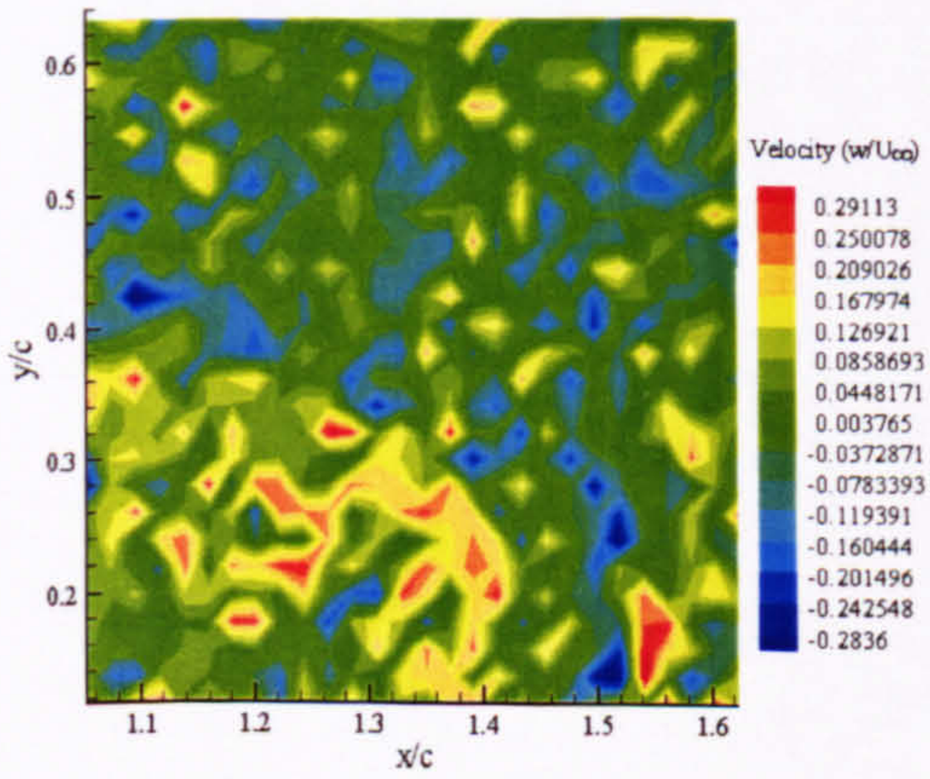

Figure 3-33 The out-of-plane velocity distribution plot for the post-interaction vortex at 1.3x/c at a distance of 0c from the interacting surface indicates a peak velocity of $0.29U_\infty$ within the vortex core. There is no clear vortex core axial flow visible in the dw component. Lightsheet aligned at 0 z/c from the blade surface at the quarterchord.

By traversing the lightsheet 0.1c to the lower surface side of the interacting blade, the persistence of the effects of the interaction can be seen. The vortex core is still greatly enlarged still at this point, similar to the appearance of the vortex core observed when the vortex was passing over the chord of the blade [Figures 3-34, 3-35].

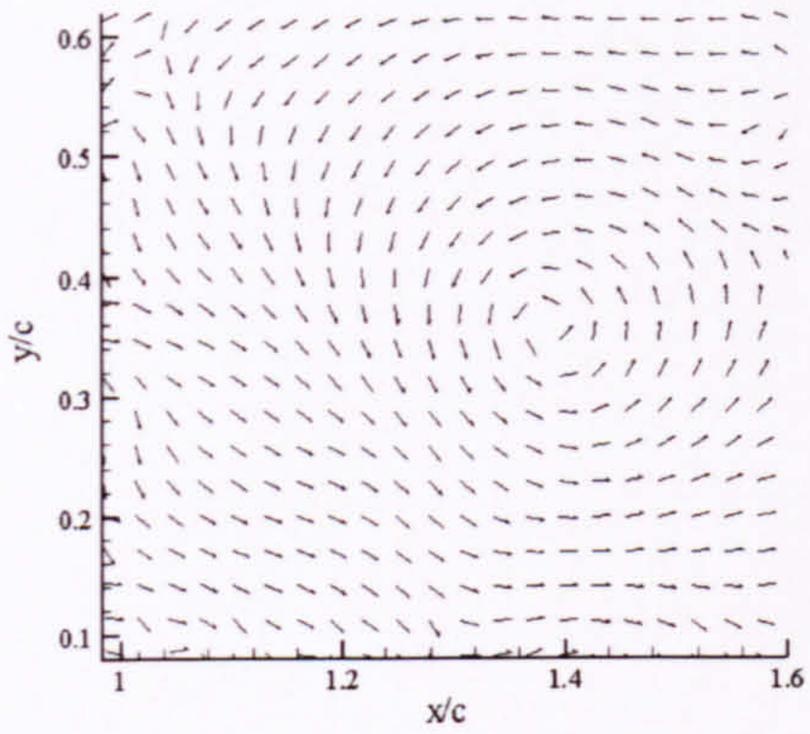

Figure 3-34 The velocity distribution plot for the post-interaction vortex at 1.3x/c at a distance of -0.1c indicates a peak velocity of $0.362U_\infty$ within the vortex core. Lightsheet aligned at 0.01 z/c from the blade surface at the quarterchord.

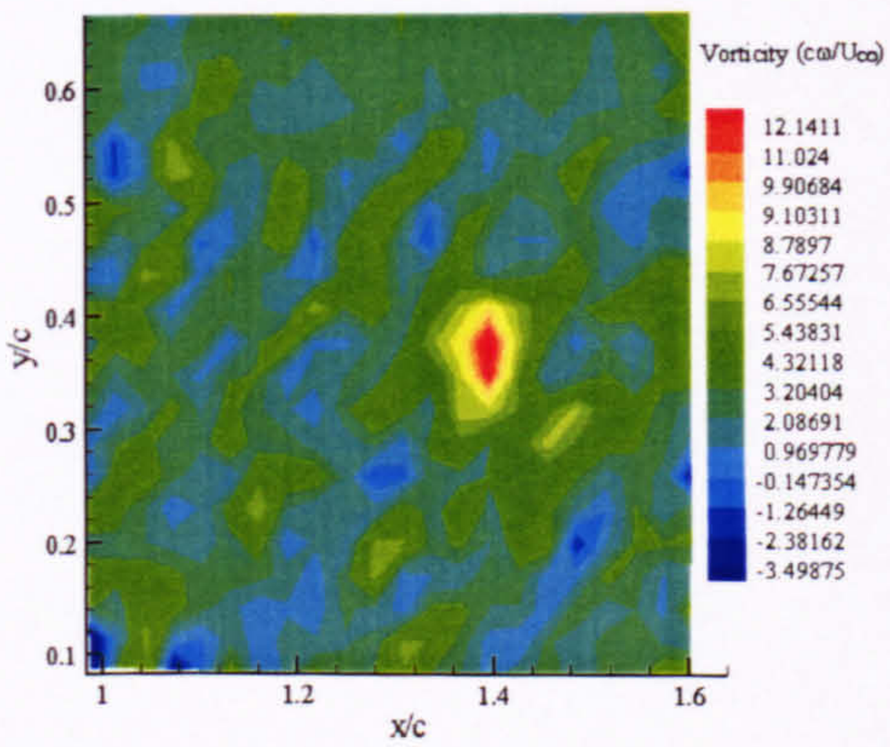

Figure 3-35 The post-interaction peak non-dimensional vorticity of $12.14\frac{U_\infty}{c\omega}$ at 1.3x/c at a distance of -0.1c from the interacting surface in the trailing edge region reveals a substantial reduction in peak vorticity levels. Lightsheet aligned at 0.01 z/c from the blade surface at the quarterchord.

The divergence indicates a large area of mass flow through the vortex core towards the blade, similar to the pattern observed when the vortex core is interacting with the blade surface.

Again, the stereoscopic view is in agreement with this, indicating the presence of a persistent radial outflow from the core, with significantly reduced axial flow velocities [Figure 3-36]. This would indicate that the effects of the interaction on the vortex core still have a significant effect even after the trailing vortex has passed well into the trailing edge region (for the given images, the vortex core is situated nearly a half chord length behind the trailing edge of the interacting blade). In addition the radial/tangential flow velocities have been substantially decreased, by approximately 20% in the case of the tangential flow components, and by substantially more in the case of the axial component.

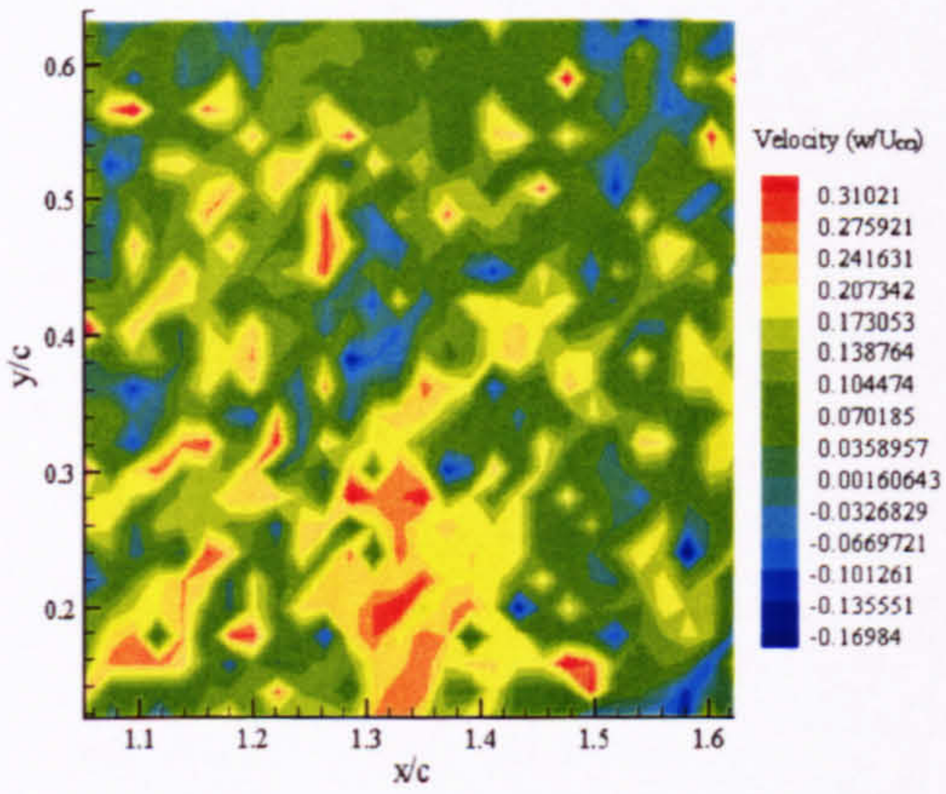

Figure 3-36 The out-of-plane velocity distribution plot for the post-interaction vortex at 1.3 x/c at a distance of -0.1c indicates a peak velocity of $0.31U_\infty$ within the vortex core. The vortex centre is located at (1.32, 0.22) as shown in the projection of the velocity vectors in the xy plane. Lightsheet aligned at 0.01 z/c from the blade surface at the quarterchord.

The lightsheet was then traversed 0.1c to the upper surface side of the trailing vortex in order to obtain a comparative set of measurements for the vortex passing over the upper surface of the interacting blade into the trailing edge region. The core structure is still easily identifiable as it passes into the trailing edge region from the upper surface, with the peak vorticity levels remaining high [Figure 3-37, 3-38].

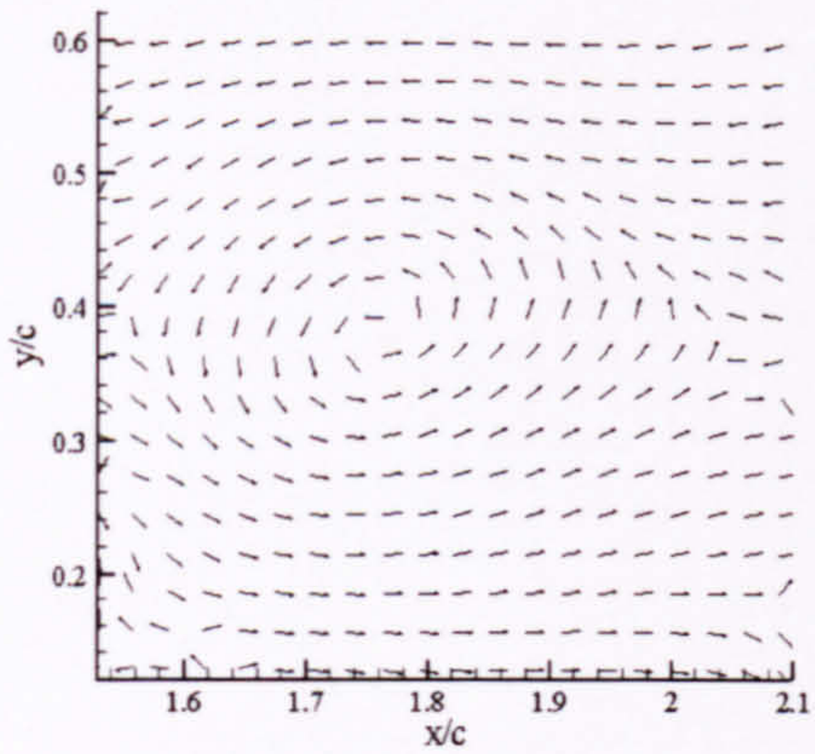

Figure 3-37 The post-interaction vortex core at 1.75x/c at a distance of +0.1c from the interacting surface in the trailing edge region reveals no significant variation from the isolated vortex core to the radial and tangential components (mean u-component removed for clarity). Peak velocity of $0.55U_{\infty}$. Lightsheet aligned at 0.01 z/c from the blade surface at the quarterchord.

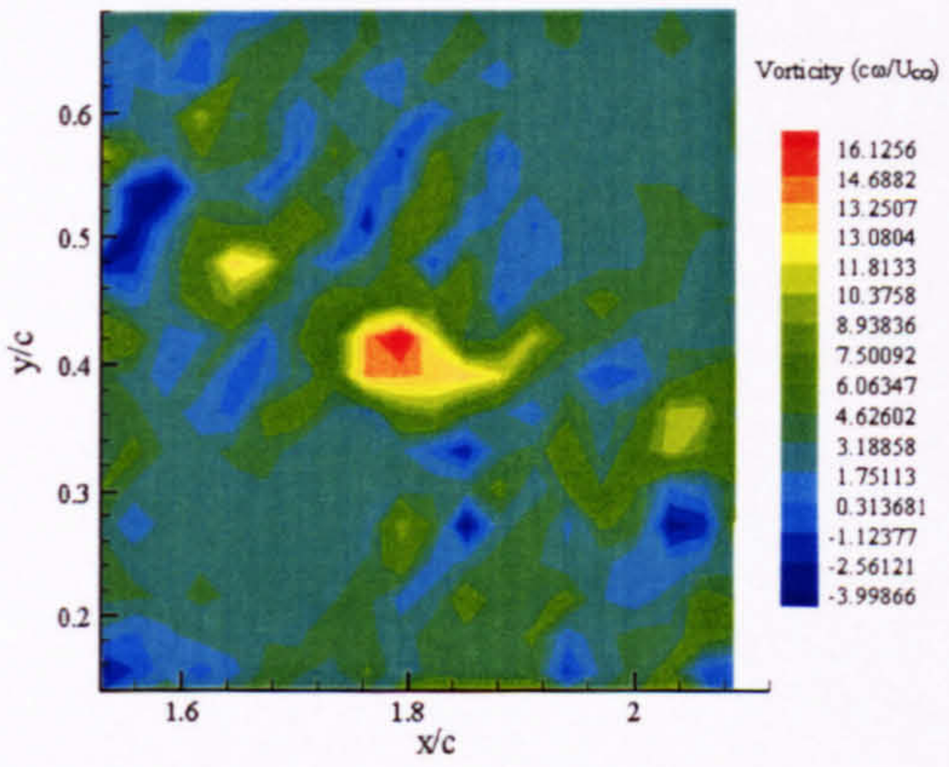

Figure 3-38 The vorticity distribution plot for the post-interaction vortex at 1.75x/c at a distance of +0.1c from the interacting surface in the trailing edge region indicates a peak vorticity of $16.13\frac{U_{\infty}}{c\omega}$ within the vortex core. Lightsheet aligned at 0.01 z/c from the blade surface at the quarterchord.

The divergence levels show a large area of positive and negative divergence over the vortex core position [Figure 3-39], which is reflected in the stereoscopic view [Figure 3-40], indicating that the behaviour of the vortex core axial flow on this side is not a mirror image of the behaviour on the lower surface side, as would be expected in a re-established core, although there is no evidence that the core is actually re-connected.

Again, the nature of the vortex core would indicate that the effects of the interaction on the vortex core persist well into the trailing edge region.

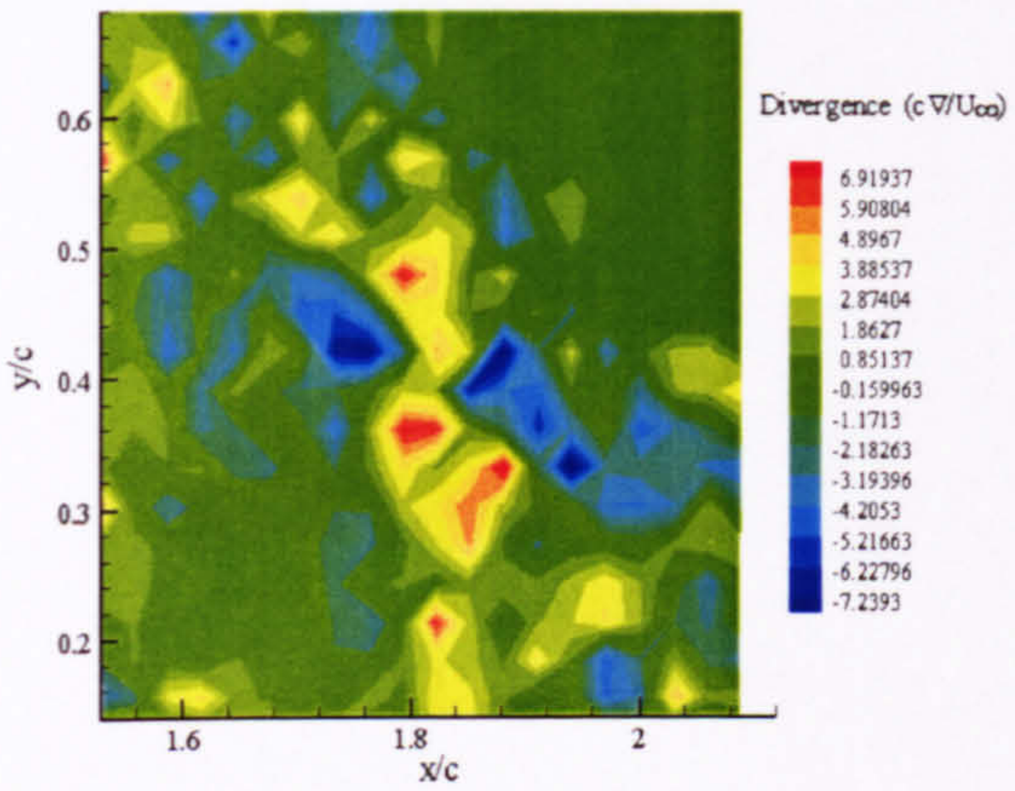

Figure 3-39 The divergence distribution plot for the post-interaction vortex at 1.75x/c at a distance of +0.1c from the interacting surface in the trailing edge region indicates a peak divergence of -7.2 $\frac{U_\infty}{c\Delta}$ within the vortex core. Lightsheet aligned at 0.01 z/c from the blade surface at the quarterchord.

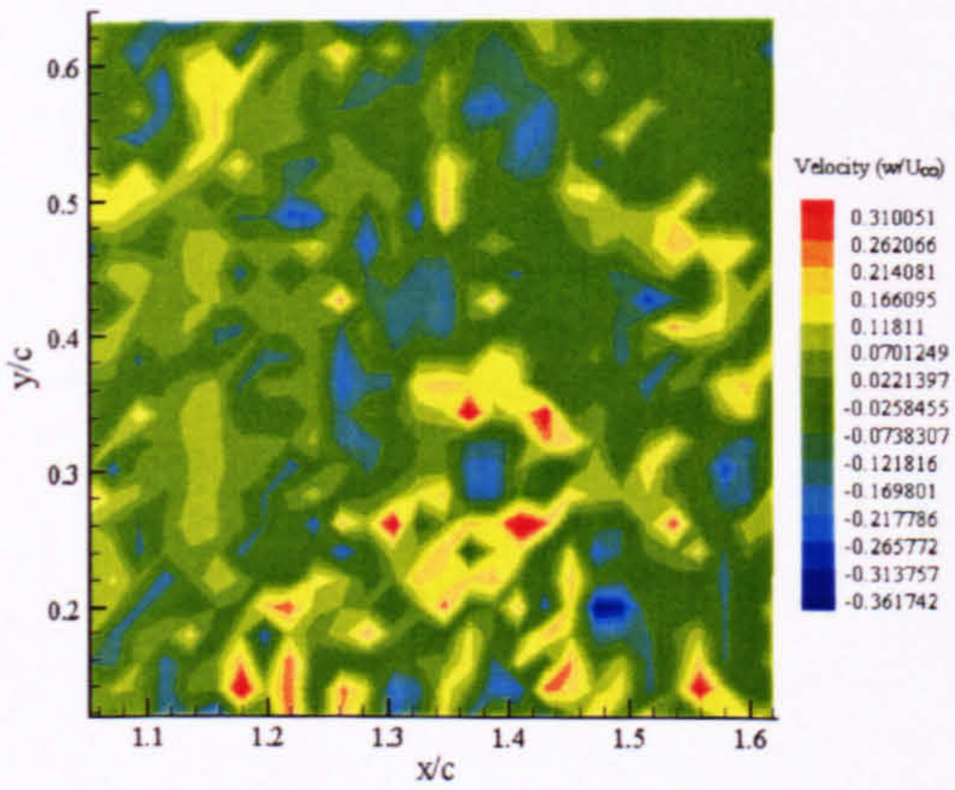

Figure 3-40 The out-of-plane velocity distribution plot for the post-interaction vortex at 1.35x/c at a distance of +0.1c indicates a peak velocity of $0.36U_\infty$ within the vortex core. Again, there are indications of regions of reversed flow measured within the dw component. The vortex centre is located at (1.36, 0.3) as indicated by the projection of obtained velocity vectors into the xy plane. Lightsheet aligned at 0.01 z/c from the blade surface at the quarterchord.

3.4 Summary of Results

As the vortex core structure passes over the leading edge of the interacting blade, a severing of the core occurs, in which the core flow is 'blocked', leading to the occurrence of two distinct regimes within the interaction. On the lower blade surface, where the vortex core axial flow impacts onto the surface of the blade, and an enlargement of the vortex core is observed near to the blade surface. This is accompanied by an observed deceleration of the vortex core axial flow as it approaches the surface of the blade. On the opposing blade surface, there is a requirement for re-establishment of the core axial flow away from the surface of the blade. Close to the surface of the blade, the core is observed to shrink, with an unusual flow pattern observed through the vortex core axial flow, with regions of accelerating and decelerating axial flow observed around the vortex core. All of these features may be tracked to the point where the vortex will be influenced by the viscous forces within the boundary layer.

In the trailing edge region of the interacting blade, the post-interaction vortex is observed to maintain an organised structure, although features that have been imparted to the core as a result of the interaction are observed to persist. Although there is no direct evidence to suggest a complete re-establishment of the vortex core axial components, a partial regeneration of the pre-interactional flow is observed, with regeneration of the vortex tangential and radial components apparent.

Chapter Five will further discuss the findings in this chapter, and by highlighting the salient features will discuss the interactional process in more detail.

Chapter 4:Visualisation of the Interaction of a Twin Vortex System with a Stationary, Rectangular Blade

Chapter One introduced the concept of rotor blade passive control, which may be utilized to overcome the effects of undesirable aerodynamic interactions. These passive control techniques function in one of two ways: either modifying the properties of the vortex core (either vortex strength or core diameter) in an attempt to reduce the severity of the interaction, or by altering the trajectory of the interacting vortex so as to induce, or increase, the miss distance. Increasing the core diameter of the interacting vortex has also been shown to lessen the effect of the interaction on the lift generation during the BVI event (Lee& Smith, 1991). As result of these studies, it is assumed that an increase in the core diameter will lead to a decrease in the BVI noise and the associated vibratory airloads.

The tip vortex diffusion introduced by many of the passive control devices is thought to destabilize the vortex core, and it is this which lessens the effect of the interaction. Numerical (Leibovich & Stewartson, 1982) and experimental (Russell et al., 1997) studies have shown that a simple relationship exists between the core radius and the stability of the vortex core.

$$|V_z| \frac{d\Omega}{dr}\left[\frac{d\Omega}{dr}\frac{d\Gamma}{dr}+\left(\frac{dV_x}{dr}\right)^2\right]<0$$

[Equation 11]

If $\frac{d|V_z(r)|}{dr}$ is small (i.e. the vortex core is diffused through the use of a passive control device), the vortex core will become unstable, due to the decrease in $\frac{d\Gamma}{dr}$, especially near

to the vortex core centre. It is this principle which is applied to many of the current passive control devices.

One of the more famous methodologies developed and successfully implemented for performance enhancement while reducing noise production, is the British Experimental Rotor Programme (BERP) tip blade (Lowson, 1992, Perry et al., 1998, Yeager et al., 1997), which alters the tip vortex produced through the modification of the blade tip section. The inclusion of a notch in the blade leading edge led to the generation of a secondary vortex at high angles of attack, whose rotation was opposite to that of the tip vortex. The combination of the inboard notch vortex and outboard tip vortex produced a wake comprising of a system of two counter-rotating vortices.

The blade has a swept back, paddle-shaped tip in order to produce the necessary vortex system, but the overall blade design was also critical to the effectiveness. Flight tests performed on rectangular blade planforms showed that the high incidence performance which is required on the retreating side was not required over the entire span of the blade, but only locally for 65-95% radius. This therefore led to the conclusion that if a thin section were to be used near the tip to avoid advancing blade tip Mach number constraints, this would impact negatively on the retreating blade stall performance in all situations, even if a thicker aerofoil section were to be used inboard.

The BERP tip uses two aerofoil sections – an RAE 9654 between 65-85% of the blade radius, which produces a high maximum coefficient of lift, necessary for good stall performance, but leads to the production of a large nose down pitching moment. This is counteracted by using the RAE 9648 section inboard of 65% radius. This section has a reflexed trailing edge and a nose up pitching moment, and as it is located inboard, the lower stall angle is not a critical factor in design.

The sweep of the BERP tip, which gives it a distinctive shape, incorporates an increased chord, which gives it a lower thickness to chord ratio, avoiding shock formation on the upper side, and consequently avoiding pitching moment changes when the blade is

advancing. In retreat, a tip vortex is initiated from the outermost part of the tip at low angles of attack, although the position of the origin of the tip vortex alters with increasing angle of attack. Further inboard, at the notch region, a secondary, counter-rotating vortex is formed, although this is only really noticeable at high angles of attack.

Testing demonstrated that a substantial reduction in noise could be achieved using this blade, up to 13dB in the negative impulse peak pressure, and up to 5dB in the low speed descent flight, compared to data available from a rectangular blade section (Lowson, 1992). As the noise production is strongly linked to the aerodynamic interactions which are undergone by the tip vortices, it is assumed that the modifications introduced through the use of the BERP blade (with introduced anhedral) led to differences in the mechanisms by which these interactions take place.

In order to replicate this flowfield, a representative 'paddle' tip blade (without anhedral) was constructed in order to produce the twin, counter-rotating vortex structures (as described in Chapter 2). In order to directly compare the results of the interaction of a twin vortex structure with that of the single vortex interaction, the rotor blade and tip section were constructed using a constant profile NACA 0015 section.

The features of a counter-rotating vortex pair have been considered in many previous studies, due to their interest for many engineering applications, especially in aerospace (Leweke & Willamson, 1998). The first three-dimensional stability analysis of a vortex pair was conducted by Crow (1970), who showed that such a pair is unstable to perturbations which are symmetric with respect to the separating plane of the vortices. This is due to the fact that each of the vortices experiences the effects of plane strain, which is induced by the other vortex. From Kelvin (1880), a sinusoidal displacement disturbance of a straight vortex filament rotates without changing shape around the vortex. In the presence of an externally produced strain field (i.e. in the presence of a second vortex), the self-induced rotation can either be (1) diminished, or (2) augmented by the azimuthal velocity component of the strain field. In the case of these two

components balancing, the radial component of the strain field leads to exponential growth of the disturbance.

With the increased tip vortex core diameter, introduced by the sweep of the blade tip, combined with the disturbances introduced as a result of the counter-rotating vortex pair, it would be anticipated that the interaction would be greatly reduced in severity (i.e. decrease pressure fluctuations over the blade surface as a result of the impact of the vortex on the blade surface).

The following study considers the structure of the flowfield produced by the blade in both steady and oscillatory environments, before examining the effect of the blade tip alteration on the progression of the OBVI.

4.1 Nearfield Investigation of the Flowfield produced by a Stationary Modified Blade Section

The wake that is produced by the rotor blade from the vortex generator is extremely complex. The modification of the blade tip section further complicates this flowfield through the introduction of a secondary 'notch' vortex, produced inboard of the outer, modified tip vortex.

In order to fully investigate the flowfield which is produced, the flow is first interrogated behind a stationary blade, so as to fully document the near field wake of the modified blade tip. There have been numerous studies conducted on the structure of the trailing tip vortex behind a rectangular blade planform (Chigier & Corsiglia, 1971), describing the vorticity distribution of the core as an indication of the relative stability of the structure in the working fluid.

The blade was mounted at the root on a ball screw assembly to allow variation in angle of incidence of the blade, with the chord of the blade parallel to the flow direction (wind

tunnel velocity 5ms^{-1}) (refer to Figure 2-8(a) for experimental arrangement). The PIV lightsheet was then introduced into the working section behind the blade, perpendicular to the blade chord line, and image capture performed using two cameras mounted downstream of the blade inside the wind tunnel, one focussed on the notch region of the blade, the other on the blade tip, both cameras configured for simultaneous image capture. The lightsheet was then traversed away from the blade trailing edge region in the y-z plane in order to track the progress of the twin vortex system as it passed away from the blade. Vorticity ($\frac{c\omega}{U_\infty}$) and strength ($\frac{\Gamma}{U_\infty c}$) have been non-dimensionalised by the blade chord length (0.1524m) and the freestream velocity, x and y locations within the interrogation plane have been non-dimensionalised with regards to the blade chord length. The reference origin is taken as being the root of the blade.

At a location 0.06c behind the blade, the tip vortex produced by the swept wing tip was clearly visible, with an average core diameter of 20mm, and vortex core strength of $0.375\frac{U_\infty c}{\Gamma}$. Over the notch region, there is no indication of a distinct vortex, although increased velocity and vorticity are present, indicating that an indistinct structure is present. Passing further downstream, the notch vortex at last becomes coherent, with indications that this vortex is of comparable strength to the accompanying tip vortex (which remains a coherent structure) [Figure 4-1, 4-2].

The counter-rotation is clearly visible within the inboard vortical structure. The main difference of note between the vortices is that the inboard vortex aspect ratio is slightly lower (the core appears to be 'compressed' in the y-direction compared to the x-direction) compared to the outboard, which is roughly symmetric in both the x and y-planes.

The counter-rotation of the two vortices remained clear up to one chord length behind the blade, and the strengths of the two vortices remained comparable [Figure 4-3, 4-4]. There is no significant deviation in the trajectory of the vortices observed, as would be

expected if there were a significant mutual velocity being induced, leading to the two vortices beginning to merge.

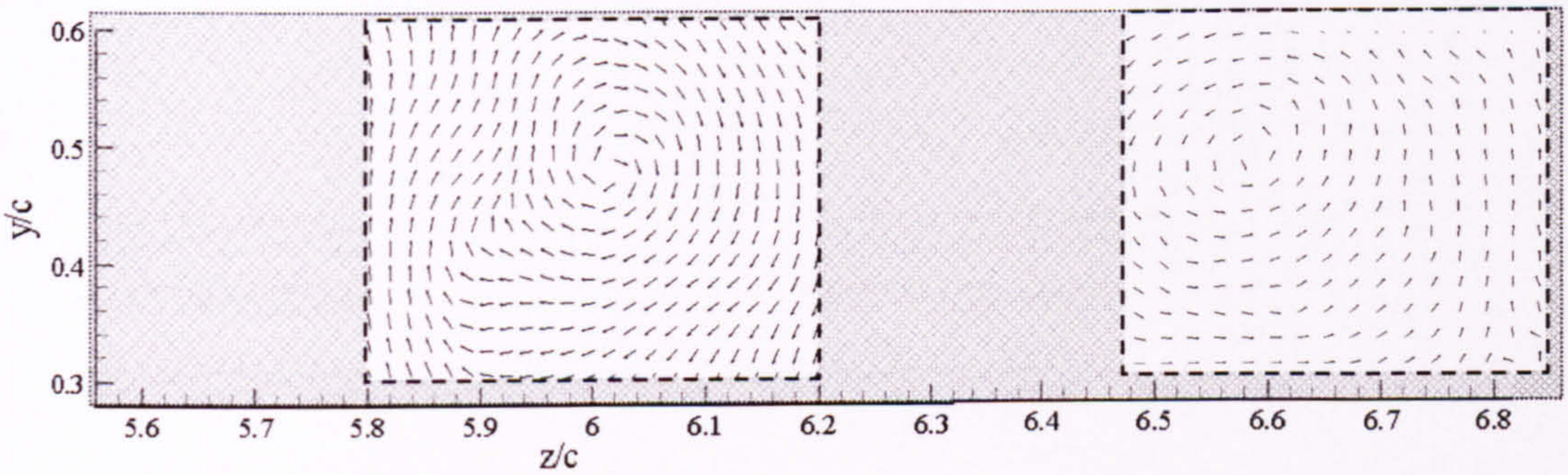

Figure 4-1 Inboard/Outboard Vortex Structure at AOA of 5° at 0.33 x/c behind the blade trailing edge. Maximum measured velocity in inboard vortex =0.906U_∞, Maximum measured velocity in outboard vortex= 1.33U_∞.

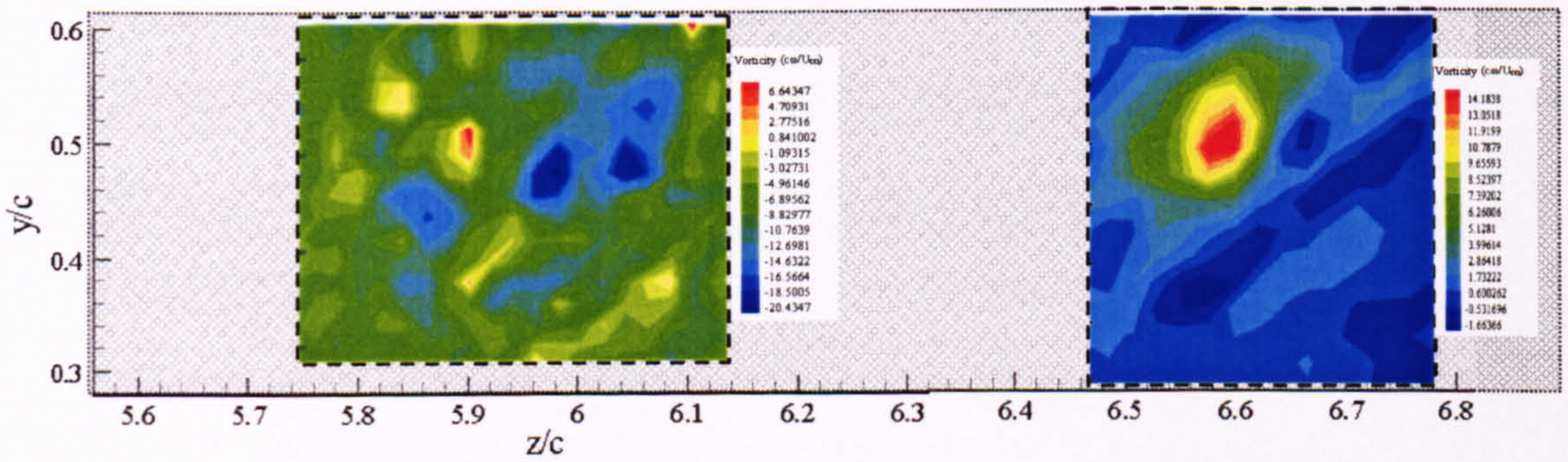

Figure 4-2 Inboard/Outboard Vortex Structure at AOA of 5°. Vorticity levels indicate an inboard maximum of $20.43\frac{U_\infty}{c\omega}$ and an outboard maximum of $14.18\frac{U_\infty}{c\omega}$ at 0.33 x/c behind the blade trailing edge.

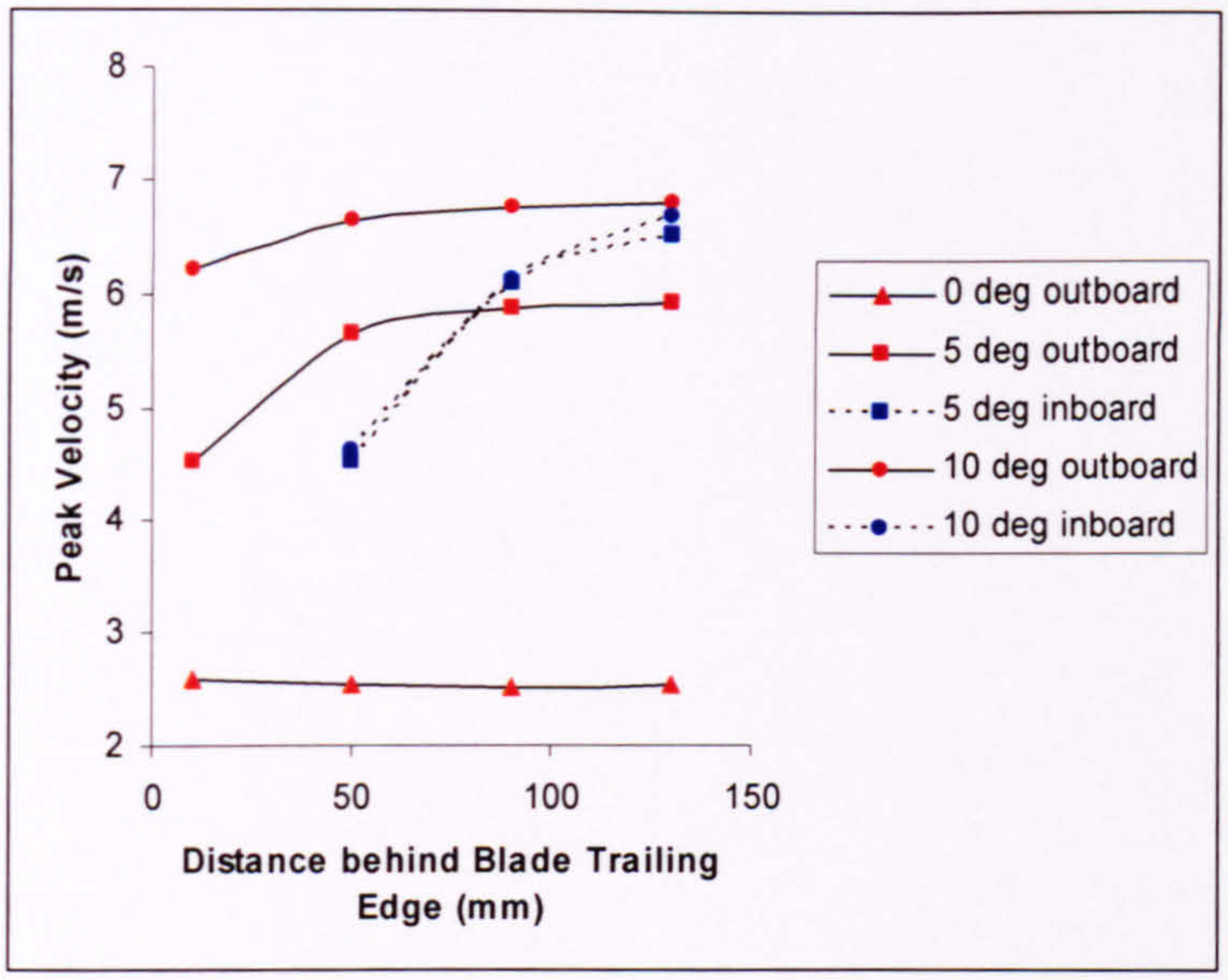

Figure 4-3 Variation in average peak vortex swirl velocity (inboard and outboard) with increasing distance behind the interacting blade. Note that no data are included for the inboard vortex at 10mm behind the blade tip as no coherent vortex was detected at this point over the notch region.

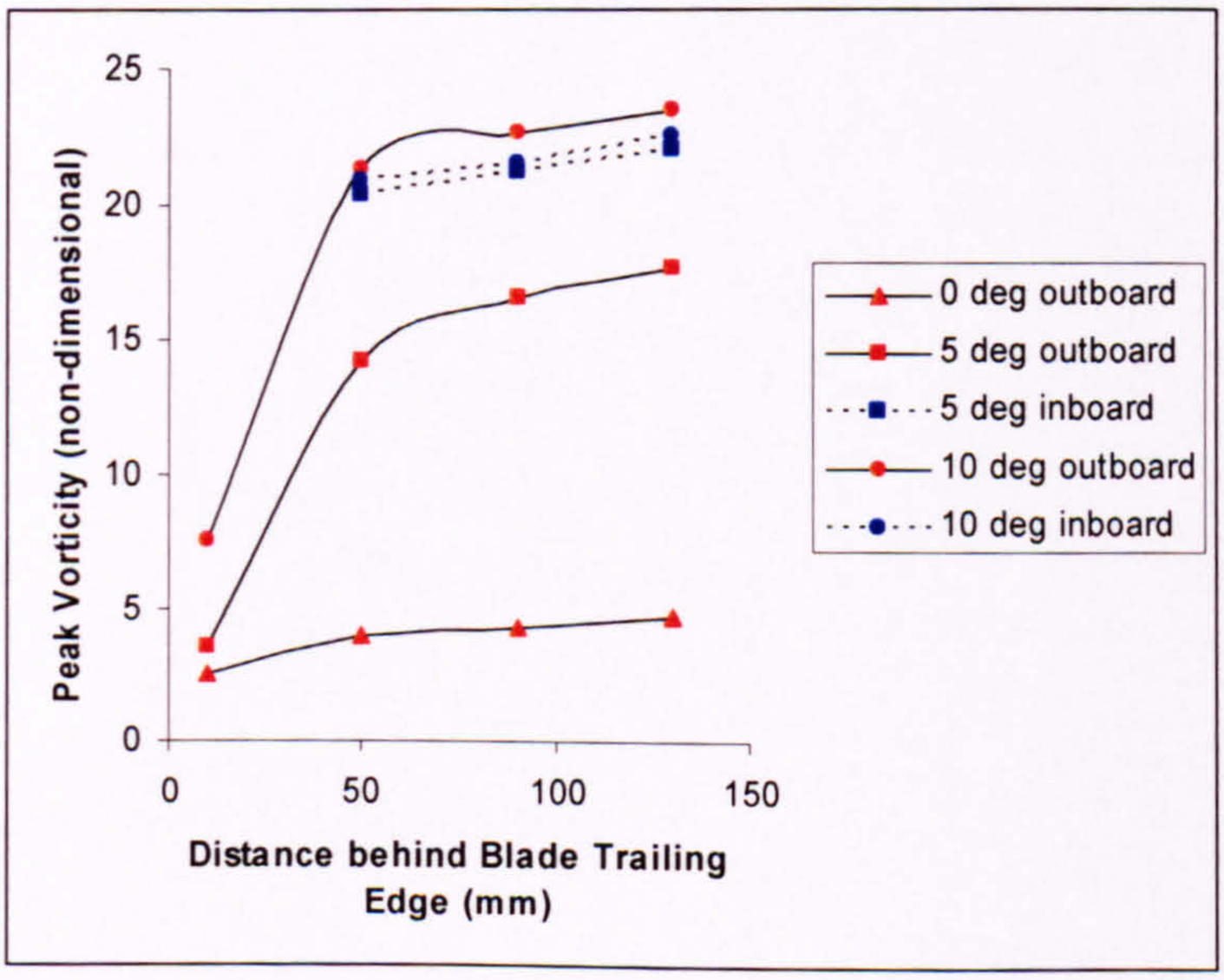

Figure 4-4 Variation in average peak vortex vorticity (inboard and outboard) with increasing distance behind the interacting blade. Note that no data are included for the inboard vortex at 10mm behind the blade tip as no coherent vortex was detected at this point over the notch region.

4.2 Nearfield Investigation of the Flowfield produced by an Oscillating Modified Blade Section

The evolution of the unsteady, three dimensional tip vortex behind the modified blade planform was examined while it was oscillating sinusoidally about its quarter-chord axis. The characterization of the near wake of the blade is important in order to be able to describe the flow which is experienced by the advancing side of the following blade (either in the main or tail rotor assembly).

Experimental visualization of the trailing tip vortex produced by a rectangular blade planform of NACA 0015 section has provided measurements of the velocity and vorticity measurements of the evolving tip vortex (Ramaprian & Zheng, 1998). This indicated that a substantial part of the shear layer roll up and gathering of axial vorticity in the wing tip occurs 1-2 chord lengths downstream of the trailing edge, and that the tip vortex becomes approximately axisymmetric beyond this distance. The mean trajectory of the interacting vortex was also equivalent to the stationary wing held at the equivalent mean incidence. The main point of note would be that although the vortex varies in a complicated manner in both time and space, the structure of the vortex core itself is retained throughout the evolution of the structure (Ramaprian & Zheng, 1998).

The current study first replicated the experiments carried out by Ramaprian & Zheng (1998) by mounting the rectangular rotor blade (NACA 0015, chord=0.1524m) within the wing tunnel working section, oscillated in pitch about its quarter-chord position. The oscillatory conditions are given by:

$$\alpha = \overline{\alpha} + \Delta\alpha \sin 2\pi f t$$

[Equation 12]

where $\overline{\alpha}$ =10deg, $\Lambda\alpha$=5deg, and f=1Hz. The mean Reynolds number is given as 9×10^{-4}. Images were then acquired at three locations downstream (x_1=0.06c, x_2=0.33c, x_3=0.6c), first behind the rectangular blade section which was previously used for the experiments

in Chapter 3, and then behind the modified blade tip section. The two sets of results were then compared. In order to directly compare the effect of the inclusion of the notch on the blade tip, the outboard vortex structure for each of the two blade configurations was examined, again using the particle image velocimetry technique.

As before, the blade was mounted at the root on a ball screw assembly to allow variation in angle of incidence of the blade, with the chord of the blade perpendicular to the flow direction. The PIV lightsheet was introduced into the working section behind the blade, perpendicular to the blade chord line (refer to Figure 2-7(a)), and image capture performed using two cameras mounted downstream of the blade inside the wind tunnel, one focussed on the notch region of the blade, the other on the blade tip, both cameras configured for simultaneous image capture. The lightsheet was then traversed away from the blade trailing edge region in order to track the progress of the twin vortex system as it passed away from the blade. Image capture was synchronised with the oscillation of the blade. Vorticity ($\frac{c\omega}{U_\infty}$) and strength ($\frac{\Gamma}{U_\infty c}$) have been non-dimensionalised by the blade chord length (0.1524m) and the freestream velocity, x and y locations within the interrogation plane have been non-dimensionalised with regards to the blade chord length. The reference origin is again taken as being the root of the blade.

Comparison of the profile of the tip vortex structures at the three downstream locations for both the blade tip with the notch and the standard square planform blade used in the study in Chapter 3 indicates that there is no significant deviation in the average peak velocities recorded in the phases of the oscillation cycle [Figure 4-5], with this persisting well downstream of the blade trailing edge. Similarly, there is little deviation in the maximum recorded vorticity [Figure 4-6], indicating that the inclusion of the notch has no significant effect on the blade tip maximum velocities or vorticity distribution.

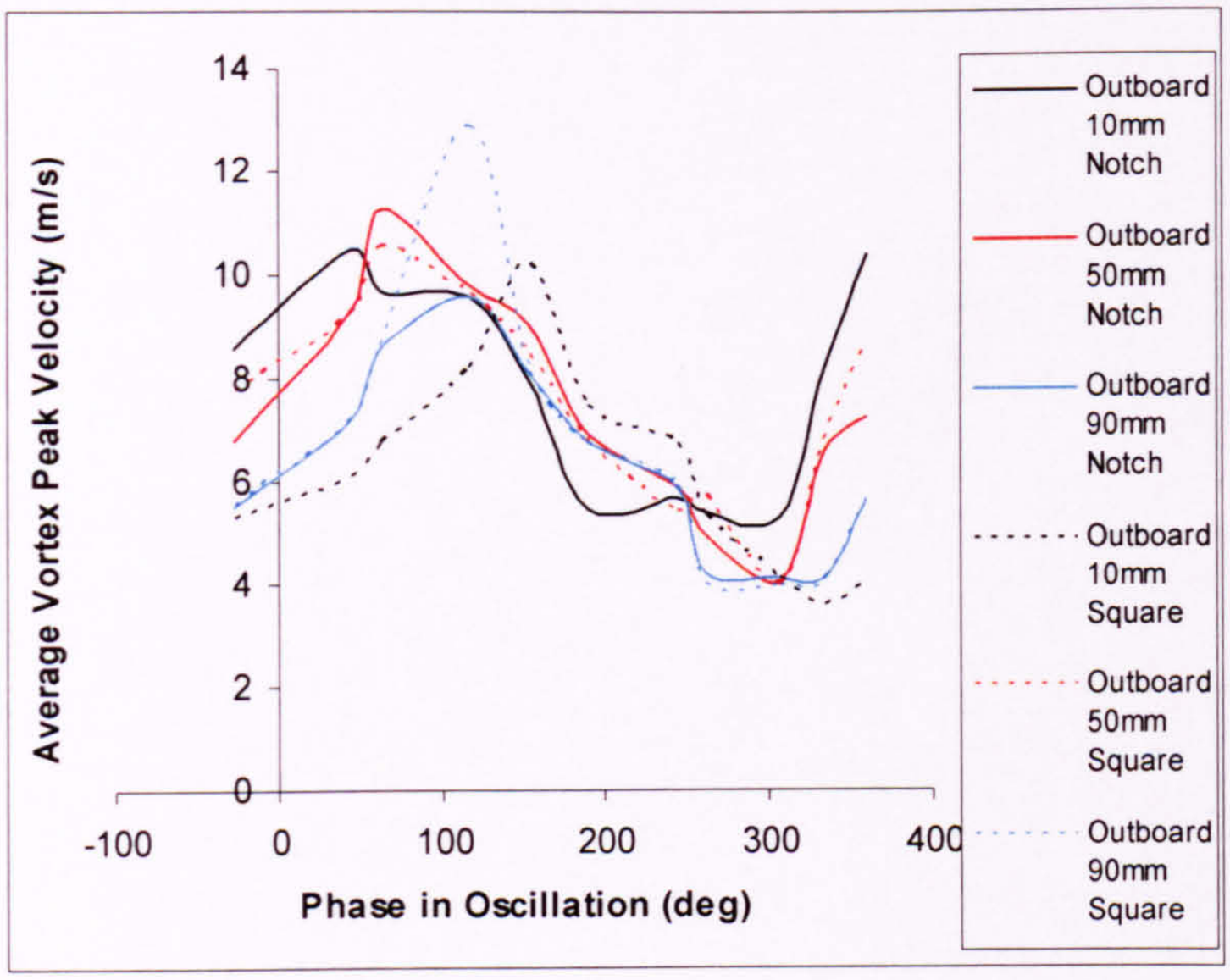

Figure 4-5 Comparison of average peak velocity measured over the oscillation of the blade. The velocity profile for the both the outboard vortices for the square and modified blade tip planform are included for direct comparison. There is little variation between the two blade - tip planform, and this remains the case with increasing distance into the downstream flow.

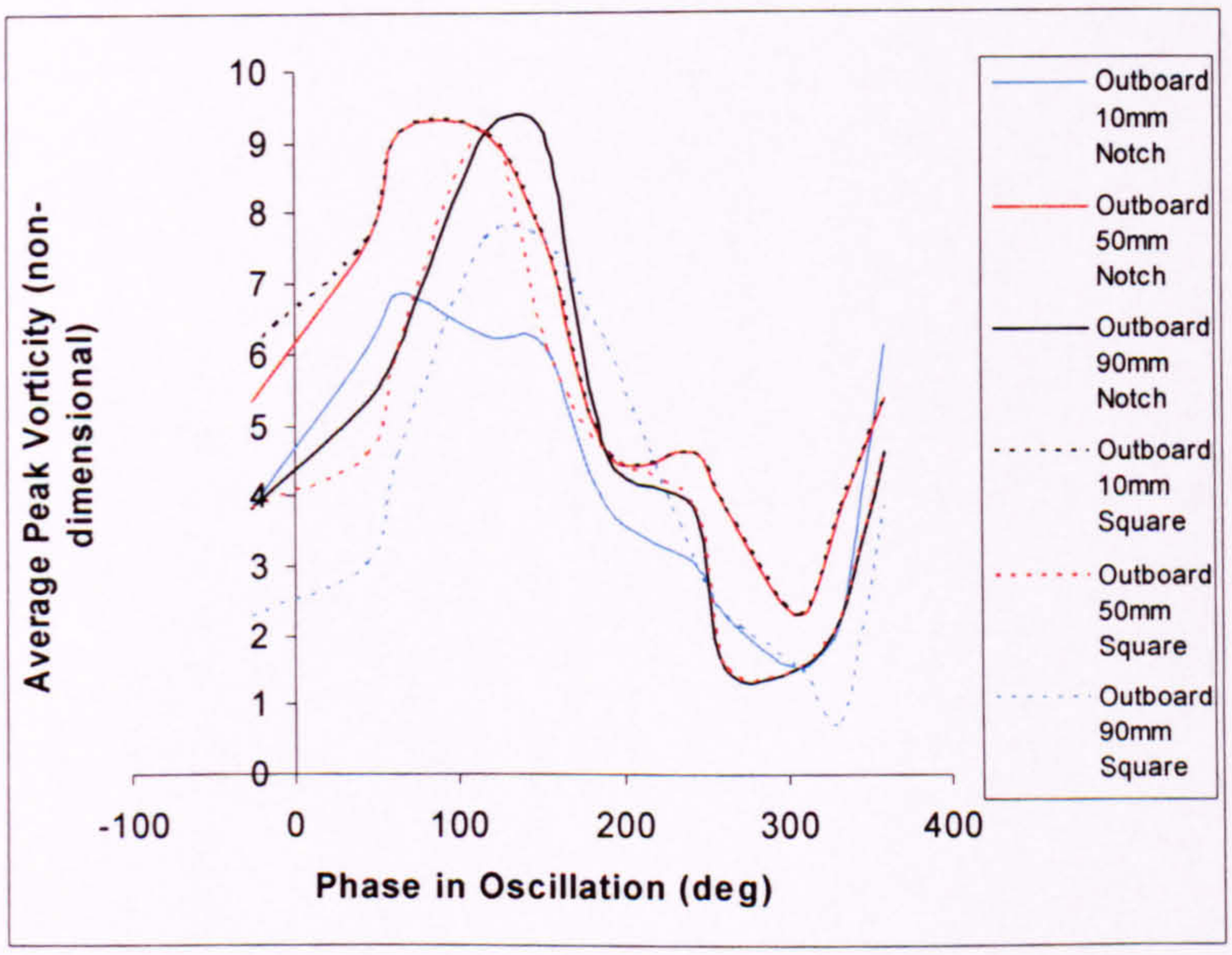

Figure 4-6 Comparison of average peak vorticity measured over the oscillation of the blade. The vorticity profile for the both the outboard vortices for the square and modified blade tip section are included for direct comparison. The peak vorticity levels for both blade sections remain similar at nearly all locations, indicating that the modified blade section has little or no effect.

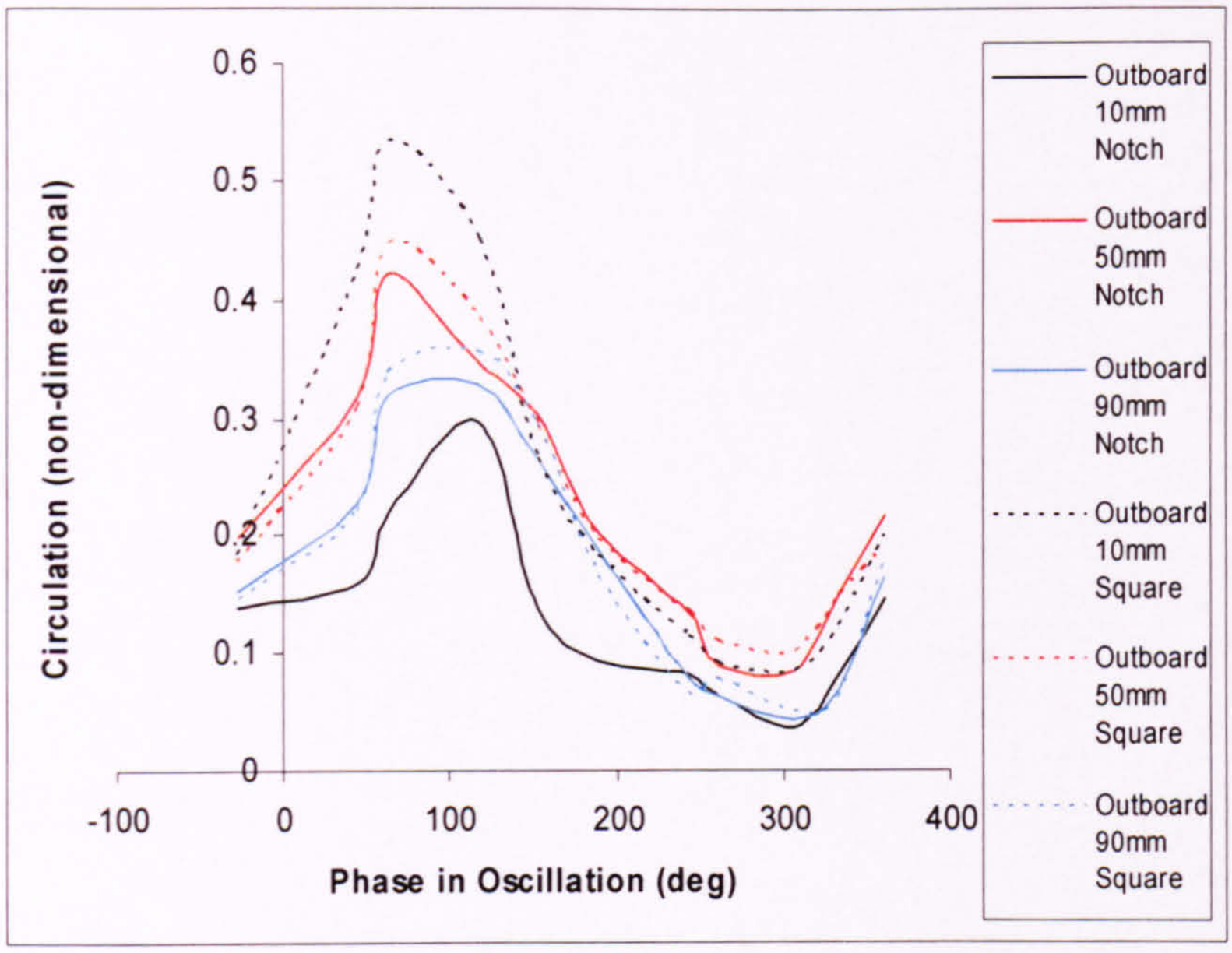

Figure 4-7 Comparison of average circulation measured over the oscillation of the blade. The circulation profile for the both the outboard vortices for the square and modified blade tip section are included for direct comparison.

4.3 Influence of the Blade Tip Modification on the Progression of the Orthogonal Blade-Vortex Interaction

The progression of the orthogonal BVI is already known to be governed by the two parameters, the thickness parameter (considered in detail in Chapter Three), and the impact parameter, $2\pi\sigma U/\Gamma$. The modification of the blade tip leads to two separate, counter-rotating vortex structures being generated, as observed in the cases of both the stationary and oscillatory blade cases, with no evidence of merging of the two vortex cores observed. Measurement of the trailing edge region of modified blade section in Section 4.1 has shown that the tip does produce a counter-rotating vortex system, in which the inboard vortex produced by the leading edge notch is of similar strength to the outboard structure, while Section 4.2 extended this to consider the behaviour of the tip vortex structure under oscillation, in which the strength of the tip vortex appeared to be substantially reduced through the inclusion of the leading edge notch and sweep.

The BERP tip has already been found to be extremely effective in a number of ways, both in increasing forward flight speed while decreasing perceived noise. In Chapter Three, the progression of the orthogonal blade-vortex interaction was examined for a single vortex structure interacting with a stationary rectangular blade. In order to extend this work, the remainder of this chapter will present the results of the effects of the modified blade tip on the progression of the BVI.

In order to conduct this study, the experimental arrangement outlined in Chapter 2 was used, with the rectangular planform blade of the vortex generator substituted with the new 'paddle' tip blade. The same tests were then performed as for Chapter 3.

4.3.1 Isolated Wake Structure

As within the previous chapter, it is first necessary to isolate those features which may be solely attributable to the interactional process in order to gain a thorough understanding of the vortex structure prior to undergoing any deformation. This was accomplished in the same manner as described in Chapter 3, in which the vortex core was studied in its isolated state (within the freestream flow with no obstruction present within the wind tunnel working section), and the PIV lightsheet aligned in the position that the blade centreline would occupy within the wind tunnel working section (as depicted in Figures 2-1, 2-8(b)). The core is then interrogated perpendicular to the sense of the core axial flow.

Vorticity ($\frac{c\omega}{U_\infty}$), divergence ($\frac{c\nabla}{U_\infty}$), and strength ($\frac{\Gamma}{U_\infty c}$) have been non-dimensionalised by the blade chord length (0.1524m) and the freestream velocity ($20ms^{-1}$), x and y locations within the interrogation plane have been non-dimensionalised with regards to the blade chordlength. As the interacting blade used to replicate the orthogonal BVI (as detailed in Chapter Three) has been removed from the experimental arrangement, there is no reference origin within the interrogation volume, and as such the origin location is arbitrary.

Initially, the entire flow was interrogated for the presence of the vortical structures by modifying the time delay between the rotor signal and the laser. By doing this, only one discernable vortex was found to be present in the flow field.

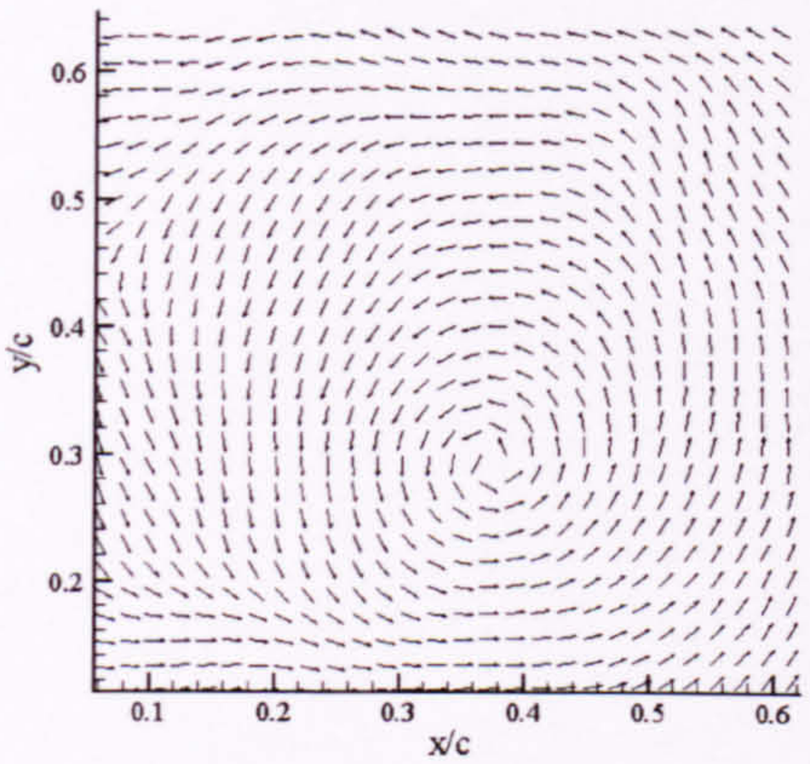

Figure 4-8 The isolated vortex core shows no evidence of radial inflow/outflow as would be expected from a fully developed vortex core. The mean u component has been removed for clarity. Measured peak velocity $0.55U_{\infty}$.

Again, the vortex core is a symmetrical structure, with no radial inflow/outflow apparent [Figure 4-8].

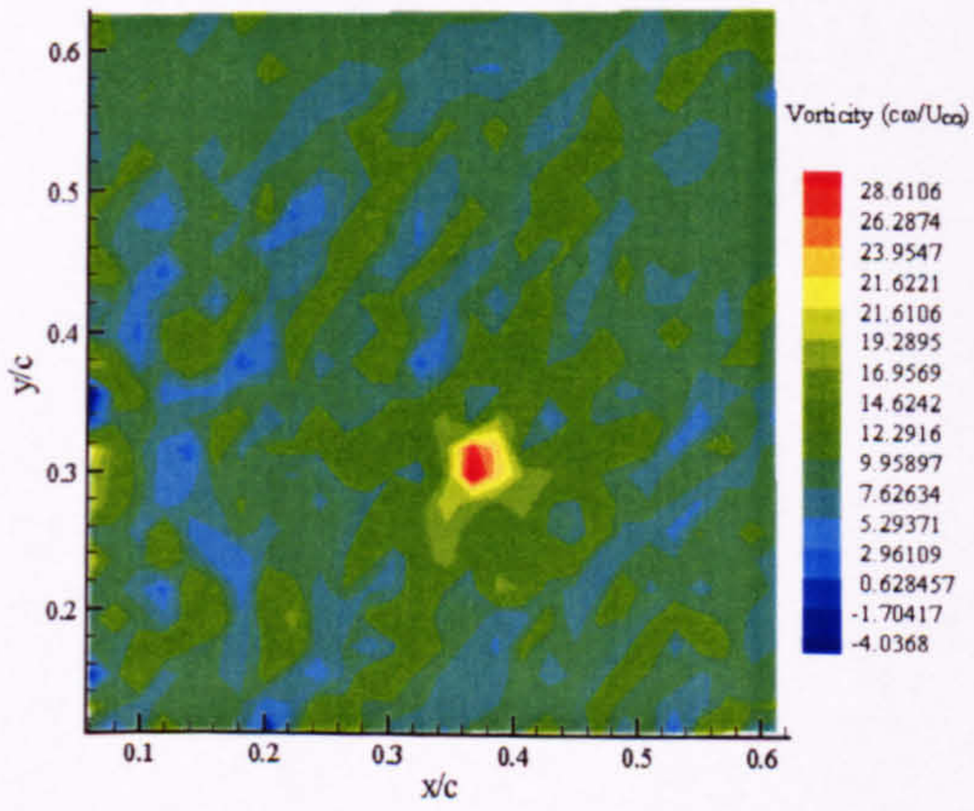

Figure 4-9 The non-dimensional vorticity of the isolated vortex core indicates a peak of $28.61\frac{U_{\infty}}{c\omega}$, with a clearly defined vortical structure observed.

The recorded peak velocity and vorticity [Figure 4-9] within the core are not significantly different from those measured for the vortex produced by the rectangular planform rotor blade, indicating that the modification in the blade tip structure has no significant effect on the isolated trailing tip vortex.

Figure 4-10 indicates the contours of divergence for the isolated flow field, showing a peak divergence measurement of 5.1 ± 0.2.

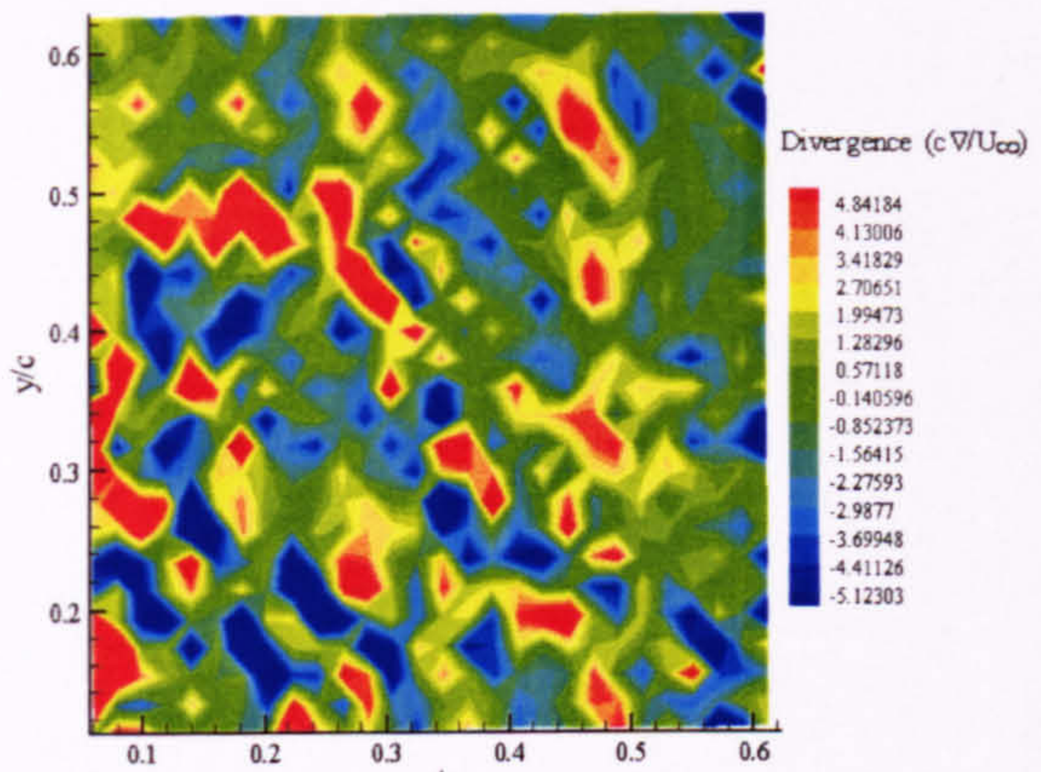

Figure 4-10 The isolated divergence contours indicate that there is no mass inflow/outflow of the vortex core, as would be expected in the undisturbed vortex state. The recorded levels of $\pm 5 \frac{U_\infty}{c\Delta}$ are consistent with noise within the flow.

As the vortex core axial flow is undisturbed in this state, it would be anticipated that low readings of divergence within the noise threshold would be obtained, as there should not be evidence of mass flow in/out of the vortex core. The levels recorded are again similar to those recorded for the previous study of the isolated vortex core (Section 3.1), and there is no distinct variation in the mass flow into or out of the vortex core axial flow.

The stereoscopic view of the isolated core [Figure 4-11] again indicates a clearly defined axial flow component, with the measured velocity of $0.57U_\infty \pm 0.08$ in good agreement with previous measurements of the axial flow associated with the vortex structure produced by the square planform blade ($0.6*U_\infty$) (see Section 3.1 and Doolan et al., 2000).

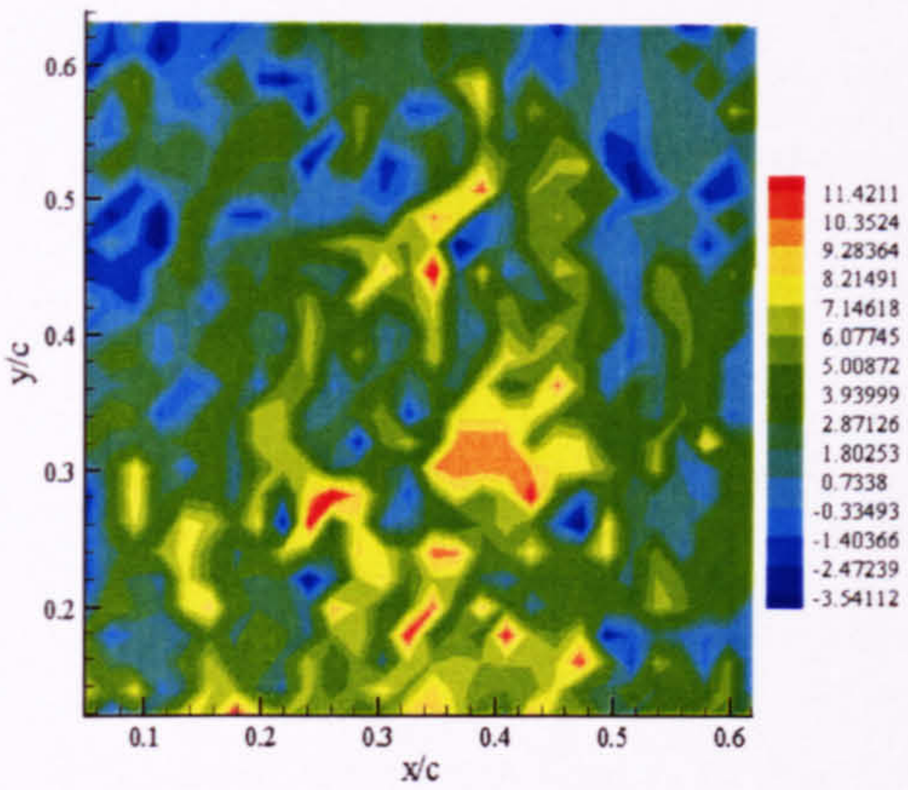

Figure 4-11 Contours of out-of-plane velocity reconstructed from the stereoscopic data. The maximum recorded out of plane velocity is $0.57U_{\infty}$. The centre of the vortex is located at (0.38, 0.32) as indicated in the 2D projection of the velocity vectors for the out-of-plane reconstruction.

Although the initial visualization of the interaction has revealed that there is no significant variation in the structure of the vortex core introduced by the inclusion of the leading edge notch, the interrogation of the flow in the isolated state does not provide a conclusive statement on whether the nature of the axial flow is the same as that produced by the rectangular blade section. As the previous study of the interaction (outlined in Chapter Three) indicated that the axial flow component was significant in the progression of the interaction, the remainder of this chapter will consider the progression of the OBVI over the interacting blade section in order to determine whether an effect on the trailing tip axial flow has been induced or not. If the nature of the axial flow has been modified, a marked difference in the features imparted to the vortex core as a result of the interactional process should be observed.

4.3.2 Post Interaction Wake Structure

As with the work contained within Chapter Three, the same notation will be used to describe the sections of the core as it interacts with the blade. As the vortex is 'cut' by the leading edge, the axial flow is blocked by the surface of the interacting blade (as

described in Section 3.3). The sense of the axial flow gives rise to two 'halves' of the vortex core (the vortex is subjected to two very different sets of flow conditions on either side of the interacting blade surface, giving rise to the distinction between the two 'halves' of the vortex core) – the lower surface in which the axial flow component is directed towards the blade surface, and the upper surface, on which the axial flow is directed away from the blade surface [Figure 2-8(c)].

Again, the interaction is tracked over either side of the blade centre line as the vortex passes across the chord using two independent camera/laser systems in order to obtain simultaneous images of each portion of the vortex core for the 2D2C PIV study. Each lightsheet was directed into the wind tunnel working section parallel to the chord of the interacting blade at 0.1c from the blade centre line on either side of the blade (as described in Section 2.3.1). Again, at the closest point, the lightsheets were situated 0.02c from the interacting blade surface. The far field effects of the interaction were again traced by moving the lightsheets away from the blade surface in 2mm stages in order to assess the transmission of the effects of the interaction back through the vortex core axial flow. All measurements are presented assuming the blade leading edge as the origin of the x-coordinate.

Using the method outlined in Section 2.3.2, a 2D3C interrogation of the flow field was implemented to reveal features pertaining to the axial flow component, but due to experimental limitations, this was conducted on each side of the interacting blade independently.

4.3.2.1 Interaction of the Wake with the Lower Blade Surface

Once the vortex system passes over the leading edge of the interacting blade, the axial flow component is blocked. On the blade lower surface, the axial flow is directed towards the blade surface, and has been associated with promoting a redistribution of

mass radially out of the vortex core due to the compression of the out-of-plane component (as shown in Section 3.3.1). The interaction of the trailing vortex system produced by the modified blade section indicates that in this case, the interaction proceeds in an almost identical fashion, with a radial outflow from the core immediately apparent [Figure 4-12], with the associated reduction in peak vorticity levels [Figure 4-13]. The expansion of the core due to the radial redistribution of mass is also observed.

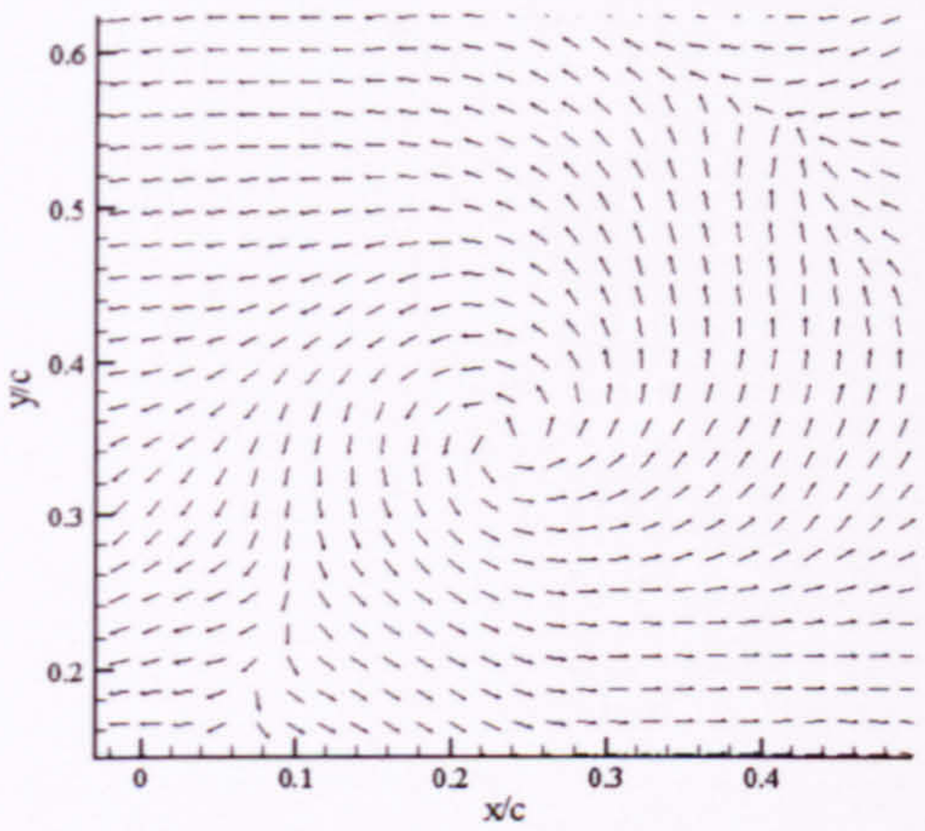

Figure 4-12 The post-interaction vortex core at 0.25 x/c reveals a significant variation from the isolated vortex core state to the radial and tangential components (mean u-component removed for clarity). Measured peak velocity of 11.09ms^{-1}. Lightsheet aligned at 0.02 z/c from the blade surface at the quarterchord.

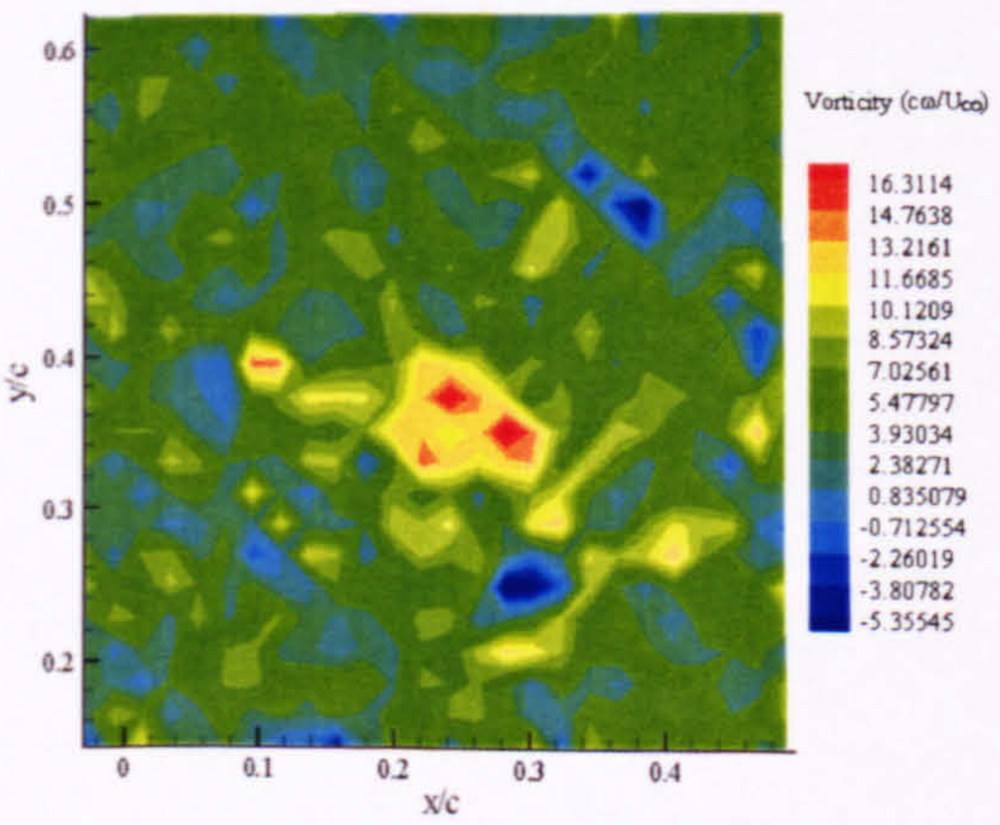

Figure 4-13 The post-interaction peak non-dimensional vorticity at 0.25x/c of 16.31 $\frac{U_\infty}{c\omega}$ reveals a significant decrease, possibly attributable to the redistribution of mass and the core expansion. Lightsheet aligned at 0.02 z/c from the blade surface at the quarterchord.

As with Section 3.3.1, the out-of-plane velocity component demonstrates a significant reduction in the axial core velocity (of approximately 25%, which is a similar reduction as measured for the single vortex interaction case) [Figure 4-14].

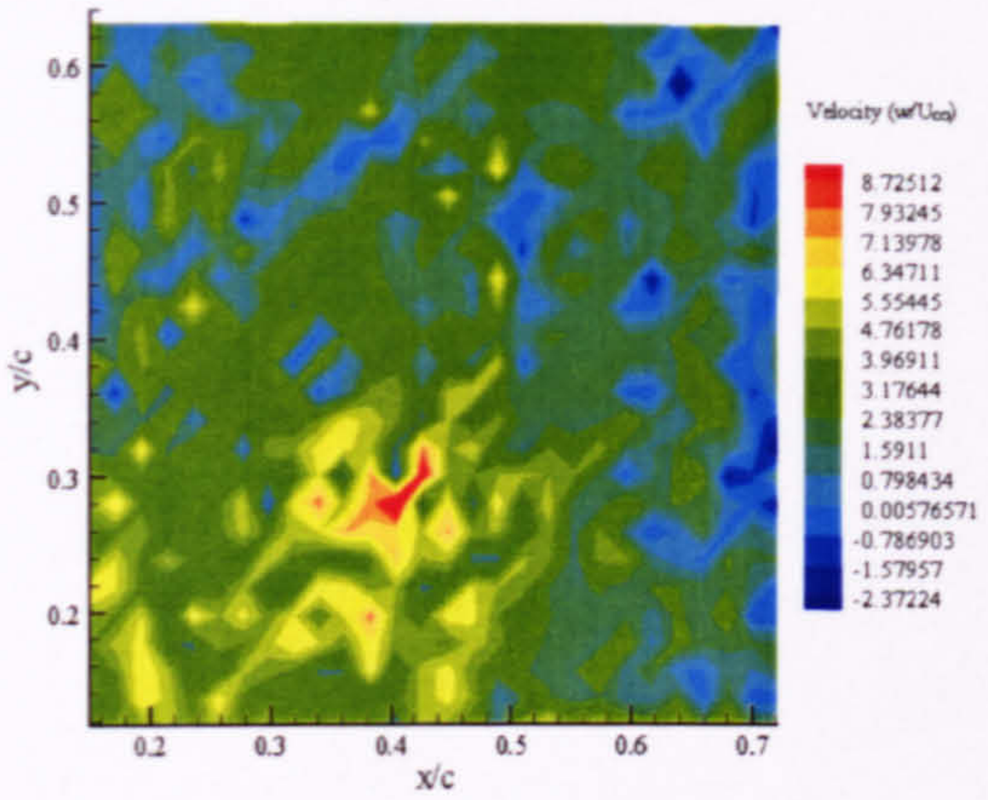

Figure 4-14 Contours of the out-of-plane velocity at 0.35x/c, with a maximum velocity of $0.436U_\infty$ measured. The vortex core centre is located at (0.38, 0.28) as indicated by the projection of the velocity into the x-y plane. Lightsheet aligned at 0.02 z/c from the blade surface at the quarterchord.

Again, as the vortex core passes further along the surface of the interacting blade, the peak vorticity levels undergo further reduction due to the compression of the axial flow component, with the core size gradually increasing due to the continuation of the significant radial outflow. This is accompanied by a continued decrease in the peak axial flow velocity through the vortex core. Further from the surface of the interacting blade, the effects of the interaction are no longer visible, with the core structure again similar to that observed in the freestream state. This again further supports the supposition in Section 3.3.1 that the disruption to the core is highly localised to the blade surface, with little or no communication back through the core.

One of the most striking features is the similarity in the measurements of the interactional process on the lower surface with those observed for the single vortex structure in the earlier chapter. There is no indication that the use of the modified blade section has any significant effect on this portion of the interactional process.

4.3.2.2 Interaction of the Wake with the Upper Blade Surface

Unlike the lower surface interaction, the progression of the interaction appears to be dictated by the need to re-establish the axial flow component further from the blade surface (as in Section 3.3.2). The vortex core does not appear to undergo any significant variation from the isolated vortex core due to the interactional process on this side of the blade [Figure 4-15], with no evidence of a radial flow component within the core. Recorded peak vorticity levels are substantially higher than those recorded for the lower surface portion of the vortex core [Figure 4-16], and there is a slight reduction in the core diameter observed (which is again in agreement with the work in Chapter 3). This slight reduction in diameter compared to the isolated vortex core would indicate that there is a slight radial inflow into the core.

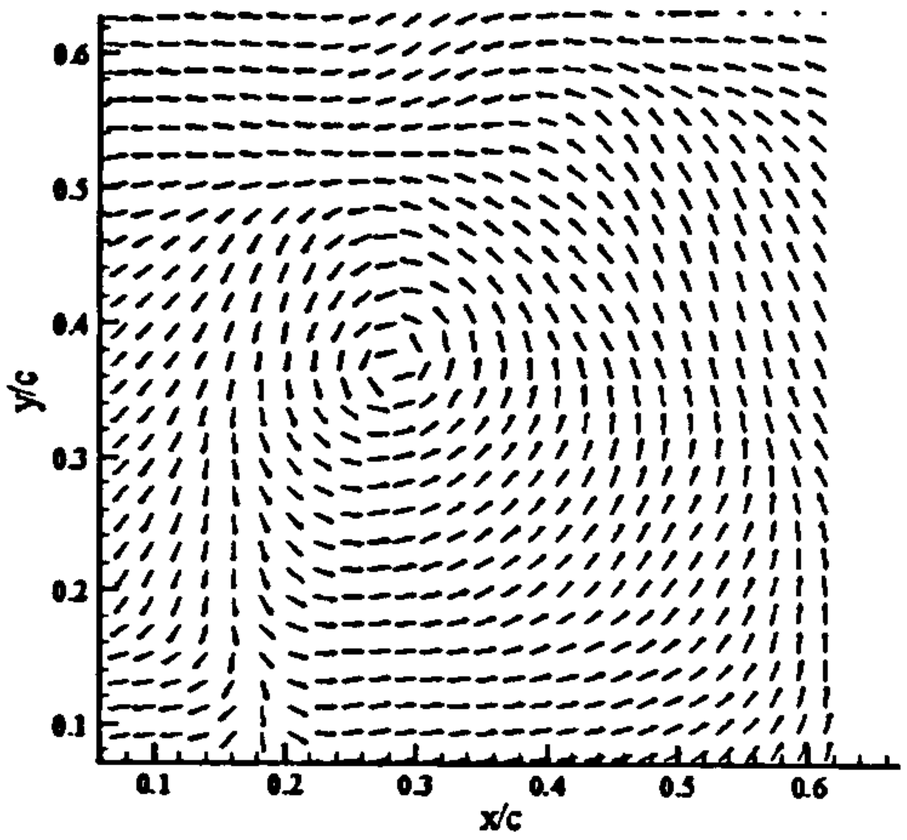

Figure 4-15 The post-interaction vortex core at 0.25 x/c reveals that there is no major variation from the isolated core to the radial and tangential components, unlike for the equivalent upper surface interaction (mean u-component removed for clarity). Peak velocity of $0.596U_\infty$. Lightsheet aligned at 0.02 z/c from the blade surface at the quarterchord.

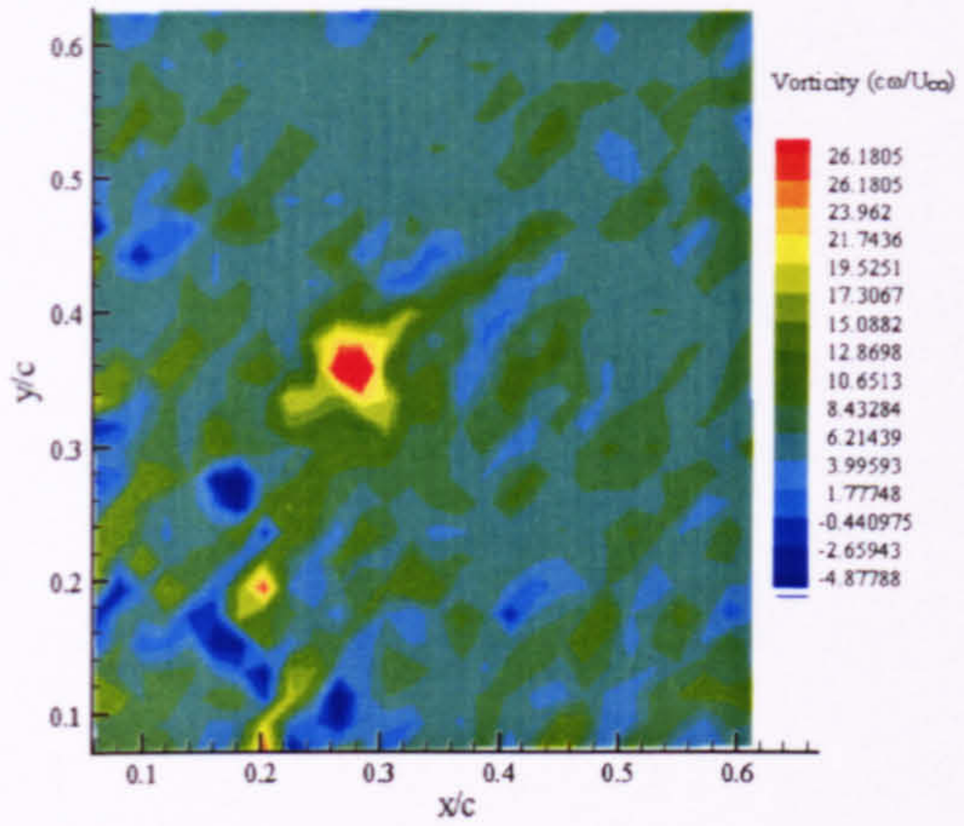

Figure 4-16 The post-interaction peak non-dimensional vorticity at 0.25 x/c of $26.18\frac{U_\infty}{c\omega}$ reveals little variation from the freestream flow condition, while a slight reduction in core diameter may be indicative of the presence of the previously identified radial inflow. Lightsheet aligned at 0.02 z/c from the blade surface at the quarterchord.

Again, the divergence plots indicate an unusual feature in the mass flow into and out of the axial flow, although this is much more clearly demonstrated in the stereoscopic view of the core [Figure 4-17]. The unusual region of reversed flow over the vortex core is again apparent, suggestive of the flow transporting mass down through the vortex core towards the blade surface in order to aid re-establishment of the flow closer to the blade surface.

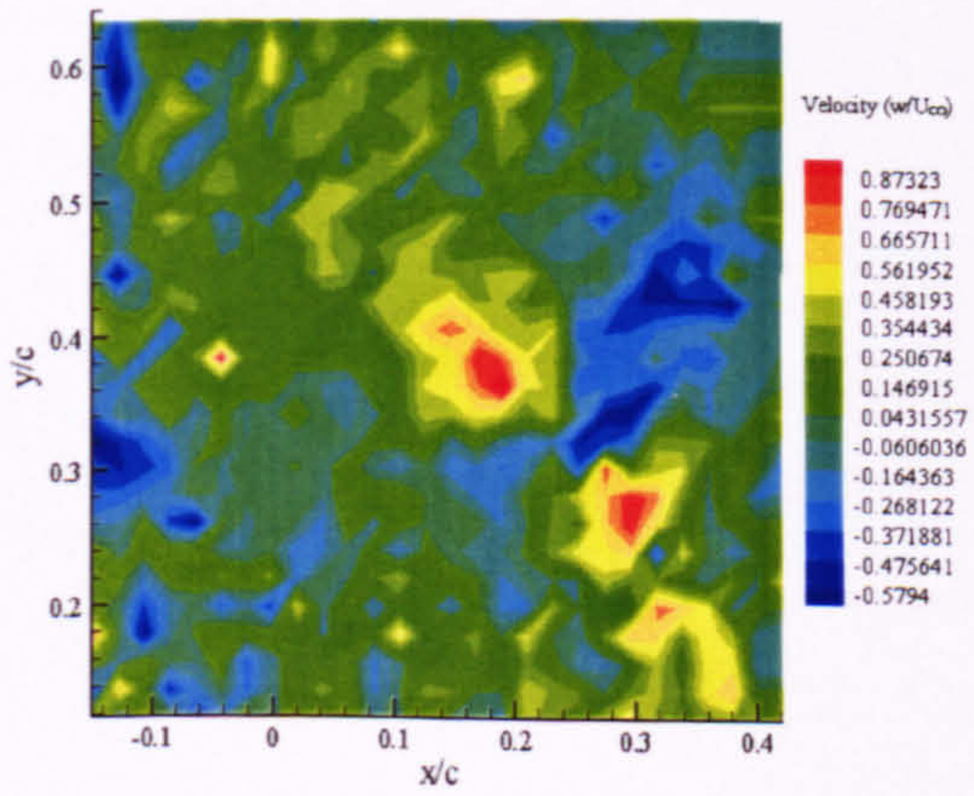

Figure 4-17 The out-of-plane velocity distribution plot for the post-interaction vortex at 0.25x/c indicates a peak velocity of $0.87U_\infty$ within the vortex core. The vortex centre is located at (0.24, 0.34) as indicated by the projection of the velocity in the xy plane. Lightsheet aligned at 0.02 z/c from the blade surface at the quarterchord.

With increasing x/c as the vortex passes further along the blade chord, the peak vorticity levels continue to increase, and the unusual split in the core axial flow component persists, indicative of the importance of this feature in the interactional process. Again, with increasing distance from the interacting blade surface, there is little evidence of the interactional effects by a distance of 0.12c from the interacting blade surface, again supporting the supposition that the interactional effects are highly localised to the blade surface.

As with the lower surface interaction, there is no indication that the introduction of the modified blade tip has any significant effect on the progression of the interaction and the nature in which the vortex core passes along the upper surface of the blade.

4.3.2.3 Structure of the Wake in the Trailing Edge Region

Due to the persistence of the trailing tip vortex, the potential regeneration of the vortical structure in the trailing edge region has also been examined, in a similar fashion to Section 3.3.3. Image capture in this area was again performed by aligning the PIV lightsheet with the trailing edge, parallel to the chord of the blade. The sheet was then traversed across the working section in order to obtain comparative measurements on the upper and lower surface sides. For notation purposes, when the lightsheet was moved to the lower surface side of the blade, this is termed negative (-0.1c), when moved to the upper surface side, this is termed positive (+0.1c). In each case, the lightsheet was traversed a distance of 0.1c in either direction to obtain comparative measurements (please refer to Figure 2-8(d) for a schematic of this setup).

As the vortex passes over the trailing edge of the interacting blade, the structure of the vortex core directly behind the trailing edge appears to remain coherent, although the peak vorticity levels are substantially reduced compared to the isolated vortex structure [Figure 4-18, 4-19]. The out-of-plane component does not appear to be coherent, with no evidence of a strong axial flow component in existence [Figure 4-20].

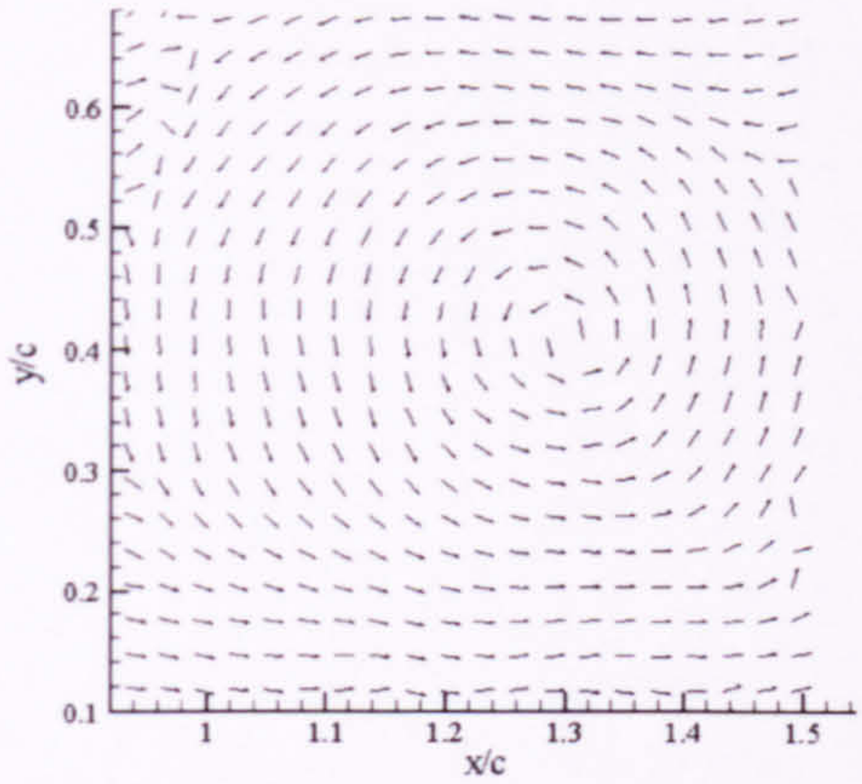

Figure 4-18 The post-interaction vortex core at 1.3x/c at a distance of 0c from the interacting surface in the trailing edge region reveals no significant variation from the isolated vortex core to the radial and tangential components (mean u-component removed for clarity) peak velocity of $0.318U_{\infty}$. Lightsheet aligned at 0 z/c from the blade surface at the quarterchord.

The measured values for both velocity and vorticity are very similar to those obtained for the measurement of the single vortex structure within the trailing edge region (refer Section 3.3.3).

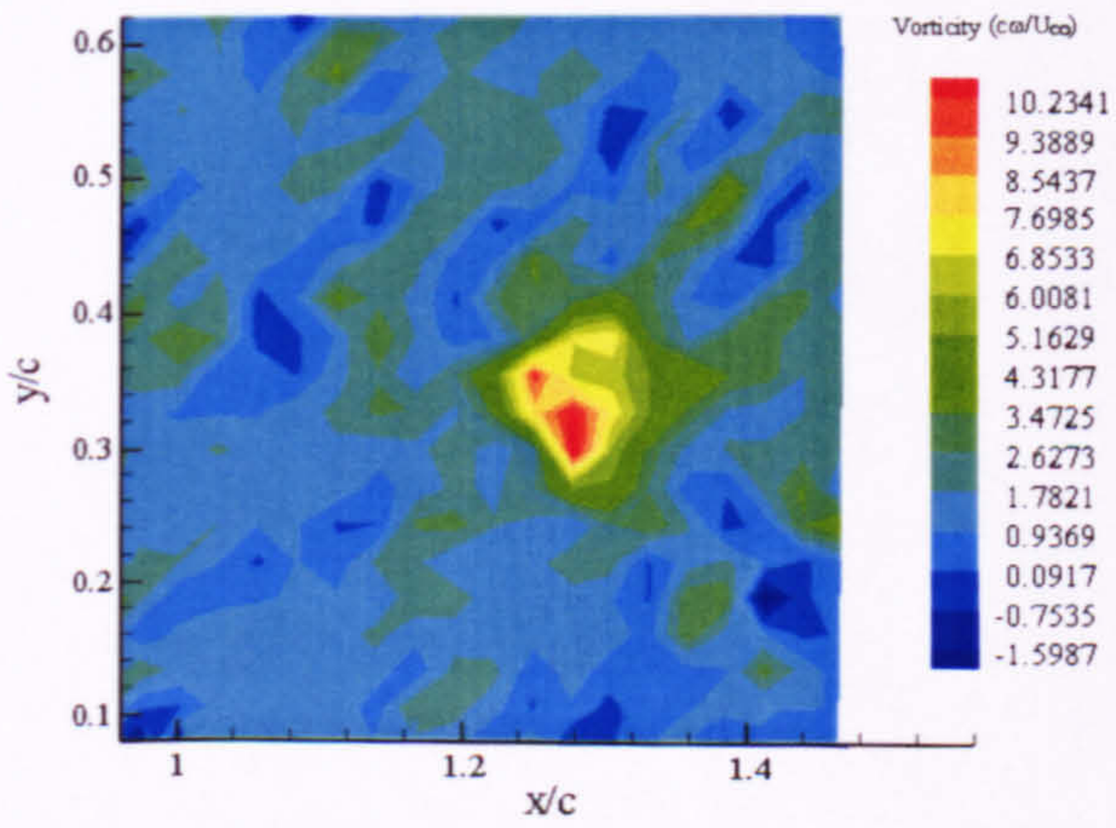

Figure 4-19 The post-interaction peak non-dimensional vorticity of $10.23\frac{U_{\infty}}{c\omega}$ at 1.3x/c at a distance of 0c from the interacting surface in the trailing edge region reveals a substantial reduction in peak vorticity levels. Lightsheet aligned at 0 z/c from the blade surface at the quarterchord.

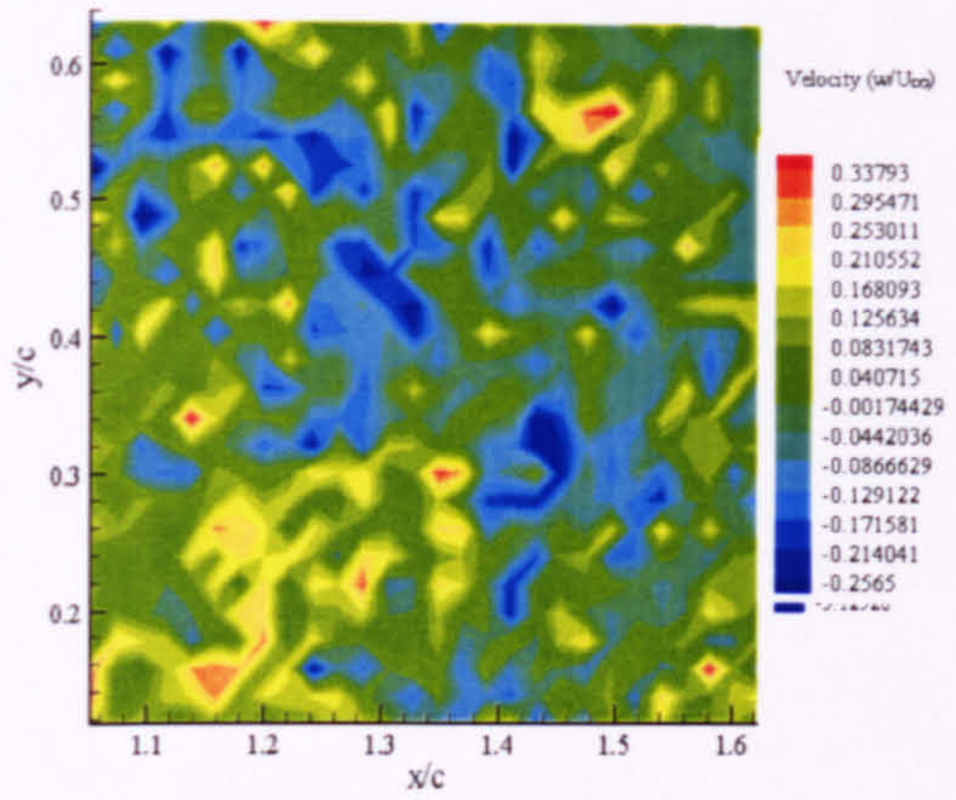

Figure 4-20 The out-of-plane velocity distribution plot for the post-interaction vortex at 1.3x/c at a distance of 0c from the interacting surface indicates a peak velocity of $0.34U_\infty$ within the vortex core. There is no clear vortex core axial flow visible in the dw component. Lightsheet aligned at 0 z/c from the blade surface at the quarterchord.

Once the lightsheet is traversed to the lower surface side of the interacting blade (-0.1c), it is possible to see that many of the features imparted to the vortex by the interactional process persist within the vortex core well into the trailing edge region. The core is still significantly enlarged compared to the isolated vortex case [Figure 4-21, 4-22, 4-23], and the distinctive radial outflow in the velocity distribution is still apparent.

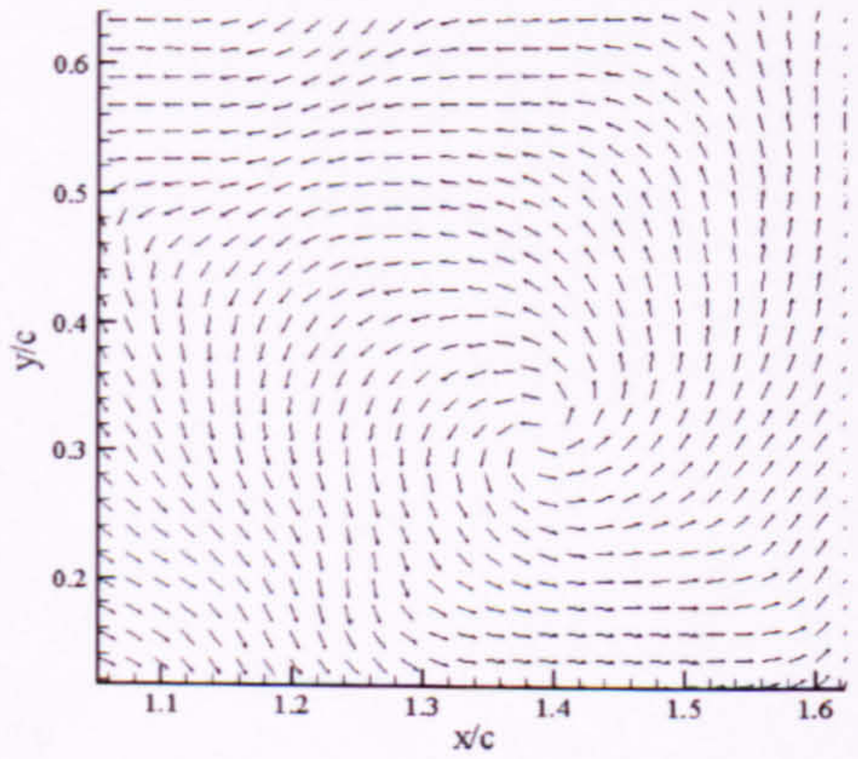

Figure 4-21 The velocity distribution plot for the post-interaction vortex at 1.3x/c at a distance of -0.1c indicates a peak velocity of $0.33U_\infty$ within the vortex core. Lightsheet aligned at 0.01 z/c from the blade surface at the quarterchord.

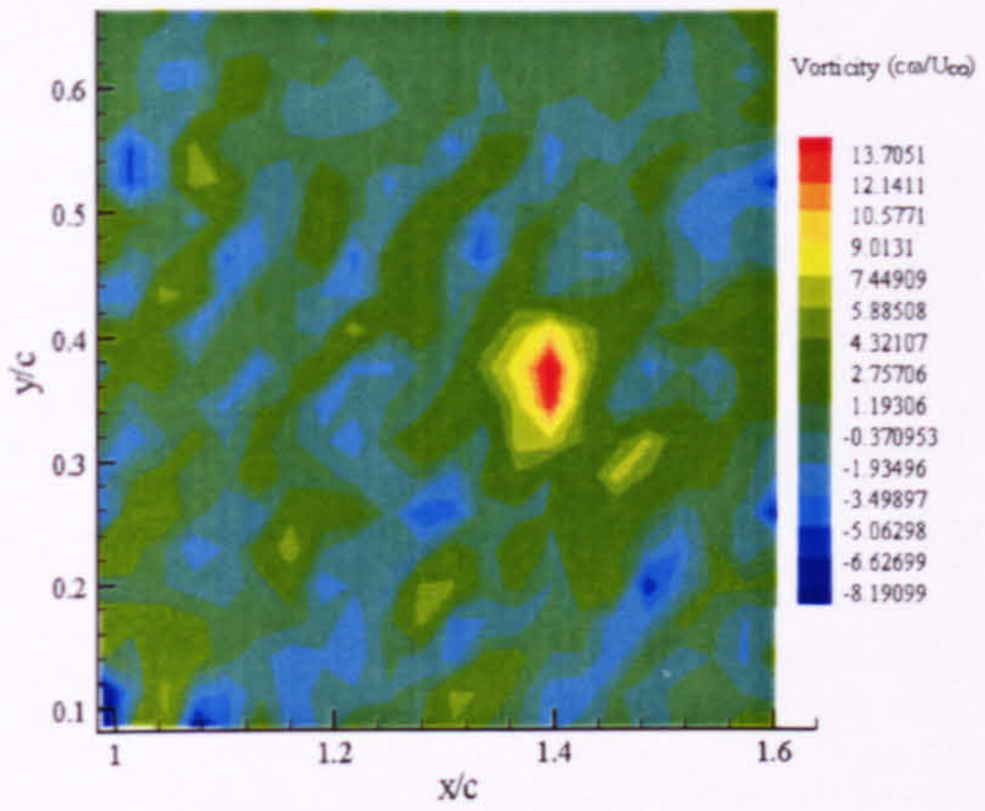

Figure 4-22 The post-interaction peak non-dimensional vorticity of 13.71 $\frac{U_\infty}{c\omega}$ at 1.3x/c at a distance of -0.1c from the interacting surface in the trailing edge region reveals a substantial reduction in peak vorticity levels. Lightsheet aligned at 0.01 z/c from the blade surface at the quarterchord.

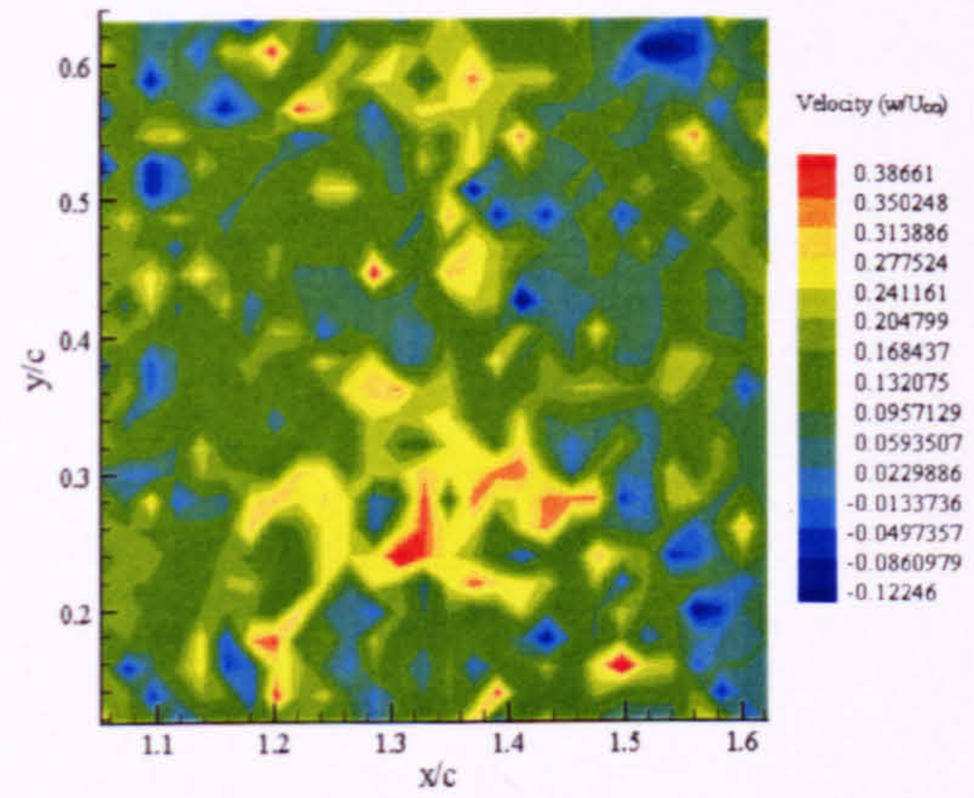

Figure 4-23 The out-of-plane velocity distribution plot for the post-interaction vortex at 1.3 x/c at a distance of -0.1c indicates a peak velocity of $0.387U_\infty$ within the vortex core. The vortex centre is located at (1.38, 0.28) as shown in the projection of the velocity vectors in the xy plane. Lightsheet aligned at 0.01 z/c from the blade surface at the quarterchord.

The lightsheet was then traversed 0.1c to the upper surface side of the trailing vortex in order to obtain a comparative set of measurements for the vortex passing over the upper surface of the interacting blade into the trailing edge region.

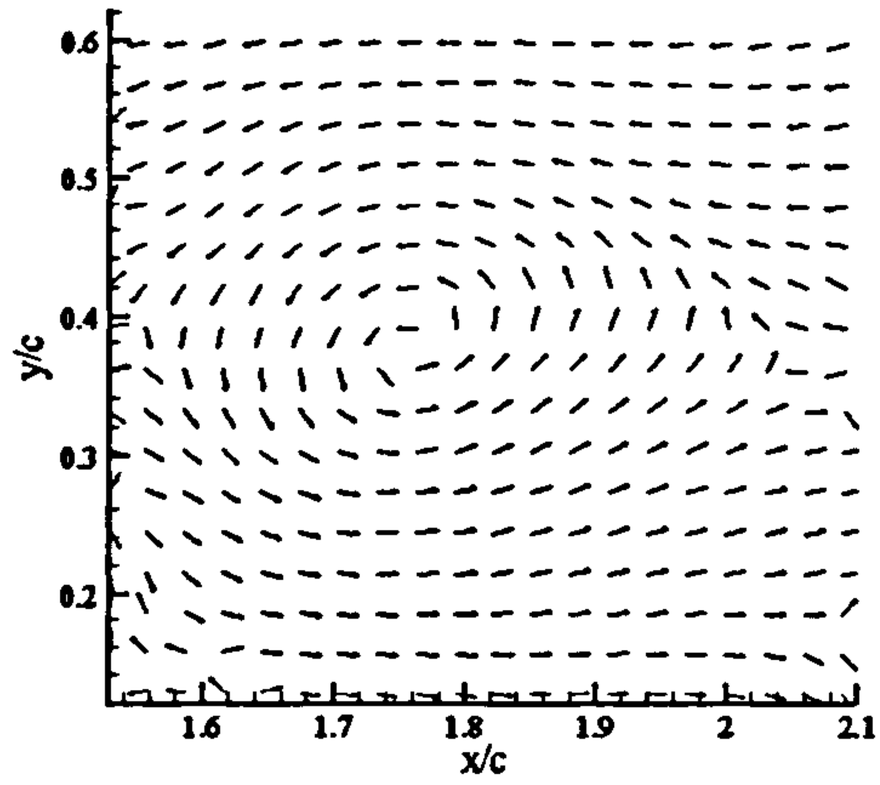

Figure 4-24 The post-interaction vortex core at 1.3x/c at a distance of +0.1c from the interacting surface in the trailing edge region reveals no significant variation from the isolated vortex core to the radial and tangential components (mean u-component removed for clarity). Peak velocity of $0.55U_{\infty}$. Lightsheet aligned at 0.01 z/c from the blade surface at the quarterchord.

As would be expected, given the nature of the interaction on the upper surface side of the blade, the vortex core structure is easily identifiable in the trailing edge region, with peak vorticity levels remaining high well into the trailing edge region [Figure 4-24, 4-25]. Again, there is no evidence of significant variation from the isolated vortex core to the tangential components of the vortex induced by a radial flow.

The divergence plot still indicates the split in mass flow through the vortex core [Figure 4-26], which is again mirrored in the out-of-plane component [Figure 4-27]. There is no indication of a potential regeneration of the vortex core at this point in the trailing edge region, but it does demonstrate that the effects of the interactional process do persist well into the trailing edge region.

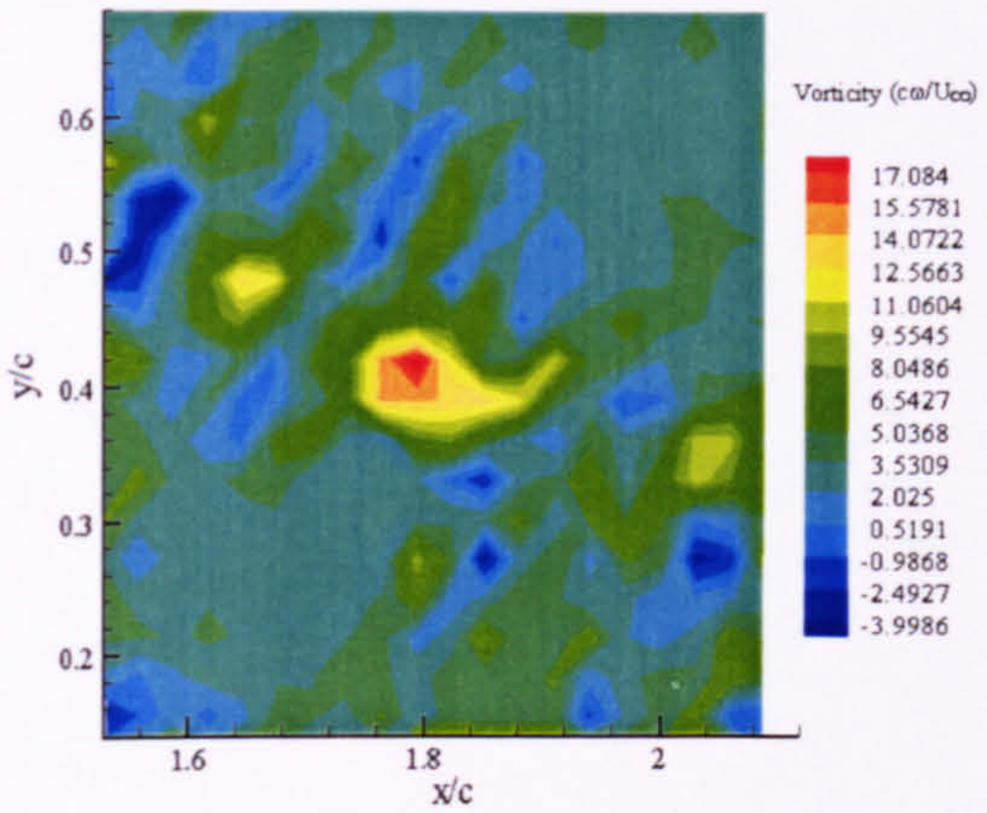

Figure 4-25 The vorticity distribution plot for the post-interaction vortex at 1.3x/c at a distance of +0.1c from the interacting surface in the trailing edge region indicates a peak vorticity of 17.01 $\frac{U_\infty}{c\omega}$ within the vortex core. Lightsheet aligned at 0.01 z/c from the blade surface at the quarterchord.

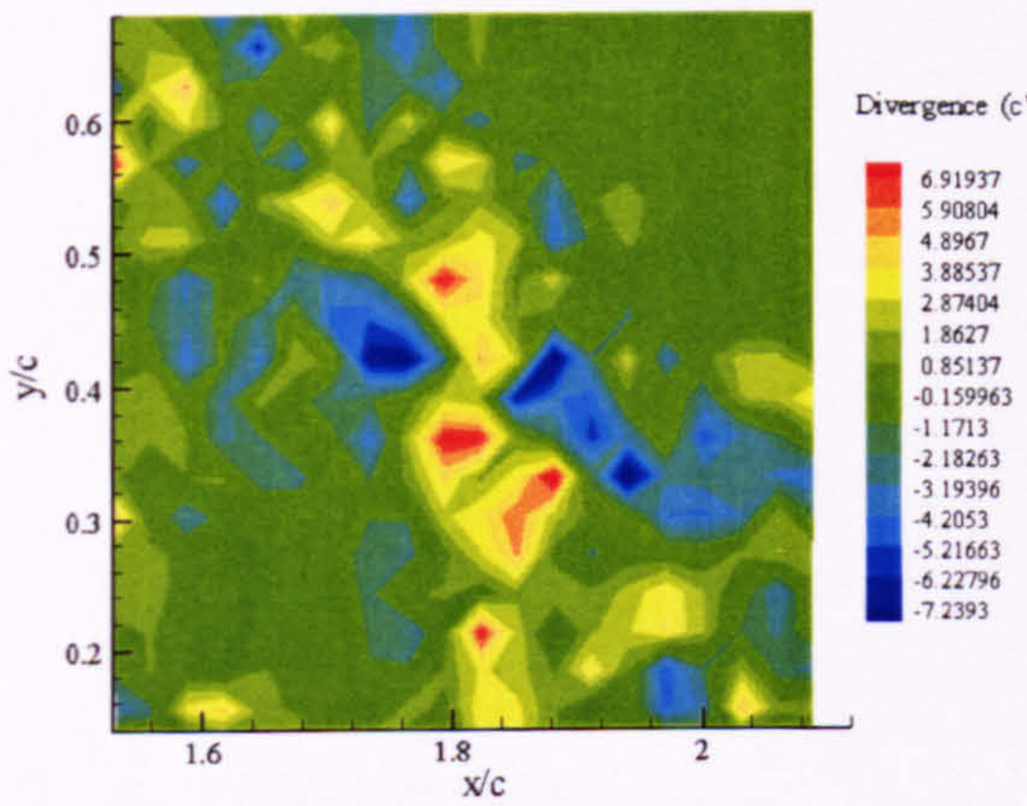

Figure 4-26 The divergence distribution plot for the post-interaction vortex at 1.3x/c at a distance of +0.1c indicates regions of both positive and negative divergence over the vortex core location ($\pm 7\frac{U_\infty}{c\Delta}$). Lightsheet aligned at 0.01 z/c from the blade surface at the quarterchord.

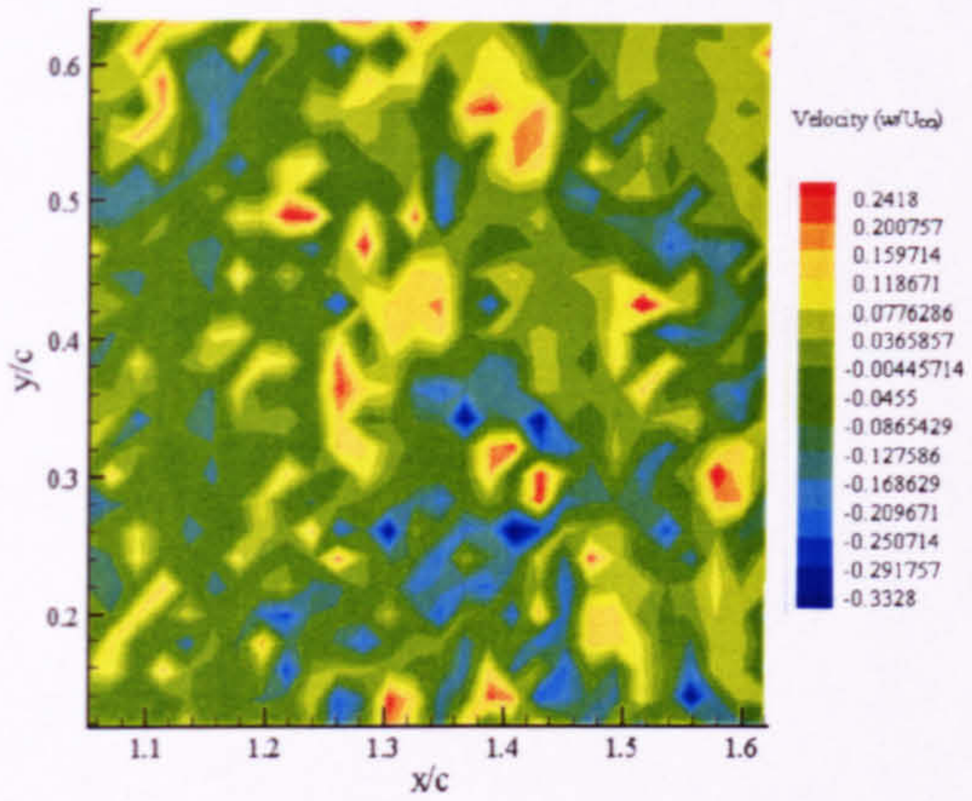

Figure 4-27 The out-of-plane velocity distribution plot for the post-interaction vortex at 1.3x/c at a distance of +0.1c indicates a peak velocity of $0.33U_\infty$ within the vortex core. Again, there are indications of regions of reversed flow measured within the dw component. The vortex centre is located at (1.38, 0.3) as indicated by the projection of obtained velocity vectors into the xy plane. Lightsheet aligned at 0.01 z/c from the blade surface at the quarterchord.

4.4 Summary of Results

The concept of passive control and its use in the control of the orthogonal blade-vortex interaction has been examined in this chapter. The modification of the blade tip in order to produce a twin vortex system was attempted, and initial characterisation of the flow demonstrated that the blade did produce a counter-rotating vortex system, with the secondary vortex being shed from the notch introduced into the leading edge. This vortex was of comparative size and strength to the equivalent tip vortex.

When compared to the rectangular planform blade used in Chapter 3 of this study, it was found that the modification had no significant impact on the tip velocity or vorticity profiles for the tip vortex structure. The blade with the modified tip was then substituted into the vortex generator in place of the rectangular planform blade used previously in this study, and the effect of the modified tip on the progression of the BVI was examined. The interaction appeared to progress in a manner very similar to that revealed in Chapter 3, with the modification in the vortex system being shed by the vortex generator having no significant impact on the progression of the orthogonal blade-vortex interaction. This was demonstrated through the examination of the progression of the interaction – while the isolated vortex core did not appear to be significantly different from the trailing tip vortex produced by the generator in Chapter Three, the examination of the details pertaining to the axial flow was not conclusive, due to relatively high measurement errors in the divergence and stereoscopic data. In this case, the visualisation of the interaction became of importance, as any significant change to the nature of the axial flow induced by the inclusion of the leading edge notch would be visible in the two-dimensional PIV data, in which the confidence level is higher due to the higher accuracy obtained in this data.

As the two-dimensional study did not demonstrate any significant variation in the nature of the interactional process, it is proposed that the modified blade tip has not introduced a significant variation in either the tangential or axial components of the flow that are visible within the core at this point downstream of the vortex generator (although this

does not preclude changes introduced into the core structure in the local region of the blade of the vortex generator).

Chapter 5 will follow on from this to discuss the work contained with Chapters 3 and 4, highlighting issues arising from the experimental programme, and potential areas of future work required.

Chapter 5: Discussion of Results

Within the context of investigating sources of undesirable acoustic and loading conditions within rotorcraft operation, the interaction of trailing tip vortex structures generated by the main rotor assembly with the surrounding airframe have become of particular interest, as they contribute significantly to impulsive airframe loading, resulting in a number of noise signatures. Sheridan and Smith (1980) identified a number of cases of specific interest, including the interaction in which the trailing tip vortex is 'cut' perpendicular to its axial flow, termed the orthogonal blade-vortex interaction. Chapter Three presented the results of a study of the interaction of a representative trailing tip vortex structure with a stationary blade, in which the passage of the vortex core over either side of the interacting blade was examined. This was then complimented in Chapter Four with consideration given to how a modification of the tip vortex structure could potentially influence the mechanics of the interaction. The remainder of this chapter will be devoted to considering the findings from these two studies, and what they represent in terms of new understanding of these interactions.

The use of the particle image velocimetry technique in order to resolve the features associated with the OBVI has provided a large dataset, in which several interesting features have been highlighted, but there are factors which need to be considered in the interpretation of this data. Chapter Two raised the subject of accuracy within the PIV measurements for both 2D2C and 2D3C techniques (Section 2.3.3), some of which are highly important for the cases currently being studied. The nature of the vortex core, due to the intense velocity distribution, will naturally eject particles out of the core and into the surrounding fluid. Therefore the PIV calculations of velocity and the associated derivatives will be less accurate due to the relative low seeding density than those which are found elsewhere in the flow, although it will still provide useful information about the global flowfield.

It has long been suggested that the three-dimensionality of the trailing vortex heavily influences the manner in which the interaction progresses, as the out-of-plane component is blocked. Chapter Three identified the isolated vortex structure as being symmetrical with an appreciable out-of-plane component (w/U_∞ = 0.6 ±0.08 over 60 records) attributable to the axial flow, confirming the findings of previous hotwire and numerical simulations. Again, as with the work of Green et al. (2005), there is a relatively large variation in the peak recorded out-of-plane component, which is attributable to the small size of the core giving rise to errors due to the PIV resolution (refer to Section 2.3.3). The curvature of the trailing vortex, attributable to the helical trajectory of the wake is also clear [Figure 3-6], also confirming that the experimental modelling of the interactional process has been implemented correctly, as the axis of the approaching vortex is parallel to the illuminating lightsheet (and therefore perpendicular to the plane of the chord of the interacting blade). Vorticity within the core is positive, with a maximum of about 21.5 (which is similar to that measured by Doolan et al, 2000, Early et al., 2002 and Green et al, 2005), with the *(u,v)* velocity and vorticity contours suggesting a core diameter of approximately σ_o=0.09c ±0.02 over 60 records (slightly higher than the three-dimensional measurements of Green et al., 2005, which observed a core size of σ_o=0.075c). Non-dimensional circulation within the vortex core indicated that the vortex strength $\Gamma_o/U_\infty c$=0.19 ±0.15 over a series of 60 records. Based upon this, the impact parameter for the interaction $I = \frac{2\pi\sigma_o U_\infty}{\Gamma} = 3.14$, and the axial flow parameter $A = \frac{2\pi\sigma_o w_o}{\Gamma} = 1.88$, which confirms that the interaction in this case is of the supercritical type identified by Liu & Marshall, 2004 (again, in agreement with the measurements performed by Green et al., 2005).

The progression of the interaction is determined by the impact parameter and the thickness parameter (T/σ_o). By increasing the thickness parameter substantially (from T/σ_o= 2 to T/σ_o= 5), it was demonstrated that the initial conditions bounding the interaction could be significantly modified. For the lower thickness parameter, the vortex core clearly exhibits the radial outflow associated with the redistribution of mass into the

surrounding flow, promoted by the blockage of the vortex core axial flow. This is the anticipated behaviour of the vortex in the case where it is interacting with the stationary blade. However, for a sufficiently high thickness parameter (given as being >5 by Marshall and Krishnamoorthy, 1994), the nature of the interactional process changes significantly. Visualisation of the initial interaction of the vortex for this higher thickness ratio clearly demonstrated that there was no appreciable variation in the core radial or tangential components promoted by the interaction after passing across the leading edge (as would be anticipated if the vortex core axial flow has been 'cut'). This is further supported by the vorticity distribution, which indicates that the vortex core size is not significantly different from the pre-interactional case (0.08c ±0.01 over 60 records), with the peak vorticity distribution (20.5 ±2 over 60 records) again showing no significant deviation from measurements obtained from the isolated state. This would point to the possibility that the core axial flow has not been 'cut', even though it has passed significantly over the interacting body leading edge. This would agree with the previous suggestions that for this thickness ratio, the interaction between the body and the vortex is 'repulsive', due to the significant induced flow which is large enough to overcome the self-induced velocity of the vortex core. In this case, it has been reported that the vortex will appear to 'bend' around the leading edge of the body, rather than separating into two halves, and it would be expected that the features observed as a result of the core axial flow impacting on the surface would not be present in the flow, as is indicated by the visualisation in this case.

For the impact of the vortex core onto the blade leading edge, the impact parameter is sufficiently high and the thickness parameter sufficiently low so as when the vortex passes over the blade leading edge, it is subjected to two very different flow conditions on either side of the interacting blade, in which the axial flow is locally blocked by the blade surface (which has been demonstrated by the consideration of the impact of the thickness parameter on the progression of the BVI). On one side of the blade (termed the lower surface), the axial flow is compressed as it impinges onto the surface of the blade, with the velocity field revealing a redistribution of the mass within the core radially outwards as a result of this (Figure 3-14 demonstrates this clearly, with a clear

asymmetry in the vortex). Again, this is confirmed by the vorticity distribution, which is now spread over a larger area ($\sigma = 0.14c \pm 0.02$ over 60 records at a distance of 0.35 x/c), with the peak vorticity continuing to drop with increasing core diameter as x/c increases. As the vortex passes onto the surface, there is a marked decrease in the w/U_∞ component (measuring 0.35 ±0.1 over 60 records at 0.35 x/c). The work of Green et al. (2005) indicated that as the vortex passes over the leading edge, the positive *w* over the vortex core is almost stagnated as it passes onto the blade, with the *w* component gradually being restored with increasing x/c (in fact, the measured levels over the midchord in this study are in agreement with the measurements here, with peak values of 0.3 w/U_∞ recorded). It is also worthy of note that the work of Early et al. (2002), when considering the divergence patterns associated with this part of the interactional process, demonstrated that there is an intense area of negative divergence over this part of the core, indicative of the blockage of the axial flow, causing the mass flow away from the vortex axis and into the surrounding flow. Green et al. (2005) suggested that by the time the vortex has passed to the midchord position of the blade, the strength of the overall interaction is in fact weakened, with a more uniform outflow from the vortex core observed than at the point of impact of the vortex. Passing further from the blade centreline, the effects of the interaction on the vortex core are reduced substantially, with little or no effect observable at a distance of 0.2c from the blade centreline, indicative of the highly localised nature of the interactional process.

On the opposing blade surface (upper surface), the vortex axial flow is directed away from the interacting surface. Unlike the lower surface interaction, the *u,v* velocity components and peak vorticity levels ($\frac{c\omega}{U_\infty} = 20 \pm 2$ over 60 records) do not indicate any substantial deformation induced by the interactional process, although the reduction in core diameter compared to the freestream state (0.06 ± 0.01 over 60 records) would indicate that there is a weak radial inflow present within the vortex core. The most interesting feature associated with this portion of the interaction is observed within the out-of-plane component, with high levels of positive and negative divergence

surrounding the vortex core (as shown in Figure 3-23). Early et al. (2002) suggested that this could be attributed to the regeneration of the axial flow component close to the blade surface, but this was not conclusively demonstrated. Green et al. (2005) further went on to suggest that while the area of negative divergence is naturally associated with the interaction on this side of the blade, it is the positive divergence which is the dominant feature. By calculation of the helicity, it was shown that while the lower surface interaction gives rise to a significant realignment in both the positive and negative *h* zones, due to the significant movement of ω_z vorticity into an area of negative *w* velocity, and the expansion of the axial flow giving rise to a larger area of negative *dw/dy* embedded in the positive u velocity. However, there was no realignment observed in the equivalent upper surface case, as the blade leading edge and vortex *w* component velocities are in the same sense. Lee et al. (1998) also suggested that the contraction of the vortex core close to the wall is due to the focussing of the swirl velocity, and that the interaction on this side is almost dominated by the radial, rather than the axial components of the vortex core, in contrast to the opposite side of the blade. The current experimental study would agree with this previous computational modelling of the interaction.

As the vortex passes into the trailing edge region, there is some evidence to suggest that the vortex core redevelops a coherent structure after passing over the trailing edge, and that it maintains this for an appreciable distance downstream of the blade. This is interesting given the degree of distortion compared to the isolated vortex core to the vortex flow in the lower surface interaction, although Green et al. (2005) have demonstrated that the effects of the interaction on the core do weaken beyond the midchord point. Previous pressure data studies (Doolan et al., 2000) indicated that the pressure history of a pre-cut vortex interaction was very similar to the 'clean' interaction case suggesting the rapid regeneration of the vortex core and its axial and tangential velocity components, even if they were of greatly reduced magnitude. With the light sheet displaced 0.1c to the lower surface side, the vortex core, although larger, is very similar to the pre-interaction case, indicating that the vortex radial outflow reduces in magnitude in a very short time after passing over the trailing edge. Traversing an

equivalent distance to the upper blade side, there are again indications of recovery of the vortex structure. This relative lack of distortion compared to the isolated vortex core in the surrounding flow again supports that the regeneration of the core components occurs within a very short space of time. There is also little evidence of disturbance within the axial flow component, pointing to a possible reestablishment of the core axial flow to a state similar to the isolated vortex core, although this is not conclusive.

As the interactional process leads to a number of negative effects in the operation of rotorcraft, there has been much interest in the use of a number of devices in order to modify the tip vortex structure in order to alter the manner in which these interactions progress. One such method, the introduction of a notch and outer blade sweep in order to generate a counter-rotating twin vortex system has been considered in Chapter Four. A NACA 0015 blade with a modified tip section in order to incorporate these features was produced, and initial examination of the flow behind the blade revealed that a clear inboard vortical structure was produced by the notch in the blade leading edge, which was of comparative strength to the equivalent outboard tip vortex structure.

However, when the effect on the interactional process was examined, it was clearly demonstrated that the inclusion of the leading edge notch had no significant effect on the mechanics of the OBVI. The isolated vortex core revealed no significant difference in the core structure observed ($\sigma_o = 0.07c \pm 0.01$, $\frac{c\omega}{U_\infty} = 28.5 \pm 2.5$ over 60 records), with the *dw* component still appreciably high ($w/U_\infty = 0.55 \pm 0.08$ over 60 records). As it is this component that dominants the interactional process, and there is no substantial difference in the pre-interaction core structure, it is unlikely that there will be any significant variation in the progression of the interaction. Tracing the interactional progress over the lower and upper surface sides confirms this supposition, with no apparent variation in the mechanics of the interaction observed due to the modification of the vortex generator.

As the isolated vortex core is showing no observable variation from the core produced by the rectangular blade planform, it is suggested that the inboard vortex structure has been

ingested by the outboard vortex close to the generating blade (i.e. the two structures have merged just downstream of the rotor, and hence why only one vortex is discernable in the flow field). Benefits associated with the use of this type of passive control device in which the twin vortex system is produced may possibly be seen if a dihedral is introduced into the blade tip in order to increase the miss distance of the tip vortex structure, and increase the vertical displacement between the inboard and outboard vortex structure, hence lessening the possibility of the vortices merging soon after generation.

There is a clear need for consideration of accuracy of the out-of-plane velocity component from the stereoscopic PIV technique. There were experimental limitations on the camera separation angles that could be used, with a large separation distance between the cameras required for even small interrogation regions such as the 10cmx10cm region that was considered here. Larger camera angles would allow for a greater amount of accuracy to be obtained with the calculation of the out-of-plane velocities, although this would be at the expense of accuracy of the x-y plane velocities. To estimate the accuracy of the out-of-plane velocity measurements, the stereo PIV system was used to measure a uniform flow in the wind tunnel, with the vortex generator switched off and the interacting blade removed from the wind tunnel. With the light sheet aligned parallel to the flow direction there should be almost no out-of-plane velocity. However, measurements showed that the out-of-plane velocity in the uniform flow may be as high $\pm 2.5 ms^{-1}$, indicating an apparent flow both into and out of the plane of interrogation. For this reason the nature of the progression of the interaction on the upper surface should still be regarded as ambiguous, since the observations of the behaviour during the interaction are not much greater than the out-of-plane velocity error.

This was also problematic for the two-component PIV study, where the divergence (used to infer out-of-plane behaviour) was not much larger than the background noise divergence. In fact the whole experiment has been challenging for PIV, since in the vortex core there are significant PIV errors occur caused by, for example, locally poor seeding caused by the particles being forced out of the vortex centre. Overall, however,

the study has revealed a number of interesting features pertaining to the global flow, and the accuracy considerations with regards the PIV should not detract from the experiment and the discernable features of the overall flowfield.

Chapter 6: Concluding Remarks and Future Work Recommendations

Results from a series of wind tunnel tests of an Orthogonal Blade-Vortex Interaction have been presented. The tests were conducted using a Particle Image Velocimetry technique in order to determine the (u,v,w) components of velocity in planes parallel to the blade.

The vortex core contains an appreciable axial flow component, which is observed to undergo a significant level of deformation as the interaction progresses. As the core passes close over the leading edge and onto the surface of the interacting blade, two highly distinctive flow patterns are observed over either side of the interacting blade. The retardation of the flow on the blade lower surface leads to a rapid redistribution of the fluid into the surrounding flow, and the corresponding enlargement and distortion to the vortex tangential velocity components promoted by the radial outflow. The effects of the interaction over the lower surface are observed to diminish quickly with increasing distance from the blade surface. As the vortex passes over the upper surface of the blade the vortex axial flow is blocked on the lower blade surface and requires reestablishment further from the blade surface. Regions of negative axial flow velocity indicate the presence of some fluid passing down through the core towards the surface of the blade, which are accompanied by a split divergence pattern around the vortex core. Moving away from the surface of the blade, there are again no real signs of persistence of the effects of the interaction on the vortex. The features observed during the upper surface interaction are so subtle, however, that the measurement noise is almost as significant as the features of the interaction. The effects immediately behind the trailing edge continue to be of interest due to the manner in which the vortex might be regenerated after the interaction and before any subsequent interactions with following blades. As the vortex passes off the trailing edge, it rapidly develops a coherent structure, although there are now striking dissimilarities between the portions from the upper to lower

surface sides of the blade. A relative lack of distortion within the out-of-plane component indicates that a rapid regeneration of the axial flow component may occur once the vortex has passed over the trailing edge.

The use of passive control techniques in reduction of the effects associated with the orthogonal BVI have also been addressed, considering the effect of a counter-rotating vortex pair on the progression of the interaction. Although the inclusion of a notch in the leading edge and outboard sweep on the rotor blade producing the representative trailing tip vortex did produce a well defined inboard vortex structure, there is evidence to suggest that this structure is ingested into the outboard tip vortex, as there is no significant modification to the progression of the OBVI.

In considering the major features of this interaction, it is clear that while the progression of the interaction on the lower surface side is relatively well understood, there are still a number of questions pertaining to the nature of the interaction on the upper surface side. Further investigation of this component is required in order to clarify the manner in which the regeneration of the axial flow component progresses, as this has not been suitably addressed through the use of PIV. Any future work should be directed to concentrate on this regeneration process in order to fully characterize the manner in which this occurs, concentrating specifically on the interactional process close to the surface of the interacting blade as it has been shown that the features imparted to the core are highly localized to the blade surface. As close interrogation of the blade surface is not possible using the PIV technique, due to the blade curvature, another technique needs to be adopted in order to examine this in more detail.

Additionally, there is a requirement for further work in the potential regeneration of the trailing vortex within the trailing edge region. As this is important in determining the potential for the vortex to undergo multiple interactions, a complete understanding of the passing of the two halves of the vortex core into the trailing edge region and their subsequent behaviour is needed. Again, as the curvature of the

blade leads to problems with obtaining information close to the trailing edge using the PIV technique, another method (LDA, HWA) should be employed in order to characterize this region of the flow.

References & Bibliography

References

Adrian, R,J. (1991) 'Particle Imaging Techniques for Experimental Fluid Mechanics' *Annu. Rev. Fluid Mech.* 23 pp 261-304

Affes, H. & Conlisk, A.T. (1993) 'Model for Rotor Tip Vortex-Airframe Interaction. Part 1: Theory' *AIAA J.* vol. 31 pp 2263-2273

Affes, H., Conlisk, A.T., Kim, J.M. & Komerath, N.M. (1993) 'Model for Rotor Tip Vortex-Airframe Interaction. Part 2: Comparison with Experiment' *AIAA J.* vol. 31 pp 2274-2282

Affes, H., Xiao, Z. & Conlisk, A.T. (1994) 'The Boundary-Layer Flow due to a Vortex Approaching a Cylinder' *J. Fluid Mech.* vol. 275 pp33-57

Affes, H., Xiao, Z., Conlisk, A.T., Kim, J.M. & Komerath, N.M. (1998) 'Model for Rotor Tip Vortex-Airframe Interaction. Part 3: Viscous Flow on Airframe' *AIAA J.* vol. 36 pp409-415

Arroyo, M.P. & Greated, C.A. (1991) 'Stereoscopic Particle Image Velocimetry' *Meas. Sci. Tech.* 2 pp 1181-1186

Bebesel, M., Ploz, G. & Shoell, E. (1999) 'Aerodynamic and Aeroacoustic Layout of the ATR (Advanced Technology Rotor)' *American Helicopter Society 55th Annual Forum*, Montreal, Canada

Bi, N. & Leishman, J.G. (1990) 'Experimental Study of Rotor/Body Interactions' *J.Aircraft* vol. 27 pp 779-788

Bi, N., Leishman, J.G. & Crouse, G.L. (1993) 'Investigation of Rotor Tip Vortex Interaction with a Body' *J. Aircraft* vol. 30 pp 879-888

Bodstein, G.C.R., George, A.R. & Hui C-Y. (1996) 'The Three Dimensional Interaction of a Streamwise Vortex with a Large Chord Lifting Surface' *J. Fluid Mech.* 322 pp51-79

Brand, A., Komerath, N.M. & McMahon, H.M. (1989) 'Results from Laser Sheet Visualization of a Periodic Rotor Wake' *J. Aircraft* 26 pp 438-443

Brentner, K.S. & Farassat, F. (1994) 'Helicopter Noise Prediction : The Current Status and Future Direction' *Journal of Sound and Vibration* 170 (1) pp 79-96

Brocklehurst, A. & Pike, A.C. (1994) 'Reduction of BVI noise using a Vane Tip' *AHS Aeromechanics Specialists Conference,* San Francisco

Brooks, T.F. (1993) 'Studies of the Blade-Vortex Interaction Noise Reduction by Rotor Blade Modification' *Proceedings of the 1993 National Conference on Noise Control,* Williamsburg, VA pp57-66

Caradonna, F. X. and Tung, C. (1981) " Experimental and Analytical Studies of a Model Helicopter Rotor in Hover, *Vertica,* vol. 5, no. 2, 1981, pp. 149-161

Cary, C.M. (1987) 'Experimental Investigation of the Chopping of Helicopter Main Rotor Tip Vortices by the Tail Rotor Part II: High Speed Photographic Study' *NASA* CR-177457

Cesnik, C.E.S., Shin, S. & Wilbur, M.L. (2001) 'Dynamic Response of Active Twist Rotor Blades' *Smart Material Struct.* 10 pp 62-76

Chen, P.C., Baeder, J.D, Evans, R.A.D. & Niemczuk, J. (2001) 'Blade-Vortex Interaction Noise Reduction Technology with Active Twist Smart Rotor Technology' *Smart Mater. Struct.* 10 pp 77-85

Chigier, N.A. & Corsiglia, V.R. (1971) 'Tip Vortices – Velocity Distributions' *27th AHS Forum*, May 1971

Cohn, R.K. & Koochesfahani, M.M. (1993) 'Effect of Boundary Conditions on Axial Flow in a Concentrated Vortex Core' Phys. Fluids A 5 pp 280-282

Conlisk, A.T. (2001) 'Modern Helicopter Rotor Aerodynamics' *Progress in Aerospace Sciences* 37 pp 419-476

Copland, C.M. (1997) 'The Generation of Tranverse and Longitudinal Vortices in Low Speed Wind Tunnels' *PhD Thesis,* Dept. Aerospace Engineering, University of Glasgow

Copland, C.M., Coton, F.N. & Galbraith, R.A.McD. (1998) 'An Experimental Study of the Idealised Vortex System of a Novel Rotor Blade Tip' *Aero. J.* pp 385-391

Coton, F. N., Green, R. B., Early, J., and Wang, T. (2001) "An Investigation of the Effect of Tip Vortex Mass Injection of Blade Vortex Interaction " *27th European Rotorcraft Forum,* Moscow, Russia, Sept. 2001

Coton, F.N., Galbraith, R.A. McD., Wang, T. & Newman, S.J. (2004) 'A wind-tunnel based study of helicopter tail rotor blade vortex interaction' *Aero. J.* vol. 1083 no.4 pp 237-244

Coton, F.N., Marshall, J.S., Galbraith, R.A.McD. & Green, R.B. (2004) 'Helicopter Tail Rotor Orthogonal Blade-Vortex Interaction' *Progress in Aerospace Sciences* 40, pp 453-486

Coudert, S.J.M. & Schon, J.P. (2001) 'Back-projection algorithm with misalignment corrections for 2D3C stereoscopic PIV' *Meas. Sci. Tech.* 12 pp 1371-1381

Crow, S.C. (1970) 'Stability Theory for Pairs of Trailing Vortices' *AIAA Journal* 8

Doolan, C.J., Green, R.B., Coton, F.N. & Galbraith, R.A.McD. (2000a) 'The Orthogonal Blade-Vortex Interaction Experimental Programme at the University of Glasgow' *26th European Rotorcraft Forum*, The Hague

Doolan, C.J., Coton, F.N. & Galbraith, R.A.McD. (2000b) ' The Effects of a Preceeding Blade on the Orthogonal Blade-Vortex Interaction' *56th American Helicopter Society Forum*

Doolan, C.J., Coton, F.N. & Galbraith, R.A.McD. (1999) 'Measurement of Three-Dimensional Vortices using a Hot Wire Anemometer' *30th AIAA Fluid Dynamics Conference*, Norfolk, VA

J.M. Early, R.B. Green & F.N. Coton (2002) 'Investigation of the Orthogonal Blade-Vortex Interaction using Particle Image Velocimetry' *The Aeronautical Journal 106, March 2002*

Edwards, B. & Cox, C. (2002) 'Revolutionary Concepts for Helicopter Noise Reduction — S.I.L.E.N.T Program' *NASA Technical Report* CR-2002-211650

Ellin, A.D.S. (1994) 'Lynx Main Rotor/ Tail Rotor Interactions : Mechanisms and Modelling' *Proc. Instn. Mech. Engrs.* 208 pp 115-128

Gossler, A.A. & Marshall, J.S. (2001) 'Simulation of normal vortex-cylinder interaction' *J. Fluid Mech.* Vol. 431 pp 371-405

Green, R.B., Doolan, C.J. & Cannon, R.M. (2000) 'Measurements of the Orthogonal Blade-Vortex Interaction using a Particle Image Velocimetry Technique' *Exp. Fluids* 29 pp 369-379

R.B. Green, F.N. Coton & J.M. Early (2005) 'Experimental Observations of the Orthogonal Blade-Vortex Interaction' *submitted to Experiments in Fluids, November 2005*

Gursul, I. & Rockwell, D. (1990) 'Vortex Sheet Impinging Upon an Elliptical Leading Edge' *J. Fluid Mechanics*, vol. 211, pp 211-242

Gray, R. B. (1992) " Vortex-Modeling for Rotor Aerodynamics - The 1991 Alexander Nikolsky Lecture " *Journal of the American Helicopter Society*, January 1992, pp.3.14

Ham, N.D. (1987) 'Helicopter Individual Blade Control research at MIT 1977-1985' *Vertica* 11 pp 109-122

Ham, N.D. (1974) 'Some Preliminary Results from an Investigation of Blade-Vortex Interaction' *Journal of the American Helicopter Society*

Hardin, J.C. & Lamkin, S.L. (1986) 'Concepts for Reduction of Blade-Vortex Interaction Noise' *Journal of Aircraft* 24, no2

Hart, D.P. (1998) 'The Elimination of Correlation Errors in PIV Processing' *9th International Symposium on Applications of Laser Techniques to Fluid Mechanics*, Lisbon, Portugal, July, 1998

Horner, M.B., Galbraith, R.A. McD., Coton, F.N., Stewart, J.N. & Grant, I. (1992) 'Examination of Vortex Deformation during Blade-Vortex Interaction' *AIAA J.* vol. 34, pp1188- 1194

Howe, M.S. (1976) 'The Influence of Vortex Shedding on the Generation of Sound Convected by Turbulence' *J. Fluid Mech.* 76 pp 711-740

Huang, H., Dabiri, D. & Gharib, M. (1997) 'On Errors of Digital Particle Image Velocimetry' *Meas.Sci. Tech.* 8 1427–1440.

Johnson, W. (1986) 'Recent Developments in Rotary-Wing Aerodynamic Theory' *AIAA Journal* vol. 24, no.8, pp 1219-1244

Johnston, R.T. & Sullivan, J.P. (1992) 'Unsteady Wing Surface Pressures in the Wake of a Propeller' *AIAA Paper 92-0277*

Kaykayloglu, C.R. & Rockwell, D. (1985) 'Vortices Incident Upon a Leading Edge: Instantaneous Pressure Fields' *J. Fluid Mech.* 156 pp 439-461

Keane, R. D. & Adrian, R. J. (1990) "Optimization of Particle Image Velocimeters' *Measurement Science and Technology, Vol. 2, pp. 1202-1215*

Keane R.D. & Adrian, R.J. (1992) "Theory of cross-correlation of PIV images," *Applied Scientific Research, Vol. 49, pp. 191-215*

Kim, J.M. & Komerath, N.M. (1995) 'Summary of the Interaction of a Rotor Wake with a Circular Cylinder' *AIAA J.* vol. 33 pp 470-478

Krishnamoorthy, S. & Marshall, J.S. (1994) 'An Experimental Investigation of "Vortex Shocks"' *Phys. Fluids 6* (11) pp 3737-3741

Krishnamoorthy, S. & Marshall, J.S. (1998) 'Three Dimensional Blade-Vortex Interaction in the Strong Vortex Regime' *Physics of Fluids*, Vol. 10, No. 11, 1998, pp 2828-2845.

Krishnamoorthy, S., Gossler, A.A. & Marshall, J.S. (1999) 'Normal Vortex Interaction with a Circular Cylinder' *AIAA J.* vol. 37 pp 50-57

Kube, R. & Klöppel, V. (2001) 'On the Role of Prediction Tools for Adaptive Rotor System Developments' *Smart Material Struct.* 10 pp 137-144

Lecuona, A., Ruiz-Rivas, U. & Nogueira, J. (2002) 'Simulation of Particle Trajectories in a Vortex Induced Flow: Application to Seed-Dependent Flow Measurement Techniques' *Meas. Sci. Tech.* 13 pp1020-1028

Lee, J.A., Burggraf, O.R. & Conlisk, A.T. (1998) ' On the Impulsive Blocking of a Vortex Jet' *J. Fluid Mech.* 369 pp 301-331

Lee, S. & Bershader, D. (1991) 'An Experimental and Computational Study of 2D Parallel BVI' *AIAA* Paper 91-3277

Lee, S. & Bershader, D. (1994) 'Head On Parallel BVI' *AIAA J.* 32 pp 16-22

Leibovich, S. & Stewartson, K. (1982) 'A Sufficient Condition for the Stability of Columnar Vortices' *Journal of Fluid Mechanics* 126

Leishman, J.G. (1996) 'Seed Particle Dynamics in Tip Vortex Flows' *J. Aircraft* vol. 33 no.4 pp823-825

Leishman, J.G., Baker, A. & Coyne, A. (1996) 'Measurements of Rotor-Tip Vortices Using Three-Component Laser Doppler Velocimetry' *Journal of the American Helicopter Society,* October 1996, pp342-353

Leishman, J.G. (1998) 'Techniques for Flow Visualization of Helicopter Rotor Wakes' *8th International Symposium on Flow Visualization,* Naples, Italy

Leverton, J.W., Pollard, J.S. & Willis, C.R. (1977) 'Main Rotor Wake Interaction' *Vertica* 1 pp 213-221

Lewecke, T. & Williamson, C.H.K. (1998) 'Cooperative Elliptic Instability of a Vortex Pair' *Journal of Fluid Mechanics* 360 pp85-119

Liou, S.G., Komerath, N.M. & McMahon, H.M. (1990) 'Measurement of the Interaction between a Rotor Tip Vortex and a Cylinder' *AIAA J.* vol. 28 no. 6 pp 975-981

Liu, X. & Marshall, J.S. (2004) 'Blade Penetration into a Vortex Core with and without Axial Flow' *J. Fluid Mech.* vol 519, pp 81-103

Lowson, M.V. (1992) 'Progress Towards Quieter Civil Helicopters' *Aero. J.* pp 209-223

Lynn, R.R., Robinson, F.D., Batra, N.H. & Duhon, J.M (1970) 'Tail Rotor Design Part I : Aerodynamics' *Journal of the American Helicopter Society*

Mahalingam, R., Wong, O. & Komerath, N. (2000) ' Experiments on the Origin of Tip-Vortices' *AIAA Paper* 2000-0278

Marshall, J.S. (2002) 'Models of Secondary Vorticity Evolution during Normal Vortex-Cylinder Interaction' *AIAA J.* 40 pp 170-172

Marshall, J.S. & Yalamanchili, R. (1994) 'Vortex Cutting by a Blade, Part II : Computations of Vortex Response' *AIAA J.* 32 (7) pp 1428-1436

Marshall J. & Krishnamoorthy, S. (1997) 'On the Instantaneous Cutting of a Columnar Vortex with Non-Zero Axial Flow' *J. Fluid Mech.* 351 pp 41-74

Martin RM, Burley CL, Elliott JW (1989). 'Acoustic test of a model rotor and tail rotor: results for the isolated roto rand combined configuration'. NASA TM 101550, 1989.

Martin, P.B. & Leishman, J.G. (2002) 'Trailing Vortex Measurements in the Wake of a Hovering Rotor Blade with Various Tip Shapes' *58th Annual Forum of the American Helicopter Society*, Montreal, Canada,

Marze, H.J. & Phillipe, J.J. (1994) 'A Quiet Helicopter – a Research Program Today, A Reality Tomorrow' *20th European Rotorcraft Forum*, Amsterdam, Netherlands

Masson, C.A., Green, R.B., Galbraith, R.A.McD. & Coton, F.N. (1997) "An experimental investigation of a loaded blade interacting with single and twin vortices", *AHS Technical Specialists Conference,* Williamsburg, Virginia, U.S.A.

Masson, C.A., Green, R.B., Galbraith, R.A.McD. & Coton, F.N. (1998) "Experimental investigation of a loaded rotor blade's interaction with a single vortex", *The Aeronautical Journal,* Vol. 102, No. 1018, December 1998

McAlister, K.W., Tung, C. and Heineck, J.T. (2001) 'Forced Diffusion of Trailing Vorticity from a Hovering Rotor' *57th AHS Forum,* Washington

McCluer, M.S. (1996) *'Helicopter Blade-Vortex Interaction Noise with Comparison to CFD calculations' NASA Tech. Memorandum* 110423, December 1996

Melling, A. (1997) 'Tracer Particles and Seeding for Particle Image Velocimetry' *Meas. Sci. Tech.* 8

Merklinger, H.M. (1996) 'Scheimpflug's Patent' *Photo Techniques* Nov/Dec 1996

Neves, J.C., Moin, P. & Moser, R.D. (1994) 'Effects of Convex Transverse Curvature on Wall-Bounded Turbulence. Part 1. The Velocity and Vorticity' J. Fluid. Mech. Vol. 272 pp 349-381

Nishimura, Y., Kondo, N., Nakamura, H., Tsujiuchi, T., Yamakawa, E., Aoyama, T. & Saito, S. (1998) 'Comparison between calculated rotor noise and experimental data obtained by DNW test' *24th European Rotorcraft Forum*, Marseilles, France

Noguiera J., Lecouna A. & Rodriguez PA (1997) 'Data validation, false vector correction and derived magnitudes calculation on PIV data'. *Meas Sci Tech 8* :1493-1501

Okamoto, K. Nishio, S., Saga, T. & Kobayashi, T. (2000) 'Standard images for particle-image velocimetry' *Meas. Sci. Technol.* 11 pp 685-691

Perry, F.J., Wilby, P.G. & Jones, A.F. (1998) 'The BERP Rotor – How does it Work, and What has it been Doing Lately' *Vertiflite* 44 (2) pp 44-48

Philippe, J.J. & Armand, C. (1978) 'ONERA Aerodynamic Research on Helicopters' *AGARD* CP223

Poling, D.R., Dadone, L., Telionis, D.P. (1987) 'Blade-Vortex Interaction' *AIAA Paper* 87-0497, Reno, Nevada

Prasad AK, Adrian RJ;, Landreth CC & Offutt PW (1992) 'Effect of resolution on the speed and accuracy of particle image velocimetry interrogation' *Exp Fluids* 13: 105-116

Prasad, A.K. & Adrian, R.J. (1993) 'Stereoscopic Particle Image Velocimetry Applied to Liquid Flows' *Exp.Fluids* 15 pp49-60

Prasad, A.K. & Jensen, K. (1995) 'Scheimpflug stereocamera for particle image velocimetry in liquid flows' *Applied Optics* 34 no. 30 pp7092-7099

Qian, L. & Vezza, M. (1999) 'Simulation of parallel blade-vortex interaction using a discrete vortex method' *Aeronautical Journal,* vol. 103, 537-543, November 1999.

Ramaprian, B.R. & Zheng, Y. (1998) 'Near Field Of the Tip Vortex Behind an Oscillating Rectangular Wing' *AIAA Journal* vol.36 no.12

Rockwell, D. (1998) 'Vortex-Body Interactions' *Ann Review of Fluid Mechanics* 30

Russell, J.W., Sankar, L.N., Tung, C. & Patterson, M.T. (1997) 'Alterations of the Tip Vortex Structure using Passive Tip Devices' *53rd AHS Forum*, Virginia, 1997

Santa Maria, O.L. (1999) 'Two Dimensional Fourier Transform Applied to Helicopter Flyover Noise' *NASA Technical Report* TM-1999-209114

Schmitz, F.H., Gopalan, G. & Sim, B.W.C (2000) 'Flight Trajectory Management to Reduce Helicopter Blade-Vortex Interaction (BVI) Noise with Head/Tailwind effects' *26th Eurpean Rotorcraft Forum*, The Hague, The Netherlands, Sept. 26-29

Sherdian, P.F. & Smith, R.F. (1980) 'Interactional Aerodynamics – a New Challenge to Helicopter Technology' *J. Am. Helicopter Soc.* 25 pp 3-21

Smith, A., Nutt, D., Wilson, S., Rich, N., Hayward, S. & Heatherley, S. (2001) 'Noise and Insomnia : A Study of Community Noise Exposure, Sleep Disturbance, Noise Sensitivity and Psychiatric Disorders' *Final Report, UK Department of Health*

Soloff, S.M., Adrian, R.J. and Liu, Z.C. (1997) 'Distortion Compensation for generalized stereoscopic particle image velocimetry' *Meas.Sci. Tech.* 8 pp 1441-1454

Srinivas, V., Chopra, I., Haas, D. & McKool, K. (1993) 'Prediction of Yaw Control Effectiveness and Tail Rotor Loads' *19th European Rotorcraft Forum*, Cernobbio, Italy

Surendriah, M. (1969) 'An Experimental Study of Rotor Blade-Vortex Interactions' *MSc. Thesis,* Pennsylvania State University.

Thomson, W. (Lord Kelvin) (1880) 'Om the Stability of Steady and of Periodic Fluid Motions' *Phil. Mag.* 10

Tucker, B. & Conlisk, A.T. (1992) 'Massive Vortex Motion in the Presence of Solid Boundaries' *Phys. Fluids A* 4 pp 290-305

Tung, C., Pucci, S.L., Caradonna, F.X. & Morse, H.A. (1983) 'The Structure of Trailing Vortices Generated by Model Rotor Blades' *Vertica* vol. 7 no.1 pp 33-43

Tyler, D.J. & Vincent, A.H. (1996) 'Future Rotorcraft Technology Developments' *Aero. J.*, December 1996

Van der Wall, B.G (2000) 'The effect of HHC on the vortex convection in the wake of a helicopter rotor' *Aerosp. Sci. Technol.*4 pp 321-336

Van Oord, J. (1997) 'The design of a stereoscopic DPIV system' *Delft University of Technology MEAH Report* 161

Vuillet, A. (1990) 'Rotor and Blade Aerodynamic Design' *AGARD-R-781,* Aerodynamics of Rotorcraft

Walker, S. (2002) 'Two-axes Scheimpflug focusing for particle image velocimetry' *Meas.Sci. Tech.* 13 pp 1-12

Wang, T., Doolan, C.J., Coton, F.N. & Galbraith, R.A.M. (2002) 'Experimental Study of the Three Dimensionality of Orthogonal Blade-Vortex Interaction' *AIAA Journal* Vol.40, no.10 pp2037-2045

Westerweel, J. (1997) 'Fundamentals of digital particle image velocimetry' *Meas. Sci. Tech.* Volume 8, Number 12, pp 1379-1392

Westerweel, J., Dabiri, D. & Gharib, M. (1997) 'The effect of a discrete window offset on the accuracy of cross-correlation analysis of digital PIV recordings' *Experiments in Fluids 23* (1997) 20-28

Widnall, S.E. & Wolfe, T.L. (1980) 'Effect of Tip Vortex Structure on Helicopter Noise due to Blade-Vortex Interaction' *J. Aircraft* 17 pp 705-711

Wilder, M.C. & Telionis, D.P. (1998) 'Parallel Blade Vortex Interaction' *Journal of Fluids and Structures*, Vol. 12, pp. 801-838

Willert, C. (1997) 'Stereoscopic digital particle image velocimetry for application in wind tunnel flows' *Meas. Sci. Tech.* 8 pp 1465-1479

Xiao, Z., Buurgraaf, O.R. & Conlisk, A.T. (1997) 'The Interacting Boundary-Layer Flow due to a Vortex Approaching a Cylinder' *J. Fluid Mech.* vol. 346 pp 319-343

Yeager, W.T., Noonan, K.W., Singleton, J.D., Wilbur, M.L. & Mirick, P.H. (1997) 'Performance and Vibratory Load Data from a Wind-Tunnel Test of Model Helicopter Main Rotor Blade with a Paddle Type Tip' *NASA Tech. Report 4754*

Yu, Y.H. (2000) 'Rotor Blade-Vortex Interaction Noise' *Progress in Aerospace Sciences* 36 pp 97-115

Yu, Y.H., Gmelin, B., Splettstoesser,W., Phillipe, J., Prieur, J. & Brooks, T.F. (1997) 'Reduction of Helciopter Blade-Vortex Interaction Noise by Active Rotor Control Technology' *Prog. Aerospace Sci.* 33 pp 647-687

Zang, W. & Prasad, A.K. (1997) 'Performance Evaluation for a Scheimpflug stereocamera for particle image velocimetry' *Applied Optics* 36 no.33 pp 8738-8744

Ziada, S. & Rockwell, D. (1982) 'Vortex Leading Edge Interaction' *J. Fluid. Mech.* 118 pp79-107

Bibliography

Basset, A.D. (1888) 'Treatise on Hydrodynamics Vol I' *Deighton, Bell & Co.*

Bramwell, A.R.S., Done, G. & Balmford, D. (2001) 'Bramwell's Helicopter Dynamics' *Butterworth-Heinemann*

Durst, F. (1981) 'Principles and Practices of Laser Doppler Anemometry' *Academic Press*

Leishman, J.G. (2000) 'Principles of Helicopter Aerodynamics' *Cambridge University Press*

Press, W.H., Teukolsky, S.A., Vettering, W.T. & Flannery, B.P. (1992) 'Numerical Recipes in C' *Cambridge University Press pp 683-638*

Prouty, R.W. (1986) 'Helicopter Performance, Stability and Control' *Boston PWS Engineering*

Raffel M, Willert C. & Kompenhaus J (1998) 'Particle Image Velocimetry' *Springer-Verlag*

Saffman, P.G. (1992) 'Vortex Dynamics' *Cambridge University Press*